



HAL
open science

Simulating the density of organic species in the atmosphere of Titan with a coupled ion-neutral photochemical model

V. Vuitton, R.V. Yelle, S.J. Klippenstein, S.M. Hörst, P. Lavvas

► **To cite this version:**

V. Vuitton, R.V. Yelle, S.J. Klippenstein, S.M. Hörst, P. Lavvas. Simulating the density of organic species in the atmosphere of Titan with a coupled ion-neutral photochemical model. *Icarus*, 2019, 324, pp.120-197. 10.1016/j.icarus.2018.06.013 . hal-03038393

HAL Id: hal-03038393

<https://hal.science/hal-03038393>

Submitted on 3 Dec 2020

HAL is a multi-disciplinary open access archive for the deposit and dissemination of scientific research documents, whether they are published or not. The documents may come from teaching and research institutions in France or abroad, or from public or private research centers.

L'archive ouverte pluridisciplinaire **HAL**, est destinée au dépôt et à la diffusion de documents scientifiques de niveau recherche, publiés ou non, émanant des établissements d'enseignement et de recherche français ou étrangers, des laboratoires publics ou privés.

Simulating the density of organic species in the atmosphere of Titan with a coupled ion-neutral photochemical model

V. Vuitton^a, R. V. Yelle^b, S. J. Klippenstein^c, S. M. Hörst^d, P. Lavvas^e

^a*Institut de Planétologie et d'Astrophysique de Grenoble, Univ. Grenoble Alpes, CNRS, Grenoble, 38000, France*

^b*Lunar and Planetary Laboratory, Univ. of Arizona, Tucson, AZ 85721, USA*

^c*Chemical Sciences and Engineering Division, Argonne National Lab., Argonne, IL 60439, USA*

^d*Department of Earth and Planetary Sciences, Johns Hopkins Univ., Baltimore, MD 21218, USA*

^e*Groupe de Spectrométrie Moléculaire et Atmosphérique, Univ. Reims Champagne-Ardenne, CNRS, Reims, 51687, France*

Abstract

We present a one-dimensional coupled ion-neutral photochemical kinetics and diffusion model to study the atmospheric composition of Titan in light of new theoretical kinetics calculations and scientific findings from the Cassini-Huygens mission. The model extends from the surface to the exobase. The atmospheric background, boundary conditions, vertical transport and aerosol opacity are all constrained by the Cassini-Huygens observations. The chemical network includes reactions between hydrocarbons, nitrogen and oxygen bearing species. It takes into account neutrals and both positive and negative ions with masses extending up to about 100 u. We incorporate high-resolution isotopic photoabsorption and photodissociation cross sections for N_2 as well as new photodissociation branching ratios for CH_4 and C_2H_2 . Ab initio transition state theory calculations are performed in order to estimate the rate coefficients and products for critical reactions.

Main reactions of production and loss for neutrals and ions are quantitatively assessed and thoroughly discussed. The vertical distributions of neutrals and ions predicted by the model generally reproduce observational data, suggesting that for the small species most chemical processes in Titan's atmosphere and ionosphere are adequately described and understood; some differences are highlighted. Notable remaining issues include (i) the total positive ion density (essentially $HCNH^+$) in the upper ionosphere, (ii) the low mass negative ion densities (CN^- , C_3N^-/C_4H^-) in the upper atmosphere, and (iii) the minor oxygen-bearing species (CO_2 , H_2O) density in the stratosphere. Pathways towards complex molecules and the impact of aerosols (UV shielding, atomic and molecular hydrogen budget, nitriles heterogeneous chemistry and condensation) are evaluated in the model, along with lifetimes and solar cycle variations.

Keywords: Titan, atmosphere, Ionospheres, Atmospheres, chemistry, Photochemistry, Organic chemistry

1. Introduction

Titan is a fascinating world, with its dense (1.5 bars on the surface) and cold (70 - 200 K) atmosphere, and its layers of orange haze that extend to almost 1000 km above its surface. As on Earth, the main atmospheric molecule is nitrogen (N_2). The second most abundant molecule in Titan's atmosphere is methane (CH_4); Titan's surface conditions are near its triple point resulting in a cycle (evaporation, condensation, precipitation) similar to that of water on Earth. Consequently, Titan is the object of the solar system whose superficial structure is the closest to that of the Earth and it has many of the same physical processes as the Earth but they are based on a completely different chemistry. The few percent of methane and the low amount of oxygen (mainly carried by carbon monoxide, CO) make the atmosphere more chemically reducing than present day Earth, where chemistry is based on oxidizing processes linked to the presence of oxygen. The study of Titan's chemistry thus provides the opportunity to determine how the organic nitrogen molecules involved in the chemistry of living organisms (e.g. nitrogen bases, amines ...) can be generated naturally in a planetary environment (Hörst et al., 2012).

Understanding the chemistry that takes place in Titan's atmosphere is an intimidating task because of the multiplicity of chemical and physical processes involved. Chemical processes begin with the dissociation and ionization of N_2 and CH_4 by solar ultraviolet radiation and energetic particles, which provide the H, C, and N atoms necessary for the synthesis of complex organic molecules. The species produced react with the ambient gas to generate a multitude of molecules which will gradually grow to become micron size solid particles, or aerosols. Thus, molecular growth is induced by gas phase reactions which involve radicals as well as positive and negative ions, possibly in excited states and also probably by heterogeneous chemistry on the surface of aerosols. The efficiency and the products of these reactions depend strongly on the physical characteristics of the atmosphere: pressure and temperature. In addition, the distribution of species is affected by molecular diffusion, vertical and horizontal winds, as well as the escape of the lightest compounds and the condensation of the heaviest compounds in the lower stratosphere. A diagram illustrating the atmospheric chemistry of Titan is shown in Figure 1 of Hörst (2017).

The Voyager 1 mission to Saturn in 1980 and subsequent Earth-based observations identified more than a dozen neutral hydrocarbons, nitriles and oxygen-bearing species. From 2004 to 2017, the Cassini spacecraft has observed Titan *in situ* and by remote sensing and has made exceptional discoveries. In the upper atmosphere, it detected the presence of positively and negatively charged ions with m/z reaching up to thousands of atomic mass units (Waite et al., 2007; Coates et al., 2009; Cray et al., 2009; Coates et al., 2010), revealing that Titan has the most compositionally complex ionosphere in the Solar System. It

42 became clear that these extremely complex particles are the precursors of the
43 aerosols known to be present at lower altitude. Also, energetic OH_x^+ ($x = 0-3$)
44 ions have been observed in Saturn’s magnetosphere in the vicinity of Titan (Har-
45 tle et al., 2006) and could be at the origin of the oxygen-bearing compounds.
46 Finally, the $^{14}\text{N}/^{15}\text{N}$ ratios in N_2 , HCN and CH_3CN have been retrieved and are
47 one of the keys to furthering our understanding of the energy sources, primary
48 processes and therefore the evolution of the atmospheric molecular complexity
49 (Vuitton et al., 2014).

50 A large number of chemical models of the atmosphere were created prior
51 to the Cassini mission, with main focus on the ionosphere (Keller et al., 1992;
52 Fox and Yelle, 1997; Keller et al., 1998; Galand et al., 1999), the stratosphere
53 (Yung et al., 1984; Toublanc et al., 1995; Lara et al., 1996), both (Banaszkiewicz
54 et al., 2000; Wilson and Atreya, 2004) or the galactic cosmic rays (GCR) in-
55 duced layer (Molina-Cuberos et al., 1999a,b, 2002). They mostly explained
56 the neutral composition in the stratosphere but their predictions regarding the
57 thermosphere turned out to be incomplete. For example, it was predicted that
58 HCNH^+ , C_2H_5^+ and CH_5^+ would be abundant but many of the ion species de-
59 tected by Cassini were not anticipated. Also, the presence of negative ions was
60 not predicted in the ionosphere. This triggered the re-examination of Titan’s
61 upper atmospheric chemistry and put a strong emphasis on ion chemistry.

62 Motivated by the return of the first in situ measurements of Titan’s upper
63 atmospheric composition, we developed a 0D ionospheric model to constrain
64 the density of minor neutral constituents (Vuitton et al., 2006b). The model
65 assumed local chemical equilibrium and adopted atmospheric conditions appro-
66 priate for the 1100 km level. The densities of neutral species were fixed at
67 values determined during the outbound portion of the T5 flyby, that was deep
68 into the nightside. The relative abundance of the primary ions was calculated
69 for a mixture of N_2 and CH_4 irradiated by 100 eV magnetospheric electrons
70 and the magnitude of the ion production was scaled to reproduce the electron
71 density measured by the Langmuir probe. The chemical network included ~ 40
72 neutrals, ~ 150 ions and ~ 1250 reactions. We showed that the most abundant
73 positive ions are closed-shell species because radical cations are not very sta-
74 ble and therefore react quickly. This implies that while odd mass channels are
75 attributed to hydrocarbon ions, peaks at even m/z are the signature of ions con-
76 taining one nitrogen atom. All ion-molecule reactions do not necessarily lead to
77 molecular growth because proton transfer to molecules having a higher proton
78 affinity, typically nitrogen-bearing species, is very efficient. We determined that
79 the density of ions depends strongly on the composition of the neutral atmo-
80 sphere and inferred the presence of the most complex molecules identified so far
81 on Titan. This includes $\text{C}_2\text{H}_3\text{CN}$ and $\text{C}_2\text{H}_5\text{CN}$, whose presence was recently
82 confirmed by ALMA (Cordiner et al., 2015b; Palmer et al., 2017).

83 In order to study the distribution of benzene, this model was later extended
84 to 1D and daytime conditions (Vuitton et al., 2008). The calculations allowed
85 retrieval of the integrated vertical production rate of C_6H_7^+ . In parallel, we
86 constructed an independent 1D neutral photochemical-diffusion model focused
87 on benzene. The model included eddy and molecular diffusion. The solar irra-

88 diation was based on a solar spectrum obtained with the EUV flux model for
89 Aeronomic Calculations (EUVAC) and was representative of a global average,
90 while the temperature and total density were representative of the equatorial re-
91 gion. The chemical network consisted of 40 hydrocarbon species, ~ 130 neutral-
92 neutral reactions and ~ 40 photodissociation reactions. These models predicted
93 that the globally averaged production rate of benzene by ion-molecule reactions
94 is $\sim 10^7 \text{ cm}^{-2} \text{ s}^{-1}$, of the same order of magnitude as the production rate by
95 neutral reactions of $\sim 4 \times 10^6 \text{ cm}^{-2} \text{ s}^{-1}$. We showed that benzene is quickly
96 photolyzed in the thermosphere and that C_6H_5 radicals, the main photodisso-
97 ciation products, react primarily with other radicals, leading to the formation
98 of complex aromatic species. These species, along with benzene, diffuse down-
99 ward, eventually condensing near the tropopause. We found a total production
100 rate of solid aromatics of $\sim 10^{-15} \text{ g cm}^{-2} \text{ s}^{-1}$, corresponding to an accumulated
101 surface layer of $\sim 3 \text{ m}$.

102 In order to investigate the chemistry of oxygen-bearing species, ten oxygen-
103 bearing species participating in 32 reactions have been added by Hörst et al.
104 (2008) to the hydrocarbon network of Vuitton et al. (2008). The sources of
105 oxygen in this model are the precipitation of O and OH or H_2O into the upper
106 atmosphere. We modeled these assuming a Chapman production function with
107 a peak at 1100 km for O (from O^+ deposition calculations) and 750 km for OH
108 and H_2O . We showed that using an oxygen flux consistent with the reported
109 observations of the Ion Mass Spectrometer (IMS), one of the sensors of the
110 Cassini Plasma Spectrometer (CAPS) and an OH flux consistent with predicted
111 production from micrometeorite ablation allowed the model to reproduce the
112 observed abundances of CO, CO_2 and H_2O available at that time.

113 Independently, Lavvas et al. (2008a,b) presented a 1D photochemical-microphysical
114 model, whose main objective was the understanding of the atmospheric pro-
115 cesses that lead to haze formation. The model incorporated detailed radiation
116 transfer calculations providing the vertical structure of the radiation field and
117 temperature profile. Gaseous species photochemistry initiated the production
118 of the haze precursors, while their evolution was described by the microphysical
119 part of the model. The calculated aerosol and gas opacities were iteratively
120 included in the radiation transfer calculations in order to investigate their effect
121 on the resulting temperature profile and geometric albedo. 68 neutral hydro-
122 carbon and nitrile species were included in the photochemical calculations, the
123 evolution of which was controlled by about 520 reactions. Ions or ion chemistry
124 were not included. Pathways providing the stronger contribution to the haze
125 production supported the incorporation of nitrogen, with a major peak between
126 500 and 900 km.

127 Following the detection of negative ions, their chemistry was taken into ac-
128 count in an ionospheric model for the first time (Vuitton et al., 2009). This
129 lead to the identification of CN^- , $\text{C}_3\text{N}^-/\text{C}_4\text{H}^-$ and C_5N^- in the negative ion
130 spectrum, which was recently confirmed by a reanalysis of the Electron Spec-
131 trometer (ELS) data, one of the sensors making up the Cassini Plasma Spec-
132 trometer (CAPS) (Desai et al., 2017). We found that these ions are essentially
133 formed by dissociative attachment of electrons with energies of a few eV onto

134 trace neutral species. Just as with positive ions, proton transfer reactions lead
135 to the formation of heavier negative ions. Finally, ions are lost by associative
136 detachment reactions with the most abundant radicals, typically H and CH₃.

137 The ion and neutral models presented in Vuitton et al. (2008) were turned
138 into a self-consistent ion-neutral chemistry model to investigate the formation of
139 NH₃ and CH₂NH in the upper atmosphere (Yelle et al., 2010). Some aspects of
140 the neutral photochemistry as well as the treatment of eddy and molecular diffu-
141 sion were based on Hörst et al. (2008), while the N chemistry was adapted from
142 Lavvas et al. (2008a). From the measured abundance of NH₄⁺ and CH₂NH₂⁺,
143 we established that NH₃ and CH₂NH have a large abundance in the upper
144 atmosphere and that it is the consequence of coupled ion and neutral chemistry.

145 Lavvas et al. (2011a) used high-resolution cross sections for the neutral pho-
146 todissociation of N₂ between 80 and 100 nm and provided a different picture
147 of energy deposition compared to results based on low-resolution cross sections.
148 Our results showed that the contributions of both photons and photoelectrons
149 are required for the accurate representation of the chemical precursors in the
150 upper atmosphere. The highly structured cross sections imply that photons
151 experience a smaller absorption by N₂ and are able to penetrate deeper in the
152 atmosphere. The main consequence is that ionization of methane to CH₄⁺ takes
153 place at lower altitudes, close to 800 km, which affects significantly the CH₄⁺
154 production.

155 Vuitton et al. (2012) included these detailed calculations for the energy de-
156 position in the coupled ion-neutral photochemical model described in Yelle et al.
157 (2010). The hydrocarbon chemistry was updated with new chemical parameters
158 for association reactions based on ab initio TST calculations. These calculations
159 indicate that association reactions are fast even at low pressure for adducts hav-
160 ing as few as four C atoms. Although the column-integrated production and
161 condensation rates of hydrocarbons change only by a factor of a few, the mole
162 fractions can increase by as much as one order of magnitude in the upper at-
163 mosphere.

164 Lavvas et al. (2015) presented a detailed model for the vibrational popula-
165 tion of all non pre-dissociating excited electronic states of N₂, as well as for the
166 ground and ionic states. The calculations demonstrate that a significant popu-
167 lation of vibrationally excited ground state N₂ survives in the upper atmosphere
168 but the implications on the ionospheric densities are negligible.

169 In this paper, we present a globally representative picture of the under-
170 standing of Titan’s atmospheric chemistry post Cassini-Huygens. We base our
171 investigations on the comparison of the Cassini data with a one-dimensional
172 coupled ion-neutral photochemical kinetics and diffusion model developed in
173 our previous targeted studies (Vuitton et al., 2006b, 2007; Hörst et al., 2008;
174 Vuitton et al., 2008, 2009; Yelle et al., 2010; Lavvas et al., 2011a; Vuitton et al.,
175 2012; Lavvas et al., 2015). In section 2, we present a detailed description of
176 the model, highlighting the new constraints brought by Cassini-Huygens for the
177 model atmosphere, boundary conditions and vertical transport, as well as our
178 improved chemical scheme. A unique aspect of the model is a detailed investi-
179 gation of numerous reaction pathways including new theoretical calculations of

180 reaction rate coefficients. The next two sections are dedicated to the main out-
 181 put of the model: the atmospheric chemical composition. In section 3, we focus
 182 on the main reaction pathways for the production and loss of ions and neutrals.
 183 A review of available observations is given in section 4 before comparing them
 184 to the present and other model results. In section 5, we pinpoint several impor-
 185 tant aspects of Titan’s chemistry, starting from molecular weight growth and
 186 the subsequent effect of aerosols, and further discussing species lifetimes and
 187 expected variations in density profiles induced over the course of a solar cycle.
 188 Finally, in section 6, we present our conclusions before reviewing the issues that
 189 are still remaining.

190 2. Photochemical Model

191 2.1. General Description

192 The development of the photochemical model described herein and the asso-
 193 ciated investigations has been motivated by the tremendous harvest of composi-
 194 tional information from the Cassini mission. Cassini has operated for more than
 195 thirteen years, but despite its extended dataset covering daily (De La Haye et al.,
 196 2008; Cui et al., 2009a), seasonal (Lebonnois et al., 2001; Bampasidis et al.,
 197 2012; Coustenis et al., 2013) and latitudinal variations (Crespin et al., 2008;
 198 Teanby et al., 2006; Teanby et al., 2008a, 2009), sampling remains inadequate
 199 to study geophysical variations and therefore constrain the circulation patterns.
 200 We therefore aim here at establishing the chemistry that is applicable to low- and
 201 mid-latitudes, a required step before more sophisticated tools capturing diurnal/
 202 latitudinal/seasonal variations can be devised. Our approach to constrain
 203 the model atmosphere and vertical transport is to average all available mea-
 204 surements in order to reproduce the global-mean conditions. We subsequently
 205 compare the species density profiles to the dayside equatorial and mid-latitude
 206 observations.

207 Our model includes the region from the surface to 1500 km, the nominal
 208 exobase, with a grid spacing of 5 km. It solves the one-dimensional coupled
 209 continuity and diffusion equation for each active species,

$$\frac{\partial N_i}{\partial t} = P_i - L_i - \frac{1}{r^2} \frac{\partial(r^2 \Phi_i)}{\partial r}, \quad (\text{E1})$$

210 where N_i is the density of species i , P_i and L_i are its chemical production and
 211 loss terms and Φ_i the vertical flux. The radius $r = (R_0 + z)$, where R_0 is the
 212 radius of Titan and z is the altitude. Steady-state conditions are assumed such
 213 that $\partial N_i / \partial t = 0$. The chemical production of the i th species is given by:

$$P_i = \sum_j \sum_k R^{i,jk} k_{jk} N_j N_k + \sum_l J^{i,l} N_l + \gamma_e^{i,m} N_m + \gamma_{GCR}^{i,n}, \quad (\text{E2})$$

214 where k_{jk} is the rate coefficient of the reaction between species j and k producing
 215 species i , $R^{i,jk}$ is the branching ratio of the channel leading to i , $J^{i,l}$ is the
 216 photodissociation/photoionization rate coefficient of species l leading to i , $\gamma_e^{i,m}$

217 is the production rate through electron impact on species m and $\gamma_{GCR}^{i,n}$ is the
 218 production rate through galactic cosmic rays.
 219 The chemical loss of the i th species is given by:

$$L_i = \sum_j k_{ij} N_i N_j + J_i N_i. \quad (\text{E3})$$

220 Here, k_{ij} is the rate coefficient of the reaction between species i and j and J_i is
 221 the photolysis rate coefficient of species i .

222 We find solutions for the chemical abundances by integrating the coupled
 223 continuity equations forward in time until a steady-state is reached. We use a
 224 fully implicit Newton-Raphson technique to advance densities to the next time
 225 step. The stability of the implicit integration allows us to achieve long simulation
 226 times. To judge if a run is converged we examine both the change in density
 227 from one time step to the next and the balance of production, loss, and flux
 228 divergence in the continuity equation. Because some molecular species on Titan
 229 have extremely long chemical lifetimes (CO in particular) the time integration
 230 must be very long to reach steady-state. This is achieved by using increasing
 231 time steps, reaching eventually 10^{20} s or larger. We know from experience with
 232 the model that even time steps of $10^8 - 10^{10}$ seconds are inadequate to reach
 233 convergence. We consider that convergence is achieved when the balance of
 234 production, loss, and flux divergence is a small fraction of the largest of those
 235 terms. This relative balance is less than 10^{-6} for all species and reaches machine
 236 precision for many species.

237 *2.2. Background Structure*

238 *2.2.1. Model Atmosphere*

239 The main reservoirs of nitrogen, carbon, hydrogen and oxygen in Titan's
 240 atmosphere are N_2 , CH_4 and CO. Their detection poses the question of their
 241 origin. They could be a primordial remnant, they could be supplied to the
 242 atmosphere from the interior or surface, or they could be delivered to the at-
 243 mosphere from an external source; their abundance has likely varied over the
 244 course of Titan's history. It is not our goal to address these questions here.
 245 Since their lifetime is extremely long compared to the time it takes to generate
 246 photochemically produced molecules (cf. section 5.4), we keep their vertical
 247 profiles fixed to their current values. However, we will see that although minor
 248 hydrocarbons and nitrogen-bearing species are the daughter species of nitrogen
 249 and methane photochemistry, the origin of minor oxygen-bearing species cannot
 250 be CO only and that an external source of oxygen is required. We will return
 251 to this in section 4.2.3.3 and focus here on the background atmosphere for our
 252 photochemical model.

253 The background atmosphere is based on Cassini observations of the main
 254 constituents, N_2 , $^{14}N^{15}N$, and CH_4 . To create a global/temporal mean we
 255 simply average all of the Ion Neutral Mass Spectrometer (INMS) measurements
 256 of these species. A similar average was presented and discussed in Cui et al.
 257 (2009b). The only difference between that average and the one used here is

258 that we now include data through T71. The average density profiles for N_2 and
 259 $^{14}N^{15}N$ are shown in Figure 1a, the average CH_4 profile in Figure 1b, and a
 260 temperature profile consistent with these averages is shown in Figure 3.

261 As discussed in Snowden et al. (2013), the temperature profile in Titan's
 262 upper atmosphere shows large pass-to-pass variations. When averaged over
 263 many passes though, the mean temperature in the upper atmosphere is 150 K.
 264 Temperatures in the stratosphere do not exhibit this pass-to-pass variability
 265 but vary strongly with season. Temperatures in the lower atmosphere vary
 266 far less, by only a few degrees from equator to pole. Our model temperature
 267 profile uses the HASI measurements below 200 km (Colombatti et al., 2008),
 268 assumes an isothermal stratosphere at 180 K between 200 and 500 km, an
 269 isothermal thermosphere at 150 K above 700 km, and connects the stratosphere
 270 and thermosphere with a linear temperature gradient. This temperature profile
 271 predicts N_2 and $^{14}N^{15}N$ density profiles that agree well with the mean of the
 272 measured values in the thermosphere, as shown in Figure 1a.

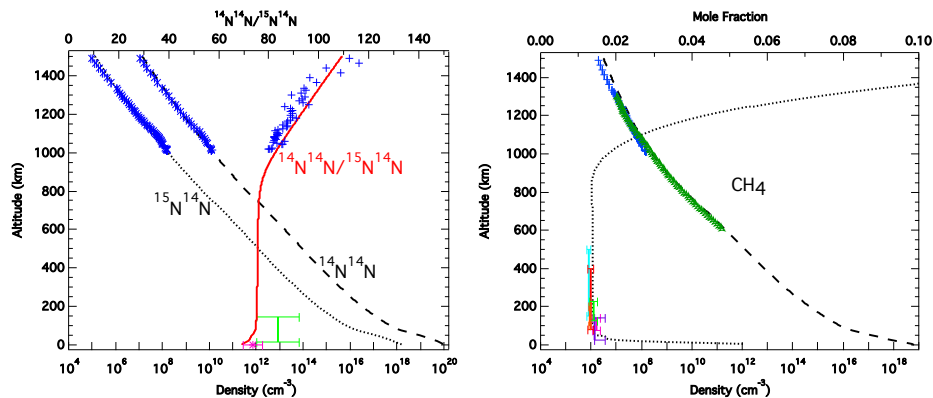


Figure 1: Density of the main constituents (model input and observations) versus altitude. Left panel: $^{28}N_2$ and $^{14}N^{15}N$ density, and $^{14}N^{14}N/^{14}N^{15}N$ ratio. The observations in the thermosphere are INMS data, while observations in the stratosphere are GCMS data from Niemann et al. (2010). Right Panel: Density (dashed line) and mole fraction (dotted line) of CH_4 . The observations are listed in Table 1.

273 The CH_4 density model is based on the mixing ratios measured with GCMS,
 274 CIRS, and DISR in the lower atmosphere reaching a value of 0.014 above the cold
 275 trap near 70 km. The mole fraction remains constant from that altitude to the
 276 lower thermosphere, near 800 km, where it starts to increase with altitude due to
 277 diffusive separation. The strength of diffusive separation, i.e. the eddy diffusion
 278 coefficient, is determined from the ^{40}Ar profile (shown in Figure 2). It has been
 279 a puzzle that this eddy coefficient over predicts the speed of diffusive separation
 280 of CH_4 . Several authors have interpreted this as evidence for enhanced escape
 281 of CH_4 (Yelle et al., 2008; Strobel, 2008; Cui et al., 2012), but the physical
 282 mechanisms for enhanced escape are not understood (Tucker et al., 2016). We
 283 do not further investigate this dilemma here but simply impose an enhanced
 284 escape velocity at the upper boundary in order to produce a CH_4 distribution

Table 1: Summary of the observational data on Titan’s methane composition.

Altitude (km)	Mixing Ratio (%)	Instrument	Reference
600-1200		UVIS	Koskinen et al. (2011)
800-1300		UVIS	Stevens et al. (2015)
150-500	1.28 ± 0.06	VIMS	Maltagliati et al. (2015)
~80-400	1.33 ± 0.07	<i>Herschel</i> -SPIRE	Courtin et al. (2011)
~100-200	1.29 ± 0.03	<i>Herschel</i> -PACS	Rengel et al. (2014)
125-225	$1.41 \pm 0.1^{(a)}$	CIRS	Lellouch et al. (2014)
75-140	1.48 ± 0.09	GCMS	Niemann et al. (2010)
27-141	$1.44(+0.27/-0.11)$	DISR-ULIS	Bézard (2014)

^(a)At 30°N.

285 that matches the observations.

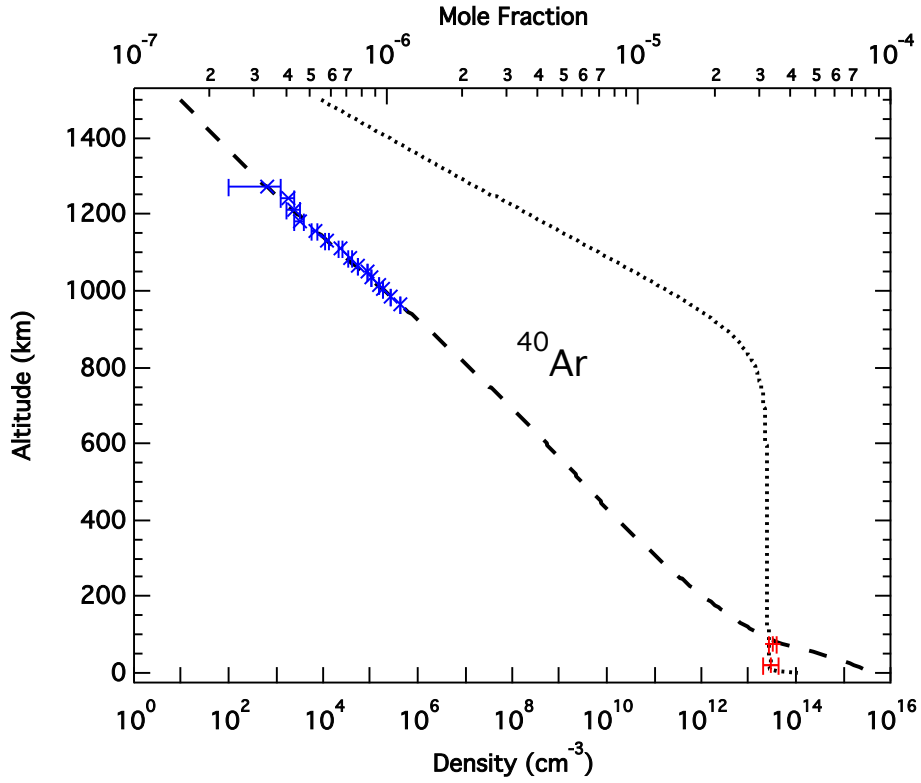


Figure 2: Density (dashed line) and mole fraction (dotted line) of ^{40}Ar (model input and observations) versus altitude. The observations in the thermosphere (blue) are INMS data, while observations in the stratosphere (red) are GCMS data from Niemann et al. (2010).

286 For some of the models discussed here we also hold the CO profile constant.

287 As discussed in section 4.2.3.3, the lifetime of CO in Titan’s atmosphere is much
288 longer than the vertical mixing time. For the models with CO held constant,
289 we fix the mole fraction at the surface to the observed value of 50 ppm and
290 calculate a diffusive equilibrium profile under the effects of molecular and eddy
291 diffusion (cf. Figure 59).

292 *2.2.2. Electron Temperature*

293 The electron temperature profile also affects the chemistry on Titan, pri-
294 marily through the temperature dependence of the electron-ion recombination
295 rate coefficient. Electron temperatures on Titan have been measured with the
296 Langmuir Probe (LP) channel of the Radio and Plasma Wave System (RPWS)
297 instrument (Wahlund et al., 2005). As with the neutral temperature profile we
298 construct an electron temperature profile that is smoothly varying and consis-
299 tent with the general trends of the LP measurements. The electron temperature
300 rises rapidly through the main ionosphere, reaching values of ~ 1000 K near the
301 exobase at ~ 1400 km. At lower altitudes, where the collision rate is large,
302 the electron temperature should be equal to the neutral temperature (Richard
303 et al., 2011). Langmuir probes are not able to measure temperatures this low.
304 We therefore set the electron temperature equal to the neutral temperature at
305 altitudes below 800 km and have it increase linearly with altitude throughout
306 the thermosphere at a rate that is consistent with the LP measurements. Results
307 are shown in Figure 3.

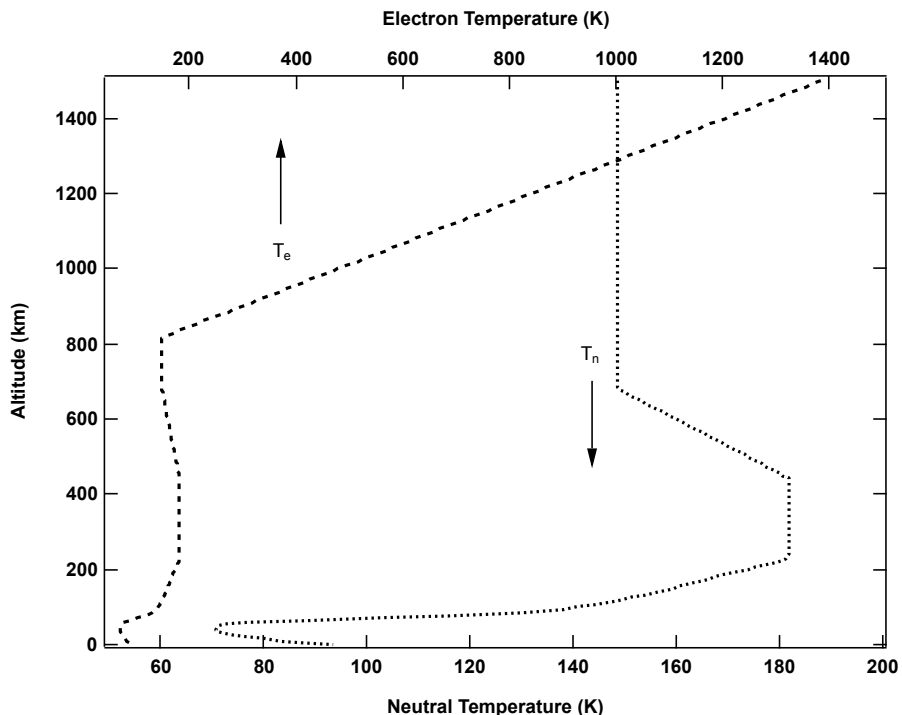


Figure 3: The neutral (lower axis) and electron temperatures (upper axis) used as model inputs. Note that the scales for T_n and T_e are different and that as a consequence, both temperatures do not overlap below 800 km, even though they are set equal.

308 2.3. Boundary Conditions

309 Most of the photochemically active species in Titan's atmosphere are too
 310 heavy to escape from the top of the atmosphere. The exceptions are atomic and
 311 molecular hydrogen and for these species we set the velocity at the top of the
 312 model equal to the Jeans escape velocity, i.e. $1.5 \times 10^4 \text{ cm}^{-2} \text{ s}^{-1}$ and 1.52×10^3
 313 $\text{cm}^{-2} \text{ s}^{-1}$, respectively. We use a zero velocity upper boundary condition for all
 314 other species. As mentioned earlier, although CH_4 may be escaping, we treat
 315 its distribution as fixed and it therefore requires no boundary condition.

316 Most of the photochemical species in Titan's atmosphere will condense near
 317 the tropopause (discussed in section 5.3.4) and the densities at lower altitudes
 318 become vanishingly small. Surface boundary conditions for these species are
 319 therefore not particularly important. We specify a downward velocity of 10^3 cm
 320 s^{-1} to simulate condensation on the surface, but these species have all condensed
 321 before they reach the surface. The exceptions are H_2 and CO which do not
 322 condense at Titan temperatures. For these species we specify zero velocity at
 323 the surface.

324 As discussed in section 4.2.3.3, the influx of oxygen species from the external
 325 environment into Titan's atmosphere has a significant affect on the chemistry.
 326 English et al. (1996) investigated the delivery of water into Titan's atmosphere

327 by precipitation of micrometeorites and calculated that peak ablation occurs
 328 around 750 km resulting in an integrated H₂O deposition rate of 2.5×10^6
 329 cm⁻² s⁻¹. CAPS detected high energy (~ 1 keV) O⁺ ions precipitating from
 330 Saturn’s magnetosphere into Titan’s atmosphere, with a flux of $\sim 10^6$ cm⁻²
 331 s⁻¹ during flyby TA (Hartle et al., 2006). They mostly charge transfer with
 332 neutrals near 1100 km, forming a flux of thermal O atoms. In our previous work
 333 (Hörst et al., 2008) we modeled the O input to the atmosphere by specifying
 334 downward fluxes at the upper boundary. In the current model we specify an
 335 internal production profile for the incoming species, modeled as a Chapman
 336 function. The magnitude of the production rate is adjusted so that the column-
 337 integrated rate is equal to the expected input fluxes of O and OH to try to
 338 reproduce the observed abundances of CO, CO₂ and H₂O.

339 2.4. Vertical Transport

340 The bulk of Titan’s ionosphere is in chemical equilibrium and ambipolar
 341 diffusion can be ignored below 1200 to 1400 km (cf. Figure 6 in Cravens et al.
 342 (2009)). This includes the region with interesting ion chemistry and where ion
 343 chemistry produces neutrals. The vertical flux for neutral species is given by

$$\Phi_i = -D_i \left(\frac{\partial N_i}{\partial z} + \frac{N_i}{H_i} + \frac{N_i(1 + \alpha_i)}{T} \frac{dT}{dz} \right) - K \left(\frac{\partial N_i}{\partial z} + \frac{N_i}{H_a} + \frac{N_i}{T} \frac{dT}{dz} \right) \quad (\text{E4})$$

344 where D_i and α_i are the molecular and thermal diffusion coefficient of species
 345 i through the background N₂ atmosphere, T is the temperature, K is the eddy
 346 mixing coefficient that parameterizes large-scale motions, and H_i is the scale
 347 height of species i

$$H_i = \frac{RT}{m_i g} \quad (\text{E5})$$

348 where R is the gas constant, m_i the molecular weight of species i and g the
 349 gravity. H_a is the scale height of the background atmosphere.

350 The binary molecular diffusion coefficient D_i (cm² s⁻¹) of a molecule i in
 351 N₂ is

$$D_i = \frac{b_i}{N_a}, \quad (\text{E6})$$

352 with N_a the density of N₂ (cm³). b_i are model input parameters that are
 353 estimated for each constituent from experimental and theoretical information
 354 (cf. Appendix B.1).

355 An important step in one-dimensional photochemical models is the choice of
 356 an eddy mixing coefficient, $K(z)$, for the inclusion of turbulent diffusion effects
 357 on the vertical distribution of long-lived species. This parameter varies with

358 altitude and since it is difficult to predict from first principles, it is usually left as
359 a free parameter that has to be adjusted to best match constituent observations.

360 It has long been recognized that $K(z)$ must be small in the lower stratosphere
361 to reproduce the observed high levels of minor species above the condensation
362 region. Essentially, just above the condensation region $K(z)$ must be very low
363 so there is a barrier between the sources at high altitude and the sink at low
364 altitude, resulting in a buildup of large densities. It is one of the main reasons
365 for this complex chemistry on Titan. This requirement was implicit in the Yung
366 et al. (1984) photochemical model and has been assumed in all subsequent
367 models but has received little discussion.

368 Measurements of the mole fraction of ^{40}Ar by GCMS just above the surface
369 and by INMS around 1000 km provided the required constraints to render the
370 determination of $K(z)$ relatively robust. ^{40}Ar being an inert species, its vertical
371 profile is entirely governed by dynamics without any spurious effects from chem-
372 istry and it is expected to be depleted as a heavy species above the homopause
373 and uniformly mixed below (Yelle et al., 2008). Another species that has been
374 measured by both GCMS and INMS is $^{15}\text{N}^{14}\text{N}$ and it has also been used as
375 an independent tracer species for constraining the homopause altitude and the
376 eddy mixing profile (Bell et al., 2011; Mandt et al., 2012b). This determina-
377 tion however depends sensitively on the inter calibration of INMS and GCMS
378 and, as a consequence, is far less precise than use of ^{40}Ar . We note that the
379 uncertainty in the ^{40}Ar densities shown in Figure 2 are far smaller than those
380 displayed in Bell et al. (2011) and Mandt et al. (2012b). This is because the
381 densities in Figure 2 are a mean of the measurements and the uncertainty on
382 the mean is quite small. Bell et al. (2011) and Mandt et al. (2012b) confuse
383 geographic variability and uncertainty. The assumption behind our approach
384 is that by averaging over all INMS measurements we obtain and average over
385 the spectrum of eddies in the atmosphere, which is the requirement for an eddy
386 mixing approach to diffusion. In this view, the uncertainty in mean profile is far
387 smaller than the geographic/temporal variability of the densities and the eddy
388 diffusion coefficients in Titan’s upper atmosphere is accurately constrained.

389 In order to find the best tracer(s) for determining the eddy mixing coefficient
390 in the stratosphere, we calculate the chemical and transport time constants for
391 C_2H_6 , C_2H_2 , H_2O and HCN . The chemical time constant is estimated from
392 $t_C = N_i/L_i$ where N_i is the species density (in cm^{-3}) and L_i is the chemical
393 loss rate (in $\text{cm}^{-3} \text{s}^{-1}$). The time constant characterizing transport (diffusion
394 and eddy mixing) is estimated through $t_K = N_i/|\vec{\nabla} \cdot \vec{F}_i|$, where $\vec{\nabla} \cdot \vec{F}_i$ is the
395 divergence of the vertical flux (in $\text{cm}^{-3} \text{s}^{-1}$). Results are presented in Figure
396 4. We find that vertical transport dominates the C_2H_2 loss only in the 800-
397 400 km altitude range, while it dominates the C_2H_6 loss from 800 km down to
398 the tropopause. Moreover, C_2H_6 does not exhibit much latitudinal variation
399 in the stratosphere (cf. upper left panel of Figure 44), making C_2H_6 a better
400 tracer than C_2H_2 . H_2O is another good tracer for vertical mixing in the lower
401 atmosphere.

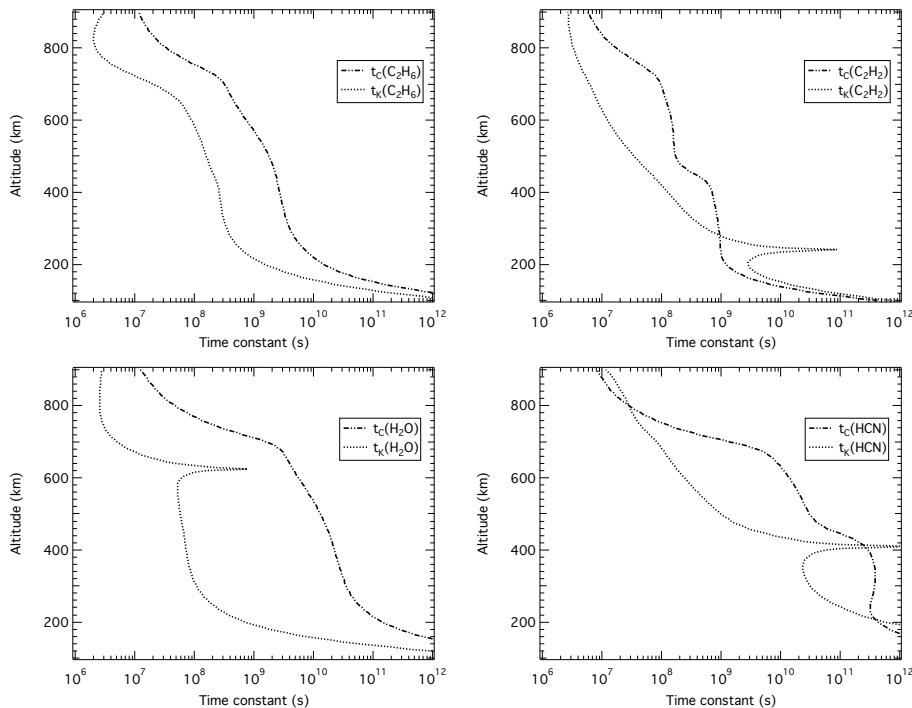


Figure 4: Chemical (t_C) and transport (t_K) time constant of C_2H_6 , C_2H_2 , H_2O and HCN versus altitude. These are results of our nominal model that are used to illustrate our choice of C_2H_6 as the best tracer. The spikes visible for t_K correspond to changes of the sign of the divergence of the vertical flux, i.e. to switches from production to loss of the transport term.

402 We computed the vertical profiles of the main neutral species with several
 403 possible profiles of the eddy mixing coefficient, obtained by varying K_0 , the
 404 lower atmosphere value, using as a starting point the values given in Yelle et al.
 405 (2008) and Hörst et al. (2008). We model the eddy mixing profile with:

$$K(z) = \frac{K_0(p_0/p)^\gamma K_\infty}{K_0(p_0/p)^\gamma + K_\infty}, \quad (E7)$$

406 where the subscript 0 refers to the value at 10^5 Pa and the subscript ∞ to the
 407 asymptotic value in the upper atmosphere. We determine that $K_0 = 300 \text{ cm}^2$
 408 s^{-1} , $K_\infty = 3 \times 10^7 \text{ cm}^2 \text{ s}^{-1}$, $p_0 = 10^5$ Pa and $\gamma = 1.5$ provide the best fit. The
 409 resulting nominal profile (K_{nom}), along with the methane molecular diffusion
 410 coefficient profile (D_{CH_4}), is shown in Figure 5, corresponding to a homopause
 411 level of 875 km. Results of the calculations with several possible K_0 are given
 412 for simple hydrocarbons (C_2H_2 , C_2H_6 , C_3H_8) and HCN , and compared with
 413 observational determinations in Figures 44, 45 and 51.

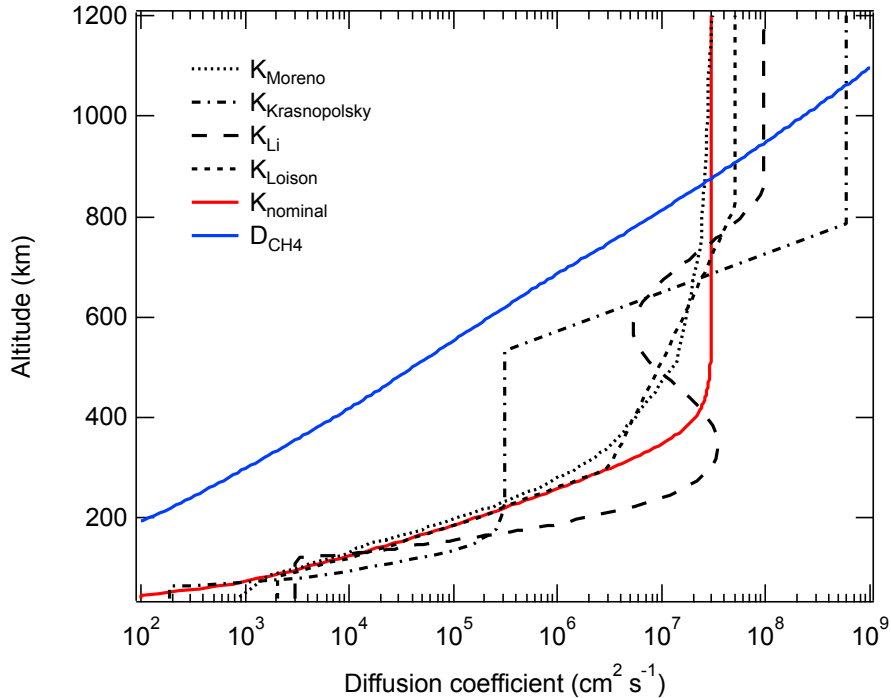


Figure 5: Plots of the nominal eddy mixing profile (solid red line) and methane molecular diffusion profile (solid blue line) used as model inputs. Also included are eddy mixing profiles from various photochemical models - Moreno et al. (2012) K2 (dotted line), Krasnopolsky (2012, 2014) (dot dashed line), Li et al. (2014) (long dashed line) and Loison et al. (2015) (short dashed line).

414 Before Cassini, a large variety of eddy mixing profiles were put forward
 415 (cf. Figure 3 of Lavvas et al. (2008b) for example). The methane vertical
 416 profile was used to retrieve the location of the homopause and the extent of
 417 turbulent mixing in the thermosphere, while hydrogen cyanide was used for
 418 the determination of mixing in the stratosphere. Nevertheless, the observations
 419 were equivocal and could not efficiently constrain $K(z)$ in the upper atmosphere.
 420 Vinatier et al. (2007a) suggested using the CIRS ethane values to constrain the
 421 eddy mixing coefficient in the stratosphere. As a saturated hydrocarbon, it has
 422 a low chemical reactivity and because its absorption cross-section in the UV
 423 region overlaps with that of methane, it is not efficiently photodissociated. The
 424 exact method is detailed in Lavvas et al. (2008b) and was used in most of the
 425 subsequent models, sometimes also adding H_2O as a tracer species (Hörst et al.,
 426 2008; Moreno et al., 2012; Loison et al., 2015). Krasnopolsky (2009, 2012) used a
 427 different approach where the eddy mixing profile is described by six parameters
 428 (three breakpoints altitudes and values) that are chosen to minimize the mean
 429 difference between the model and 63 observational points. The resulting profile
 430 differs significantly from all the other profiles with the homopause located at

431 1000 km instead of ~ 800 km (cf. Figure 5). Li et al. (2014) developed an
432 optimization method to retrieve the eddy mixing profile, with acetylene as the
433 tracer species. They base their choice of C_2H_2 on the low sensitivity of its
434 abundance to the uncertainties in reaction rate coefficients, which is attributed
435 to the dominant effect of vertical transport. The retrieved eddy profile features
436 are similar to the other profiles at the exception of a low eddy diffusion zone
437 near 550 km (cf. Figure 5), which the authors rationalize by aerosol heating
438 in the detached haze layer. Another interpretation of this feature is that it is
439 actually a wave (Koskinen et al., 2011), in which case the feature should not be
440 interpreted in terms of $K(z)$. The retrieved eddy mixing profiles are presented
441 in Figure 5.

442 2.5. Condensation

443 Because of the cold temperatures in Titan’s lower stratosphere, many gases
444 become saturated and condense according to their saturation vapor pressures.
445 We treat condensation in an empirical manner by specifying a chemical produc-
446 tion/loss rate that is proportional to the difference between the partial pressure
447 of the constituent and its saturation vapor pressure at the local atmospheric
448 temperature. We determine a proportionality constant of $10^6 \text{ erg}^{-1}\text{s}^{-1}$ through
449 trial and error. This value ensures that the partial pressure never significantly
450 exceeds the saturation vapor pressure, nor does it caused numerical stability
451 problems. The reader is referred to Lavvas et al. (2011b) for a discussion of the
452 detailed physics of the condensation process and its effect on the constituent
453 densities in the troposphere. The saturation expressions governing condensa-
454 tion are given for each neutral molecule in Table B.2.

455 2.6. Energy Input

456 Ionization and dissociation sources in the atmosphere of Titan include solar
457 extreme ultraviolet (EUV) and ultraviolet (UV) radiation, energetic photoelec-
458 trons (produced by solar X-ray and EUV radiation) and Saturnian magneto-
459 spheric electrons and ions. On the dayside, the dominant energy source is solar
460 UV radiation and associated photoelectrons (Lavvas et al., 2011a). Saturnian
461 magnetospheric electrons are dominant on the nightside but their contribution
462 is always much lower than solar radiation on the dayside (Ågren et al., 2009;
463 Galand et al., 2010). Cravens et al. (2008) demonstrate that energetic protons
464 and oxygen ions can also ionize the neutral species between 500 and 1000 km al-
465 titude but their contribution is small under typical conditions. Molina-Cuberos
466 et al. (2001) predict meteoritic ablation in the altitude range 600-800 km and
467 creation of long-lived metallic ions but this represents a weak source of ioniza-
468 tion overall. Galactic cosmic rays (GCR) generate some ionization in the lower
469 atmosphere, with a peak contribution around 100 km and a magnitude compa-
470 rable to ionization by solar photons in the upper atmosphere (Gronoff et al.,
471 2009). Our model accounts for solar UV and EUV photons, photoelectrons
472 and cosmic rays but neglects magnetospheric electrons and protons. Although
473 oxygen ions and meteorite influx of H_2O are considered as a source of oxygen
474 (section 2.3), they do not contribute to the overall ionization.

475 *2.6.1. Photons*

476 The model includes photolysis driven by absorption of solar photons between
477 0 and 300 nm. We use the TIMED/SEE level 3 data to represent the solar flux
478 at wavelengths from 0-80 nm and 100-200 nm (Woods et al., 2005). The solar
479 flux and photoabsorption cross sections in these regions are tabulated on a 1
480 nm wavelength grid. When cross sections are available at higher spectral res-
481 olution they are averaged to a 1 nm resolution for consistency with the solar
482 spectrum. This procedure is followed except between 80 and 100 nm, where ac-
483 curate representation of the high resolution structure of the N₂ cross section is
484 essential. In this region, we use the SOHO/SUMER whole disc spectra (Curdt
485 et al., 2013) to represent the shape of the solar spectrum. The SOHO/SUMER
486 spectrum is tabulated at a sampling of 0.0045 nm. For consistency with lower
487 and higher wavelengths, we normalize the net flux in the 80-100 nm region
488 for the SOHO/SUMER spectrum to be equal to that in the lower resolution
489 TIMED/SEE spectrum. We use the SOURCE SOLSTICE solar spectrum be-
490 tween 200 and 300 nm (Snow et al., 2005).

491 Cassini arrived at Saturn near the end of solar cycle 23 and the major-
492 ity of the observations of Titan were made during the extended solar mini-
493 mum between cycles 23 and 24. For most of the models presented here we use
494 TIMED/SEE spectra for 5 January 2008, the date of the T40 encounter. The
495 solar F10.7 index on this date was 75 sfu (Solar Flux Unit), close to its lowest
496 value. In section 5.5 we also consider the effects of higher solar activity levels
497 on Titan photochemistry and for these studies we use the solar spectrum for 7
498 April 2014, the date of the T100 encounter, when the F10.7 index was 109 sfu
499 (cf. Figure 6).

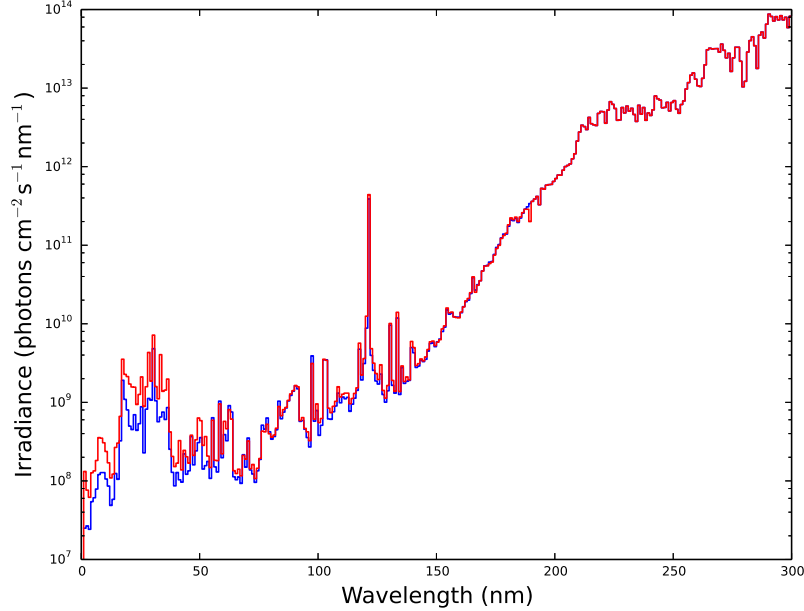


Figure 6: Solar irradiance at 1 AU (photons $\text{cm}^{-2} \text{s}^{-1} \text{nm}^{-1}$) versus wavelength (nm) used as model input. They were recorded on 5 January 2008, corresponding to solar minimum conditions (blue line) and 7 April 2014, corresponding to solar maximum conditions (red line).

500 Photolysis rate coefficients are given by

$$J_i^i(z) = \int_{\lambda} R_i^i(\lambda) \sigma_i(\lambda) I(z, \lambda) d\lambda \quad (\text{E8})$$

501 where λ is the wavelength, $\sigma_l(\lambda)$ is the absorption/ionization cross-section of
 502 species l as a function of wavelength, $R_l^i(\lambda)$ is the branching ratio of the channel
 503 leading to i and $I(z, \lambda)$ is the solar flux at altitude z and wavelength λ . To
 504 reproduce global mean conditions, all photolysis rates are calculated for a solar
 505 zenith angle of 60° and the solar flux at the top of the atmosphere is divided
 506 by 2 for diurnal averaging. This ensures that the column-integrated photolysis
 507 rates are $\frac{1}{4}$ the sub-solar values, as they should be for a global average.

508 2.6.2. Photoelectrons

509 The photoionization of a neutral species leads to the production of a positive
 510 ion along with a free electron (photoelectron). Suprathermal photoelectrons col-
 511 lide with neutral species, producing secondary ionization events and the cascade
 512 continues until the electrons have energies smaller than the ionization thresholds
 513 of the neutral species. Our calculations include photoelectron energy degrada-
 514 tion using a local energy deposition model, which is described in Lavvas et al.

515 (2011a). The model has been validated against the electron fluxes measured by
 516 CAPS and the far ultraviolet (FUV) emissions detected by UVIS. The resulting
 517 differential flux for electrons of less than 10 eV deviates from the CAPS ob-
 518 servations for altitudes above 1200 km, where the effects of electron transport
 519 are no longer negligible (cf. Figure 5a in Lavvas et al. (2011a)). However, the
 520 secondary electron production rates, with and without suprathermal electron
 521 transport, only differ by a factor of a few up to 1400 km (cf. Figure 5b in
 522 Lavvas et al. (2011a)). The calculated differential electron fluxes used as input
 523 in the model are presented in Figure 7 at several altitudes.

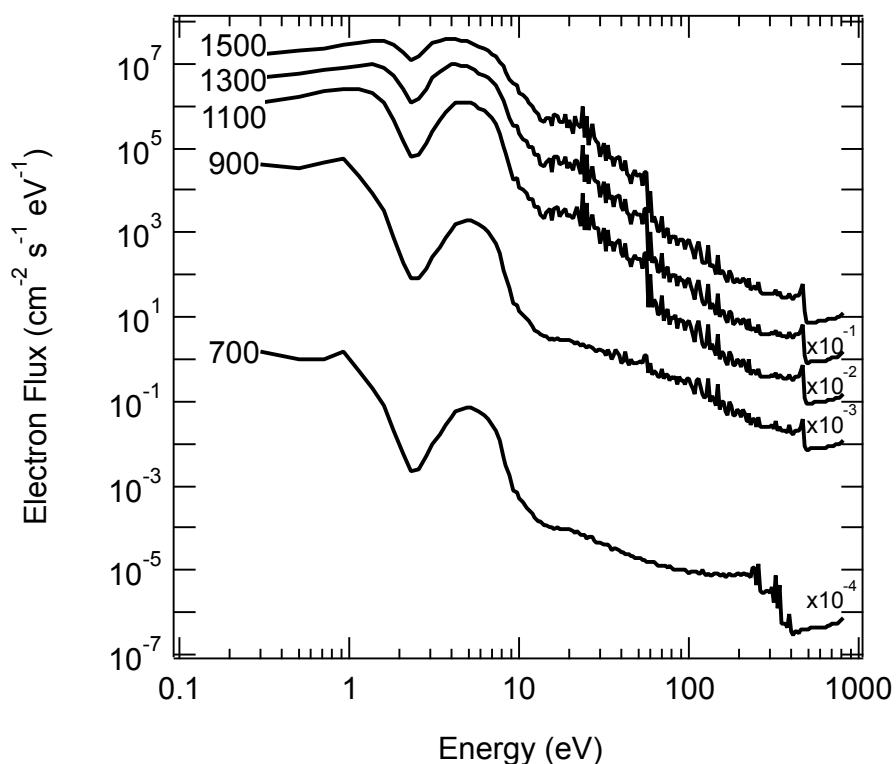


Figure 7: Calculated differential electron flux ($\text{cm}^{-2} \text{s}^{-1} \text{eV}^{-1}$) versus energy (eV) at 1500, 1300, 1100, 900 and 700 km.

524 2.6.3. Cross Sections and Branching Ratios

525 2.6.3.1. *Dissociation and Ionization.* We include in our model the photolysis
 526 of 47 species. The calculated rates of photodissociation $J_1^i(z)$ (equation E8)
 527 rely on the knowledge of their absorption cross-sections and branching ratios.
 528 They are obtained through dedicated laboratory experiments and/or theoretical
 529 calculations. The cross-sections and branching ratios used are listed in Tables
 530 B.5, B.6, B.7, B.8 and B.9. We describe the dissociation and ionization of N_2
 531 and CH_4 by both photons and photoelectrons from their dissociation threshold

532 (100 and 160 nm, respectively) to 1.5 and 11 nm, respectively. CO is largely
533 shielded from photolysis by N_2 and CH_4 but we do include photodissociation
534 and photoionization below 100 nm while predissociation in the electronic band
535 systems is not included. We also ignore H_2 photodissociation. H_2 photodis-
536 sociation occurs through predissociation in highly structured electronic bands,
537 like N_2 . Most of the photons will be absorbed in the more abundant N_2 and
538 CH_4 . Moreover, considering that CH_4 photolysis will produce far more H than
539 H_2 photolysis we choose to neglect H_2 photodissociation. Because its photolysis
540 cross-section is essentially unknown, we do not include either photodissociation
541 or photoisomerization of HNC in the model. HNC is highly reactive with all
542 radicals and photolysis is not expected to be a major loss for this species (cf.
543 discussion in Petrie (2001)). Hébrard et al. (2012) find that photolysis is a mi-
544 nor loss for HNC, assuming identical cross-sections and branching ratios as for
545 HCN. Photodissociation of other stable neutral molecules is considered between
546 their dissociation threshold and their ionization threshold. Again, nitrogen and
547 methane largely dominate the photon absorption in the region where ionization
548 of minor species becomes possible (typically below 145 nm, cf. Figure 15) and
549 the latter is therefore not included. In some cases (HC_3N , C_2N_2 , C_4N_2), cross-
550 sections are not available for the entire wavelength range and we fill in the gap
551 in the cross-sections by performing a linear interpolation between the available
552 datasets.

553 The cross-sections and branching ratios are often uncertain for several rea-
554 sons:

- 555 • Cross-sections are only known for a limited wavelength range, leading to
556 some systematic underestimation of the rate of photodissociation. For ex-
557 ample, Gladstone et al. (1996) points out that CH_3 cross-sections are only
558 available around 215 and 150 nm although photodissociation at shorter
559 wavelengths is expected. Another case is the lack of data at longer wave-
560 length for molecules that have a monotonically decreasing cross-section.
561 The solar flux increases rapidly in this wavelength range and even small
562 cross-sections can still substantially contribute to the total photodissocia-
563 tion. For example, Bénilan et al. (2000) showed that 25% of the rate
564 of dissociation of C_2H_2 is due to absorption above 205 nm, even though
565 the C_2H_2 cross-section decreases by four orders of magnitude between 150
566 and 220 nm.
- 567 • The temperature dependence of cross-sections is unavailable, leading to
568 some uncertainty in the rate of photodissociation. Cross-sections at 150 K
569 typically vary by tens of percents from the room temperature values, where
570 the majority of the cross-section data are measured (Jolly and Bénilan
571 (2008) and references therein). For our calculations, we utilize the values
572 obtained at the available temperature the closest to 150 K. The exact
573 temperature is indicated for each dataset in Table B.6.
- 574 • The determination of photo fragments is complex and there often are huge
575 discrepancies between branching ratios measured by different teams. A

576 most illuminating example is that of CH_4 for which the branching ratios
 577 at Lyman- α (121.6 nm) have been a subject of debate for more than
 578 50 years, as discussed in the review of laboratory experiments by Smith
 579 and Raulin (1999) and further below. Although fragments are known to
 580 be wavelength dependent, branching ratios are in the best case scenario
 581 available at only a few specific wavelengths and have to be extrapolated
 582 over the entire wavelength range, adding some huge uncertainty. As an
 583 example of highly unconstrained branching ratios, see the discussion about
 584 C_3H_6 further below.

585 The photochemistry of stable molecules has been studied in previous works
 586 (Hörst et al., 2008; Lavvas et al., 2008a; Krasnopolsky, 2009; Hébrard et al.,
 587 2013) and will not be discussed in detail here, except where revision is needed
 588 either because newer data have become available or because species have recently
 589 been detected on Titan and deserve some more scrutiny. We specifically discuss
 590 below the cross-sections and branching ratios for nine species: N_2 , $^{14}\text{N}^{15}\text{N}$, CH_4 ,
 591 C_2H_2 , C_3H_6 , C_4H_2 , HC_3N , $\text{C}_2\text{H}_3\text{CN}$ and $\text{C}_2\text{H}_5\text{CN}$.

592 **N_2 and $^{14}\text{N}^{15}\text{N}$.** The photodissociation and photoionization of $^{28}\text{N}_2$ have
 593 already been extensively discussed in Lavvas et al. (2011a) and a similar scheme
 594 is being used here (cf. Figure 8a). Table B.5 lists the adiabatic energy thresh-
 595 olds for the N_2 dissociation and ionization channels and the references used to
 596 establish their branching ratios and cross-sections.

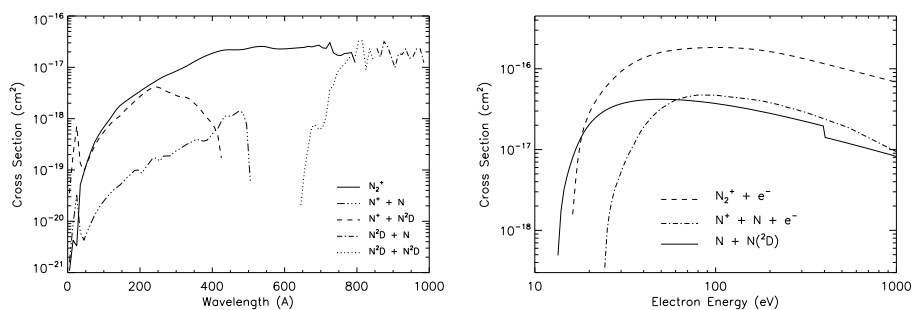


Figure 8: N_2 cross-sections for ionization and dissociation used as model inputs. (a) photons, (b) electrons.

597 Briefly, although the dissociation energy of N_2 is at 127 nm, absorption
 598 becomes significant only near 100 nm, mainly through predissociation transi-
 599 tions to Rydberg and valence states. These states have long enough lifetimes
 600 to display rotational and vibrational structures. The vibrational bands of the
 601 two isotopes $^{28}\text{N}_2$ and $^{29}\text{N}_2$ can be shifted by tens of wavenumbers and as the
 602 solar spectrum is also highly structured in this spectral region (cf. Figure 6),
 603 the radiative transfer calculation requires photoabsorption, photodissociation
 604 and photoionization cross-sections of high spectral resolution for both $^{28}\text{N}_2$ and

605 $^{29}\text{N}_2$. Isotope-selective shielding has been proposed to explain the ^{15}N enrich-
 606 ment observed in HCN compared to N_2 and to impact the vertical profiles of
 607 some minor species such as C_2H_6 and HCN (Liang et al., 2007; Luspay-Kuti
 608 et al., 2015; Dobrijevic et al., 2016).

609 Down to 79.5 nm, $^{28}\text{N}_2$ and $^{29}\text{N}_2$ cross-sections are computed at 150 K us-
 610 ing a coupled-channel Schrödinger equation quantum-mechanical model (Heays
 611 et al., 2011) and are presented in Figure 9. However, their accuracy decreases
 612 at shorter wavelengths and lower resolution laboratory measurements (Samson
 613 et al., 1987), which represent a lower limit to the true cross-sections, are used
 614 between 83.5 nm and the ionization threshold at 79.5 nm. Although formation
 615 of dissociative neutral Rydberg states can still occur below this wavelength, this
 616 process is largely dominated by the formation of N_2^+ . Between 79.5 and 66 nm,
 617 we improve on the Lavvas et al. (2011a) study by using the high resolution cross-
 618 sections measured by Shaw et al. (1992) that demonstrate significant structure
 619 in this wavelength range. With N_2^+ being essentially formed by photoionization
 620 above 1000 km, the convolution of the high resolution cross-sections with the
 621 solar flux could have some impact on the N_2^+ production rates.

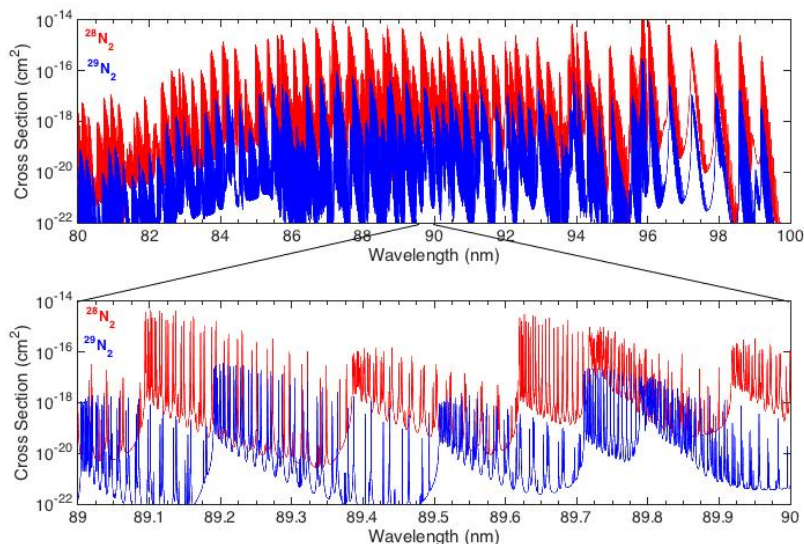


Figure 9: $^{28}\text{N}_2$ and $^{29}\text{N}_2$ photoabsorption cross-sections with a resolution of $3 - 5 \times 10^{-6}$ nm between 80 and 100 nm (upper panel) and in the narrow region between 89 and 90 nm (lower panel) used as model inputs.

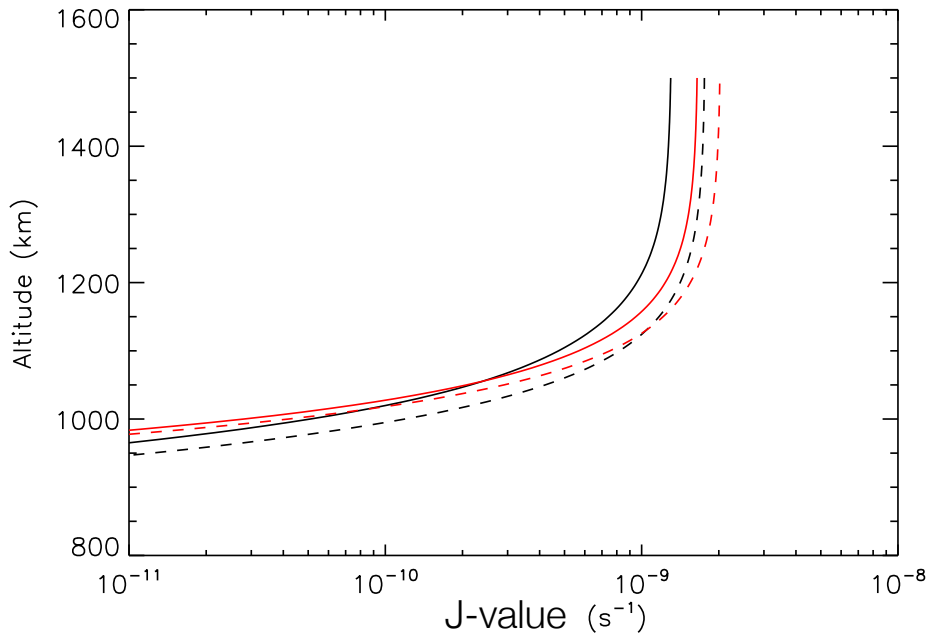
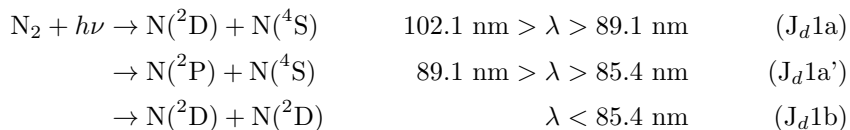


Figure 10: Photolysis rate coefficients (J values) for N_2 (solid lines) and CH_4 (dashed lines) from photons between 80 and 66 nm. Black lines correspond to calculations with the Shaw et al. (1992) cross-sections and red lines to the calculations with the Samson et al. (1987) cross sections.

622 Figure 10 compares the resulting photolysis rate coefficients (from photons
623 in the range 80 to 66 nm) with those derived with the model based on the lower
624 resolution (Samson et al., 1987) cross-sections. We see that the N_2 photolysis
625 rate coefficient in this region is lower with the higher resolution (Shaw et al.,
626 1992) cross-sections. This statement also holds for CH_4 , which is attributed to
627 the increase of the N_2 cross-sections in some regions of the spectrum. It is clear
628 though that the highly structured N_2 cross-section allows for more photons to
629 interact with CH_4 relative to the low resolution cross-sections. However, the
630 cross-sections update has little effect on the N_2^+ production rate, essentially
631 because of the small wavelength range impacted by the high resolution cross-
632 sections.

633 The $N(^4S)$, $N(^2D)$ and $N(^2P)$ production yields display a complex behavior
634 and are not well constrained. As explained in Lavvas et al. (2011a), a simplified
635 scheme that matches the experimental measurements is put forward and given
636 here:



637 Because of the low chemical reactivity of $N(^2P)$ and because its relative production
 638 versus that of $N(^2D)$ is not well constrained, we assume that all $N(^2P)$
 639 is converted to $N(^2D)$, as discussed in section 2.7.2.2.

640 Finally, the model includes electron-impact dissociation and ionization of
 641 N_2 from 15 to 1000 eV (cf. Table B.5 and Figure 8b). These cross sections are
 642 extensively reviewed in Lavvas et al. (2011a) and Lavvas et al. (2015) and the
 643 interested reader is referred to these paper for discussion of these processes.

644 **CH₄.** Table B.5 lists the adiabatic energy thresholds for the CH₄ dissociation
 645 and ionization channels and the references used to establish their branching
 646 ratios and cross-sections. With the exception of the dissociation branching ra-
 647 tios, the scheme used here is the same as in Lavvas et al. (2011a).

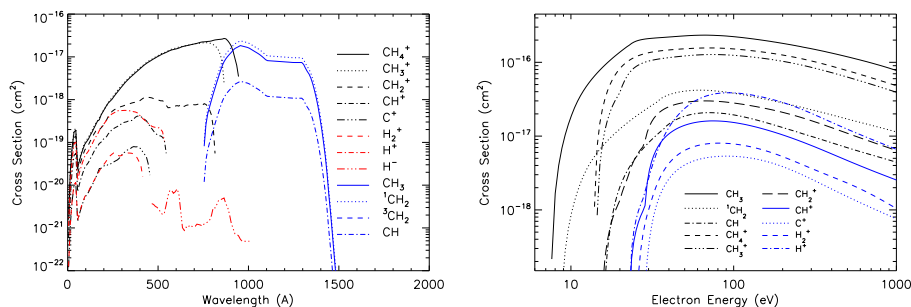


Figure 11: The CH₄ cross-sections for ionization and dissociation by photons (left panel) and electrons (right panel) used as model inputs.

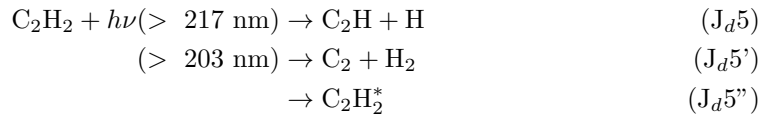
648 The dominant role of solar hydrogen Lyman- α in CH₄ photolysis was recog-
 649 nized early (Strobel, 1974; Allen et al., 1980; Yung et al., 1984). But, despite
 650 the large number of studies performed, the photodissociation of methane has
 651 long provided serious challenges to theoreticians and experimentalists alike: the
 652 branching ratios at Lyman- α have been accurately constrained only recently
 653 (Gans et al., 2011). The major improvement of this study is accurate character-
 654 ization of the molecular products of the various channels. A secondary finding of
 655 Gans et al. (2011) is that branching ratios are strongly wavelength-dependent.
 656 While Lyman- α contributes predominantly to the fragmentation of methane
 657 from the top of the atmosphere to 650 km, non-Lyman- α wavelengths become
 658 important below 700 km and branching ratios for these wavelengths are required
 659 as well (cf. section 2.6.4). We use a wavelength-dependent model (<121.6 nm
 660 / 121.6 nm / >121.6 nm) for CH₄ photolysis branching ratios, based on the
 661 values measured experimentally by Gans et al. (2011) and the sensitivity study
 662 of Gans et al. (2013):

	< 121.6 nm	121.6 nm	> 121.6 nm	
$\text{CH}_4 + h\nu \rightarrow \text{CH}_3 + \text{H}$	0.26	0.42	0.50	(J _d 2a)
$\rightarrow {}^1\text{CH}_2 + \text{H}_2$	0.17	0.48	0.50	(J _d 2b)
$\rightarrow \text{CH} + \text{H}_2 + \text{H}$	0.09	0.07	0.00	(J _d 2c)
$\rightarrow {}^3\text{CH}_2 + \text{H} + \text{H}$	0.48	0.03	0.00	(J _d 2d)

663 Photoionization of CH_4 into CH_x^+ ($x = 0-4$) and H_y^+ ($y = 1-2$) based on
664 Samson et al. (1989) is also included in the model (cf. Table B.5 and left panel
665 of Figure 11). The electron impact cross-sections for methane are presented in
666 the right panel of Figure 11. They are based on the references listed in Table
667 B.5, after Lavvas et al. (2011a).

668 **C₂H₂.** Acetylene plays an important role in the atmosphere of Titan, as
669 it absorbs significantly up to 235 nm (Bénilan et al., 2000), a region where the
670 intensity of solar radiation is significantly greater than in the regions of CH_4
671 (<160 nm) or N_2 (<100 nm) absorption. It is in this way that C_2H_2 participates
672 in the catalytic dissociation of CH_4 in the stratosphere as first described in Allen
673 et al. (1980).

674 A number of experiments were performed to determine the branching ratios
675 of the primary products of C_2H_2 photodissociation at various UV energies. All
676 the relevant studies have been summarized by Hébrard et al. (2006). Early
677 experiments (mainly performed employing static sample photolysis with end-
678 product analysis) indicated that the branching ratio for $\text{C}_2\text{H} + \text{H}$ was 0.10-0.30
679 and for $\text{C}_2 + \text{H}_2$ between 0.10 and 0.15. The main photochemical process was
680 believed to be the formation of an electronically excited metastable acetylene
681 and/or vinylidene molecule (Seki and Okabe, 1993):



682 Therefore, those two C_2H_2 dissociation channels have been considered in all the
683 photochemical models with comparable branching ratios. For instance, Lavvas
684 et al. (2008a) use 0.1 for the first channel, and for the second one use 0.1 at $\lambda <$
685 124 nm, 0.3 at $124 < \lambda < 150$ nm, 0.06 at $150 < \lambda < 190$ nm and 0.3 at 190
686 $< \lambda < 225$ nm. Krasnopolsky (2009) use a branching ratio of 0.3 for $\text{C}_2\text{H} + \text{H}$
687 and 0.1 for $\text{C}_2 + \text{H}_2$ in the entire wavelength range.

688 More recent experiments, performed under single collision conditions, have
689 questioned the validity of this assumption (cf., for instance, Boyé et al. (2002),
690 and references therein). Finally, the acetylene dissociation dynamics after pho-
691 toexcitation at 193 nm and at Lyman- α were studied under collision free con-
692 ditions by Läuter et al. (2002) and Kovács et al. (2010), who obtained an absolute

693 branching ratio for H atom formation close to unity, thus suggesting that the
694 ethynyl (C_2H) radical is the only molecular primary product for both energies.
695 In other words, C_2 is not formed directly by UV photolysis of C_2H_2 and we use
696 a branching ratio of one for channel (J_d5) from 100 to 225 nm, as reported in
697 Table B.6.

698 **C_3H_6 .** Nixon et al. (2013) reported the presence of propene in CIRS spec-
699 tra of Titan’s stratosphere, completing the detection of the C_3 -hydrocarbons
700 family, along with C_3H_8 and CH_3CCH . C_3H_6 absorbs up to 200 nm (Fahr and
701 Nayak, 1996) and although a dozen early studies have focused on the deter-
702 mination of its stable photodissociation products at five different wavelengths
703 ranging from 123.6 to 184.9 nm, the major channels are still far from being well
704 established.

705 The branching ratios used in previous photochemical models are presented
706 in Table 2 and highlight some huge discrepancies in the interpretation of the
707 published data. While Lavvas et al. (2008a) and Krasnopolsky (2009) use a
708 roughly similar photodissociation scheme with $C_3H_5 + H$ (J_d10b) being the ma-
709 jor products at longer wavelength, $C_3H_4 + H_2$ (J_d10e,f) at shorter wavelength
710 and $C_2H_3 + CH_3$ (J_d10c) throughout, Li et al. (2015) consider wavelength in-
711 dependent branching ratios giving only $C_3H_5 + H$ and $C_2H_3 + CH_3$. Hébrard
712 et al. (2013) utilized completely different channels with similar production of
713 $C_2H_2 + CH_4$ (J_d10a), $C_3H_5 + H$ (J_d10b), $C_2H_3 + CH_3$ (J_d10c) and $C_3H_3 + H_2 + H$
714 (J_d10g) at longer wavelength and a dominant production of $C_2H_2 + CH_4$ (J_d10a)
715 at shorter wavelength.

716 Considering the studies of Borrell et al. (1971) at 184.9 nm, of Collin and
717 coworkers (Collin et al., 1979; Collin, 1988) at 163.3, and of Niedzielski and
718 coworkers (Niedzielski et al., 1982; Naroznik and Niedzielski, 1986; Gierczak
719 et al., 1988) at 123.6 and 147.0 nm, we independently come to the conclusion
720 that $C_3H_5 + H$ (J_d10b) and $C_2H_3 + CH_3$ (J_d10c) as well as $C_3H_4 + H_2$ (J_d10e,f)
721 at shorter wavelengths should be the dominant photodissociation products, as
722 shown in Table B.6. This scheme is somewhat similar to that presented in Lavvas
723 et al. (2008a) and Krasnopolsky (2009) but is nevertheless highly uncertain.
724 Fortunately, we find that photodissociation only accounts for $\sim 15\%$ of the total
725 C_3H_6 loss, as explained in section 3.2.1.

Table 2: Branching ratios for C₃H₆ photolysis in several photochemical models.

Wavelength (nm)	Lavvas et al. (2008a)				Krasnopolsky (2009) ^(a)				Hébrard et al. (2013)	Li et al. (2015)	
	<135	<155	<175	<195	<135	<155	<175	<195	<160	< 190	all
(J _d 9a) C ₂ H ₂ + CH ₄ ^(b)	0.05	0.05	0.05	0.04	0.05	0.03	0.05	0.04	0.7	0.2	0.0
(J _d 9b) C ₃ H ₅ + H	0.0	0.0	0.565	0.60	0.0	0.0	0.56	0.41	0.0	0.2	0.6
(J _d 9c) C ₂ H ₃ + CH ₃	0.21	0.27	0.335	0.34	0.21	0.27	0.34	0.40	0.0	0.3	0.4
(J _d 9d) C ₂ H ₄ + ¹ CH ₂	0.06	0.04	0.02	0.0	0.06	0.04	0.02	0.03	0.0	0.0	0.0
(J _d 9e) CH ₃ CCH + H ₂	0.25	0.24	0.015	0.01	0.28	0.33	0.02	0.02	0.1	0.1	0.0
(J _d 9f) CH ₂ CCH ₂ + H ₂ ^(c)	0.43	0.40	0.015	0.01							
(J _d 9g) C ₃ H ₃ + H ₂ + H	0.0	0.0	0.0	0.0	0.0	0.0	0.0	0.0	0.2	0.2	0.0

^(a)The branching ratios do not sum to one in Krasnopolsky (2009).

^(b)C₂H₂ + CH₃ + H instead of C₂H₂ + CH₄ in Hébrard et al. (2013).

^(c)CH₃CCH + H₂ and CH₂CCH₂ + H₂ are undifferentiated in Krasnopolsky (2009), Hébrard et al. (2013) and Li et al. (2015).

726 **C₄H₂**. Diacetylene can absorb at even longer wavelengths than acetylene,
 727 up to 250 nm (Smith et al., 1998), to produce reactive species that can instigate
 728 catalytic hydrogen atom abstraction cycles as well as leading to the formation
 729 of heavier species, such as longer-chain polyynes (cf. section 3.2).

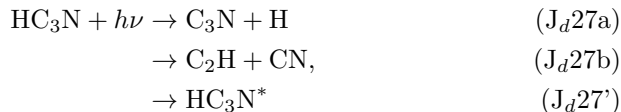
730 The photochemistry of diacetylene has been studied at 147.0, 184.9, 228.8
 731 and 253.7 nm in a pioneering study by Glicker and Okabe (1987). At 147
 732 nm, three dissociation channels were deduced (J_d12a,b,c). At the three other
 733 wavelengths, the disappearance of diacetylene was ascribed to the formation
 734 of an electronically excited metastable state, C₄H₂^{*}, assumed to be the lowest
 735 triplet state. Numerous laser-based studies, principally at 231 and 243 nm,
 736 investigated the reactivity of C₄H₂^{*} and found no evidence for radical products
 737 (Robinson et al. (2002) and references therein).

738 Lavvas et al. (2008a) and Krasnopolsky (2009) relied heavily on the study
 739 of Glicker and Okabe (1987) and both considered the following branching ratios
 740 for the photolysis of C₄H₂:

	< 165	165 – 205	> 205	
C ₄ H ₂ + hν → C ₄ H + H	0.20	0.00	0.00	(J _d 12a)
→ C ₂ H ₂ + C ₂	0.03	0.01	0.00	(J _d 12b)
→ C ₂ H + C ₂ H	0.10	0.06	0.00	(J _d 12d)
→ C ₄ H ₂ [*]	0.67	0.93	1.00	(J _d 12')

741 A recent experimental investigation of the photochemistry of diacetylene under
 742 collisionless conditions and after excitation at 121.6, 157.0, 193.3 and 212.0
 743 nm, coupled to statistical calculations suggests instead that radical formation,
 744 and in particular C₄H, is dominant at all wavelengths (Silva et al., 2008). We
 745 follow this study and adopt the branching ratio reported in Table B.6. As a
 746 consequence, there is no production reaction of C₄H₂^{*} in the model and it is not
 747 considered.

748 **HC₃N**. Cyanoacetylene is the nitrogen-bearing analog of diacetylene and
 749 the first member of the cyanopolyne family. Like C₄H₂, it exhibits strong
 750 absorption bands in the far ultraviolet (Bénilan et al., 1994) and is easily pho-
 751 todissociated in Titan’s atmosphere. There have been few investigations into
 752 the primary processes resulting from its UV irradiation. Halpern et al. (1988,
 753 1990) identified two photodissociation channels and an excited state HC₃N^{*}:



754 They determined a branching ratio of 0.05±0.02 at 193 nm for channel (J_d27b).
 755 Later on, Seki et al. (1996) reported a branching ratio of 0.30±0.05 for channel

756 (J_d27a) and an upper limit for channel (J_d27b) of 0.02. These results confirmed
757 that, at 193 nm, $C_2H + CN$ are minor products and the authors suggested that
758 the major photochemical process is the formation of a metastable HC_3N^* . At
759 185 nm, Clarke and Ferris (1995) determined a branching ratio of ~ 0.09 for
760 channel (J_d27a).

761 These results led Lavvas et al. (2008a) and Krasnopolsky (2009) to use a
762 branching ratio of 0.3 and 0.05, respectively, for channel (J_d27b) and 0.09 for
763 channel (J_d27a), implying the formation of some excited state, whose reactivity
764 is not considered.

765 More recently, the photodissociation of cyanoacetylene has been studied in
766 a molecular beam under collisionless conditions and the experimental approach
767 was augmented by statistical calculations (Silva et al., 2009). The results indi-
768 cate that at 212 and 193 nm, the only products are $C_3N + H$, while at 157
769 and 121.6 nm, this same channel represents only 57% of the products, with
770 channel (J_d27b) accounting for the difference. There is again no evidence for
771 a metastable state up to the dissociation threshold of (J_d27a), at 214 nm. We
772 use the results of this latter study to constrain our branching ratios, as shown
773 in Table B.6.

774 **C_2H_3CN .** Palmer et al. (2017) reported very recently the presence of
775 acrylonitrile in ALMA spectra of Titan’s stratosphere. Acrylonitrile exhibits
776 a strong absorption in the far UV range (Eden et al., 2003), making it a par-
777 ticularly reactive species. There have been various experimental studies of the
778 primary fragments, mostly at 193.0 nm, but also at 157.6 nm. They reported the
779 detection of CH_2CCN , HC_3N , HCN , C_2H_2 and minor amounts of CN , although
780 few branching ratio measurements have been performed (Fahr and Laufer, 1992;
781 North and Hall, 1996; Blank et al., 1998; Guo et al., 2001). The theoretical work
782 of Derecskei-Kovacs and North (1999) led to quantitative branching ratios at
783 193.0 nm. Wilhelm et al. (2009) observed with time-resolved infrared emission
784 spectroscopy the appearance of HNC as well as HCN and spectral modeling
785 allowed for the determination of the ratio HCN/HNC again at 193 nm.

786 Lavvas et al. (2008a) adopt a wavelength independent photodissociation
787 scheme based on the results from Derecskei-Kovacs and North (1999). Krasnopol-
788 sky (2009) uses a single channel, $CN + C_2H_3$ (J_d28e), while Loison et al. (2015)
789 assumes that $HCN + C_2H_2$ (J_d28c) are the major products with smaller amounts
790 of $HC_3N + H_2$ (J_d28a), $HNC + C_2H_2$ (J_d28b) and $CH_2CCN + H$ (J_d28d). As
791 indicated in Table B.6, we follow Lavvas et al. (2008a) and use throughout
792 our wavelength range, the branching ratios calculated by Derecskei-Kovacs and
793 North (1999) but with the HCN/HNC ratio measured by Wilhelm et al. (2009),
794 which is supported by more recent theoretical calculations (Homayoon et al.,
795 2011).

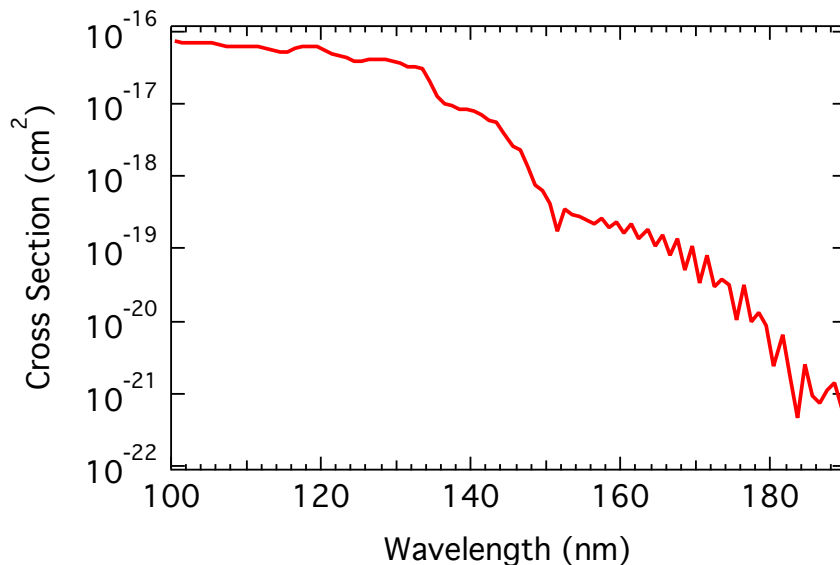


Figure 12: The cross-section of propionitrile ($\text{C}_2\text{H}_5\text{CN}$) versus wavelength used as model inputs (adapted from Kanda et al. (1999), see text).

796 **$\text{C}_2\text{H}_5\text{CN}$.** Cordiner et al. (2015b) recently reported the presence of propi-
 797 onitrile in ALMA spectra of Titan’s stratosphere. The absorption spectrum of
 798 $\text{C}_2\text{H}_5\text{CN}$ has only been recorded up to 152 nm (Kanda et al., 1999) although it
 799 may extend beyond 200 nm (Y. Bénilan, private communication, 2015). As this
 800 extended absorption to longer wavelength may play a crucial role, we assume
 801 that in the missing range the $\text{C}_2\text{H}_5\text{CN}$ cross sections are the same as for C_2H_2
 802 (cf. Figure 12). We note that Krasnopolsky (2009) assumes the same J value
 803 as for $\text{C}_2\text{H}_3\text{CN}$ and that Loison et al. (2015) do not consider any absorption
 804 beyond 150 nm.

805 As far as we know, there are no branching ratios available for $\text{C}_2\text{H}_5\text{CN}$.
 806 Krasnopolsky (2009) assumes that photodissociation leads to a single channel:
 807 $\text{C}_2\text{H}_5 + \text{CN}$ (J_d29c), while Loison et al. (2015) speculates that three other chan-
 808 nels are open: $\text{HCN} + \text{C}_2\text{H}_4$ (J_d29a), $\text{C}_2\text{H}_3\text{CN} + \text{H}_2$ (J_d29b) and $\text{CH}_2\text{CN} + \text{CH}_3$.
 809 We base our photodissociation scheme on that of $\text{C}_2\text{H}_3\text{CN}$ which translates into
 810 $\text{C}_2\text{H}_3\text{CN} + \text{H}_2$ being the main channel (cf. Table B.6).

811 **Radicals.** Radicals often absorb from the UV up to the visible part of
 812 the spectrum where the solar flux is highest. Nevertheless, these absorptions
 813 have been much less studied than for stable molecules and the subject is seldom
 814 discussed in the context of Titan.

815 In their pioneering work, Yung et al. (1984) state that photolysis of CH_2 and
 816 C_2H_5 is relatively unimportant but do include the dissociation of CH_3 , C_3H_3
 817 and HCO (cf. their Table 3). For the photolysis of CH_3 they consider the band
 818 at 216 nm and assume a branching ratio of unity towards $^1\text{CH}_2 + \text{H}$, based on

819 spin conservation. They however find that this process is marginally important
 820 compared with removal of CH_3 by chemical reactions. Nevertheless, methyl
 821 photolysis has been included in all subsequent photochemical models for Titan's
 822 atmosphere. Both Wilson and Atreya (2000) and Lavvas et al. (2008b) note
 823 that it is a significant source of excited methylene radicals. $^1\text{CH}_2$, unlike CH_3 ,
 824 can further react with CH_4 to produce two CH_3 radicals. Methyl photolysis
 825 therefore enhances methane's destruction and hence affects the production of
 826 all hydrocarbons.

827 Like Yung et al. (1984), subsequent models (Toublanc et al., 1995; Lara
 828 et al., 1996; Lebonnois et al., 2001) did consider a similar photolysis scheme
 829 for radicals. As models became more sophisticated, the photolysis of a couple
 830 more radical hydrocarbons beyond CH_3 and C_3H_3 were considered: C_2H_3 , C_2H_5
 831 and C_3H_5 in Wilson and Atreya (2004), C_2H , C_2H_3 and C_2H_5 in Lavvas et al.
 832 (2008a,b) and C_2H_3 , C_2H_5 , C_3H_2 and C_3H_5 in Krasnopolsky (2009). The latter
 833 also considers the photolysis of two nitrogen-bearing species: NH_2 and CH_2CN .
 834 Neither of these authors, however, discuss the importance of these reactions for
 835 the overall chemistry.

836 Dobrijevic et al. recently revisited their chemistry of C_3H_p hydrocarbons,
 837 HCN and oxygen species in the stratosphere and included the photodissociation
 838 of C_3 , C_3H (2 isomers), C_3H_2 (3 isomers), C_3H_3 , C_3H_5 , C_3H_7 , H_2CN , OH
 839 and HCO (Hébrard et al., 2012, 2013; Dobrijevic et al., 2014). The cross-
 840 sections, branching ratios and dissociation limits are extensively discussed in
 841 the appendices. They find that photolysis of H_2CN is responsible for 7% of the
 842 HCN production at 1300 km. They also report that because HCO is efficiently
 843 destroyed through visible-UV photolysis, its steady state abundance is low and
 844 that this process controls the $\text{HCO} \rightleftharpoons \text{H} + \text{CO}$ equilibrium (Dobrijevic et al.,
 845 2014).

846 Our model includes all the radicals discussed above and, in addition, C_6H_5
 847 and C_7H_7 , as listed in Table B.9. Cross-sections are represented in Figure 13.

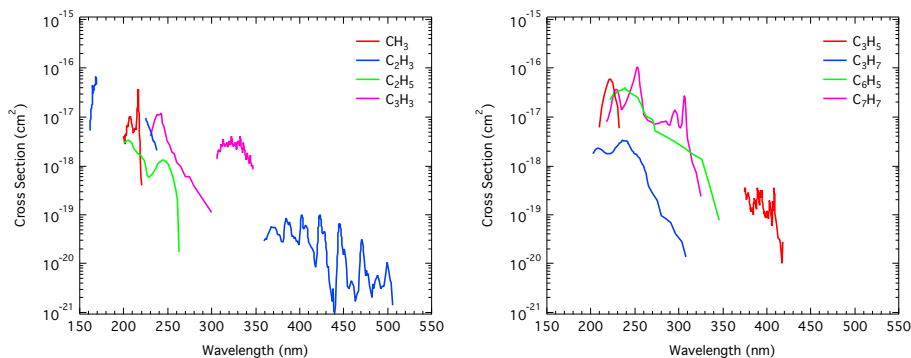


Figure 13: Cross-sections of radicals versus wavelength used as model inputs: CH_3 , C_2H_3 , C_2H_5 , C_3H_3 (left panel) and C_3H_5 , C_3H_7 , C_6H_5 , C_7H_7 (right panel). References are given in Table B.9.

848 *2.6.3.2. Rayleigh Scattering.* Most of the molecules considered here only absorb
849 radiation but we have also considered scattering by N₂ and aerosols. Aerosol
850 scattering properties are based on the DISR observations (Tomasko et al., 2008;
851 Lavvas et al., 2010) while N₂ scattering properties are based on the Rayleigh
852 scattering cross section (Dalgarno et al., 1967). We have modeled the effects of
853 scattering with a two-stream radiative transfer code, but find that the resulting
854 chemistry is similar to that obtained when scattering is neglected. This is due
855 to the low single scattering albedo of the aerosols. For the runs presented here
856 we do not include scattering because the effects of scattering on the radiation
857 field are smaller than the uncertainties caused by our approximate knowledge
858 of the aerosol distribution.

859 *2.6.3.3. Aerosol Opacity.* Aerosol opacities for fractal aggregates were taken
860 from Lavvas et al. (2010), using aerosol single scattering albedos and extinction
861 retrieved by DISR (Tomasko et al., 2008). A newer analysis of DISR data
862 (Doose et al., 2016) implies a different aerosol scale height above 80 km. The
863 impact of this recent study on the aerosol opacity has not been investigated
864 yet. A sensitivity study of the effect of aerosol opacity on the model results is
865 presented in section 5.3.

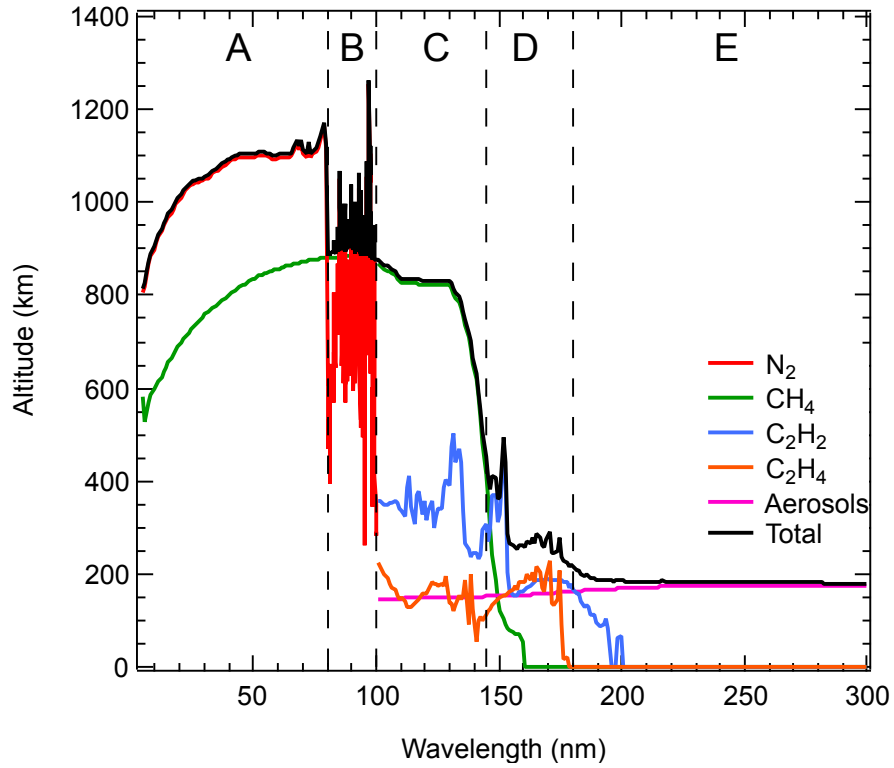


Figure 14: Photon penetration altitude as a function of wavelength.

Table 3: Main absorbers as a function of wavelength.

Band	Wavelength range (nm)	Main absorber
A	0-80	N ₂ (Ionization)
B	80-100	N ₂ (Dissociation)
C	100-145	CH ₄
D	145-180	C ₂ H ₂ - C ₂ H ₄
E	180-300	Aerosols

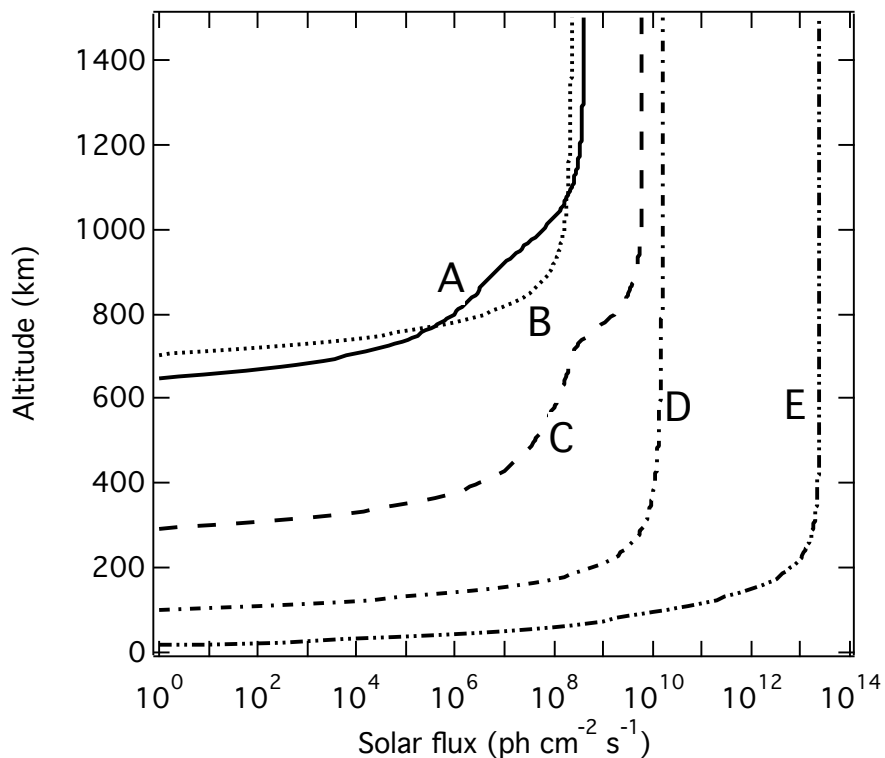


Figure 15: Solar flux in bands as a function of altitude.

867 Figure 14 displays the altitude at which the optical depth equals one for the
 868 main absorbers and for the total atmosphere. This graph can be separated into
 869 five distinct bands corresponding to wavelength regions where the dominant
 870 process differs, as shown in Table 3 and Figure 15. Plotted in this figure is
 871 the flux for an overhead sun for the 5 bands shown in Figure 14 and listed
 872 in Table 3. Below 100 nm, the optical depth is dominated by N_2 absorption,
 873 which occurs at altitudes from 800-1200 km. The threshold region near 80
 874 nm is not well described. The problem is that numerous high lying energy
 875 states contribute right near threshold and these high energy states are not well
 876 understood. Unlike Figure 15 that is accurate, Figure 14 only gives a very rough
 877 indication of the altitudes in the N_2 dissociation region because the actual $\tau=1$
 878 level varies strongly on very small wavelength scales in this region (Lavvas et al.,
 879 2011a, 2015). For this reason we should not expect a precise agreement between
 880 this plot and the altitude profile of N production, for example. Between 100
 881 and 145 nm, CH_4 is the dominant photon absorber, with the unit optical depth
 882 level decreasing from 800 to 400 km. Between 145 and 180 nm, C_2H_2 and C_2H_4
 883 contribute mostly to the optical depth, with a maximum absorption located
 884 between 400 and 200 km. Finally, above 180 nm, the opacity is entirely due to

885 aerosols with $\tau=1$ at 200 km. As a consequence, the entire solar ultraviolet flux
 886 is essentially absorbed before it can reach the tropopause/ surface (cf. Figure
 887 16).

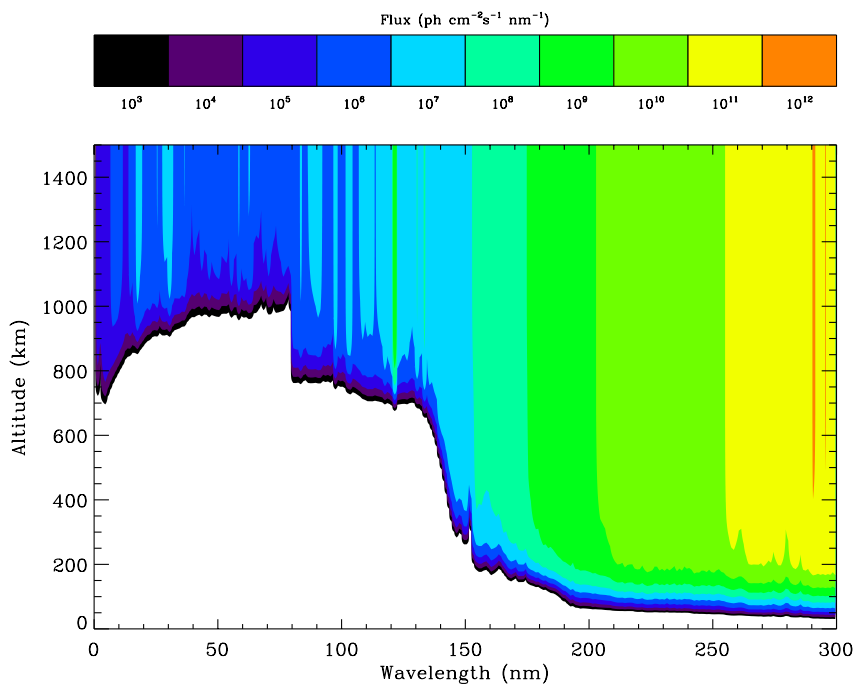


Figure 16: Photon flux versus altitude and wavelength, between 1.5 and 300 nm. White denotes no flux (complete absorption).

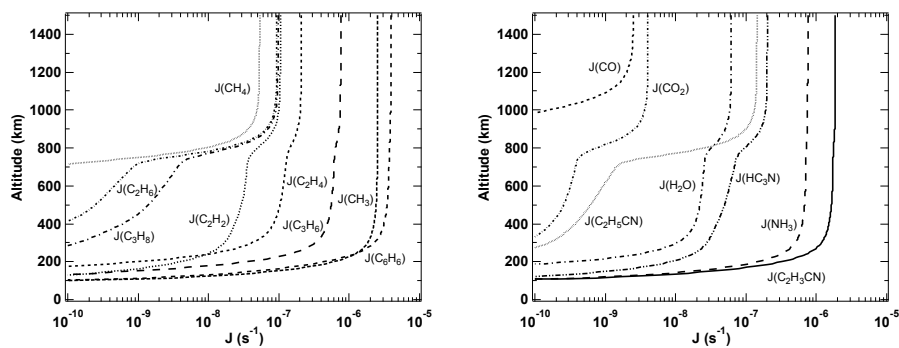


Figure 17: Photolysis rate coefficients (J values) versus altitude for selected hydrocarbons (left panel), and nitrogen and oxygen bearing species (right panel).

888 The model calculated photolysis rate coefficients for the most important
 889 hydrocarbons (left panel), and nitrogen and oxygen bearing species (right panel)
 890 are shown in Figure 17. A secondary photolysis region below 700 km for some
 891 of the species is due to their extended absorption cross section profiles above the
 892 methane dissociation limit at 145 nm and their presence in significant amounts.

893 2.6.5. Galactic Cosmic Rays

894 GCR, due to their high energy, penetrate deep in the atmosphere and deposit
 895 their energy in the lower stratosphere and troposphere (Capone et al., 1983;
 896 Molina-Cuberos et al., 2001). The alpha particles of the cosmic shower as well as
 897 the cascade of secondary electrons generated are degraded in energy along their
 898 path, leading to the ionization and dissociation of the main gaseous compounds.
 899 For the production rates of the different N_2 and CH_4 fragments (cf. Figure 18
 900 and Table B.13), we use the results from the energy deposition models described
 901 in Gronoff et al. (2009, 2011) and Lavvas et al. (2014). Molina-Cuberos et al.
 902 (2000) discussed the formation of negative ions from hypothetical electrophilic
 903 species and concluded that one would not expect there to be a large anion
 904 population in the lower atmosphere. As a consequence, we do not consider the
 905 formation of negative ions in the GCR region.

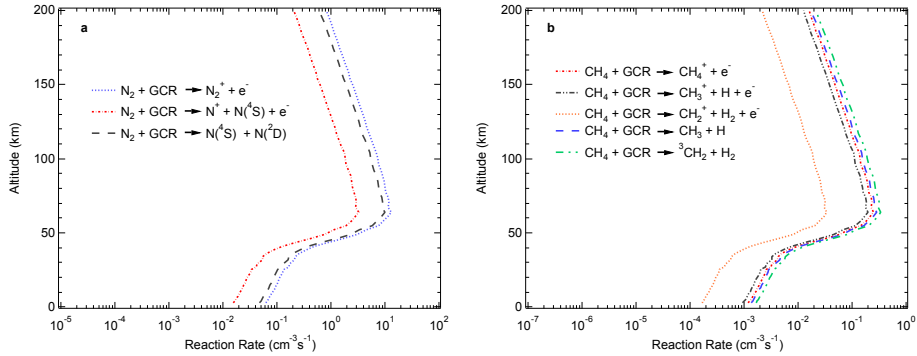


Figure 18: Production rates from Galactic Cosmic Rays for N_2 (left panel) and CH_4 (right panel).

906 2.7. Chemical Network

907 2.7.1. Equations

908 The model simulations require simple representations of the temperature and
 909 pressure dependence of the rate coefficients. Here, the temperature dependence
 910 of the various rate coefficients are represented with modified Arrhenius forms:

$$k(T) = AT^B \exp(C/T), \quad (\text{E9})$$

911 where T is the temperature and A, B, and C are fitting parameters. Properly
 912 representing the pressure dependence is more difficult. The well-known, but

913 rather approximate, Lindemann mechanism yields an expression for the associ-
 914 ation rate coefficient that smoothly interpolates from a linear dependence (k_0
 915 $[M]$) on pressure at low pressure (or density $[M]$) to a pressure independent value
 916 at high pressure (k_∞):

$$k(T, [M]) = k_\infty k_0 [M] / (k_\infty + k_0 [M]), \quad (\text{E10})$$

917 Master equation simulations long ago showed that at intermediate pressures the
 918 association rate coefficient is generally lower than predicted by the Lindemann
 919 expression. This deviation from the low and high pressure limits is commonly
 920 accounted for through the introduction of an empirical broadening factor F :

$$k(T, [M]) = F k_\infty k_0 [M] / (k_\infty + k_0 [M]) \quad (\text{E11})$$

921 In the combustion literature, the broadening factor F is generally represented
 922 with the empirical Troe form (Troe, 1979, 1983; Gilbert et al., 1983),

$$\log_{10}(F) = \log_{10}(F_c) / 1 + [(\log_{10}(P_r) + C) / (N - 0.14(\log_{10}(P_r) + C))]^2 \quad (\text{E12})$$

923 with the reduced pressure, P_r , given by $k_0[M]/k_\infty$, $N = 0.75 - 1.27\log_{10}(F_c)$,
 924 and $C = -0.4 - 0.67\log_{10}(F_c)$. The fitting parameter F_c generally takes values
 925 between 0 and 1. For reactions where radiative stabilization is unimportant, we
 926 use E11 to represent the pressure dependence with separate modified Arrhenius
 927 representations for the rate coefficients k_0 and k_∞ . The F_c parameter is taken
 928 as a constant independent of temperature.

929 Radiative stabilization complicates the representation of the pressure depen-
 930 dence, as the association rate coefficient then becomes independent of pressure
 931 in the low-pressure limit, rather than linearly dependent on pressure (Vuitton
 932 et al., 2012). To see this, consider the modified strong collider/TST derivation
 933 of the rate constant (which provides a qualitatively useful description). The
 934 pressure dependent stabilization rate constant may be written as

$$k(T, [M]) = \int k_{ass}(E) P_{stab}(E) P_{Boltz}(E) dE, \quad (\text{E13})$$

935 where $k_{ass}(E)$ is the microcanonical rate constant for the capture rate, $P_{stab}(E)$
 936 is the probability that the initially formed complex is stabilized, and $P_{Boltz}(E)$
 937 is the Boltzmann probability, $\rho(E) \exp(-\beta E) / Q(T)$, with $\rho(E)$ as the density
 938 of states of the reactants, $\beta = 1/(k_B T)$, k_B is Boltzmann's constant, and
 939 $Q(T)$ is the partition function of the reactants. Within transition state the-
 940 ory, $k_{ass}(E) = N^\ddagger(E) / [h\rho(E)]$, where N^\ddagger is the number of available states for
 941 motion on the transition state dividing surface separating reactants from prod-
 942 ucts, and h is Planck's constant. With the modified strong collider assumption
 943 the stabilization probability is given by the probability of a stabilizing collision
 944 occurring during the lifetime of the collision complex:

$$P_{stab}(E) = \beta_c k_c [M] / (\beta_c k_c [M] + k_{diss}(E)), \quad (\text{E14})$$

945 where β_c is the probability that any one collision is stabilizing, and k_c is the
 946 inelastic collision rate. Allowing for an energy dependent radiative emission
 947 rate, $k'_R(E)$, modifies the stabilization probability:

$$P_{stab}(E) = (\beta_c k_c [M] + k'_R(E)) / (\beta_c k_c [M] + k'_R(E) + k_{diss}(E)), \quad (\text{E15})$$

948 The pressure dependent association rate constant is then expressed as

$$k(T, [M]) = [1/hQ(T)] \int N^\ddagger(E) \exp(-\beta E) (\beta_c k_c [M] + k'_R(E)) / (\beta_c k_c [M] + k'_R(E) + k_{diss}(E)) dE \quad (\text{E16})$$

949 In the low pressure limit, this form reduces to the pressure independent radiative
 950 stabilization rate constant

$$k_R(T) = [1/hQ(T)] \int N^\ddagger(E) \exp(-\beta E) k'_R(E) / (k'_R(E) + k_{diss}(E)) dE \quad (\text{E17})$$

951 Unfortunately, there does not appear to be a standard literature form for repre-
 952 senting the effect of radiative emission on the pressure dependence. We employ
 953 a simple modification to the Troe form:

$$k(T, [M]) = k_R + F k'_\infty k_o [M] / (k'_\infty + k_o [M]) \quad (\text{E18})$$

954 where $k'_\infty = k_\infty - k_R$. This form approaches k_R in the low pressure limit, retains
 955 the Troe form when k_R is small, and approaches k_∞ in the high pressure limit or
 956 when k_R is large (cf. Figure 19). At intermediate pressures, the parameter F_c ,
 957 which determines the broadening factor F, allows for a reasonable reproduction
 958 of our explicit master equation calculations. A representative illustration of the
 959 quality of the fit provided by Eq. (E18) is given in Figure 20 for the $\text{C}_2\text{H}_5 + \text{CH}_3$
 960 recombination reaction at 140 K.

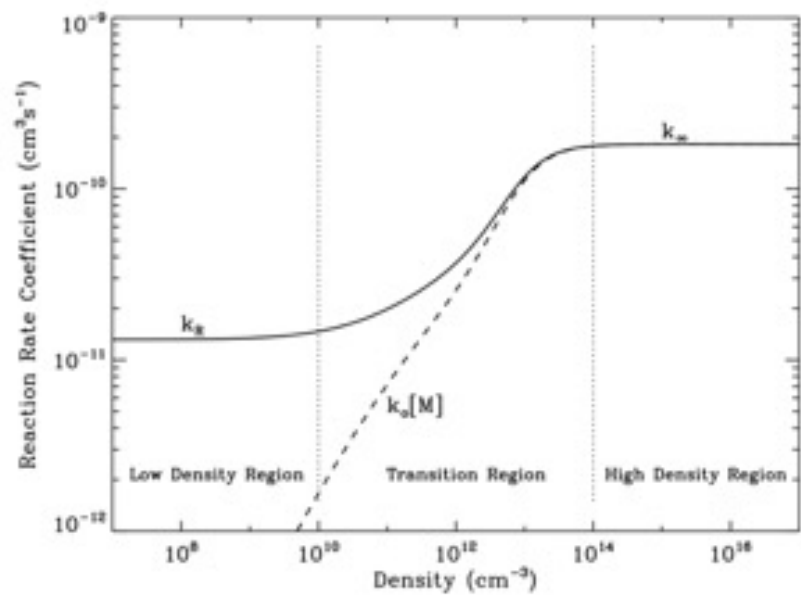


Figure 19: Representative illustration of an association reaction rate coefficient versus density.

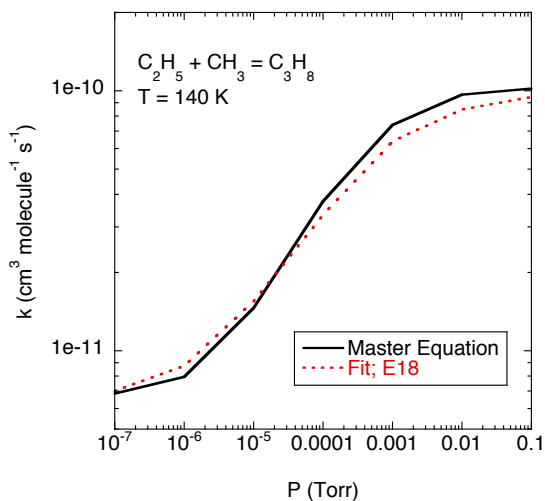


Figure 20: Plot of the pressure dependence of the master equation based theoretical predictions for the $\text{C}_2\text{H}_5 + \text{CH}_3$ recombination rate constant together with the fit based on Eq. (E18).

961 *2.7.2. Species*

962 *2.7.2.1. Neutrals.* The chemically active neutral species in our model are listed
 963 in Table B.3 and consist of 38 molecules and 45 radicals (not counting ^{15}N
 964 isotopologues, see section 2.7.4). We consider a complete reaction set for the
 965 C through C_4 hydrocarbons as well as the polyynes C_6H_2 and the aromatic
 966 compounds C_6H_6 and C_7H_8 . We also consider several species involving N and
 967 O but deliberately focus exclusively on those species for which observational
 968 constraints are available. We include coupling between oxygen and nitrogen
 969 chemistries. We do not consider sulfur-bearing species since their source is not
 970 well constrained and expected to be small and unimportant for the abundance
 971 profiles of other species (Nixon et al., 2013; Hickson et al., 2014).

972 The fact that some products are not tracked in this work does represent
 973 a minor inconsistency in conservation of elements in the model, but as later
 974 discussed in section 5.2, the column-integrated rate of these reactions sum to
 975 $\sim 5 \times 10^8 \text{ cm}^{-2} \text{ s}^{-1}$. Even though a fast catalytic recycling of C- C_4 species
 976 from C_5 or higher hydrocarbons cannot be ruled out, the non-detection of the
 977 latter implies that their abundances are small, so that their effect on the system
 978 is probably of minor importance.

979 Molecules having more than two atoms exhibit several isomers. Since we
 980 expect the less stable forms to be less abundant, we have deliberately chosen to

Table 4: Lifetime of some metastable states. Those included in the model are in bold.

Species	Lifetime	Reference
$\bar{\text{N}}_2(\text{A } ^3\Sigma_u^+)$	2.4 s	Piper (1993)
$\text{N}(^2\text{D})$	14 h and 37 h ^(a)	Ralchenko et al. (2011)
$\text{N}(^2\text{P})$	11 s and 10 s ^(b)	Ralchenko et al. (2011)
$\text{CH}_2(\text{a } ^1\text{A}_1)$	18 s	Jacox (2003)
$\text{C}(^1\text{D})$	54 min	Schofield (1979)
$\text{O}(^1\text{D})$	2.5 min	Okabe (1978)
$\text{O}(^1\text{S})$	770 ms	Koyano et al. (1975)

^(a)Lifetimes for the $\text{N}(^2\text{D}_{3/2})$ and $\text{N}(^2\text{D}_{5/2})$ states, respectively.

^(b)Lifetimes for the $\text{N}(^2\text{P}_{1/2})$ and $\text{N}(^2\text{P}_{3/2})$ states, respectively.

981 consider only the most stable isomer. There are two exceptions to this: C_3H_4
 982 and HCN for which a less stable form has been (at least tentatively) detected
 983 on Titan: methylacetylene, CH_3CCH / allene, CH_2CCH_2 (Roe et al., 2011),
 984 and hydrogen cyanide HCN / hydrogen isocyanide HNC (Moreno et al., 2011).
 985 We discuss $\text{CH}_3\text{CCH}/\text{CH}_2\text{CCH}_2$ in section 4.2.3.1 and HCN/HNC in section
 986 4.2.3.2.

987 Hébrard et al. (2013) revisited the chemistry of C_3H_x hydrocarbons and in-
 988 cluded in their chemical network two C_3H isomers: 2-cyclopropyn-1-yl (c- C_3H)
 989 and 2-propynylidyne (l- C_3H), and three C_3H_2 isomers: cyclopropenylidene (c-
 990 C_3H_2), propadienylidene (l- C_3H_2) and propynylidene (t- C_3H_2). However, be-
 991 cause none of the reactions involving these species are identified as key reactions
 992 responsible for uncertainties on major C_3H_x compounds (cf. their Table 3), we
 993 decided to only consider one isomer for both species. We indeed find that nei-
 994 ther C_3H or C_3H_2 has any impact on the overall chemistry because of their low
 995 production rate.

996 *2.7.2.2. Metastable Species.* It was soon recognized that electronically excited
 997 atomic nitrogen ($\text{N}(^2\text{D})$, the ground state is $\text{N}(^4\text{S})$), methylene ($\text{CH}_2(\text{a } ^1\text{A}_1)$, the
 998 ground state is X^3B_1) and atomic oxygen ($\text{O}(^1\text{D})$, the ground state is $\text{O}(^3\text{P})$),
 999 formed in the photodissociation of N_2 , CH_4 , H_2O and CO , respectively, have a
 1000 radiative lifetime long enough to contribute to Titan’s atmospheric chemistry
 1001 (Yung et al., 1984; Toubanc et al., 1995). The production of excited $\text{N}(^2\text{D})$
 1002 atoms is an important step in the chemical evolution of the upper atmosphere
 1003 of Titan, as nitrogen atoms in this state are much more reactive than those
 1004 in the ground ^4S state and are not efficiently quenched by collisions with N_2
 1005 (the room temperature recommended value is $k = 1.7 \times 10^{-14} \text{ cm}^3 \text{ s}^{-1}$ Herron
 1006 (1999)). $\text{N}(^2\text{D})$, $\text{CH}_2(\text{a } ^1\text{A}_1)$ and $\text{O}(^1\text{D})$ are to date the only excited states that
 1007 have been included in Titan photochemical models. However, four other excited
 1008 species are metastable and could have some impact on the chemistry as well:
 1009 $\text{N}_2(\text{A } ^3\Sigma_u^+)$, $\text{N}(^2\text{P})$, $\text{C}(^1\text{D})$ and $\text{O}(^1\text{S})$. Their lifetimes are given in Table 4.

1010 The production of $\text{N}_2(\text{A } ^3\Sigma_u^+)$, $\text{N}(^2\text{D})$ and $\text{N}(^2\text{P})$ by interaction with pho-
 1011 tons and photoelectrons of N_2 is discussed in Lavvas et al. (2011a, 2015). $\text{N}(^2\text{D})$

1012 and $N(^2P)$ are also formed in the electron-ion recombination of N_2^+ but their
 1013 production rate through this pathway is small since most N_2^+ react with CH_4 .
 1014 $N_2(A^3\Sigma_u^+)$ and $N(^2P)$ are quite nonreactive with N_2 , H_2 and CH_4 , quen-
 1015 ching into $N_2(X)$ and $N(^2D)$, respectively being the main channels. Reaction of
 1016 $N_2(A^3\Sigma_u^+)$ with unsaturated hydrocarbons leads to the dissociation of the lat-
 1017 ter (Herron, 1999; Dutuit et al., 2013) but the mole fraction of $N_2(A^3\Sigma_u^+)$ has
 1018 been calculated to be only about 10^{-9} (Lavvas et al., 2015) and we therefore
 1019 did not include this species in the chemical network. The production of $N(^2P)$
 1020 relative to $N(^2D)$ is not well constrained by measurements both for photons and
 1021 photoelectrons. Based on this argument, and also because the reaction prod-
 1022 ucts of $N(^2P)$ are unknown (Herron, 1999; Dutuit et al., 2013), we assume in
 1023 the calculations that all $N(^2P)$ formed results in $N(^2D)$ (section 2.6.3). $C(^1D)$
 1024 is a product in the photodissociation of CO as shown in Table B.5. CO being
 1025 efficiently shielded by N_2 , the production rate of $C(^1D)$ is small ($5 \times 10^4 \text{ cm}^{-2}$
 1026 s^{-1}) and we assume that the atomic carbon ground state, $C(^3P)$, is formed in-
 1027 stead. We consider that the excited state of neutral oxygen $O(^1S)$, produced in
 1028 the reaction of $N(^2D)$ and NO (R_n584c), is converted very rapidly to $O(^1D)$.

1029 *2.7.2.3. Positive Ions.* The chemical network contains 196 positive ions (from
 1030 $m/z = 1$ to ~ 100 , which corresponds to the mass range of INMS) containing
 1031 carbon, nitrogen, oxygen and hydrogen that are listed in Table B.4. It is based
 1032 on Vuitton et al. (2007) but has been improved in several ways:

- 1033 • In order to better describe the oxygen chemistry in the upper atmosphere,
 1034 14 new oxygen bearing species (O^+ , OH^+ , CO^+ , HCO^+ , HO^+ , CH_2O^+ ,
 1035 CH_2OH^+ , HC_2O^+ , CH_2CO^+ , CH_3CO^+ , CH_3COH^+ , HC_3O^+ , $C_2H_2CO^+$
 1036 and $C_2H_3CO^+$) and 4 new oxygen and nitrogen bearing species (NO^+ ,
 1037 HNO^+ , NCO^+ and $HNCO^+$) are considered.
- 1038 • In order to couple the ion and neutral chemistry, the neutral products of
 1039 electron recombination reactions have been included.
- 1040 • In order not to lose ions in a bottomless sink, ions with a mass-to-charge
 1041 ratio above 100 all fall in a generic bin called “ $C_xH_yN_z^+$ ”. This virtual
 1042 species is not involved in further ion-molecule reactions but does recombine
 1043 with electrons to produce untracked neutral species.
- 1044 • In order to describe the lower ionospheric layer induced by GCR, we in-
 1045 clude cluster ions.

1046 Because of the lack of kinetic data, we do not distinguish different isomers,
 1047 with the exception of linear/cyclic $C_3H_3^+$, HCN^+/HNC^+ , CNC^+/C_2N^+ and
 1048 HCO^+/HOC^+ , for which some information is available.

1049 Nicolas et al. (2003b) estimated that in the photoionization of N_2 about
 1050 15% of the N^+ ions are produced in the first excited state, $N(^1D)$, which has
 1051 a lifetime of 258 s (Wiese and Fuhr, 2007). Even though the branching ratios
 1052 of the products formed by $N(^1D)$ with methane are quite different from the
 1053 products formed by $N(^3P)$ (Alcaraz et al., 2004), a sensitivity study showed

1054 that taking into account the $N^+(^1D)$ state has no relevant effect on the model
1055 predictions (Carrasco et al., 2008) and therefore we decided to ignore it.

1056 Lilensten et al. (2005) investigated the presence of a N_2^{++} layer in the upper
1057 atmosphere of Titan, considering production by double photoionization and
1058 photoelectron impact of N_2 and loss by dissociative recombination with electrons
1059 and chemical reactions with N_2 and CH_4 . They predicted a maximum density
1060 of 10^{-2} cm^{-3} at 1100 km. Because this represents only about 10^{-5} of the total
1061 ion density and because the predicted emissions (fluorescence from $D \ ^1\Sigma_u^+$ to
1062 $X \ ^1\Sigma_g^+$) have not been detected so far by UVIS (Ajello et al., 2007), we do not
1063 consider N_2^{++} in the chemical network.

1064 *2.7.2.4. Negative Ions.* The chemical network is similar to that described in
1065 Vuitton et al. (2009). It contains 12 negative ions listed in Table B.4. A few
1066 cross-sections and rate coefficients have been updated and a few new reactions
1067 have been added, as described in section 2.7.3.3. Also, we include specific prod-
1068 ucts for ion recombination and associative detachment reactions, in order to
1069 couple the ion to the neutral chemistry. However, the negative ion density is
1070 low, at the ionospheric peak typically 1% of the positive ion density, and the
1071 presence of negative ions does not have any impact on the abundance of neutral
1072 or positive ion species.

1073 *2.7.3. Gas Phase Reactions*

1074 The chemical network is based on the ion chemistry presented in Vuitton
1075 et al. (2007) and Vuitton et al. (2009), and the neutral chemistry presented
1076 in Hörst et al. (2008), Yelle et al. (2010) and Vuitton et al. (2012) for oxygen
1077 bearing species, nitrogen bearing species and hydrocarbons, respectively. In the
1078 present work, many rate coefficients have been updated and numerous reactions
1079 have been added. The reaction network has been last updated in December 2016
1080 and reflects the state-of-the-art of the laboratory measurements and theoretical
1081 calculations available at that time. The different families of reactions included
1082 in the model are listed in Table 5 and are further described in the next sections.

1083 *2.7.3.1. Neutrals.*

1084 **General Description.** The model includes 572 reactions among neutral
1085 species. These are listed in Table B.15 along with the parameters for calcu-
1086 lation of the rate coefficients as a function of pressure and temperature. The
1087 reaction list has been compiled mainly for a carbon, nitrogen-rich and oxy-
1088 gen poor atmosphere, for temperatures at or below 300 K. It consists of re-
1089 actions we have identified, based on available kinetics or thermodynamics, as
1090 being important for the understanding of the chemistry in the atmosphere of
1091 Titan. We rule out endothermic processes and reactions known to exhibit an
1092 energy barrier, at the exception of a few cases where they have been specifi-
1093 cally studied down to low temperature (see further down). Kinetic parameters
1094 are primarily taken from databases and we refer to the compilations of Baulch
1095 et al. (2005) and Sander et al. (2011). A smaller number come from the online

Table 5: Classes of reactions included in the photochemical model.

Reaction class	Chemical equation
Neutral Species	
Photodissociation	$AB + h\nu \rightarrow A + B$
Electron dissociation	$AB + e_S^- \rightarrow A + B + e^-$
Bimolecular reactions	$A + BC \rightarrow AB + C$
Termolecular association	$A + B + M \rightarrow AB + M$
Radiative association	$A + B \rightarrow AB + h\nu$
Positive ions	
(Dissociative) photoionization	$AB + h\nu \rightarrow AB^+(A^+ + B) + e^-$
(Dissociative) electron ionization	$AB + e_S^- \rightarrow AB^+(A^+ + B) + 2e^-$
Bimolecular reactions	$A^+ + BC \rightarrow AB^+ + C$
Termolecular association	$A^+ + B + M \rightarrow AB^+ + M$
Radiative association	$A^+ + B \rightarrow AB^+ + h\nu$
Dissociative recombination	$AB^+ + e_T^- \rightarrow A + B$
Radiative recombination	$A^+ + e_T^- \rightarrow A + h\nu$
Negative ions	
Ion-pair formation	$AB + h\nu \rightarrow A^- + B^+$
Dissociative attachment	$AB + e_S^- \rightarrow A^- + B$
Radiative attachment	$A + e_T^- \rightarrow A^- + h\nu$
Bimolecular reactions	$A^- + BC \rightarrow AB^- + C$
Photodetachment	$A^- + h\nu \rightarrow A + e^-$
Ion recombination	$A^- + BC^+ \rightarrow AB + C$
Associative detachment	$A^- + B \rightarrow AB + e^-$

e_S^- and e_T^- stand for supra-thermal and thermal electrons, respectively.

1096 database KIDA (Wakelam et al. (2012, 2015), <http://kida.obs.u-bordeaux1.fr>),
1097 where a small subset of reactions has been evaluated by a panel of physical
1098 chemists. For those reactions that were not referenced in these evaluations or
1099 when more recent experiments or calculations have been undertaken, we had
1100 to make choices among the different measurements available in the National
1101 Institute of Standards and Technology (NIST) Chemical Kinetics Database
1102 (<http://kinetics.nist.gov/kinetics/index.jsp>), an uncritical compilation, and in
1103 the recent literature. For some important reactions for which there was inade-
1104 quate kinetic data, we have performed theoretical estimates based on transition
1105 state theory. This is described further below and in section Appendix A.

1106 Laboratory experiments are usually performed at room temperature (300
1107 K) and do not provide any information on the variation of the rate coefficient
1108 with temperature. When a temperature dependence is investigated, it is of-
1109 ten motivated by the importance of the given reaction in combustion studies
1110 (500-2000 K). Consequently, it is important to keep in mind that the majority
1111 of published results are obtained at higher temperatures than are found in the
1112 atmosphere of Titan (75-200 K). Fortunately, in the 90's, there was renewed
1113 interest in astronomy in the physical-chemistry community and experiments
1114 based on the CRESU technique (a French acronym for Cinétique de Réaction
1115 en Ecoulement Supersonique Uniforme) were designed to reach the low tem-
1116 peratures encountered in planetary atmospheres and the interstellar medium.
1117 Building on these results, Smith et al. (2006) correlated the values of the rate
1118 coefficients for the reactions between radicals and unsaturated hydrocarbons
1119 and their dependence on temperature with differences between the ionization
1120 energy (I.E.) of the molecular reagent and the electron affinity (E.A.) of the
1121 radical. They came to the conclusion that when (I.E. - E.A.) is less than ~ 8.75
1122 eV, then it is likely that the reaction will remain rapid at low temperature.

1123 When no experimental or theoretical studies are available for a given reac-
1124 tion, we applied the extremely valuable approach from Smith et al. (2006) to
1125 determine if the reaction has to be included in the model or not. As a first
1126 approximation, it can be considered that the reaction of H, C, CH, $^1\text{CH}_2$, C_2 ,
1127 C_2H , C_4H , $\text{N}(^2\text{D})$, NH, CN, C_3N , $\text{O}(^1\text{D})$ and OH with unsaturated species is
1128 fast. If room temperature data are available, we used the long-range capture
1129 theory to extend those measurements towards low temperature (Faure et al.,
1130 2009). If no kinetic data are available, we estimate the rate coefficient on the
1131 basis of chemical similarity with the one or more of the relatively small number
1132 of reactions for which rate coefficients have been measured at low temperatures.
1133 For example, the reaction of $^1\text{CH}_2$ with C_2H_2 and C_2H_4 has been studied, even
1134 at low temperatures, and rate coefficients were found to be close to the collision
1135 limit (Gannon et al., 2010a). We assume that this is also true for reactions of
1136 $^1\text{CH}_2$ with larger alkenes and alkynes.

1137 Radical-radical association reactions are amongst those that are the least
1138 constrained experimentally at low pressure and temperature. For many of these
1139 reactions only the high pressure limit rate coefficient (k_∞) is available and the
1140 buffer gas is rarely N_2 . Moreover, we showed that radiative association is effi-
1141 cient for adducts having as little as four C atoms, a process that can only be

1142 evaluated with state-of-the-art ab initio calculations (Vuitton et al., 2012). We
1143 follow our previous approach for hydrocarbons and extend it to nitrogen and
1144 oxygen containing species.

1145 We estimate k_∞ from the following rule: for H + radical, $k_\infty = 2 \times 10^{-10}$
1146 $\text{cm}^3 \text{s}^{-1}$; for cross reactions (two different radicals), $k_\infty = 8 \times 10^{-11} \text{cm}^3$
1147 s^{-1} and for self-reactions (two identical radicals), $k_\infty = 5 \times 10^{-11} \text{cm}^3 \text{s}^{-1}$.
1148 These empirical estimates are based on prior theoretical studies of H + alkyl
1149 radical reactions (Harding et al., 2005) and alkyl + alkyl reactions (Klippenstein
1150 et al., 2006), and from our knowledge of the low-temperature behavior of rate
1151 coefficients (Georgievskii and Klippenstein, 2005). For k_o and k_R , we consider
1152 that the rate coefficient depends primarily on the number N of heavy atoms (C,
1153 N, O) involved. The formulae, $k_R = 6 \times 10^{-16} N^{7.5}$ and $k_o = 8 \times 10^{-30} e^{4.7N}$, are
1154 fits to the theoretically predicted rate coefficients for five reactions (cf. Table 1
1155 and Figure 1 in Vuitton et al. (2012)).

1156 The identities of product species and associated branching ratios are rarely
1157 determined along with the measurements of kinetic rate coefficients, even at
1158 room temperature. Only a handful have been obtained at low temperature
1159 (Gannon et al., 2007, 2010a). Collision free experiments are the principal source
1160 of information when it comes to products (cf. for example Jones et al. (2010)
1161 and Zhang et al. (2009)) but they are often performed at high collision energy
1162 (10-50 kJ mol^{-1}). Unlike rate coefficients, branching ratios are difficult to guess
1163 from first principles (beyond the fact that the reaction should be exothermic)
1164 and a new generation of experiments is mandatory. Therefore, estimates of the
1165 probable products are offered based on various chemical arguments.

1166 For many unsaturated molecules, there are multiple stable isomers that may
1167 be formed, and the barriers between them are large enough to prohibit thermal
1168 isomerization. For example, for $\text{CH}_3\text{CCH}/\text{CH}_2\text{CCH}_2$ the barrier separating the
1169 two species is 65.1 kcal/mol (Alnama et al., 2007), while for HCN/HNC the
1170 barrier is 30.2 kcal/mol (Herbst et al., 2000). For simplicity, unless otherwise
1171 specified, we presume the formation of the most stable of these isomers. In many
1172 cases, the reaction that produces a given species is exothermic enough that there
1173 is a rapid equilibration of the isomers prior to stabilization. In this instance, the
1174 most stable isomer will be the dominant species. Furthermore, in many cases,
1175 the sequence of radical (e.g., H atoms) addition, followed by isomerization, and
1176 then identical radical loss can serve to catalyze the conversion to the lower
1177 energy isomer. Similarly, photoexcitation followed by collisional or radiative
1178 cooling, will also generally lead to production of the most stable isomer.

1179 **Theoretical Calculations of Rate Coefficients.** For 70 neutral reac-
1180 tions we have used the ab initio transition state theory based master equation
1181 (AITSTME) approach (Harding et al., 2007; Truhlar et al., 1996; Miller and
1182 Klippenstein, 2006; Klippenstein, 2017) to predict the temperature and pres-
1183 sure dependence of the rate coefficient. We chose the most significant and/or
1184 less constrained reactions as discussed in section 3.2. A list of these reactions
1185 can be found in Tables A.1-A.3.

1186 The AITSTME approach involves three distinct calculations. First, the sta-
1187 tionary points on the potential energy surface connecting reactants and prod-
1188 ucts are explored with ab initio electronic structure theory. Then, transition
1189 state theory is used to predict the microcanonical rate constants for each of the
1190 chemical processes occurring on that potential energy surface. Next, these mi-
1191 crocanonical rate constants are coupled with simple models for collisional energy
1192 transfer and radiative emission to form a linear master equation describing the
1193 time dependence of the energy resolved species populations. Finally, the eigenso-
1194 lution for this master equation directly yields the global phenomenological rate
1195 coefficients at arbitrary temperatures and pressures (Miller and Klippenstein,
1196 2006). The chemical model employs simple representations of these theoretic-
1197 ally predicted temperature (i.e., modified Arrhenius) and pressure (i.e., Troe
1198 format) dependent rate coefficients. A brief overview of the present implemen-
1199 tation of this general methodology is provided next, with more reaction specific
1200 details provided in Appendix A.

1201 Many of the reactions of interest have small positive barriers, and the pre-
1202 dicted kinetics is then strongly dependent on the estimated barrier height and
1203 tunneling frequency. Here, for many species we have employed the coupled clus-
1204 ter method with singles doubles and perturbative triples [CCSD(T)] method
1205 (Raghavachari et al., 1989) with the cc-pVTZ basis set (Dunning, 1989) to pre-
1206 dict the rovibrational properties of the saddle point and other stationary points
1207 of relevance to the kinetics. This method provides high accuracy partition func-
1208 tions, tunneling frequencies, and geometries. For some of the larger species
1209 computational limitations lead us to instead employ B3LYP density function
1210 theory (Becke, 1993) rovibrational evaluations. Higher accuracy barrier height
1211 estimates are generally obtained here from further CCSD(T) calculations with
1212 larger basis sets in an attempt to produce the CCSD(T)/CBS (complete basis
1213 set) limit. For some cases, we include a number of high level corrections, such
1214 as the CCSDT(Q) correction for quadruple excitations, core-valence, relativis-
1215 tic, diagonal Born-Oppenheimer, and vibrational anharmonicity corrections. A
1216 number of these higher level energy evaluations employ an early version of the
1217 ANL0 scheme (Klippenstein et al., 2017), which has been shown to yield 2σ
1218 uncertainties on the order of 0.2 to 0.3 kcal/mol, as do other high level ab initio
1219 methods, such as the HEAT (Bomble et al., 2006) and W4 (Karton et al., 2006)
1220 protocols.

1221 For radical-radical reactions, and any other reactions where the barrier is
1222 submerged below the reactants, we implement the variable-reaction coordinate
1223 transition state theory (VRC-TST) approach (Klippenstein, 1992; Georgievskii
1224 and Klippenstein, 2003) with direct multireference wavefunction based potential
1225 energy surface evaluations (Harding et al., 2005). This approach yields high-
1226 pressure capture rates that appear to generally be accurate to within about 20%
1227 (Klippenstein et al., 2006). Typically, the direct orientational sampling is per-
1228 formed at the CASPT2 level employing modest basis sets (e.g., cc-pVTZ) with
1229 one-dimensional corrections incorporated from higher-level calculations [larger
1230 basis sets, larger active spaces, multi-reference configuration interaction (MRCI)
1231 evaluations, and/or including geometry relaxation effects] along the minimum

1232 energy path. Our kinetic analyses for the small barrier reactions generally em-
1233 ploy Eckart tunneling corrections, one-dimensional hindered rotor treatments,
1234 and variational transition state theory treatments as appropriate. For the bar-
1235 rierless reactions, the TST analysis is implemented at the energy E and angular
1236 momentum J resolved level. For reactions with a barrier, and in all the master
1237 equation treatments, the analyses are implemented at the microcanonical level.
1238 For many cases, these kinetic analyses are either identical to or are slightly mod-
1239 ified from earlier analyses carried out for the higher temperatures of relevance to
1240 combustion. In some instances these prior studies included modest adjustments
1241 of barrier heights (e.g. a few tenths of a kcal/mol) to improve agreement with
1242 experimental data.

1243 The pressure dependence of the kinetics was obtained from the one-dimensional
1244 master equation employing Lennard-Jones collision frequencies and the expo-
1245 nential down model for energy transfer. The exponential parameter α , which
1246 correlates closely with the average downwards energy transfer $\langle \Delta E_{down} \rangle$,
1247 was generally represented with the form $A(T/300)^n$, with the parameters A
1248 and n empirically chosen from experience, from prior reaction specific studies,
1249 or from consideration of related trajectory analyses (Jasper and Miller, 2011;
1250 Jasper et al., 2015). The radiative emission rates were obtained from an aver-
1251 age over the harmonic approximation to the radiative emission rate for a given
1252 vibrational state and the statistical distribution of vibrational state populations
1253 (Klippenstein et al., 1996).

1254 The present CCSD(T), CASPT2, and MRCI calculations were performed
1255 with MOLPRO (Werner et al., 2012), with the CCSDT(Q) corrections obtained
1256 with Kallays add-on to MOLPRO (Kállay and Surján, 2001). The density func-
1257 tional calculations were obtained with Gaussian09 (Frisch et al., 2009), while the
1258 diagonal Born-Oppenheimer corrections were obtained with CFOUR (Stanton
1259 et al., 2010). The variable reaction coordinate transition state theory calcula-
1260 tions were performed with VaReCoF (Georgievskii et al., 2016). The master
1261 equation analyses were mostly performed with the VariFlex code (Klippenstein
1262 et al., 2011), with a few of the more recent analyses employing the MESS code
1263 (Georgievskii et al., 2013; Georgievskii and Klippenstein, 2016).

1264 It is generally difficult to ascertain the uncertainty in theoretical predictions,
1265 especially for reactions occurring at low temperatures over complex multiple
1266 well potential energy surfaces. In general, the uncertainties in our predicted
1267 bimolecular rate coefficients are larger the smaller the predicted rate coefficient.
1268 If it is near the collision limit, as for many of the radical-radical reactions with
1269 larger radicals, the uncertainty in the predictions may be as low as 20 or 30%. In
1270 contrast, when the rate coefficients are as low as 10^{-17} $\text{cm}^3 \text{s}^{-1}$, it is likely that
1271 our uncertainties are closer to an order of magnitude. For rate coefficients in
1272 the 10^{-13} $\text{cm}^3 \text{s}^{-1}$ neighborhood, the uncertainty in the predictions is perhaps
1273 a factor of three. For a recent study on how the uncertainties in reaction rates
1274 and branching ratios propagate in Titan models and how they affect the model
1275 output, see Dobrijevic et al. (2014) and previous work from the same group.

1276 In the end, the chemical network consists of 727 neutral reactions (not includ-
1277 ing ^{15}N isotopologues), amongst which 497 rate coefficients had to be estimated

1278 because no experiments or calculations were available (cf. Table B.15). We will
1279 discuss later those unconstrained but nevertheless important reactions.

1280 2.7.3.2. Positive Ions.

1281 **Ion-Neutral Reactions.** The chemical network contains 1882 ion-neutral
1282 reactions that are presented in Table B.16. They mostly originate from the
1283 compilations by Anicich (1993), McEwan and Anicich (2007), Wakelam et al.
1284 (2012, 2015) and Dutuit et al. (2013), although a specific literature search has
1285 been conducted for many other reactions that were not listed in those papers.
1286 New relevant data that have been obtained since 2007 can be found in Edwards
1287 et al. (2008, 2009), Fondren et al. (2009), Gerlich and Borodi (2009), Stavish
1288 et al. (2009), Žabka et al. (2009), Adams et al. (2010), Dryahina et al. (2011),
1289 Gerlich et al. (2011), Mathews and Adams (2011), Plašil et al. (2011), Demarais
1290 et al. (2013) and Lin et al. (2013). They represent about 170 reactions.

1291 In Vuitton et al. (2007), we pointed out that the production and loss reac-
1292 tions of most nitrogen bearing ions were not well characterized in the litera-
1293 ture. There is however convincing theoretical evidence that proton transfer in
1294 ion molecule reactions can have no barrier when the reactions are exothermic
1295 (Lindinger et al., 2000). We therefore made the general hypothesis that protons
1296 flow from species with a low proton affinity (typically hydrocarbons) to species
1297 having a high proton affinity (typically nitrogen bearing species) and assumed
1298 that these reactions occurred with a rate $k = 3 \times 10^{-9} \text{ cm}^3 \text{ s}^{-1}$, a simple and
1299 often reasonable approximation of the rate coefficient in the capture limit. How-
1300 ever, better capture theory estimates for rate coefficients can be made rather
1301 easily, as long as the relevant parameters are known.

1302 For non-polar neutral species (H_2 , CH_4 , C_2H_4 , etc.), we use the Langevin
1303 expression k_L :

$$k_L = 2\pi e(\alpha/\mu)^{1/2}, \quad (\text{E19})$$

1304 where e is the electronic charge of the ion, α is the dipole polarizability of the
1305 neutral and μ is the reduced mass of the reactants.

1306 For neutrals having a permanent dipole moment (such as nitrogen bear-
1307 ing species), the Langevin expression no longer applies and we use the Su-
1308 Chesnavich expression instead (Woon and Herbst, 2009). The ion-dipole rate
1309 coefficient k_D can be referenced to the Langevin value via the equations:

$$k_D/k_L = 0.4767x + 0.6200 \text{ if } x \geq 2 \quad (\text{E20})$$

1310 and

$$k_D/k_L = (x + 0.5090)^2/10.526 + 0.9754 \text{ if } x < 2, \quad (\text{E21})$$

1311 with x defined as:

$$x = \frac{\mu_D}{(2\alpha kT)^{1/2}}, \quad (\text{E22})$$

1312 where μ_D is the dipole moment of the neutral, k is the Boltzmann constant and
1313 T is the temperature. α and μ_D are obtained from Woon and Herbst (2009).

1314 Although the Langevin rate is temperature independent, the Su-Chesnavich
1315 expression exhibits a complex temperature dependence with k_D increasing with
1316 decreasing temperature. We did not implement this temperature dependence
1317 in the model but used a temperature independent rate coefficient, calculated
1318 for $T = 150$ K. Using expression (E22), it can be shown that decreasing the
1319 temperature from 300 to 150 K leads to an increase of the rate coefficient by
1320 a few tens of percent at best. Therefore, for those reactions that occur at the
1321 capture rate, the temperature dependence of the rate coefficient is expected
1322 to be small. The temperature dependence can however, be much stronger for
1323 those reactions that are rather slow at room temperature and we made sure
1324 to use temperature dependent rate coefficients when they were available in the
1325 literature. Unfortunately, a large majority of the rate coefficients have only been
1326 measured at 300 K.

1327 Ion production by cosmic rays is now included in the model and is a source
1328 of ion-neutral chemistry below 100 km. Three-body reactions are efficient in the
1329 lower atmosphere and 118 new chemical reactions to calculate the concentration
1330 of 15 new ions are considered. Most of these reactions were compiled in previous
1331 models by Capone et al. (1976, 1981) and Molina-Cuberos et al. (1999a, 2002),
1332 and originate from review papers by Anicich and McEwan (1997), Anicich et al.
1333 (2000) and McEwan and Anicich (2007). Other sources of information include
1334 the works of Smith et al. (1978a), Dheandhanoo et al. (1984), McEwan and
1335 Anicich (1995), Speller et al. (1995), Vacher et al. (1997), Milligan et al. (2001)
1336 and Hiraoka et al. (2003). We assume that protonated hydrocarbon ions (such as
1337 CH_5^+ and C_2H_7^+) form $\text{C}_n\text{H}_m^+\cdot\text{CH}_4$ electrostatic clusters with methane rather
1338 than additional C-C covalent bond type ions such as $\text{C}_3\text{H}_{11}^+$ (Capone et al.,
1339 1979).

1340 **Positive Ion Loss.** The ultimate loss for positive ions is radiative or dis-
1341 sociative electron recombination. The 492 recombination reactions present in
1342 the network are listed in Table B.17. Rate constants originate from a thor-
1343 ough literature search. Since 2007, new data have been obtained for CH_4^+
1344 (Thomas et al., 2013), CH_5^+ (Kamińska et al., 2010), C_4H_4^+ , C_5H_6^+ and C_7H_7^+
1345 (Fournier et al., 2013), C_6H_6^+ and C_6H_7^+ (Hamberg et al., 2011), C_7H_9^+ (Os-
1346 borne et al., 2011), $\text{C}_2\text{H}_3\text{NH}^+$ (Vigren et al., 2008), HC_3N^+ and HC_3NH^+ (Vi-
1347 gren et al., 2012a), $\text{C}_2\text{H}_3\text{CNH}^+$ (Vigren et al., 2009), $\text{C}_3\text{H}_5\text{NH}^+$ (Vigren et al.,
1348 2010a), $\text{C}_4\text{H}_5\text{NH}^+$ (Osborne et al., 2011), $\text{C}_5\text{H}_5\text{NH}^+$ (Adams et al., 2010; Os-
1349 borne et al., 2011), N_2H^+ (Vigren et al., 2012b) and CH_3CHO^+ (Vigren et al.,
1350 2010b).

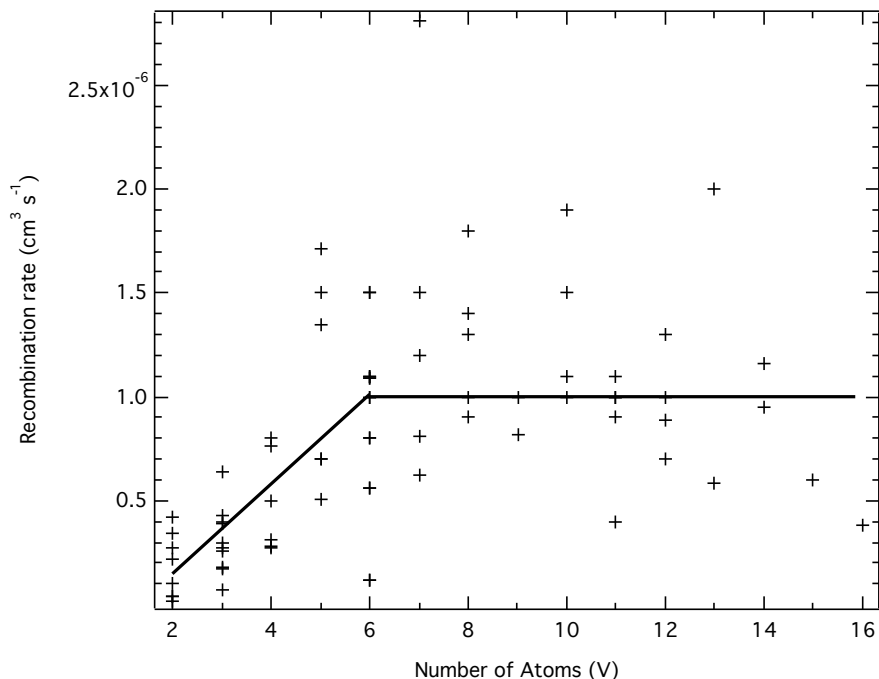


Figure 21: Dissociative recombination rate at an electron temperature of 300 K against the number of atoms constituting the ion.

1351 When no literature data were available, we assumed, in Vuitton et al. (2007),
 1352 a rate $\alpha = 7.0 \times 10^{-7} \text{ cm}^3 \text{ s}^{-1}$ at $T_e = 300 \text{ K}$, which corresponded to an average
 1353 of the rates that had been measured at that time. However, Vigren et al. (2013)
 1354 pointed out that for simple ions, there is a trend of increasing rate coefficient
 1355 with the number of atoms in the recombining ion. Building on this approach,
 1356 we present in Figure 21 the recombination rate at 300 K of the 67 ions present
 1357 in the reaction network for which a rate is available in the literature, against
 1358 the number of atoms present in the ion, V . This plot confirms the clear trend
 1359 of increasing rate coefficient up to about 6 atoms, followed by a leveling off for
 1360 more complex ions. To implement unknown recombination rates in the network,
 1361 we therefore use a linear fit of the data in Figure 21 for $2 \leq V \leq 6$, given by:

$$\alpha_{300}(V) = (2.15 \times V - 2.80) \times 10^{-7}, \quad (\text{E23})$$

1362 and a constant value $\alpha_{300} = 10^{-6} \text{ cm}^3 \text{ s}^{-1}$ for $V > 6$. The dependence with
 1363 electron temperature is set to $T_e^{-0.7}$, which corresponds to the average of the
 1364 available temperature dependences in our reaction network. The number of
 1365 electrons is set equal to the total modeled positive ion content minus the total
 1366 modeled negative ion content.

1367 Small clusters recombine with electrons with a high efficiency. For those
 1368 formed in Earth's stratosphere, $\text{H}_3\text{O}^+ \cdot (\text{H}_2\text{O})_n$ and $\text{NH}_4^+ \cdot (\text{NH}_3)_n$, recombination

1369 rates as large as $6.0 \times 10^{-6} \text{ cm}^3 \text{ s}^{-1}$ have been found, with the rate increasing
1370 with the cluster complexity (Mitchell, 1990). For the GCR induced layer of
1371 Titan, a general recombination coefficient with the same order of magnitude
1372 ($4\text{-}5 \times 10^{-6} \text{ cm}^3 \text{ s}^{-1}$), has been applied by Borucki et al. (1987) and Molina-
1373 Cuberos et al. (1999a). In the absence of experimental values relevant to Titan's
1374 atmosphere, we assume a mean dissociative recombination rate of $5 \times 10^{-6} \text{ cm}^3$
1375 s^{-1} for clusters.

1376 For product branching ratios, the situation is much more complex than for
1377 rate coefficients. Experiments are not always available and the proposed theo-
1378 retical models fail to provide correct predictions of dissociative recombination
1379 branching ratios for most of the poly-atomic molecules considered, or even ap-
1380 propriate guidance for their determination. The frequent assumptions to con-
1381 sider H loss or the most exothermic products as the only channel has been shown
1382 to be incorrect for most studied hydrocarbon or nitrogen bearing ions. Instead,
1383 dissociative recombination tends to break bonds between heavy atoms and gen-
1384 erate multiple fragments (up to four), giving many different product channels.
1385 Recently, Chabot et al. (2013) put forward that fragmentation-branching ratios
1386 of electronically excited molecular species (as in dissociative recombination)
1387 exhibit a statistical behavior. Therefore, they could be deduced from a combi-
1388 nation of the large set of experimental data measured in high velocity collisions
1389 and semi empirical models. However, this approach has only been applied to a
1390 subset of ions so far, amongst which only three are relevant to Titan.

1391 In the absence of clearly established empirical rules correlating breakup pat-
1392 terns to easily estimated physical properties, we made some gross assumptions
1393 to estimate product branching ratios:

- 1394 • The structure of the ions is taken from the Kinetic Database for Astro-
1395 chemistry (cf. Wakelam et al. (2012, 2015) or <http://kida.obs.u-bordeaux1.fr/>).
- 1396 • H loss occurs for every reaction with a branching ratio of 50%. We do not
1397 consider loss of multiple H atoms, or loss of H_2 (cf. bullet 3).
- 1398 • Breakage of bounds between heavy atoms (C-C, C-N, C-O) accounts for
1399 the rest of the channels, with the same branching ratio.
- 1400 • For a given set of products only one bound is allowed to break, which
1401 implies that double and triple bonds stay intact and that there are no
1402 multiple products.
- 1403 • We minimize rearrangement of the atoms, especially when it comes to
1404 choosing between different isomers (such as HCN versus HNC). When the
1405 situation is unclear, we assume the formation of 50% of each isomer.

1406 We acknowledge that this is overly simplistic and probably quite different from
1407 reality. Pernot et al. (2011) proposed a novel approach, based on probabilistic
1408 trees, to fully account for partially available information. However, this method
1409 requires some *a priori* information and has not been implemented for totally
1410 unconstrained reactions.

1412 **Negative Ion Production.** Production mechanisms for negative ions in-
 1413 clude photoionization (ion-pair formation) as well as dissociative and radiative
 1414 electron attachment. Photoionization is presented in Table B.10, dissociative
 1415 electron attachment in Table B.11 and radiative electron attachment in Table
 1416 B.14.

1417 The dissociative electron attachment cross-sections for CH_4 , C_2H_2 , C_4H_2
 1418 and HCN have been updated since Vuitton et al. (2009). For CH_4 , we prefer
 1419 the measurements of Rawat et al. (2008) to that of Sharp and Dowell (1967). In
 1420 both studies, a broad peak centered at 9.8 eV is attributed to the H^- channel,
 1421 while a one order of magnitude smaller and relatively narrow peak centered at
 1422 10.4 eV is attributed to the CH_2^- channel. However, it appears that the cross-
 1423 sections for H^- have been underestimated by a factor of almost 20 by Sharp and
 1424 Dowell (1967), which Rawat et al. (2008) rationalize in terms of kinetic energy
 1425 discrimination. The contribution for the CH_2^- channel is also higher in Rawat
 1426 et al. (2008) but differs only by a factor of about 2.

1427 For C_2H_2 , the studies by May et al. (2008, 2009) supersede the data obtained
 1428 by Rutkowski et al. (1980). The main difference is that the peak close to 7.9
 1429 eV and previously assigned to C_2H^- is now attributed to H^- . Also, the cross-
 1430 sections are a factor of about two smaller.

1431 Because of the absence of any study available at that time, we used in Vuit-
 1432 ton et al. (2009) the C_2H_2 data for C_4H_2 and C_6H_2 . The absolute cross-sections
 1433 obtained by May et al. (2008) for the two former species are clearly different
 1434 from one another (cf. Table B.11) and do not support our previous assump-
 1435 tion. As a consequence, we use the values now available for C_4H_2 and in the
 1436 absence of a reliable way to estimate the cross-sections, no longer consider dis-
 1437 sociative electron attachment to C_6H_2 (or HC_5N , previously assumed to behave
 1438 as HC_3N).

1439 For HCN , we prefer the recent values obtained by May et al. (2010) to that of
 1440 Inoue (1966). The peak of the CN^- band is at somewhat lower energy (1.9 versus
 1441 2.5 eV), which can be explained by the absence of electron monochromator and
 1442 the relatively crude method of energy scale calibration of the early work. Also,
 1443 the cross-section is about one order of magnitude lower than the value previously
 1444 estimated (9.4×10^{-18} versus 2.0×10^{-16} cm^2). Finally, dissociative electron
 1445 attachment to H_2 (Krishnakumar et al., 2011), CH_3CCH (Janečková et al.,
 1446 2012), NH_3 (Rawat et al., 2008), HNC (Chourou and Orel, 2009) and C_4N_2
 1447 (Graupner et al., 2008) are now included, as some data became available since
 1448 our previous publication.

1449 The radiative electron attachment rate coefficients are essentially the same
 1450 as those presented in Table 2 of Vuitton et al. (2009), with the exception of
 1451 those for H (Stancil and Dalgarno, 1998), C_4H , C_6H (Carelli et al., 2013) and
 1452 C_5N (Walsh et al., 2009), which have been updated. The changes made for the
 1453 radiative electron attachment rates are not significant (factor of 2 at most).

1454 **Ion-Neutral Reactions.** Ion-neutral reactions are presented in Table B.18.
 1455 Some reaction rates have been updated since Vuitton et al. (2009): Biennier
 1456 et al. (2014); Martinez et al. (2010), Su & Chesnavich at 150 K (cf. positive
 1457 ions).

1458 Mackay et al. (1977) measured the rate coefficient for the proton transfer
 1459 reaction of H^- with C_2H_2 and reported $k = 4.4 \pm 1.1 \times 10^{-9} \text{ cm}^3 \text{ s}^{-1}$, a
 1460 value that we used in Vuitton et al. (2009). Recently, Martinez et al. (2010)
 1461 obtained $k = 3.1 \pm 0.9 \times 10^{-9} \text{ cm}^3 \text{ s}^{-1}$ with a similar technique. Although
 1462 the measurements overlap within combined error bars, the faster rate of Mackay
 1463 et al. (1977) can be rationalized by the presence of acetone (used to safely store
 1464 acetylene) as a contaminant in their experiment and we prefer the recent rate
 1465 of Martinez et al. (2010).

1466 Because HCN is less acidic than HC_3N , we assumed in Vuitton et al. (2009)
 1467 that the products of the reaction between CN^- and HC_3N are C_3N^- and HCN
 1468 and that the reaction occurs at every collision. This assumption has since been
 1469 validated experimentally (Biennier et al., 2014).

1470 We finally include the reaction of C_4H^- and C_6H^- with N atoms, which
 1471 primarily form CN^- but are rather slow, with rate coefficients close to 10^{-11}
 1472 $\text{cm}^3 \text{ s}^{-1}$ (Eichelberger et al., 2007).

1473 **Negative Ion Loss.** Loss mechanisms for negative ions include photode-
 1474 tachment (cf. Table B.12), recombination with positive ions (cf. Table B.17)
 1475 and associative detachment with neutrals (cf. Table B.19).

1476 For the photodetachment calculations, we adopt a cross-section σ (cm^2) that
 1477 depends on the photon energy ϵ (eV), according to the empirical formula:

$$\text{for } \epsilon \geq EA, \sigma = \sigma_\infty (1 - EA/\epsilon)^{0.5}, \quad (\text{E24})$$

1478 where σ_∞ denotes the asymptotic cross-section (cm^2) for large photon energies
 1479 and EA the electron affinity (eV) of the corresponding neutral (Millar et al.,
 1480 2007). Ion traps have recently been successfully employed to study absolute
 1481 photodetachment cross-sections for O^- and OH^- (Hlavenka et al., 2009), C_2H^- ,
 1482 C_4H^- and C_6H^- (Best et al., 2011), and CN^- and C_3N^- (Kumar et al., 2013).
 1483 For these ions, σ_∞ is derived from fits to the measured cross-sections using
 1484 Equation (E24) and literature electron affinities. For the other ions for which
 1485 no experimental data are available, we assume σ_∞ to be equal to 10^{-17} cm^2 .
 1486 The electron affinities and asymptotic cross-section values are given in Table
 1487 (B.12).

1488 The parameterization of Hickman (1979) for the recombination of negative
 1489 with positive ions has been revised by Miller et al. (2012), following a new set
 1490 of measurements. We therefore use the updated expression,

$$k = 2.8 \times 10^{-7} EA^{-0.13} \mu^{-0.5} (T/300)^{-0.9} \text{ cm}^3 \text{ s}^{-1}, \quad (\text{E25})$$

1491 where EA is the electron affinity of the corresponding neutral, μ is the reduced
 1492 mass of the collision partners and T is the temperature of the gas. For the ions

1493 of interest here, we obtain rate coefficients varying from 5×10^{-8} to 3×10^{-7}
 1494 $\text{cm}^3 \text{s}^{-1}$ at 300 K.

1495 We now consider reaction products and, in the absence of data, we use the
 1496 general scheme: $A^- + BH^+ \rightarrow A + B + H$. In the case of HCNH^+ , it is assumed
 1497 that the product is only HCN (no HNC), the most stable isomer, as explained
 1498 in section 2.7.3.1. We elaborate on possible HCNH^+ states in the discussion,
 1499 section 5.1.

1500 We consider associative detachment with H and CH_3 as in Vuitton et al.
 1501 (2009), and now also include reaction with N atoms that exhibit an abundance
 1502 similar to CH_3 in the ionosphere. Gerlich et al. (2012) studied the formation of
 1503 H_2 via associative detachment in $\text{H}^- + \text{H}$ collisions between 10 and 135 K and
 1504 reports a rate coefficient of $5.5 \times 10^{-9} \text{cm}^3 \text{s}^{-1}$ at 135 K, which we prefer to
 1505 the room temperature value of Fehsenfeld et al. (1973).

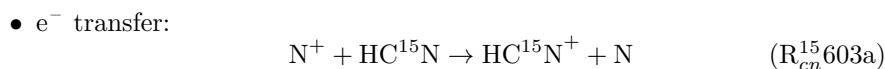
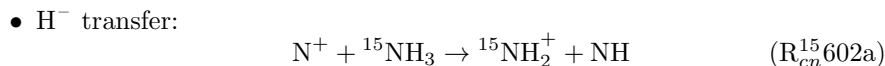
1506 We also update the rate coefficients for CN^- , C_3N^- and C_5N^- with H atoms
 1507 (Yang et al., 2011; Snow et al., 2009). For CN^- , the reported rate coefficient
 1508 ($6.3 \times 10^{-10} \text{cm}^3 \text{s}^{-1}$) agrees well with the previous results of Fehsenfeld et al.
 1509 (1973): $8 \times 10^{-10} \text{cm}^3 \text{s}^{-1} \pm$ factor of 2. We note that in Vuitton et al. (2009),
 1510 we reproduced an incorrect value ($1.3 \times 10^{-9} \text{cm}^3 \text{s}^{-1}$) cited in Fehsenfeld
 1511 (1975). For C_3N^- and C_5N^- , the rate coefficient is a factor of ~ 2 smaller than
 1512 the assumption (after Petrie and Herbst (1997)) reported in our previous paper.

1513 The reactions with N atoms use the rate coefficients reported in Eichelberger
 1514 et al. (2007) and Ferguson (1973) for C_2H^- and OH^- , respectively. For the other
 1515 ions, we assume that the rate coefficient is the same as that for the reaction with
 1516 H atoms.

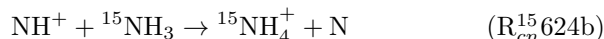
1517 Again, we now consider reaction products and, in the absence of data, use
 1518 the general scheme: $A^- + B \rightarrow AB + e^-$. In the case of C_3H_4 , it is assumed that
 1519 the products are equal amounts of CH_3CCH and CH_2CCH_2 (cf. Table B.14).

1520 2.7.4. ^{15}N Species

1521 In order to take into account ^{15}N bearing species, we start from our ^{14}N
 1522 chemistry and generate analogous reactions in which ^{14}N is replaced by ^{15}N .
 1523 Because they do not impact nitrogen chemistry, we do not include reactions
 1524 of ^{15}N species with oxygen species and negative ions. Reactions in which both
 1525 reactants contain nitrogen or in which a species contains more than one nitrogen
 1526 atom create special problems and some general rules have to be applied. First
 1527 of all, we leave out reactions where ^{15}N species would react with each other
 1528 (i.e. $\text{C}^{15}\text{N} + \text{HC}^{14}\text{N}$ and $\text{C}^{14}\text{N} + \text{HC}^{15}\text{N}$ are taken into account but not C^{15}N
 1529 + HC^{15}N). If the reaction consists in some exchange reaction (H^+ , H^- and e^-
 1530 transfer), we assume that there is no rearrangement and that the ^{15}N is not
 1531 allowed to change molecule during reaction, as shown in the three following
 1532 examples:

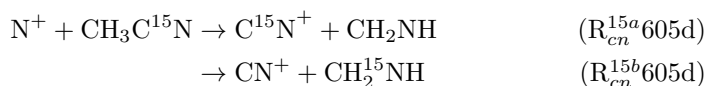


- H⁺ transfer:



1533 If the reaction is some more intricate process, which may involve an inter-
 1534 mediate complex with possible rearrangement, we arbitrarily assign statistical
 1535 branching ratios to the individual channels. Thus, for the two product channels
 1536 in the reaction below, a statistical ratio of 0.5 is applied to each.

- Intermediate complex:

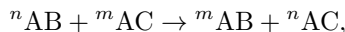


1537 Fortunately, we find that the only reactions that turn out to be important
 1538 are proton exchange reactions and that therefore the assumption made above
 1539 does not have any impact.

1540 Once the list of reactions of ¹⁵N species has been established, it remains to
 1541 evaluate their rate coefficients. Substitution of an atom in the reactants of a
 1542 chemical reaction with one of its isotopes results in a change in rate coefficient,
 1543 a mechanism referred to as a kinetic isotope effect. The difference can be rati-
 1544 onalized by noting that the mass of an atom affects the vibrational frequency
 1545 of the chemical bond that it forms, even if the electron configuration is nearly
 1546 identical. Heavier atoms will lead to lower vibration frequencies, or, viewed
 1547 quantum mechanically, will have lower zero-point energy. With a lower zero-
 1548 point energy, more energy must be supplied to break the bond, resulting in a
 1549 higher activation energy for bond cleavage, which in turn lowers the measured
 1550 rate coefficient according to the Arrhenius equation.

1551 A direct consequence is that rate coefficient changes are most pronounced
 1552 when the relative mass change of the isotopes is greatest. For instance, substi-
 1553 tuting a hydrogen atom to deuterium represents a 100% increase in mass and
 1554 the rate coefficient of a reaction involving a C-H bond is typically 6-10 times
 1555 faster than for the corresponding C-D bond. However, when replacing ¹²C with
 1556 ¹³C, the mass increases by only 8% and a ¹²C reaction is only ~1.04 times faster
 1557 than the corresponding ¹³C reaction (even though, in both cases, the isotope is
 1558 one atomic mass unit heavier). Since replacing a ¹⁴N with ¹⁵N represents only
 1559 a 7% increase in mass, we neglect mass-dependent kinetic isotope effects when
 1560 generating our ¹⁵N reaction network. This assumption is supported by recent
 1561 laboratory experiments (Kuga et al., 2014; Sebree et al., 2016), which show little
 1562 nitrogen isotopic fractionation in tholins, ¹⁵N being depleted by δ¹⁵N=+0.8/-
 1563 25‰ relative to the initial N₂ gas. This is to be compared to the δ¹⁵N~+2000‰
 1564 fractionation observed between HCN and N₂.

1565 Another possible isotopic fractionation mechanism is equilibrium fractiona-
 1566 tion, which is the partial separation of isotopes between two or more substances
 1567 in chemical equilibrium, owing to exothermicity. In an isotopic exchange reac-
 1568 tion such as:



1569 where A, B, and C are chemical elements and m and n refer to the atomic
1570 masses of two isotopes of A, the equilibrium coefficient $K(T)$ can be written as:

$$K(T) = k_f/k_r = f(B, m)\exp(\Delta E_0/kT), \quad (\text{E26})$$

1571 where k_f and k_r are the forward and reverse rate coefficients and ΔE_0 , the
1572 zero-point vibrational energy difference between the reactants and the prod-
1573 ucts, is defined to be positive for exothermic reactions. $f(B, m)$ refers to ratios
1574 of partition functions and, in most cases, is close to the molecular symmetry
1575 factor, which depends on the rotational constants, masses and symmetries of
1576 the reactants and products. Equilibrium fractionation is therefore strongest at
1577 low temperatures and isotopes of light elements (hydrogen, carbon, nitrogen,
1578 oxygen, sulfur) tend to be separated to a greater degree. However, the exother-
1579 micity of isotopic exchange reactions being typically less than 40 K (Terzieva
1580 and Herbst, 2000), we neglect this mechanism in our reaction network.

1581 At the end, we have 26 neutrals, 72 positive ions, 285 neutral reactions, 1453
1582 ion-neutral reactions, and 169 ion-electron recombination reactions involving the
1583 ${}^{15}\text{N}$ isotope.

1584 2.7.5. Heterogeneous Processes

1585 The presence of aerosols in the atmosphere can interfere with the purely gas
1586 phase chemistry described so far. Heterogeneous processes that can occur on
1587 the surfaces of aerosol particles include:

- 1588 1. Simple adsorption of gaseous species.
- 1589 2. Recombination of gaseous species at the surface of aerosols and release of
1590 a new species in the gas phase.
- 1591 3. Reaction of gaseous species with the chemical constituents of the aerosols
1592 with subsequent release in the gas phase.

1593 However, heterogeneous processes have been poorly described in photochemical
1594 models so far, the only species ever considered being atomic hydrogen, follow-
1595 ing Sekine et al. (2008a) who investigated heterogeneous reactions of atomic
1596 hydrogen in conditions relevant to Titan (tholins material, low temperature).
1597 They showed that hydrogenation of tholins (process 1) is about one order of
1598 magnitude more important than H_2 recombination (process 2), with a reaction
1599 probability $\eta_{\text{hydro}} = 2.08(\pm 0.64) \times \exp(-1000/T)$.

1600 In this model, we include a loss of atomic hydrogen to the aerosols with
1601 a reaction probability of 2.65×10^{-3} , which corresponds to η_{hydro} at 150 K
1602 (Sekine et al., 2008a). For the aerosol distribution (cf. Figure 22), we use the
1603 mean particle size and density predicted by the microphysical model of Lavvas
1604 et al. (2010), which are consistent with the haze optical properties retrieved by
1605 the DISR observations (Tomasko et al., 2008).

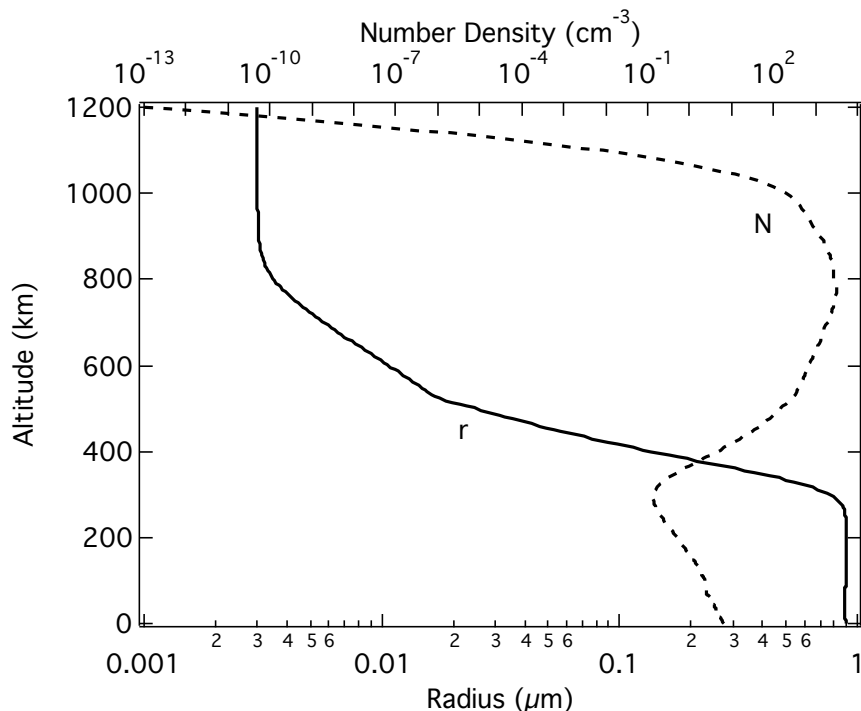


Figure 22: Altitude variation of the aerosol radius and density.

1606 **3. Chemical Composition**

1607 *3.1. The Upper Ionosphere*

1608 *3.1.1. Positive Ions*

1609 Solar radiation and associated photoelectrons are mostly deposited above 600
 1610 km and are at the origin of Titan’s upper ionosphere. We review here our current
 1611 knowledge on the major ion-molecule reactions involved in the chemistry. We
 1612 focus first on the primary ions (N_2^+ , N^+ and CH_4^+) and follow the chemical
 1613 evolution to complex hydrocarbon ions and nitrogen-bearing ions, and finish
 1614 with oxygen-bearing ions. All the numbers listed are from the nominal model,
 1615 as described in section 4.2.3.

1616 *3.1.1.1. Primary Ions.* Primary ions are produced upon interaction of N_2 and
 1617 CH_4 with solar photons and suprathreshold photo- and secondary electrons. Ta-
 1618 ble 6 presents the N_2 and CH_4 loss rates from photons, photoelectrons and
 1619 chemistry. Our calculated rates are similar to those presented in Lavvas et al.
 1620 (2011a), which was to be expected since we use similar cross-sections. Lavvas
 1621 et al. (2011a) compared the primary N_2 loss rates obtained by different photo-
 1622 chemical models and we do not repeat this discussion here.

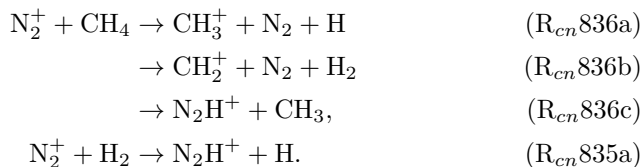
1623 From Table 6, N_2^+ , N^+ and CH_4^+ are the major primary ionization products
 1624 from N_2 and CH_4 , all the other ions being mostly formed by secondary chemical

Table 6: Calculated column production rate (cm^{-2}) for the fragments of the ionization of CH_4 and N_2 from photons, photoelectrons and chemistry.

Products	Photons	Photoelectrons	Chemistry	Total
N_2^+	1.6×10^8	8.9×10^7	1.1×10^4	2.5×10^8
N^+	3.8×10^7	1.1×10^7	2.0×10^3	4.8×10^7
CH_4^+	2.4×10^7	2.5×10^6	3.4×10^6	3.0×10^7
CH_3^+	7.4×10^6	1.8×10^6	2.3×10^8	2.4×10^8
CH_2^+	2.3×10^5	2.4×10^5	2.1×10^7	2.1×10^7
CH^+	6.9×10^4	8.9×10^4	5.7×10^5	7.3×10^5
C^+	1.5×10^4	2.4×10^4	1.1×10^4	5.0×10^4
H_2^+	1.3×10^4	3.8×10^4	1.0×10^6	1.1×10^6
H^+	9.9×10^4	1.5×10^5	4.4×10^4	2.9×10^5

1625 reactions involving these primary ions. The primary production rates of N_2^+ ,
 1626 N^+ and CH_4^+ are shown in Figure 11 of Lavvas et al. (2011a).

1627 N_2^+ , N^+ . N_2^+ reacts efficiently with CH_4 and H_2 , leading directly or via
 1628 N_2H^+ (section 3.1.1.3) to the ionization of hydrocarbons without any net loss
 1629 for N_2 and therefore any production of active nitrogen:



1630 The kinetics of the reaction of N_2^+ with CH_4 has been extensively studied at
 1631 300 K and the latest determinations are all in good agreement suggesting that
 1632 the rate coefficient is equal within experimental uncertainties to the capture
 1633 rate, i.e. $1.2 \times 10^{-9} \text{ cm}^3 \text{ s}^{-1}$ (Dutuit et al., 2013). The rate coefficient seems
 1634 unchanged over the temperature range 70-300 K and the recommended value is
 1635 the same at 150 K and 300 K (Rowe et al., 1989).

1636 Most studies are in agreement concerning the production of the dissocia-
 1637 tive charge transfer products, CH_2^+ and CH_3^+ , but there is an important
 1638 disagreement concerning the production of N_2H^+ , its detection being difficult
 1639 because of mass overlaps. The recommended branching ratios at 300 K are
 1640 0.86/0.09/0.05 for the three channels $(\text{R}_{cn}836a)/(\text{R}_{cn}836b)/(\text{R}_{cn}836c)$ (Nico-
 1641 las et al., 2003b). The branching ratios seem to be constant as a function
 1642 of temperature (Gichuhi and Suits, 2011). A recent study (Xu et al., 2013)
 1643 shows, however, that the branching ratios determined at $E_{cm} = 0.05 \text{ eV}$ (380
 1644 K) are $0.68 \pm 0.05/0.26 \pm 0.04/0.06 \pm 0.01$, which is quite different from previous
 1645 measurements. Since the branching ratios are found to be almost constant with
 1646 collision energy (Nicolas et al., 2003b; Xu et al., 2013), it is reasonable to expect

1647 the same values at 300 K. The difference seems to be due to the occurrence of
 1648 secondary reactions that were not corrected for in the previous studies.

1649 The reaction between N_2^+ and H_2 has been extensively studied and all rate
 1650 coefficient measurements at 300 K are in good agreement. They give a value
 1651 nearly equal to the Langevin rate ($1.6 \times 10^{-9} \text{ cm}^3 \text{ s}^{-1}$), which is the value
 1652 recommended by Dutuit et al. (2013). When the temperature decreases, the rate
 1653 coefficient goes through a minimum and increases again at lower temperature.
 1654 The recommended value at 150 K is $1.3 \times 10^{-9} \text{ cm}^3 \text{ s}^{-1}$ (Rowe et al., 1989;
 1655 Randeniya and Smith, 1991).

1656 The products have been the subject of extensive experimental investigations.
 1657 The hydrogen transfer channel ($\text{R}_{cn}835a$) is strongly favored over the charge
 1658 transfer channel ($\text{R}_{cn}835b$), with recommended branching ratios at 300 K of
 1659 0.99/0.01 (Dutuit et al. (2013) and references therein). There are no studies
 1660 available at lower temperature.

1661 N^+ is essentially formed by photoionization above 900 km and by photoelec-
 1662 tron impact down to 700 km. Like N_2^+ , it reacts efficiently with CH_4 and H_2 ,
 1663 but leading to the formation of reactive nitrogen-bearing ions (HCNH^+ , NH^+ ,
 1664 HCN^+) and radicals (NH , $\text{N}(^4\text{S})$).



1665 The recommended total rate coefficient at 300 K for the reaction of N^+ with
 1666 CH_4 is the mean value of the available experimental values, i.e. 1.2×10^{-9}
 1667 $\text{cm}^3 \text{ s}^{-1}$ (McEwan and Anicich, 2007; Dutuit et al., 2013). The rate coefficient
 1668 seems to decrease with decreasing temperature (Rowe et al., 1985) and a rate
 1669 coefficient of $1.0 \times 10^{-9} \text{ cm}^3 \text{ s}^{-1}$ is recommended at 150 K (Dutuit et al., 2013).

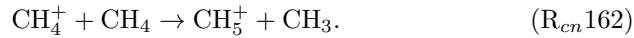
1670 The recommended branching ratios at 300 K are 0.50/0.35/0.10/0.05 for
 1671 the channels ($\text{R}_{cn}593a$)/($\text{R}_{cn}593b$)/($\text{R}_{cn}593c$)/($\text{R}_{cn}593d$), respectively (McE-
 1672 wan and Anicich, 2007; Dutuit et al., 2013). The branching ratios of ($\text{R}_{cn}593b$)
 1673 and ($\text{R}_{cn}593c$) increase when the collision energy decreases from 0.2 to 0.05
 1674 eV, at the expense of channels ($\text{R}_{cn}593a$) and ($\text{R}_{cn}593d$) (Dheandhanoo et al.,
 1675 1984).

1676 In order to obtain the branching ratios at 150 K, Carrasco et al. (2008) ex-
 1677 trapolated the data of Figure 5 in Dheandhanoo et al. (1984) assuming an expo-
 1678 nential variation and for channels ($\text{R}_{cn}593a$)/($\text{R}_{cn}593b$)/($\text{R}_{cn}593c$)/($\text{R}_{cn}593d$)
 1679 obtained 0.47/0.40/0.12/0.02, respectively. However, they showed that using
 1680 the 150 K extrapolated branching ratios in their chemical model instead of the
 1681 values at 300 K has almost no impact on the density of major ions. Because
 1682 of this result and because the extrapolation of kinetic parameters outside their

1683 range of validity is always subject to caution, we decide to use the 300 K branch-
 1684 ing ratios in the model.

1685 The reaction between N^+ and H_2 has been extensively studied both experi-
 1686 mentally and theoretically, at room temperature and below. It is endothermic
 1687 by 17 meV and is therefore very sensitive to temperature (cf. Zymak et al.
 1688 (2013) and references therein). For the rate coefficient at 300 K, extensive liter-
 1689 ature reviews were performed by McEwan and Anicich (2007) and Dutuit et al.
 1690 (2013) who recommend a value of $5.0 \times 10^{-10} \text{ cm}^3 \text{ s}^{-1}$ and $3.8 \times 10^{-10} \text{ cm}^3 \text{ s}^{-1}$,
 1691 respectively. Here, we choose to use the temperature dependent rate coefficient
 1692 retrieved from the Marquette et al. (1988) data obtained between 8 and 163 K,
 1693 that is $4.2 \times 10^{-10} \exp(-41.9/T) \text{ cm}^3 \text{ s}^{-1}$.

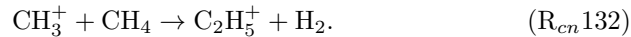
1694 **CH_4^+** . CH_4^+ is mostly formed by photoionization of CH_4 , photoelectron
 1695 impact representing only about 10% of the total production rate, as does re-
 1696 action between N^+ and CH_4 ($\text{R}_{cn}593d$). It is mostly lost by reaction with
 1697 methane:



1698 The evaluated rate coefficient at 300 K, i.e. $1.1 \times 10^{-9} \text{ cm}^3 \text{ s}^{-1}$, is based
 1699 on an extensive literature review (McEwan and Anicich (2007) after Anicich
 1700 et al. (2003)). The rate coefficient seems to slightly decrease with decreasing
 1701 temperature since a value of $9.0 \times 10^{-10} \text{ cm}^3 \text{ s}^{-1}$ has been measured at 90 K
 1702 (Bowers et al., 1977).

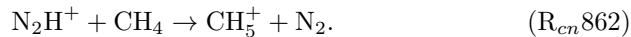
1703 3.1.1.2. *Hydrocarbon Ions.*

1704 **CH_3^+ , CH_5^+** . The chemistry of CH_3^+ is extremely simple, as it is almost
 1705 exclusively produced by dissociative charge transfer from the major primary ion,
 1706 N_2^+ , to methane ($\text{R}_{cn}836a$) and lost through reaction with methane:



1707 The evaluated rate coefficient at 300 K, i.e. $1.1 \times 10^{-9} \text{ cm}^3 \text{ s}^{-1}$, is based on
 1708 an extensive literature review (McEwan and Anicich (2007) after Anicich et al.
 1709 (2003)). The rate coefficient has not been measured at low temperature but
 1710 since it is fast at room temperature, the temperature dependence is expected to
 1711 be small.

1712 The CH_5^+ production is similar to that described in Vuitton et al. (2007).
 1713 It is closely linked to the ionization of both CH_4 through reaction ($\text{R}_{cn}162$) and
 1714 N_2 through the intermediate species N_2H^+ (formed through reactions ($\text{R}_{cn}835a$)
 1715 and ($\text{R}_{cn}836c$), section 3.1.1.3):



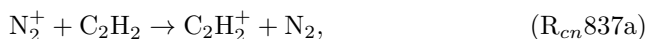
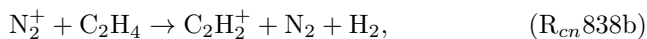
1716 As in Vuitton et al. (2007), this ion is mostly lost through proton transfer
 1717 reactions to HCN , C_2H_4 and C_2H_2 ($\text{R}_{cn}194, \text{R}_{cn}180, \text{R}_{cn}179$), and through dis-
 1718 sociative electron recombination ($\text{R}_{er}14$).

1719 The reaction between CH_5^+ and HCN has never been studied. Keller et al.
 1720 (1992) made the assumption that the only channel is a proton transfer from the
 1721 ion to the neutral and that the rate coefficient is equal to the Langevin rate. It
 1722 is now understood that for neutrals having a permanent dipole moment, such
 1723 as HCN, the Langevin expression does not apply and we use the Su-Chesnavich
 1724 expression instead (Woon and Herbst, 2009). Using literature values for the
 1725 dipole polarizability and dipole moment for HCN (CRC Handbook of Chemistry
 1726 and Physics, 87th Edition) leads to a rate coefficient at 150 K of 5.8×10^{-9}
 1727 $\text{cm}^3 \text{s}^{-1}$, five times higher than the rate used in Keller et al. (1992).

1728 The evaluated rate coefficients at 300 K for $\text{CH}_5^+ + \text{C}_2\text{H}_4$ and $\text{CH}_5^+ + \text{C}_2\text{H}_2$
 1729 (McEwan and Anicich, 2007), i.e. $1.5 \times 10^{-9} \text{cm}^3 \text{s}^{-1}$ in both cases, are based
 1730 on the measurements of Fiaux et al. (1974) and Mackay et al. (1977), and close
 1731 to the Langevin rate, as should be expected for such proton transfer reactions.

1732 CH_5^+ dissociative recombination experiments have been performed at both a
 1733 heavy-ion storage ring (CRYRING) and in a flowing afterglow and they present
 1734 some significant discrepancies in terms of both rate coefficient and branching
 1735 fractions of the products. While the former set of studies reports the dominance
 1736 of $\text{CH}_3 + \text{H} + \text{H}$ (Semaniak et al., 1998; Kamińska et al., 2010), the latter observes
 1737 $\text{CH}_4 + \text{H}$ as the major products (Adams et al., 2009; Molek et al., 2009). A
 1738 possible explanation is that a two-step process via the production of a CH_4
 1739 intermediate with sufficient energy to fragment further to $\text{CH}_3 + \text{H}$ plays an
 1740 important role. The disagreement could therefore be due to a different pressure
 1741 in these two experimental set-ups ($< 10^{-11}$ mbar in CRYRING versus ~ 1 mbar
 1742 in the flow tube). The storage ring conditions being closer to that of Titan's
 1743 upper atmosphere, we prefer the values presented in Kamińska et al. (2010).

1744 C_2H_2^+ , C_2H_3^+ , C_2H_4^+ , C_2H_5^+ , C_2H_7^+ . C_2H_2^+ is formed by (disso-
 1745 ciative) charge transfer to ethylene and acetylene:



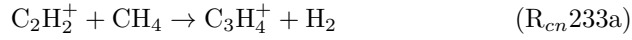
1746 The evaluated rate coefficient of the reaction between N_2^+ and C_2H_4 is equal
 1747 to $1.3 \times 10^{-9} \text{cm}^3 \text{s}^{-1}$, which corresponds to the Langevin rate and is therefore
 1748 temperature independent (Dutuit et al. (2013) after McEwan et al. (1998)).
 1749 The three studies that focus on the product branching ratios of this reaction,
 1750 including that of Gichuhi and Suits (2011) at ~ 45 K, agree that $\text{C}_2\text{H}_3^+ + \text{H} + \text{N}_2$
 1751 are the main products and that a secondary channel gives $\text{C}_2\text{H}_2^+ + \text{H}_2 + \text{N}_2$.
 1752 A third channel leading to a small amount of $\text{N}_2\text{H}^+ + \text{C}_2\text{H}_3$ remains to be
 1753 confirmed (Dutuit et al., 2013).

1754 The evaluated rate coefficient of the $\text{N}_2^+ + \text{C}_2\text{H}_2$ reaction ($4.2 \times 10^{-10} \text{cm}^3$
 1755 s^{-1} at 300 K) is significantly smaller than the Langevin rate and decreases

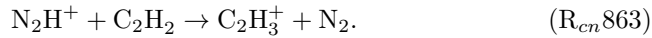
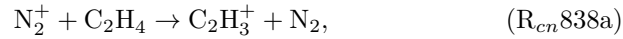
1756 with increasing temperature according to $E_{CM}^{-1/2}$, as expected for charge transfer
 1757 reactions. Extrapolation of the reaction cross section obtained at 928 K down
 1758 to 150 K gives a rate coefficient of $1.0 \times 10^{-9} \text{ cm}^3 \text{ s}^{-1}$ (Dutuit et al., 2013). All
 1759 studies concur that $\text{C}_2\text{H}_2^+ + \text{N}_2$ are the major products; the high $\text{N}_2\text{H}^+ + \text{C}_2\text{H}$
 1760 branching ratio mentioned in the compilation of McEwan and Anicich (2007),
 1761 disagreeing with Anicich et al. (2004), is probably an error (Dutuit et al., 2013).

1762 The evaluated rate coefficient of the reaction of N^+ with C_2H_2 (1.4×10^{-9}
 1763 $\text{cm}^3 \text{ s}^{-1}$) is very close to the Langevin rate (Dutuit et al. (2013) after McEwan
 1764 et al. (1998)). The McEwan and Anicich (2007) recommendation gives $\text{C}_2\text{H}_2^+ +$
 1765 N as the major products at room temperature. At 150 K, the yield of the
 1766 other products, which originate from a chemical reaction requiring a long-lived
 1767 complex intermediate, is expected to increase relatively to the C_2H_2^+ ions,
 1768 coming from charge transfer. In the absence of data, we nevertheless use the
 1769 branching ratios resulting from the experimental outputs at 300 K.

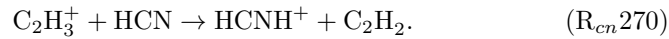
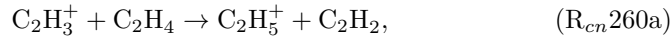
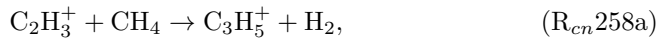
1770 C_2H_2^+ is lost through reaction with methane:



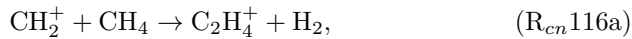
1771 C_2H_3^+ is produced through a variety of reactions involving H^+ , e^- , H^- and
 1772 H transfer:



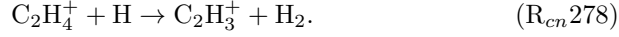
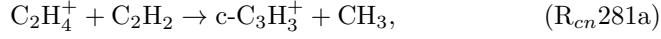
1773 It is lost through condensation and proton transfer reactions:



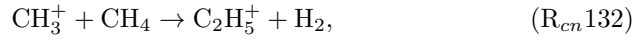
1774 C_2H_4^+ is formed through one condensation reaction and through one charge
 1775 transfer reaction:



1776 It is lost through electron recombination above 1200 km ($\text{R}_{er}20$) and some ion-
 1777 neutral reactions below:



1778 The production and loss terms of C_2H_5^+ have been discussed in Vuitton
1779 et al. (2007). Production is related to the ionization of both N_2 (via CH_3^+) and
1780 CH_4 (via CH_5^+):



1781 Loss occurs through proton transfer to HCN and HNC ($\text{R}_{cn}316, \text{R}_{cn}317$), disso-
1782 ciative electron attachment ($\text{R}_{er}21$) and reaction with C_2H_4 :



1783 The evaluated rate coefficient at 300 K for the reaction $\text{C}_2\text{H}_5^+ + \text{HCN}$ ($\text{R}_{cn}316$),
1784 i.e. $2.7 \times 10^{-9} \text{ cm}^3 \text{ s}^{-1}$ (McEwan and Anicich, 2007), is based on the only study
1785 available to date (Mackay et al., 1980). The capture rate at 300 K is 3.7×10^{-9}
1786 $\text{ cm}^3 \text{ s}^{-1}$, which implies that the measured rate coefficient corresponds to 73%
1787 of the capture rate. The rate coefficient for the reaction of C_2H_5^+ with HNC
1788 ($\text{R}_{cn}317$) has never been studied and we assume that it is equal to the capture
1789 rate, i.e. $5.2 \times 10^{-9} \text{ cm}^3 \text{ s}^{-1}$ at 150 K, which according to what has been
1790 observed for $\text{C}_2\text{H}_5^+ + \text{HCN}$, might be slightly overestimated.

1791 The rate coefficient at 300 K for the reaction of C_2H_5^+ with C_2H_4 ($\text{R}_{cn}302\text{a}$),
1792 i.e. $3.6 \times 10^{-10} \text{ cm}^3 \text{ s}^{-1}$, is based on a literature review (McEwan and Ani-
1793 cich (2007) after Anicich (1993)). The rate coefficient is rather slow and might
1794 exhibit some temperature dependence but no studies are available at low tem-
1795 perature.

1796 Three older studies suggest that the recombination rate of C_2H_5^+ with elec-
1797 trons is quite slow at 300 K, i.e. $6.0 - 9.0 \times 10^{-7} \text{ cm}^3 \text{ s}^{-1}$ (Adams and Smith,
1798 1988b; Gougousi et al., 1997; Lehfaoui et al., 1997). McLain et al. (2004) ob-
1799 tain a slightly faster rate coefficient at room temperature (i.e. $1.2 \times 10^{-6} \text{ cm}^3$
1800 s^{-1}) and studied its evolution with temperature. The rate exhibits two distinct
1801 temperature dependencies, i.e. $\text{T}^{-0.8}$ for $80 < \text{T}_e < 300 \text{ K}$ and $\text{T}^{-1.2}$ for $300 <$
1802 $\text{T}_e < 600 \text{ K}$, which seem consistent with theoretical models.

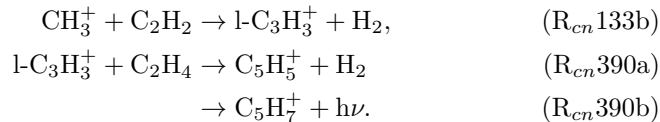
1803 Since the RPWS LP reports electron temperatures above typically 500 K,
1804 we use the McLain et al. (2004) temperature dependence appropriate for the
1805 higher temperature range (i.e. $\text{T}^{-1.2}$). However, if the electron temperature
1806 is closer to the neutral temperature as suggested by Richard et al. (2011), the
1807 temperature dependence for the lower temperature range (i.e. $\text{T}^{-0.8}$) would be
1808 more appropriate for altitudes below $\sim 1150 \text{ km}$.

1809 The branching ratios for channels ($\text{R}_{er}21\text{a}$)/($\text{R}_{er}21\text{b}$)/($\text{R}_{er}21\text{c}$)/($\text{R}_{er}21\text{d}$)/($\text{R}_{er}21\text{e}$)
1810 are 0.29/0.27/0.17/0.13/0.12 according to the only available study, which was

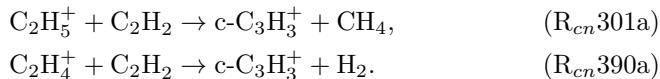
1811 made on C_2D_5^+ (Geppert et al., 2004a). The branching ratios have been di-
 1812 vided by 0.98 for the sum to be equal to one (W. Geppert, private communi-
 1813 cation, 2013). Although lighter isotopologues react much faster than heavier
 1814 ones, branching ratios in dissociative recombination reactions have not shown
 1815 pronounced effects on deuteration (see e.g. Geppert et al. (2006)). Therefore,
 1816 using the branching ratios for C_2D_5^+ should be mostly accurate.

1817 The chemistry of C_2H_7^+ is poorly characterized. In our model, it is mostly
 1818 an intermediate in the proton transfer chain as ethane takes a proton from CH_5^+
 1819 ($\text{R}_{cn}181\text{b}$) to transfer it to hydrogen cyanide ($\text{R}_{cn}352\text{a}$). Above 1150 km, the
 1820 main loss is dissociative electron recombination ($\text{R}_{er}24$) but both rate coefficient
 1821 and products are unknown and had to be estimated.

1822 C_3H_3^+ , C_3H_5^+ , C_3H_7^+ . C_3H_3^+ has two low-energy isomers, the cyclo-
 1823 propenylum ion $c\text{-C}_3\text{H}_3^+$ ($\Delta H_f^\circ = 1075 \text{ kJ mol}^{-1}$) and the linear propargyl
 1824 ion $l\text{-C}_3\text{H}_3^+$ ($\Delta H_f^\circ = 1179 \text{ kJ mol}^{-1}$) (Lias et al., 1988). Because of their very
 1825 different reactivity, it is important to discriminate these two species in chemical
 1826 models (Carrasco et al., 2008). The major source and sink for $l\text{-C}_3\text{H}_3^+$ are:

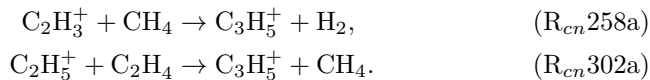


1827 Although $c\text{-C}_3\text{H}_3^+$ is also produced in reaction ($\text{R}_{cn}133\text{a}$), it is essentially
 1828 formed in reactions that do not produce $l\text{-C}_3\text{H}_3^+$ (McEwan and Anicich (2007)
 1829 and M.J. McEwan, private communication):

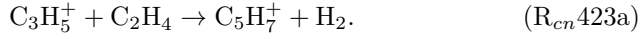
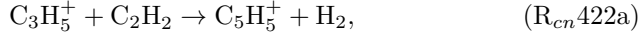


1830 In contrast with $l\text{-C}_3\text{H}_3^+$, $c\text{-C}_3\text{H}_3^+$ is nonreactive with most hydrocarbons
 1831 and its main loss is dissociative electron recombination ($\text{R}_{er}29$).

1832 As in Vuitton et al. (2007), C_3H_5^+ is efficiently produced in reactions with
 1833 methane and ethylene:



1834 Following the suggestion by Demarais et al. (2013), we include the proton transfer
 1835 reaction between HCNH^+ and methylacetylene ($\text{R}_{cn}697$), which, with our
 1836 estimated rate coefficient, substantially contributes to the formation of C_3H_5^+
 1837 as well. Above 1000 km, C_3H_5^+ is mostly lost by reactions with acetylene and
 1838 ethylene:

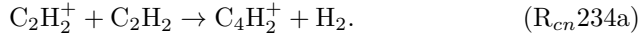


1839 Below 1000 km, electron dissociative recombination ($\text{R}_{er}32$) becomes the main
 1840 loss process, as in Vuitton et al. (2007). The electron recombination of C_3H_5^+
 1841 has not been investigated experimentally. Using general concepts based on
 1842 the data available for other $\text{C}_{2,3}\text{H}_y^+$ ions Janev and Reiter (2004) estimated
 1843 both its rate coefficient and product branching ratios. The rate coefficient is
 1844 expressed as a function of the number of hydrogen atoms for a given number
 1845 of carbon atoms and possesses a somewhat complex temperature dependence.
 1846 The values calculated with this expression are not necessarily in agreement
 1847 with experimental data obtained since 2004 (for C_2H_5^+ , C_3H_3^+ and C_3H_4^+ , for
 1848 example) and as a consequence, we stick to our own fitting expression that uses
 1849 a wider dataset. For comparison, for C_3H_5^+ , we obtain a value of $10^{-6} \text{ cm}^3 \text{ s}^{-1}$
 1850 while the Janev and Reiter (2004) expression would give $7.2 \times 10^{-7} \text{ cm}^3 \text{ s}^{-1}$
 1851 for an electron temperature of 300 K. In the absence of a better approach, we
 1852 however use their branching ratios, which consist mostly of multiple hydrogen
 1853 loss and to a lesser extent, carbon bond break-up.

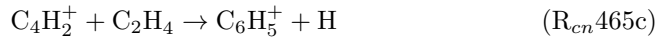
1854 C_3H_7^+ is essentially formed through reaction of protonated hydrogen cyanide
 1855 with propene ($\text{R}_{cn}699$). It is lost through dissociative electron recombination
 1856 ($\text{R}_{er}34$) above 950 km and reaction with ethane below:



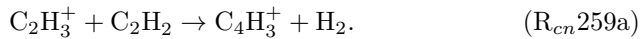
1857 C_4H_2^+ , C_4H_3^+ , C_4H_5^+ , C_4H_7^+ , C_4H_9^+ . C_4H_2^+ is essentially formed
 1858 through a reaction involving C_2H_2^+ ions:



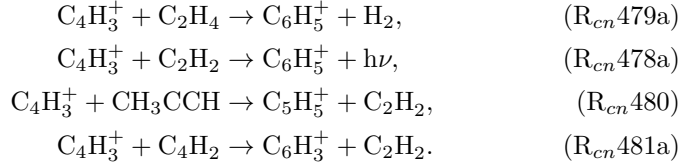
1859 It is lost by electron recombination ($\text{R}_{er}38$) above 1100 km and reaction with
 1860 C_2H_4 below:



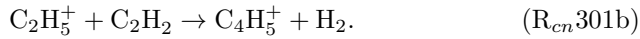
1861 As in Vuitton et al. (2007, 2008), C_4H_3^+ is formed by proton transfer from
 1862 HCNH^+ and C_2H_5^+ to diacetylene ($\text{R}_{cn}700, \text{R}_{cn}308$) in the bulk of the iono-
 1863 sphere, while above 1300 km, a condensation reaction kicks in:



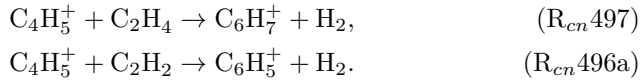
1864 It is lost through electron dissociative recombination ($\text{R}_{er}39$) above 1000 km
 1865 and several condensation reactions below:



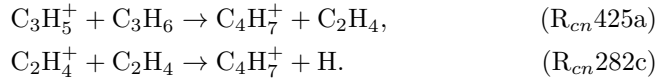
1866 C_4H_5^+ is formed through a branch of the reaction between C_2H_5^+ and acetylene:
1867



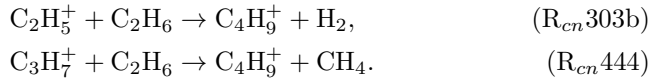
1868 It is lost through dissociative electron recombination ($\text{R}_{er}42$) below 1000 km
1869 and reaction with ethylene and acetylene above:



1870 C_4H_7^+ is formed through two condensation reactions:

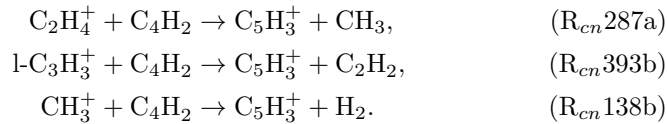


1871 C_4H_9^+ is formed by two reactions involving ethane, below and above 1000
1872 km, respectively:

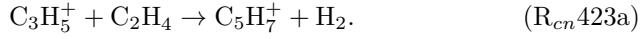
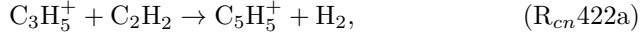


1873 C_4H_7^+ and C_4H_9^+ are both lost by dissociative electron recombination ($\text{R}_{er}44, \text{R}_{er}46$).

1874 C_5H_3^+ , C_5H_5^+ , C_5H_7^+ . C_5H_3^+ is formed by three condensation reac-
1875 tions involving diacetylene:

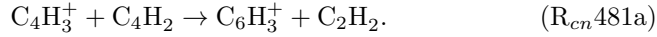


1876 C_5H_5^+ and C_5H_7^+ are almost exclusively formed through the reactions:

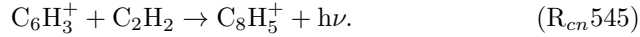


1877 C_5H_3^+ , C_5H_5^+ and C_5H_7^+ are lost through dissociative electron recombination
1878 ($\text{R}_{er}49, \text{R}_{er}51, \text{R}_{er}53$).

1879 C_6H_3^+ , C_6H_5^+ , C_6H_7^+ . C_6H_3^+ is mostly formed through proton ex-
1880 change between the most abundant ions and C_6H_2 ($\text{R}_{cn}702, \text{R}_{cn}310$), and the
1881 reaction:

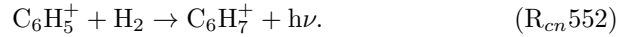
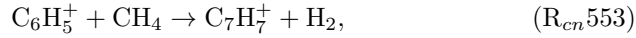


1882 It is lost through dissociative electron attachment ($\text{R}_{er}60$) above 1000 km and
1883 radiative association to acetylene below:

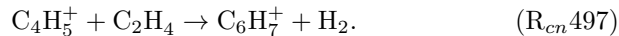
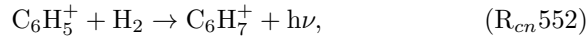
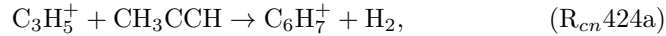


1884 C_6H_5^+ is formed through reactions of C_4H_3^+ and C_4H_5^+ with ethylene and
1885 acetylene ($\text{R}_{cn}479a, \text{R}_{cn}478a, \text{R}_{cn}496a$). This is somewhat different from the
1886 scheme presented in Vuitton et al. (2008) where ($\text{R}_{cn}496a$) was not a major
1887 production reaction. We nevertheless still expect that C_6H_5^+ is the phenylium
1888 ion, the ground state cyclic isomer, as discussed in Vuitton et al. (2008) and use
1889 rate coefficients corresponding to c- C_6H_5^+ , if available.

1890 C_6H_5^+ is mostly lost by dissociative electron recombination ($\text{R}_{er}62$), as well
1891 as by reaction with methane and hydrogen:

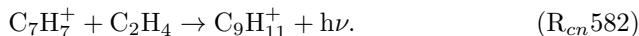


1892 C_6H_7^+ is formed through multiple reactions having about the same impor-
1893 tance:



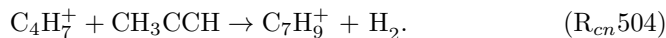
1894 It is lost through dissociative electron recombination ($\text{R}_{er}64$), whose rate co-
1895 efficient, including its evolution with electron temperature, has been recently
1896 determined (Hamberg et al., 2011). At the exception of reaction ($\text{R}_{cn}424a$),
1897 this is the same set of reactions as in Vuitton et al. (2008).

1898 $\mathbf{C_7H_7^+}$, $\mathbf{C_7H_9^+}$. $\mathbf{C_7H_7^+}$ is lost through electron dissociative recombina-
 1899 tion (R_{er75}) above 1000 km and reaction with ethylene below:



1900 $\mathbf{C_7H_7^+}$ has been famously observed as both the tropylium (7 member ring)
 1901 and benzylium (6 member ring) isomers. $\mathbf{C_7H_7^+}$ dissociative recombination has
 1902 been studied by Rebrion-Rowe et al. (2000) and Fournier et al. (2013) who
 1903 found a very different reactivity for the two states, tropylium ions recombining
 1904 with a rate coefficient of $3.2 \times 10^{-7} \text{ cm}^3 \text{ s}^{-1}$ and benzylium ions with a rate
 1905 coefficient of $11.6 \times 10^{-7} \text{ cm}^3 \text{ s}^{-1}$. In our case, $\mathbf{C_7H_7^+}$ ions are mostly formed
 1906 in the reaction of phenylium ions ($\mathbf{c-C_6H_5^+}$) with methane (R_{cn553}) and were
 1907 identified as tropylium ions because of their lack of reactivity with aromatic
 1908 molecules (Ausloos, 1982; Ausloos et al., 1989).

1909 $\mathbf{C_7H_9^+}$ is formed by proton transfer from the most abundant ions to toluene
 1910 (R_{cn705}, R_{cn313}) as well as through a condensation reaction:



1911 It is exclusively lost by dissociative electron recombination (R_{er77}). Osborne
 1912 et al. (2011) have studied the dissociative electron-ion recombination of the
 1913 protonated six membered ring toluene $\mathbf{C_6H_5CH_4^+}$ and have obtained a room
 1914 temperature rate coefficient of $3.8 \times 10^{-7} \text{ cm}^3 \text{ s}^{-1}$. Although the nature of
 1915 the $\mathbf{C_7H_9^+}$ isomer formed in reaction (R_{cn504}) is unknown, it is likely that
 1916 protonation of toluene gives $\mathbf{C_6H_5CH_4^+}$.

1917 3.1.1.3. Nitrogen-Bearing Ions.

1918 $\mathbf{N_2H^+}$. As mentioned in section 3.1.1.2, $\mathbf{N_2H^+}$ is an important interme-
 1919 diate in the formation of $\mathbf{CH_5^+}$. It is mostly formed by reaction of $\mathbf{N_2^+}$ with
 1920 hydrogen (R_{cn835a}) and methane (R_{cn836c}), and lost through reaction with
 1921 methane (R_{cn862}).

1922 $\mathbf{NH_4^+}$. The formation of $\mathbf{NH_4^+}$ is discussed in Yelle et al. (2010). A chan-
 1923 nel based on the addition of H onto $\mathbf{NH_x^+}$ ($x = 0 - 3$) by reaction with $\mathbf{CH_4}$
 1924 and $\mathbf{H_2}$ has been proposed (Atreya, 1986) but most of the $\mathbf{NH^+}$ formed by re-
 1925 action of $\mathbf{N^+}$ with $\mathbf{H_2}$ reacts with $\mathbf{N_2}$ to form $\mathbf{N_2H^+}$, therefore short-circuiting
 1926 the production of $\mathbf{NH_4^+}$. Instead, $\mathbf{NH_4^+}$ is created by reaction of $\mathbf{NH_3}$ with
 1927 other protonated molecules, especially $\mathbf{HCNH^+}$ and $\mathbf{C_2H_5^+}$ (R_{cn707}, R_{cn315}),
 1928 and lost by electron recombination (R_{er84}).

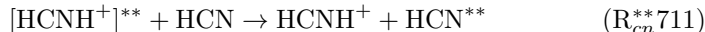
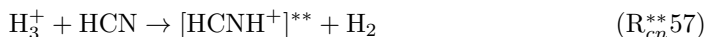
1929 $\mathbf{HCNH^+}$, $\mathbf{CH_2NH_2^+}$. Proton exchange of $\mathbf{C_2H_5^+}$ and $\mathbf{CH_5^+}$ with hy-
 1930 drogen cyanide and isocyanide ($R_{cn316}, R_{cn194}, R_{cn317}, R_{cn195}$) are responsible
 1931 for the $\mathbf{HCNH^+}$ production, various ion-neutral reactions contributing to only
 1932 $\sim 10\%$ of the total production (Vuitton et al., 2007). These reactions have never
 1933 been studied. We make the assumption that the only channel is a proton transfer

1934 from the ion to the neutral and that the rate constant is equal to the capture
 1935 rate. Using literature values for the dipole polarizability and dipole moment
 1936 for HCN (CRC Handbook of Chemistry and Physics, 87th Edition) and HNC
 1937 (Blackman et al., 1976; Woon and Herbst, 2009), leads to a rate constant at 150
 1938 K of $5.8 \times 10^{-9} \text{ cm}^3 \text{ s}^{-1}$ and $6.0 \times 10^{-9} \text{ cm}^3 \text{ s}^{-1}$, respectively.

1939 Again, below 1050 km, electron dissociative recombination is its main loss:



1940 The electron recombination of HCNH^+ has been investigated with two different
 1941 experimental techniques: the flowing-afterglow langmuir probe (FALP) at the
 1942 University of Georgia (Adams and Smith, 1988a; Adams et al., 1991; McLain
 1943 et al., 2009; McLain and Adams, 2009) and the heavy ion storage ring CRYRING
 1944 (Semaniak et al., 2001). In McLain et al. (2009) and McLain and Adams (2009),
 1945 HCNH^+ is created by the reactions:



1946 where ** indicates rovibronic internal excitation. The authors argue that be-
 1947 fore recombination occurs, resonant proton transfer, reaction (R_{cn}^{**}711) rapidly
 1948 quenches any rovibronically excited species created by the exothermicity of re-
 1949 action (R_{cn}^{**}57). In Semaniak et al. (2001), the cross-sections are measured after
 1950 5.5 s of storage time, which is estimated to be long enough to allow the ions to
 1951 be vibrationally relaxed.

1952 The values measured for the rate coefficient at 300 K are in good agreement
 1953 with each other within experimental uncertainties and give a value of ~ 3.0
 1954 $\times 10^{-7} \text{ cm}^3 \text{ s}^{-1}$ (McLain et al., 2009; Semaniak et al., 2001). However, the
 1955 dependence with electron temperature is significantly different: $T_e^{-1.38}$ for 180
 1956 $< T_e < 600 \text{ K}$ (McLain and Adams, 2009) against $T_e^{-0.65}$ for $T_e < 1000 \text{ K}$
 1957 (Semaniak et al., 2001).

1958 Adams et al. (1991) report a fraction of H atoms of 0.6 ± 0.2 , suggesting that
 1959 the dissociation channel giving $\text{CN} + \text{H}_2$ must be quite efficient. The branching
 1960 ratios retrieved later with the CRYRING experiment, i.e. $(0.68 \pm 0.02)/(0.32 \pm 0.03)/(0.00 \pm 0.02)$
 1961 for channels $(\text{R}_{er}\text{-88a} + \text{R}_{er}\text{-88b})/(\text{R}_{er}\text{-88c})/(\text{R}_{er}\text{-88d})$ give a fractional H contri-
 1962 bution of 1.32 (Semaniak et al., 2001) in strong disagreement with the earlier
 1963 results. The experimental measurements cannot discriminate between the HCN
 1964 and HNC isomers but theoretical calculations suggest that they are both formed
 1965 in equivalent amount (Shiba et al., 1998; Talbi and Ellinger, 1998). We will re-
 1966 turn to this in section 3.2.2, while discussing the formation of HNC.

1967 In the KIDA framework, W. Geppert produced an evaluation datasheet for
 1968 this reaction. He recommends using the CRYRING data because (i) the electron
 1969 temperature range investigated is wider, and (ii) the FALP measurements are in-
 1970 direct and therefore subject to larger uncertainties. We follow this recommenda-
 1971 tion and use a rate coefficient of $2.8 \times 10^{-7} \times (T_e/300)^{-0.65} \text{ cm}^3 \text{ s}^{-1}$ and branch-
 1972 ing ratios of 0.34/0.34/0.32/0.00 for channels (R_{er88a})/(R_{er88b})/(R_{er88c})/(R_{er88d}).

1973 Below 1050 km, proton transfer to a variety of different molecules with a
 1974 high proton affinity (C_4H_2 , $\text{C}_2\text{H}_3\text{CN}$, etc.) becomes the dominant HCNH^+ loss
 1975 process. The evaluated rate coefficient at 300 K for $\text{HCNH}^+ + \text{C}_4\text{H}_2$, i.e. 1.8
 1976 $\times 10^{-9} \text{ cm}^3 \text{ s}^{-1}$ (McEwan and Anicich, 2007), is based on the study of Petrie
 1977 et al. (1991b). The Langevin rate for this reaction is $1.5 \times 10^{-9} \text{ cm}^3 \text{ s}^{-1}$ and
 1978 we use this value as the rate coefficient instead.

1979 The ion-molecule chemistry of acrylonitrile has been investigated by Petrie
 1980 et al. (1991a, 1992), who find a rate coefficient at 300 K of $4.5 \times 10^{-9} \text{ cm}^3 \text{ s}^{-1}$
 1981 for its reaction with HCNH^+ , which is equal to the capture rate coefficient.

1982 CH_2NH_2^+ has a very high proton affinity (852.9 kJ/mol) and as a conse-
 1983 quence is produced by proton exchange reactions with most of the protonated
 1984 species in Titan’s atmosphere and lost by electron recombination (Yelle et al.,
 1985 2010). We emphasize that although the rate coefficient for the proton trans-
 1986 fer from HCNH^+ and C_2H_5^+ to CH_2NH has now been determined (Edwards
 1987 et al., 2008), both rate coefficient and products for the electron recombination
 1988 of CH_2NH_2^+ still need to be measured.

1989 **CH_3CNH^+** . As in Vuitton et al. (2007), CH_3CNH^+ is efficiently produced
 1990 by proton transfer from HCNH^+ and C_2H_5^+ (R_{cn713} , R_{cn320}) and lost by
 1991 electron recombination (R_{er100}). However, a new reaction (section 2.7.3.1) is
 1992 responsible for about half of the CH_3CNH^+ production:



1993 **HC_3NH^+ , $\text{C}_2\text{H}_3\text{CNH}^+$, $\text{C}_2\text{H}_5\text{CNH}^+$** . As in Vuitton et al. (2007),
 1994 HC_3NH^+ is mostly formed by proton transfer from HCNH^+ and C_2H_5^+ to
 1995 HC_3N (R_{cn714} , R_{cn321}). However, below 1150 km, a new reaction in our scheme
 1996 surpasses dissociative electron recombination (R_{er104}) as the main loss:



1997 $\text{C}_2\text{H}_3\text{CNH}^+$ is mostly formed by proton transfer from HCNH^+ and C_2H_5^+
 1998 to $\text{C}_2\text{H}_3\text{CN}$ (R_{cn715} , R_{cn322}) and lost by electron recombination (R_{er106}). We
 1999 note that since Vuitton et al. (2007), both rate coefficient and products of the
 2000 electron recombination of $\text{C}_2\text{H}_3\text{CNH}^+$ have been determined experimentally
 2001 (Geppert et al., 2007; Vigren et al., 2009). Below 950 km, proton transfer
 2002 reactions from $\text{C}_2\text{H}_3\text{CNH}^+$ to $\text{C}_2\text{H}_5\text{CN}$ and CH_2NH (R_{cn816} , R_{cn812}) become
 2003 important as well.

2004 $\text{C}_2\text{H}_5\text{CNH}^+$ is mostly formed by proton transfer from HCNH^+ and C_2H_5^+
 2005 to $\text{C}_2\text{H}_5\text{CN}$ (R_{cn716} , R_{cn323}) and lost by electron recombination (R_{er108}). We

2006 note that since Vuitton et al. (2007), the proton transfer reaction from HCNH^+
 2007 to $\text{C}_2\text{H}_5\text{CN}$ has now been confirmed experimentally and is fast, with a rate
 2008 coefficient of $4.2 \times 10^{-9} \text{ cm}^3 \text{ s}^{-1}$ (Edwards et al., 2008). The temperature
 2009 dependence of the rate coefficient as well as the products of the electron re-
 2010 combination of $\text{C}_2\text{H}_5\text{CNH}^+$ have also been determined (Vigren et al., 2010a).
 2011 Below 800 km, proton transfer from $\text{C}_2\text{H}_5\text{CNH}^+$ to CH_2NH ($R_{cn}819$) becomes
 2012 a competitive loss process for $\text{C}_2\text{H}_5\text{CNH}^+$.

2013 **HC_5NH^+ .** HC_5NH^+ is mostly formed by proton transfer from HCNH^+
 2014 and C_2H_5^+ to $\text{C}_2\text{H}_5\text{CN}$ ($R_{cn}719, R_{cn}326$) and lost by electron recombination
 2015 ($R_{er}122$). We note that since Vuitton et al. (2007), the proton transfer reactions
 2016 from C_2H_5^+ and HCNH^+ to $\text{C}_2\text{H}_5\text{CN}$ have now been confirmed experimentally
 2017 and are fast, with rate coefficients of $4.7\text{-}4.8 \times 10^{-9} \text{ cm}^3 \text{ s}^{-1}$ (Edwards et al.,
 2018 2009).

2019 **Other ions.** Other ions that can be identified in the INMS spectrum are
 2020 $\text{C}_4\text{H}_3\text{NH}^+$, $\text{C}_4\text{H}_5\text{NH}^+$, $\text{C}_5\text{H}_5\text{NH}^+$, $\text{C}_6\text{H}_3\text{NH}^+$ and $\text{C}_6\text{H}_7\text{NH}^+$ (Vuitton et al.,
 2021 2007). As we do not track the associated neutrals, we adjust their density for
 2022 the ions to match the INMS data.

2023 *3.1.1.4. Oxygen-Bearing Ions.* We only discuss the three ions that happen to
 2024 have predicted densities above 0.1 cm^{-3} . All other oxygen ions, including those
 2025 containing both oxygen and nitrogen are unimportant species.

2026 As in Vuitton et al. (2007), H_3O^+ is mostly formed by proton transfer from
 2027 C_2H_5^+ and CH_5^+ to H_2O ($R_{cn}333, R_{cn}211$) and lost by proton transfer to HCN
 2028 and electron recombination ($R_{cn}955, R_{er}157$) (Neau et al., 2000).

2029 The chemistry of HCO^+ in our model is fairly simple. It is mostly an in-
 2030 termediate in the proton transfer chain as carbon monoxide takes a proton
 2031 from CH_5^+ ($R_{cn}212$) to transfer it to hydrogen cyanide ($R_{cn}983$) and acetylene
 2032 ($R_{cn}980$).

2033 The chemistry of CH_2OH^+ (protonated formaldehyde) is pretty well con-
 2034 strained. In our model, H_2CO takes a proton from C_2H_5^+ ($R_{cn}334$) and its
 2035 main loss is dissociative electron recombination ($R_{er}165$) (Hamberg et al., 2007).
 2036 H_2CO has the peculiarity to have almost the same proton affinity as HCN and
 2037 therefore, a proton can cycle back and forth between both species ($R_{cn}725/R_{cn}1001$),
 2038 although the overall flux is towards HCNH^+ .

2039 *3.1.2. Negative Ions*

2040 **H^- , CH_2^- , CH_3^- .** H^- and CH_2^- are essentially formed by dissociative
 2041 electron attachment to CH_4 ($J_{dea}2$) with a column integrated rate of 9.4×10^4
 2042 and $6.9 \times 10^3 \text{ cm}^2 \text{ s}^{-1}$, respectively. CH_3^- is exclusively formed by radiative
 2043 attachment to CH_3 , with a total column integrated rate of $3.2 \times 10^3 \text{ cm}^2 \text{ s}^{-1}$. All
 2044 three are mostly lost by proton abstraction from HCN and associative detach-
 2045 ment with H atoms. Above 1300 km, photodetachment becomes a competitive
 2046 loss process for CH_2^- and CH_3^- because of their small electron affinity (cf.
 2047 Table B.12).

2048 C_2H^- , C_4H^- , C_6H^- . C_2H^- is mostly formed by proton abstraction from
2049 C_2H_2 by H^- with a column integrated rate of $1.0 \times 10^4 \text{ cm}^2 \text{ s}^{-1}$. Because of
2050 their larger number of carbon atoms, radiative electron attachment to C_4H and
2051 C_6H is efficient and is the main formation process of C_4H^- and C_6H^- (3.0×10^4
2052 and $5.7 \times 10^4 \text{ cm}^2 \text{ s}^{-1}$, respectively). Like other hydrocarbon ions, they are
2053 mostly lost by proton abstraction from HCN and associative detachment with
2054 H atoms.

2055 CN^- , C_3N^- , C_5N^- . The major production reactions of CN^- are proton
2056 transfers from HCN by H^- (mostly above 1100 km), C_6H^- and to a lesser ex-
2057 tent C_4H^- . Dissociative electron attachment to HCN (J_{dea22}) also contributes
2058 over the whole altitude range. These are the same processes as in Vuitton et al.
2059 (2009), although the relative importance of the proton exchange reactions has
2060 increased because of the larger abundance of H^- and C_6H^- and the lower dis-
2061 sociative electron attachment cross-section to HCN in the present model (cf.
2062 section 2.7.3.3).

2063 The main production reactions of C_3N^- are proton abstraction from HC_3N
2064 by several anions (CN^- , C_6H^- , H^- , C_4H^- by decreasing order of importance).
2065 Again the higher density of H^- and C_6H^- here compared to Vuitton et al. (2009)
2066 induces an increased importance of proton transfer in the production of C_3N^-
2067 but the main production processes remain the same.

2068 C_5N^- is almost exclusively formed by radiative electron attachment to C_5N .
2069 The main loss for all three species is associative detachment to H atoms.

2070 O^- , OH^- . O^- is formed by dissociative electron attachment to CO (J_{dea3})
2071 and H_2O (J_{dea33b}). It is lost by proton abstraction from C_2H_2 and CH_4 , the
2072 latter being the major production reaction of OH^- along with radiative attach-
2073 ment to OH and dissociative electron attachment to H_2O (J_{dea33a}). OH^- is
2074 lost by proton abstraction from HCN and C_2H_2 and by associative detachment
2075 with H atoms.

2076 3.2. Neutral Atmosphere

2077 The neutral chemistry is initiated by the destruction of methane and ni-
2078 trogen and the subsequent formation of radicals that are reactive species. The
2079 process by which this occurs depends on the atmospheric level. As we will show,
2080 above 600 km, the driving mechanism is direct photolysis of methane and ni-
2081 trogen, which leads to the production of numerous species, including C_2H_2 and
2082 HCN. These species are transported downward to the stratosphere where the
2083 photolysis of acetylene is indirectly responsible for the dissociation of methane,
2084 through catalytic processes. The peaks of radical production are at ~ 800 and
2085 ~ 200 km, respectively. For each CH_x fragment, the mole fractions are shown
2086 in Figure 23, while the column production rates are presented in Table 7.

2087 3.2.1. Hydrocarbons

2088 **Methane (CH_4) and photofragments (CH_3 , $^1\text{CH}_2$, $^3\text{CH}_2$, CH , C).**

Table 7: Primary and secondary column loss or production rates for CH_x species above and below 600 km. Primary loss / production refers to the dissociation of CH_4 by photons. Secondary production refers to reactions involving the primary products (see text for further details). Values are given in $\text{cm}^{-2} \text{s}^{-1}$ scaled to the surface.

Products	Above 600 km			Below 600 km		
	Primary	Secondary	Total	Primary	Secondary	Total
CH_4	-2.6×10^9	-2.5×10^9	-5.1×10^9	-3.7×10^7	-1.6×10^{10}	-1.6×10^{10}
CH_3	1.1×10^9	5.8×10^8	1.7×10^9	1.9×10^7	1.1×10^{10}	1.1×10^{10}
$^1\text{CH}_2$	1.0×10^9	7.2×10^8	1.8×10^9	1.9×10^7	1.7×10^8	1.9×10^8
$^3\text{CH}_2$	4.1×10^8	1.1×10^9	1.6×10^9	0	1.4×10^8	1.4×10^8
CH	1.4×10^8	7.2×10^8	1.7×10^9	0	9.5×10^7	9.5×10^7
C	0	3.4×10^6	3.4×10^6	0	4.1×10^3	4.1×10^3

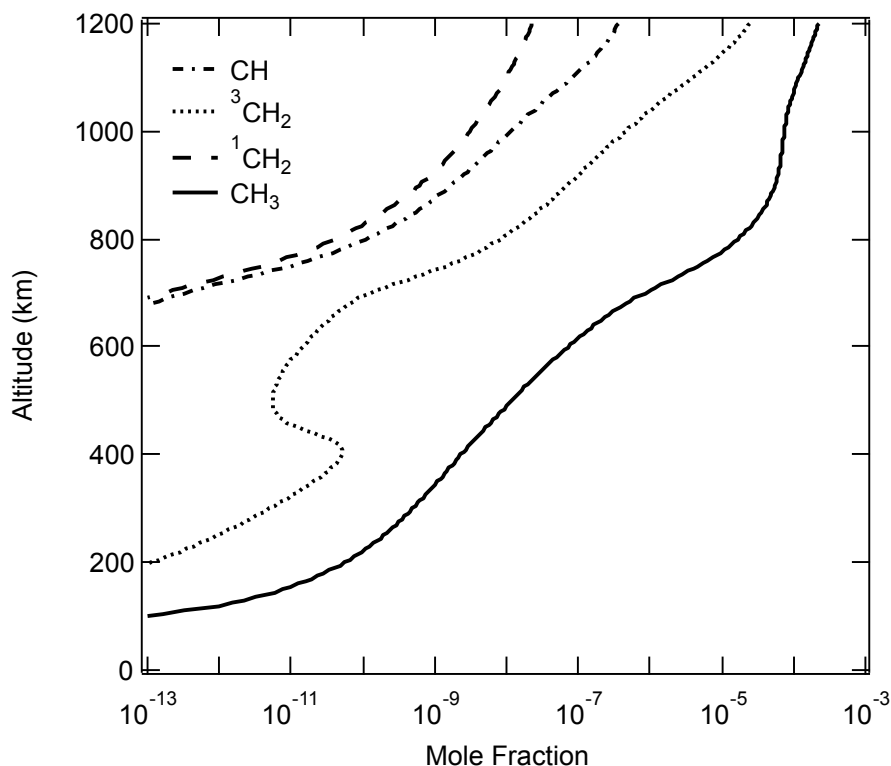
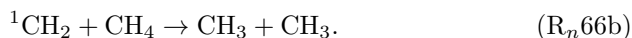


Figure 23: Model results for the mole fraction of the CH, $^3\text{CH}_2$, $^1\text{CH}_2$, and CH_3 radicals.

2089 The reactive species formed from methane essentially react with each other
 2090 and with methane to form more complex molecules. Methyl (CH_3), methy-
 2091 lene (CH_2 in both ground $X^3\text{B}_1$ and first excited $\alpha^1\text{A}_1$ electronic states) and
 2092 methylidyne (CH) radicals are all produced in the photolysis of CH_4 (J_d2), which
 2093 represents 50% of its loss above 600 km. Secondary reactions of these primary
 2094 products are competitive loss pathways for CH_4 and formation pathways for the
 2095 radicals, as presented in Table 7 and detailed below.

2096 In the upper atmosphere, most of the methyl radicals originate from the
 2097 photolysis of methane (J_d2a) but about 35% are formed through the reaction
 2098 of excited methylene radicals with methane:

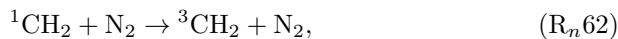


2099 The excited state of methylene ($^1\text{CH}_2$) is however recycled through photolysis
 2100 of methyl radicals:



2101 This reaction represents 40% of the $^1\text{CH}_2$ production rate in the upper atmo-
 2102 sphere, the rest being attributed to the photolysis of methane (J_d2b). Ground

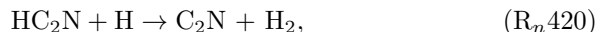
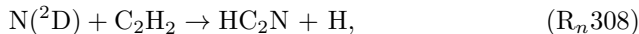
2103 state methylene radicals ($^3\text{CH}_2$) are efficiently produced through quenching of
 2104 the excited state by N_2 or through its radiative emission:



2105 These processes represent most of the $^3\text{CH}_2$ production, the photolysis of methane
 2106 (J_d2d) only accounting for 25%. Once formed, the ground state methylene rad-
 2107 icals react with the most abundant radicals in the upper atmosphere, hydrogen
 2108 atoms, to produce methylidyne radicals:

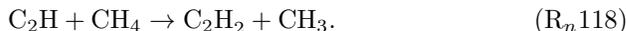


2109 The photolysis of methane (J_d2c) accounts for 15% of the total methylidyne
 2110 formation in the upper atmosphere. Carbon atoms are not formed by direct
 2111 methane photolysis but instead through a complex set of secondary reactions
 2112 involving nitrogen-bearing species:



2113 However, the total C production rate is small (cf. Table 7) and although, as
 2114 first pointed out in Hébrard et al. (2013), it is at the origin of C_3 and C_3H ,
 2115 these radicals have a very minor impact on the overall hydrocarbon chemistry.

2116 The photons that can dissociate methane ($\lambda < 145$ nm) are all absorbed
 2117 above 600 km (cf. section 2.6.4) but in the lower atmosphere, the photodisso-
 2118 ciation of acetylene (and to a lower extent, of the other polyynes, C_4H_2 and
 2119 C_6H_2) leads to a secondary dissociation of CH_4 , as originally proposed by Allen
 2120 et al. (1980) and validated experimentally by Vuitton et al. (2006a):



2121 This scheme is the main driver of the chemistry in the lower atmosphere, through
 2122 production of methyl radicals. Methylidyne and methylene radicals are formed
 2123 locally through a similar set of secondary reactions as in the upper atmosphere
 2124 (reactions (J_d38), (R_n62) and (R_n3)). Less than 5% of the methane destroyed by
 2125 the above mentioned mechanisms is recycled back throughout the atmosphere:



2126 To our knowledge, reaction (R_n396) has never been studied either experimen-
 2127 tally or theoretically. We assume that the rate coefficient of the isoelectronic
 2128 NH₂ + H₂CN reaction makes a good surrogate.

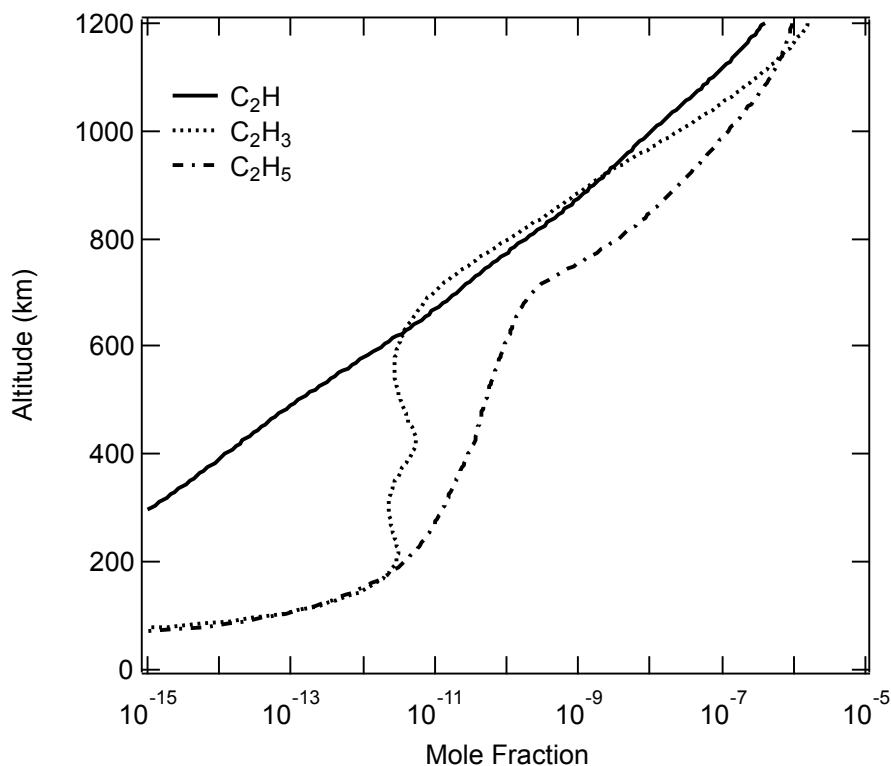


Figure 24: Model results for the mole fraction of the C₂H, C₂H₃ and C₂H₅ radicals.

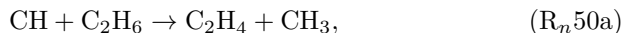
2129 **Ethane (C₂H₆), Ethylene (C₂H₄), Acetylene (C₂H₂).** The rate co-
 2130 efficient of the recombination of methyl radicals has been calculated in the
 2131 present work (cf. Figure A.3c) and this reaction is the origin of essentially
 2132 all C₂H₆:



2133 The production maxima are centered around 800 and 200 km, which corresponds
 2134 to the peak of methane and acetylene photolysis, respectively, and subsequent
 2135 CH₃ production as described above.

2136 After production, the majority of C₂H₆ flows downward until it condenses
 2137 near the tropopause (cf. Table 19). A small fraction diffuses upward and is
 2138 responsible for the presence of ethane above 900 km. There, ethane is mostly

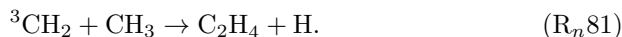
2139 lost by photodissociation (J_d7) and to some minor extent, by reaction with CH
 2140 and $^1\text{CH}_2$ radicals, and CH_5^+ ions:



2141 The main bulk of ethylene is formed in the upper atmosphere, by methyl-
 2142 dyne reacting with methane:



2143 A secondary channel involves the reaction of ground state methylene radicals
 2144 with methyl radicals:

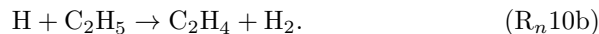
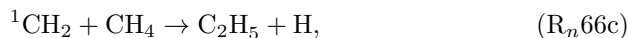


2145 The main fate of ethylene is to diffuse down and be photolysed (J_d6).

2146 Ions do contribute to both a minor production and loss of ethylene through
 2147 reaction of C_2H_5^+ :



2148 The presence of ethylene below 700 km is a combination of downward flux from
 2149 the upper atmosphere and local production through the formation of ethyl radi-
 2150 cals (C_2H_5 , cf. Figure 24) and their subsequent reaction with atomic hydrogen:



2151 However, below 500 km, the reaction of hydrogen atoms with ethylene becomes
 2152 more important than reaction (R_n10b) and along with photodissociation (J_6)
 2153 becomes the dominant loss of ethylene to reform ethyl radicals:



2154 The rate coefficient of reaction (R_n9a) is from Vuitton et al. (2012) (cf. Figure
 2155 A.1b). Around 200 km, the photolysis of butadiene ($J_{14\text{a}}$) becomes a significant
 2156 production of ethylene.

2157 The photolysis of ethylene is, in turn, the main source of acetylene in the
 2158 bulk of the atmosphere (J_d6). In the upper atmosphere, hydrogen abstraction
 2159 from vinyl radicals (C_2H_3 , cf. Figure 24) and as first highlighted by Plessis et al.
 2160 (2012) (based on the T19 INMS ion densities and the diurnally averaged model

2161 of Hébrard et al. (2009)), dissociative recombination of $C_2H_5^+$ ($R_{er}21a,d$), are
2162 the dominant production of C_2H_2 :



2163 The rate coefficient of the addition channel (R_n8a) has been calculated in the
2164 present work and remains negligible throughout the atmosphere (cf. Figure
2165 A.3a).

2166 At these altitudes, vinyl radicals originate from several reactions, includ-
2167 ing electron recombination of $C_2H_5^+$ ($R_{er}21b$) and $C_2H_3CNH^+$ ($R_{er}106c$), and
2168 neutral-neutral reaction of imidogen radicals (NH, cf. Figure 31) and ethylene
2169 (R_n332). Interestingly, NH radicals are essentially being formed by ion chem-
2170 istry ($R_{cn}593a$).

2171 Downward transport, photolysis (J_d5) and reaction with methylidyne (R_n48)
2172 and cyano radicals (R_n370) are acetylene's main losses above 800 km. Ion
2173 chemistry also contributes to the loss of acetylene through its reaction with
2174 $C_3H_5^+$ ($R_{cn}422$).

2175 Although the addition of reactive hydrogen atoms with acetylene to produce
2176 C_2H_3 is not very efficient (Vuitton et al. (2012) and Figure A.1a), it does become
2177 the main loss of C_2H_2 below 500 km:



2178 However, a substantial fraction of vinyl radicals further reacts with atomic hy-
2179 drogen (R_n8b) and methyl radicals (R_n92c) to reform acetylene.

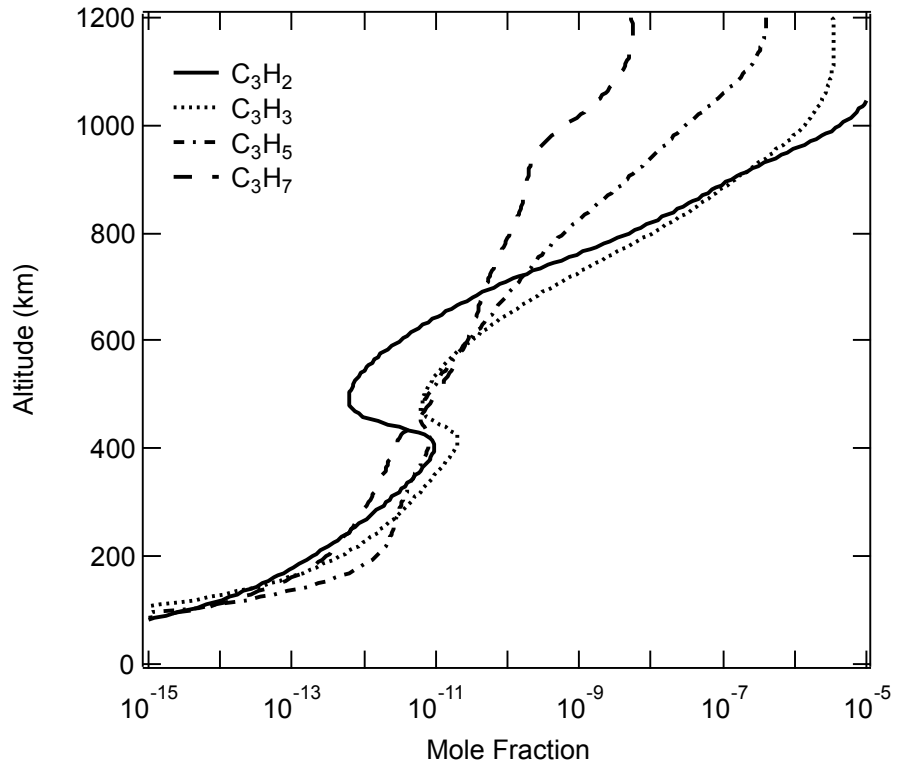


Figure 25: Model results for the mole fraction of the C_3H_2 , C_3H_3 , C_3H_5 and C_3H_7 radicals.

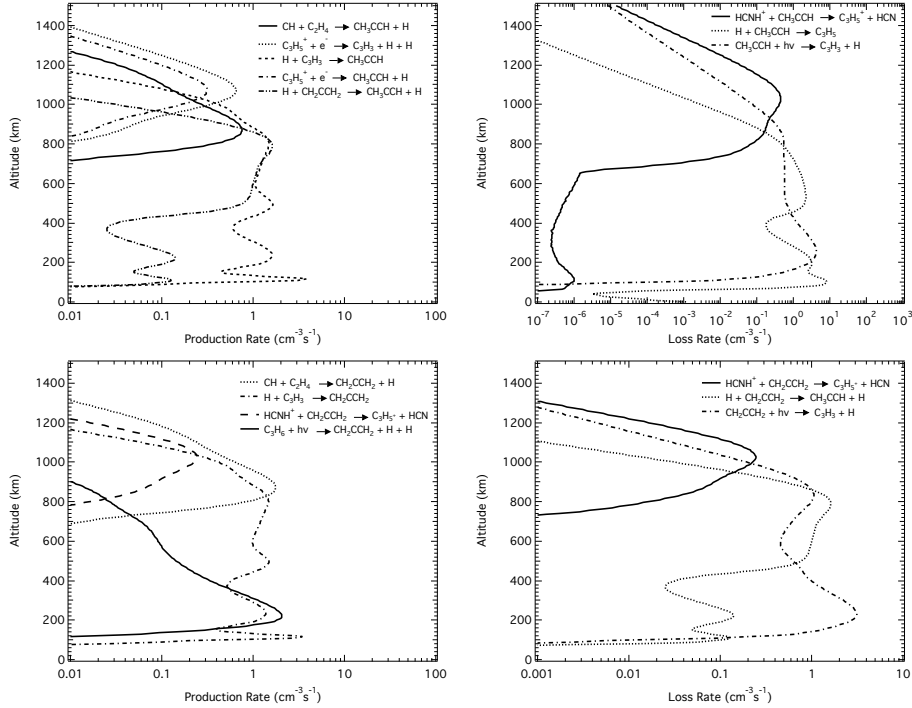
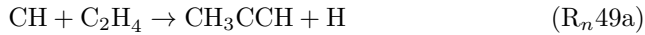


Figure 26: Production (left panel) and loss (right panel) rates of methylacetylene (top panel) and allene (bottom panel).

2180 **Methylacetylene (CH₃CCH), Allene (CH₂CCH₂), Propylene (C₃H₆),**
 2181 **Propane (C₃H₈).** In the upper atmosphere, methylacetylene and its isomer,
 2182 allene, are formed through electron recombination of C₃H₅⁺ (R_{er}32b) and the
 2183 reaction of methylidyne radicals with ethylene (cf. left panels in Figure 26):

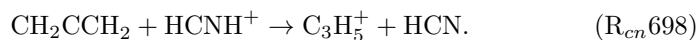
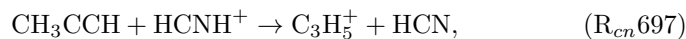


2184 Propargyl radicals (C₃H₃, cf. Figure 25), formed through reactions (R_{er}32a,c)
 2185 and photodissociation of butadiene (J_d14c), contribute as well to the production
 2186 of methylacetylene and allene, via their addition of hydrogen atoms:



2187 Neither species is efficiently destroyed above 1100 km and they mostly flow
 2188 downward. There is a main loss channel at the peak of the ionosphere (around
 2189 1000 km) due to proton transfer from HCNH⁺ to both isomers, which we assume

2190 is efficient based on their respective proton affinity (cf. right panels in Figure
2191 26):



2192 Photodissociation, although extremely efficient, does not lead to a net loss of
2193 methylacetylene since the major channel is the formation of propargyl (J_d8b),
2194 and subsequent reformation of CH₃CCH and CH₂CCH₂ through (R_n14).

2195 The addition of hydrogen atoms onto allene is efficient below 200 km but
2196 above that altitude the main outcome of this reaction is the isomerization of
2197 CH₂CCH₂ into CH₃CCH (cf. Figure A.1d):



2198 A more complex isomerization scheme involves the photodissociation of allene
2199 to form propargyl radicals (J_d9b) and their subsequent reaction with hydrogen
2200 (R_n14a).

2201 Methylacetylene is finally lost by reaction with hydrogen atoms to produce
2202 allyl radicals (C₃H₅, cf. Figure 25), addition being the main channel throughout
2203 the atmosphere, thanks to the radiative component (cf. Figure A.1c):

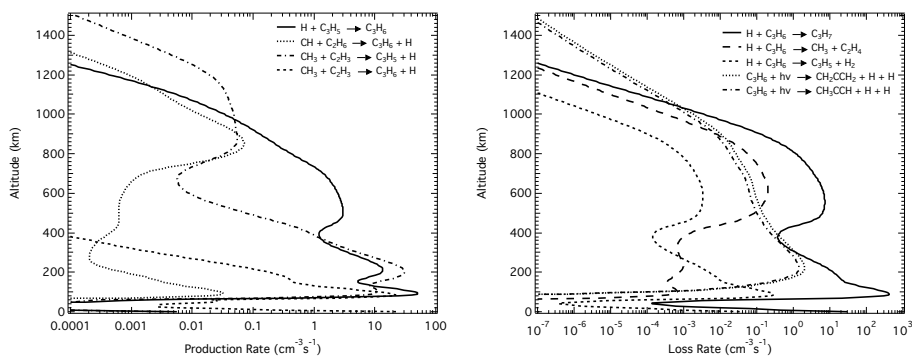
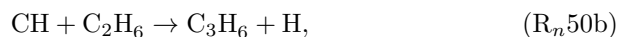
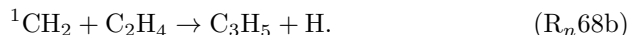
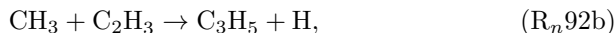


Figure 27: Production (left panel) and loss (right panel) rates of propylene.

2204 In the upper atmosphere, the main reactions that contribute to the formation
2205 of propylene are (cf. left panel in Figure 27):



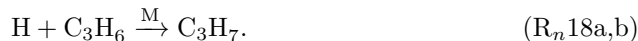
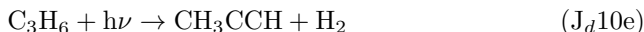
2206 Below 850 km, only reaction (R_n17a) is important for forming propylene and,
 2207 as discussed above, C₃H₅ is produced by addition of H to CH₃CCH (R_n15a,b).
 2208 Above 1000 km and around 200 km, the recombination of methyl and vinyl
 2209 radicals (R_n92b) is responsible for the production of allyl radicals; between
 2210 1000 and 800 km, it is the reaction between excited methylene and ethylene
 2211 (R_n68):



2212 The rate coefficient of reaction (R_n92) has been calculated (cf. Figure A.3d).
 2213 Bimolecular product formation (C₃H₅ + H, channel b) is the major channel,
 2214 adduct stabilization (C₃H₆, channel a) only kicking in below 150 km.

2215 Gannon et al. (2010a,b) experimentally studied reaction (R_n68) at low pressure
 2216 (~1 mbar) and over a broad temperature range (195-498 K). Removal of
 2217 ¹CH₂ occurs by electronic relaxation to ground state triplet methylene (channel
 2218 a) and chemical reaction (channel b). The H atom yield doubles from 195 K to
 2219 298 K, while the total rate coefficient exhibits a negative temperature depen-
 2220 dence. We adopt this temperature dependent rate coefficient with branching
 2221 ratios obtained at 195 K. We neglect collisional stabilization that has been cal-
 2222 culated to compete with the other channels only at pressures above 260 mbar.

2223 The fate of propylene is to recycle back to methylacetylene and allene via
 2224 photodissociation and to form propyl radicals (C₃H₇, cf. Figure 25) by addition
 2225 of hydrogen atoms (cf. right panel in Figure 27):



2226 Hébrard et al. (2013) highlighted (R_n18) as another key reaction responsible for
 2227 uncertainties on C₃H₆ at 600 and 200 km and the rate coefficient of this reaction
 2228 has again been calculated in the present work (cf. Figure A.1e). Adduct stabi-
 2229 lization leading to i-C₃H₇ (channel b) is dominant throughout the atmosphere,
 2230 bimolecular product formation (C₂H₄ + CH₃ and C₃H₅ + H₂, channels c and d)
 2231 being essentially negligible.

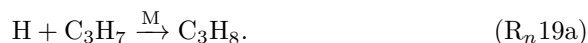
2232 The production of ethyl radicals by reaction (R_n66c) opens a pathway for
 2233 producing propane in the upper atmosphere:



2234 Hébrard et al. (2013) highlighted (R_n93a) as a key reaction responsible for
 2235 uncertainties on C₃H₈ throughout the atmosphere. The rate coefficient of this
 2236 reaction has therefore been calculated in the present work (cf. Figure A.3e).
 2237 Adduct stabilization leading to C₃H₈ (channel a) is important throughout the

2238 atmosphere, bimolecular product formation ($C_2H_4 + CH_4$, channel b) being
 2239 nevertheless significant above 800 km.

2240 A secondary pathway is through the addition of hydrogen atoms onto propyl
 2241 radicals (formed through (R_n18a,b)):



2242 Propane efficiently reacts with ethynyl radicals (formed through (J_d5)) to pro-
 2243 duce propyl radicals:



2244 However, since propyl radicals mostly react with hydrogen atoms to reform
 2245 propane (R_n19a), this reaction does not lead to a net loss of propane. Instead,
 2246 propane is lost by photolysis to reform propylene (J_d11b) and by downward flow
 2247 that ultimately leads to condensation (cf. Table 19).

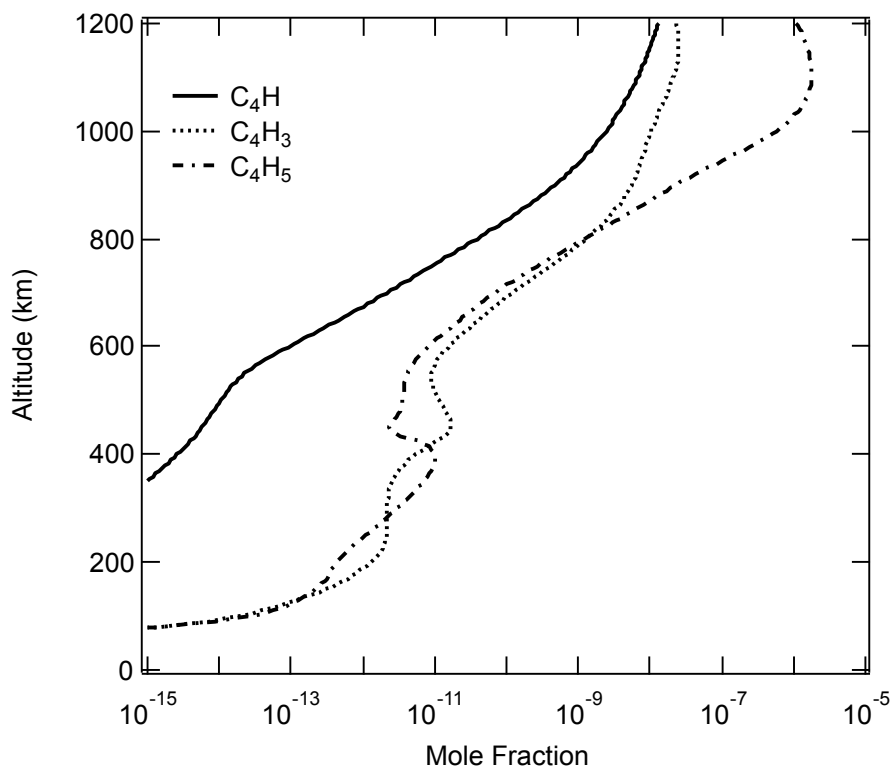
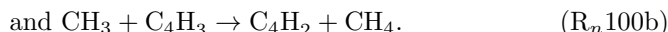
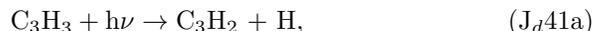


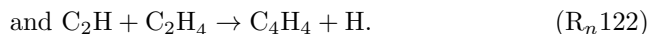
Figure 28: Model results for the mole fraction of the C_4H , C_4H_3 and C_4H_5 radicals.

2248 **Diacetylene (C_4H_2), Vinylacetylene (C_4H_4), Butadiene (C_4H_6),**
 2249 **Butene (C_4H_8), Butane (C_4H_{10}).** Above 1200 km, diacetylene is formed

2250 through a complex scheme involving C_4H_3 radicals (cf. Figure 28), which are
 2251 produced via the reaction of methylene and propadienylidene radicals (C_3H_2 ,
 2252 cf. Figure 25). The latter are formed by photolysis of propargyl radicals and
 2253 reaction of methylidyne radicals with acetylene:

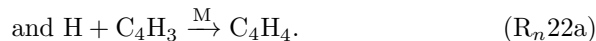
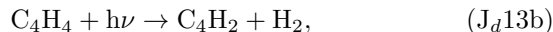


2254 In the bulk of the atmosphere, the chemistry of diacetylene is closely related
 2255 to that of vinylacetylene and a direct consequence of the presence of acetylene.
 2256 Diacetylene and vinylacetylene are mostly produced through the reaction of
 2257 ethynyl radicals (the main product of acetylene photolysis (J_d5)) with acetylene
 2258 and ethylene, respectively:



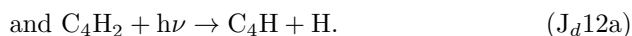
2259 At the turn of the century, the rate coefficients for the reaction of C_2H (cf.
 2260 Figure 24) with C_2H_2 and C_2H_4 (R_n120 , R_n122) have been determined at Titan-
 2261 relevant temperatures and were found to be near the collision limit (Opansky
 2262 and Leone, 1996; Chastaing et al., 1998; Vakhtin et al., 2001a,b). However, it
 2263 has only been recently confirmed experimentally that the only products were
 2264 diacetylene and vinylacetylene, even at low temperature (Kovács et al., 2010;
 2265 Bouwman et al., 2012).

2266 Vinylacetylene and diacetylene are efficiently recycled into one another through
 2267 a scheme involving C_4H_3 radicals:



2268 The rate coefficients for both reaction (R_n21) and (R_n22a) were presented in
 2269 Vuitton et al. (2012). The addition of hydrogen atoms onto diacetylene is quite
 2270 efficient ($\sim 10^{-13} \text{ cm}^3 \text{ s}^{-1}$) throughout the atmosphere thanks to radiative
 2271 stabilization. $H + C_4H_3$ leads to two product channels with similar importance,
 2272 addition and abstraction, the former dominating below 600 km and the latter
 2273 above (cf. Figure A.3b).

2274 Above 1100 km, vinylacetylene and diacetylene are mostly lost through
 2275 downward transport but in the bulk of the atmosphere, they are consumed
 2276 by reaction with H atoms and photodissociation, respectively:



2277 The rate coefficient of reaction (R_n23) has been calculated in the present work
 2278 (cf. Appendix A) and is close to $10^{-13} \text{ cm}^3 \text{ s}^{-1}$ throughout the atmosphere,
 2279 thanks to radiative association.

2280 Similar to C₂H/C₂H₂, a large fraction (75%) of C₄H (cf. Figure 28) is
 2281 recycled back to C₄H₂ through reaction with methane, despite the fact that the
 2282 rate coefficient is quite small at 150 K ($\sim 5 \times 10^{-13} \text{ cm}^3 \text{ s}^{-1}$), according to
 2283 Berteloite et al. (2008, 2010b). However, because of the low abundance of C₄H
 2284 this cycle is only responsible for $\sim 10\%$ of the methane loss:



2285 Once C₄H₅ (cf. Figure 28) is produced by reaction (R_n23), butadiene can
 2286 be efficiently formed through the reaction of C₄H₅ with H atoms:



2287 Photodissociation of butadiene (J_d14) is its almost exclusive loss process but
 2288 about one third of the butadiene destroyed is formed back through the addition
 2289 of methyl and propargyl radicals:



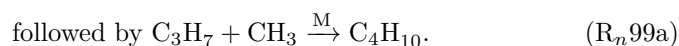
2290 Butene is formed through the addition of methyl and allyl radicals and lost
 2291 by photodissociation:



2292 About 20% of the C₄H₇ radicals formed by photodissociation recycle back to
 2293 butene through addition with H atoms:



2294 The formation of butane occurs essentially through the addition of methyl
 2295 and propyl radicals, the latter being formed via reaction (R_n128) and addition
 2296 of hydrogen atoms on propylene:



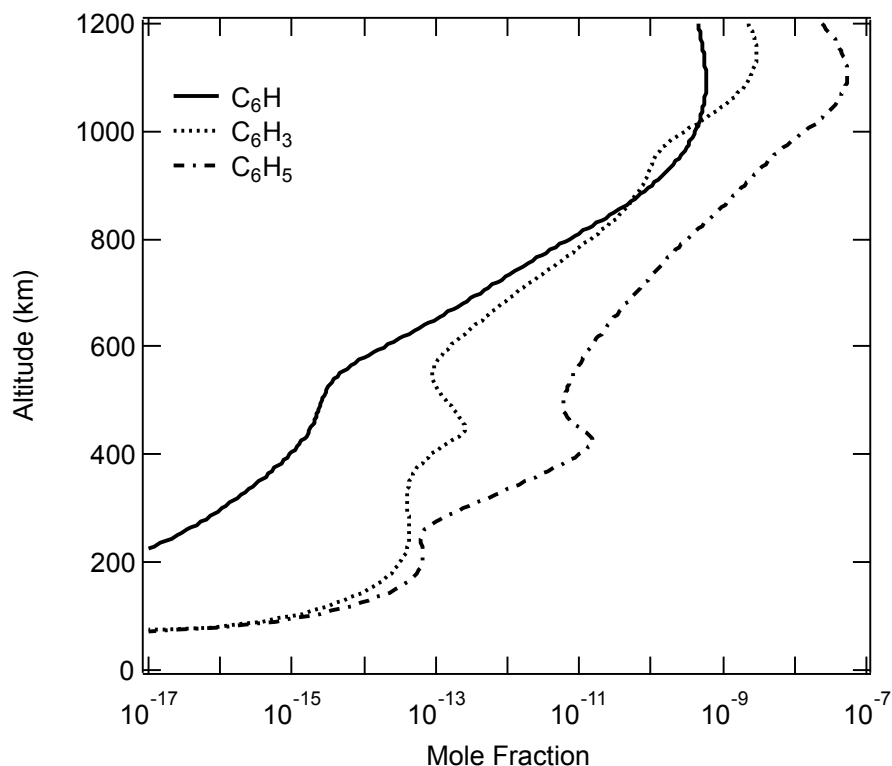
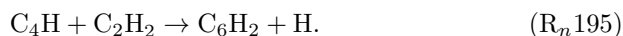


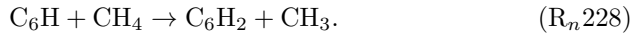
Figure 29: Model results for the mole fraction of the C_6H , C_6H_3 and C_6H_5 radicals.

2297 **Triacetylene (C_6H_2), Benzene (C_6H_6).** The production of triacety-
 2298 lene occurs almost exclusively through:



2299 In early models, the rate coefficient of this reaction was taken as equal to that
 2300 of $C_2H + C_2H_2$. Measurements by Berteloite et al. (2008, 2010b) show that
 2301 the rate coefficient for $C_4H + C_2H_2$ is actually about two times faster than the
 2302 rate coefficient measured by Chastaing et al. (1998) and Vakhtin et al. (2001b)
 2303 for $C_2H + C_2H_2$, which essentially validates the assumption that those rate
 2304 coefficients should be similar. A theoretical study of the C_6H_3 (cf. Figure 29)
 2305 potential energy surface predicts that the $C_4H + C_2H_2$ reaction readily produces
 2306 triacetylene + H (Landera et al., 2008).

2307 The main loss of C_6H_2 is essentially through photodissociation ($J_d 17$), but
 2308 below 500 km, most of the C_6H radicals (cf. Figure 29) formed in the process
 2309 recycle back to triacetylene by reaction with methane:

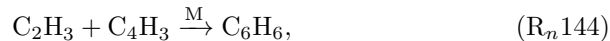


2310 As highlighted in past studies (Wilson et al., 2003; Vuitton et al., 2008), elec-
 2311 tron recombination of C_6H_7^+ ($\text{R}_{er}64$) controls benzene production in the upper
 2312 atmosphere. We note that the assumption that benzene is the sole product of
 2313 the electron recombination of C_6H_7^+ has now been validated experimentally
 2314 (Hamberg et al., 2011).

2315 The main loss of benzene is downward transport above 1000 km and pho-
 2316 todissociation (J_d18) to phenyl radicals (C_6H_5 , cf. Figure 29) throughout the
 2317 bulk of the atmosphere. However, radiative association of hydrogen atoms with
 2318 phenyl radicals makes this reaction pressure independent and extremely fast
 2319 ($1.6 \times 10^{-10} \text{ cm}^3 \text{ s}^{-1}$) throughout the atmosphere (Vuitton et al., 2012), leading
 2320 to the recycling of $\sim 80\%$ of the benzene destroyed:



2321 Below 400 km, two radical-radical reactions dominate the production of benzene:



2322 The addition reaction $\text{C}_2\text{H}_3 + \text{C}_4\text{H}_3$ (R_n144) has never been studied and had
 2323 to be estimated (Appendix A). This general scheme is similar to what has been
 2324 extensively described in Vuitton et al. (2008).

2325 3.2.2. Nitrogen-Bearing Species

Table 8: Column production rates for nitrogen atoms from different energy sources.

Products	Photons	Photoelectrons	Chemistry	Total
$\text{N}(^2\text{D})$	5.2×10^7	3.4×10^7	2.2×10^6	8.8×10^7
$\text{N}(^4\text{S})$	6.7×10^7	4.5×10^7	4.4×10^7	1.6×10^8

2326 **N_2 photofragments: $\text{N}(^2\text{D})$, $\text{N}(^4\text{S})$.** Table 8 and Figure 30 summarize
 2327 the major sources and production rates for nitrogen fragments. Their formation
 2328 is initiated by the dissociation and ionization of molecular nitrogen above 600
 2329 km. The photodissociation of N_2 is effective between 80 and 100 nm (cf. Figure
 2330 15) and it is a dominant formation mechanism of both excited ($\text{N}(^2\text{D})$) and
 2331 ground-state ($\text{N}(^4\text{S})$) nitrogen atoms. Nevertheless, dissociative ionization of
 2332 N_2 , which only occurs below 80 nm, is the major formation channel of $\text{N}(^4\text{S})$.
 2333 The production of $\text{N}(^2\text{D})$ and $\text{N}(^4\text{S})$ due to dissociation by photoelectrons is
 2334 only ~ 1.5 times less than the production due to direct EUV photolysis. $\text{N}(^4\text{S})$

2335 is also produced from relaxation of $N(^2D)$ and reaction of the latter with N_2 .
 2336 Dissociative electron recombination of N_2^+ represents $\sim 2\%$ of the total nitrogen
 2337 atom production. It is noteworthy that a few percents of $N(^2D)$ come from the
 2338 photodissociation of $^{14}N^{15}N$. The resulting mole fractions of $N(^4S)$ and $N(^2D)$
 2339 are presented in Figure 31.

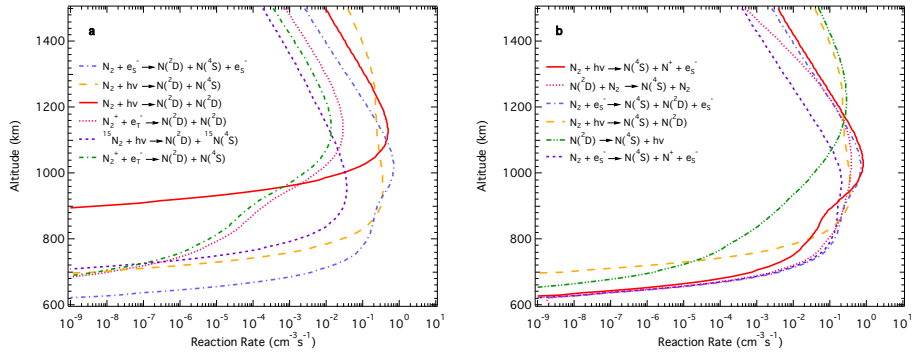


Figure 30: Major production rates of nitrogen fragments $N(^2D)$ (left panel) and $N(^4S)$ (right panel).

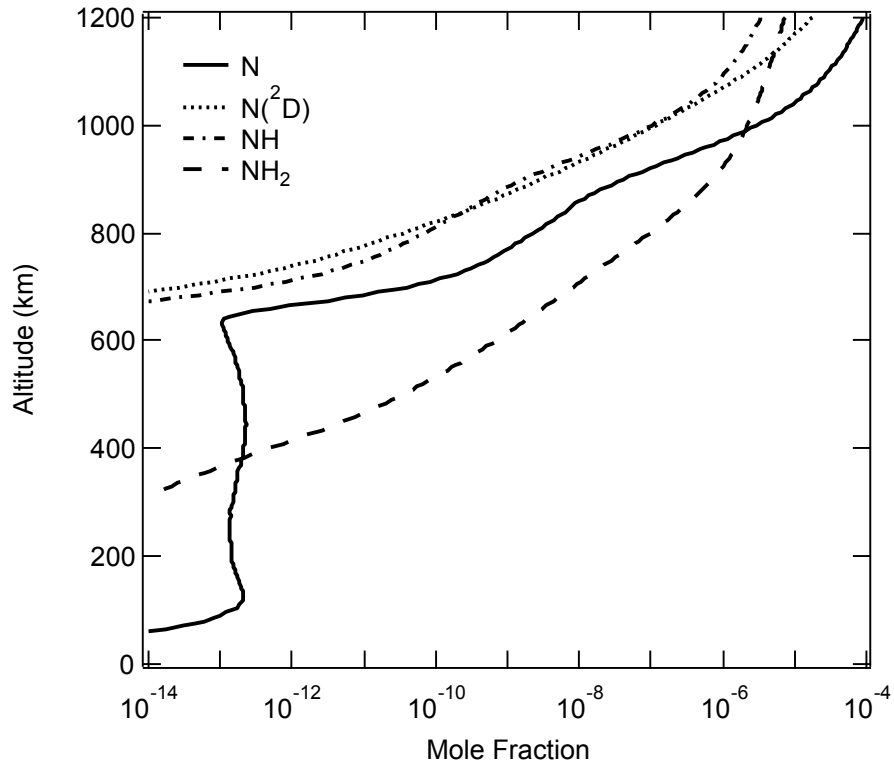
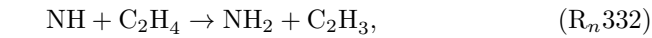
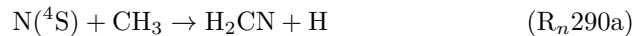


Figure 31: Model results for the mole fraction of the $N(^4S)$, $N(^2D)$, NH and NH_2 radicals.

2340 **Ammonia (NH_3), Hydrazine (N_2H_4).** Figure 3 in Yelle et al. (2010)
 2341 illustrates the chemical pathways leading to the formation of ammonia. It is pro-
 2342 duced primarily through reaction of amino (NH_2 , cf. Figure 31) with methylene-
 2343 amidogen (H_2CN , cf. Figure 33) radicals:



and



lead to



2344 There is only one available experimental study of the $N(^4S) + CH_3$ reaction
 2345 (Marston et al., 1989a,b). A rate coefficient with a strong and complex tem-
 2346 perature dependence has been measured over the temperature range 200-423 K,
 2347 with a value of $(6.4 \pm 2.1) \times 10^{-11} \text{ cm}^3 \text{ s}^{-1}$ at 200 K. The results suggest that
 2348 at colder temperatures, the rate coefficient will not be substantially lower than

2349 that value. We therefore follow Hébrard et al. (2012) and Dutuit et al. (2013)
 2350 who recommend the use of $6.2 \times 10^{-11} \text{ cm}^3 \text{ s}^{-1}$ in the 150-200 K range.

2351 Product measurements lead to a major channel ($\text{H}_2\text{CN} + \text{H}$) and a mi-
 2352 nor production of HCN, which can either originate from some H_2CN having
 2353 enough internal energy to further dissociate, or from secondary reactions of
 2354 H_2CN with nitrogen atoms. Taking into account the various uncertainties, we
 2355 use the branching ratios recommended by Hébrard et al. (2012) and Dutuit et al.
 2356 (2013), that is 90% for $\text{H}_2\text{CN} + \text{H}$ and 10% for $\text{HCN} + \text{H} + \text{H}$.

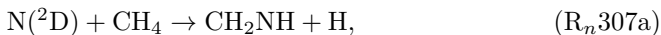
2357 As already explained in section 3.1.1.3, NH_3 quickly reacts with protonated
 2358 molecules to create NH_4^+ ($R_{cn}707, R_{cn}315$) but electron recombination of the
 2359 latter reforms NH_2 and NH_3 ($R_{er}84$), and therefore these reactions do not lead
 2360 to a net loss of ammonia. Instead, it is mostly lost by photodissociation (J_d20).

2361 The amino radical is also responsible for the production of hydrazine:

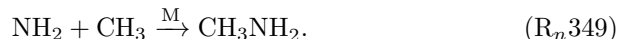


2362 Photodissociation (J_d21) is hydrazine’s main loss. Its ion chemistry is poorly
 2363 known but its proton affinity (853.2 kJ/mol) is such that it should efficiently
 2364 react with most of the ionospheric ions to produce N_2H_5^+ , which will recombine
 2365 with electrons. This latter process is unlikely to lead solely to $\text{N}_2\text{H}_4 + \text{H}$ and
 2366 will therefore induce an extra loss for N_2H_4 in the upper atmosphere.

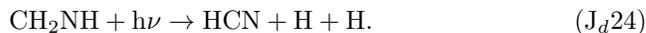
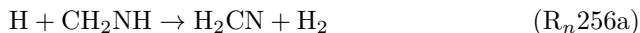
2367 **Methanimine (CH_2NH), Methylamine (CH_3NH_2).** Methanimine is
 2368 produced by two main reactions, which dominate above and below 800 km,
 2369 respectively:



2370 The latter reaction (J_d25) is the main loss for methylamine, while it is formed
 2371 by the addition of the methyl and amino radicals:



2372 As mentioned in section 3.1.1.3, CH_2NH can abstract a proton from most of the
 2373 protonated species in Titan’s atmosphere. Electron recombination of CH_2NH_2^+
 2374 is the major loss for CH_2NH above 1000 km because, although the products are
 2375 unknown, it is unlikely that they are 100% CH_2NH . Down to 400 km, reaction
 2376 with hydrogen atoms is methanimine’s main loss, while further below it is mostly
 2377 destroyed by photodissociation:



2378 We calculated the rate coefficient of reaction (R_n256) (cf. A.2c). Bimolecular
 2379 product formation (H₂CN + H₂, channel a), is dominant throughout the at-
 2380 mosphere, adduct stabilization leading to CH₂NH₂ (channel b) and to a lesser
 2381 extent CH₃NH (channel c) being nevertheless significant. Because of the lack
 2382 of information on the differential reactivity of CH₂NH₂ versus CH₃NH, we do
 2383 not differentiate the two isomers. As emphasized in Lavvas et al. (2008b), the
 2384 photodissociation cross-section of CH₂NH has only been measured in the wave-
 2385 length range 235-260 nm.

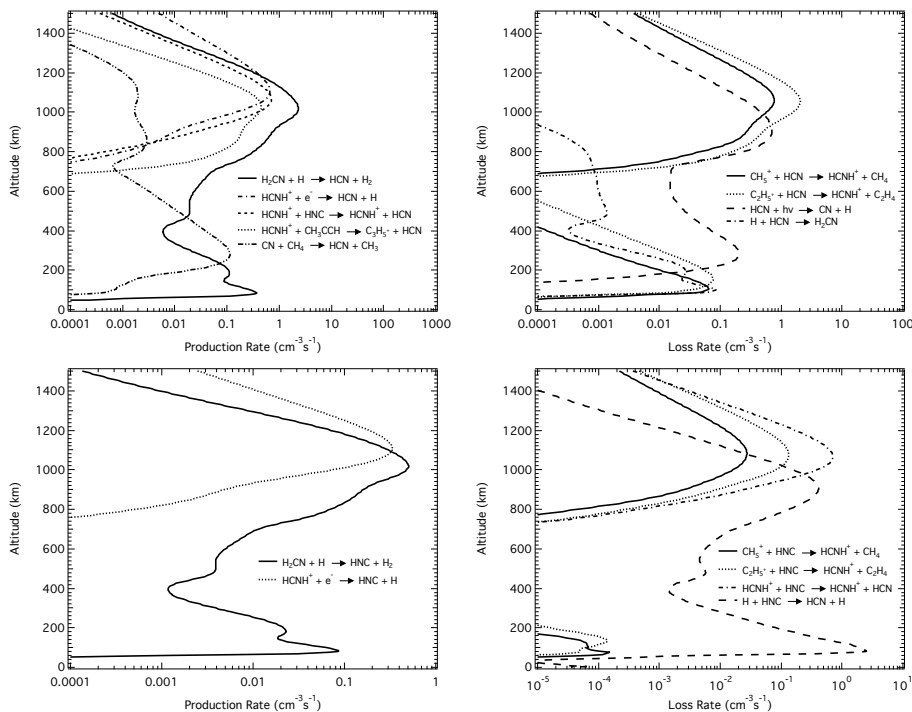
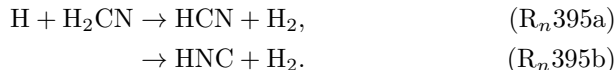


Figure 32: Production and loss rates of hydrogen cyanide and hydrogen isocyanide.

2386 **Hydrogen Cyanide (HCN), Hydrogen Isocyanide (HNC), Acetoni-**
 2387 **trile (CH₃CN).** The main production channel of both HCN and its iso-
 2388 mer HNC is the reaction of hydrogen atoms with methylene-amidogen radicals,
 2389 whose production mechanism has been described in the previous subsection (cf.
 2390 left panels in Figure 32):

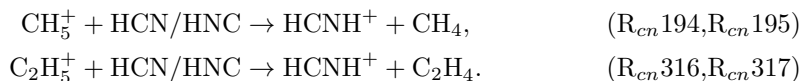


2391 Once formed, the triple C≡N bond in HCN is extremely stable and difficult to

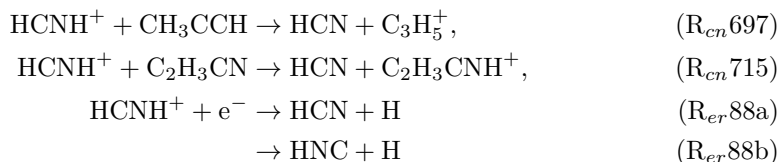
2392 break up. As a consequence, its main fate is to be incorporated in more complex
 2393 nitrile species.

2394 Hébrard et al. (2012) argue that the discrepancy between their calculated
 2395 and observed HNC mole fraction can be partly explained by the poor knowledge
 2396 of this reaction. We therefore performed theoretical calculations (cf. A.3f) that
 2397 indicated that channel (a) was dominant over channel (b) with rate coefficients
 2398 of $\sim 2.3 \times 10^{-10}$ and $\sim 5.0 \times 10^{-11} \text{ cm}^3 \text{ s}^{-1}$, respectively and little temperature
 2399 variation. These values are a factor 4-5 higher than those presented in Hébrard
 2400 et al. (2012). The adduct channel giving CH_2NH is negligible.

2401 Around the ionospheric peak, both isomers efficiently react with protonated
 2402 ions, whose associated neutrals have a lower proton affinity ($\text{PA}(\text{HCN}) = 712.9$
 2403 kJ/mol and $\text{PA}(\text{HNC}) = 772.0 \text{ kJ/mol}$), such as CH_5^+ and C_2H_5^+ :

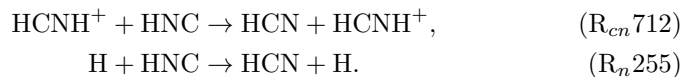


2404 HCNH^+ can in turn react with neutrals having a higher proton affinity ($\text{R}_{cn}697, \text{R}_{cn}715$)
 2405 and recombine with electrons ($\text{R}_{cn}88$), which induces the recycling of HCN and
 2406 HNC:



2407 The overall rate coefficient for the electron recombination of HCNH^+ measured
 2408 by different techniques can be regarded as similar but the branching fraction
 2409 between the different product channels is still under debate (cf. KIDA data
 2410 sheet 2815 V1 for a brief review). For our purpose, an important question is the
 2411 distribution between the HCN and HNC production. Theoretical calculations
 2412 conclude that they are produced in equal amounts (Talbi and Ellinger, 1998;
 2413 Hickman et al., 2005). This is supported by an experiment showing that the
 2414 internal energy of the fragments is extremely high, far exceeding the isomeriza-
 2415 tion barrier, which implies an isomeric production ratio in a narrow range near
 2416 unity (Mendes et al., 2012).

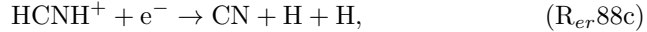
2417 On Titan, the lifetime of HNC is short (cf. section 5.4) as it quickly iso-
 2418 merizes to HCN through the following reactions (cf. lower right panel in Figure
 2419 32):



2420 Reaction (R_{cn}712), although tentative, is based on the suggestion by Cotton
 2421 et al. (2013) that the interaction of HCNH⁺ with HNC would immediately
 2422 proceed through a barrier-less proton transfer reaction to isomerize HNC to
 2423 HCN.

2424 Hébrard et al. (2012) performed a global sensitivity analysis to study how
 2425 the poor knowledge of this second reaction rate coefficient propagates in their
 2426 model and reached the conclusion that it limits strongly the accuracy of the
 2427 model. This is highlighted for HNC on their Figure 2. We therefore performed
 2428 theoretical calculations (cf. Figure A.2b) to reduce the uncertainty associated
 2429 to this reaction and found a rate coefficient of $\sim 10^{-13} \text{ cm}^3 \text{ s}^{-1}$, that is one
 2430 order of magnitude faster than the recommended value of Hébrard et al. (2012).

2431 A third channel in the electron recombination of HCNH⁺ as well as photol-
 2432 ysis do lead to a net loss of HCN (cf. upper right panel in Figure 32):

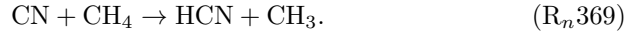


2433 but its main fate is to diffuse down. Below 650 km, the reaction between
 2434 hydrogen atoms and HCN becomes important:



2435 Theoretical calculations for this reaction are described in Appendix A. The rate
 2436 coefficient is temperature and pressure dependent and reaches a maximum of
 2437 $\sim 10^{-17} \text{ cm}^3 \text{ s}^{-1}$ around 200 km (cf. Figure A.2a). Although this is extremely
 2438 slow, it is significantly faster than the rate coefficient presented in Hébrard
 2439 et al. (2013) ($< 10^{-23} \text{ cm}^3 \text{ s}^{-1}$). The low value of the rate coefficient is coun-
 2440 terbalanced by the large density of hydrogen atoms, which makes this reaction
 2441 non-negligible.

2442 This reaction cancels out the production through reaction H₂CN+H (R_n395a)
 2443 and therefore, H + HNC (R_n255) becomes the major HCN source. Similarly,
 2444 the cyano radicals (CN, cf. Figure 33) produced by photodissociation of HCN
 2445 (J_d22) react with methane to recycle back some HCN:



2446 Finally, condensation near the tropopause amounts to about 40% of the HCN
 2447 total loss (cf. Table 19).

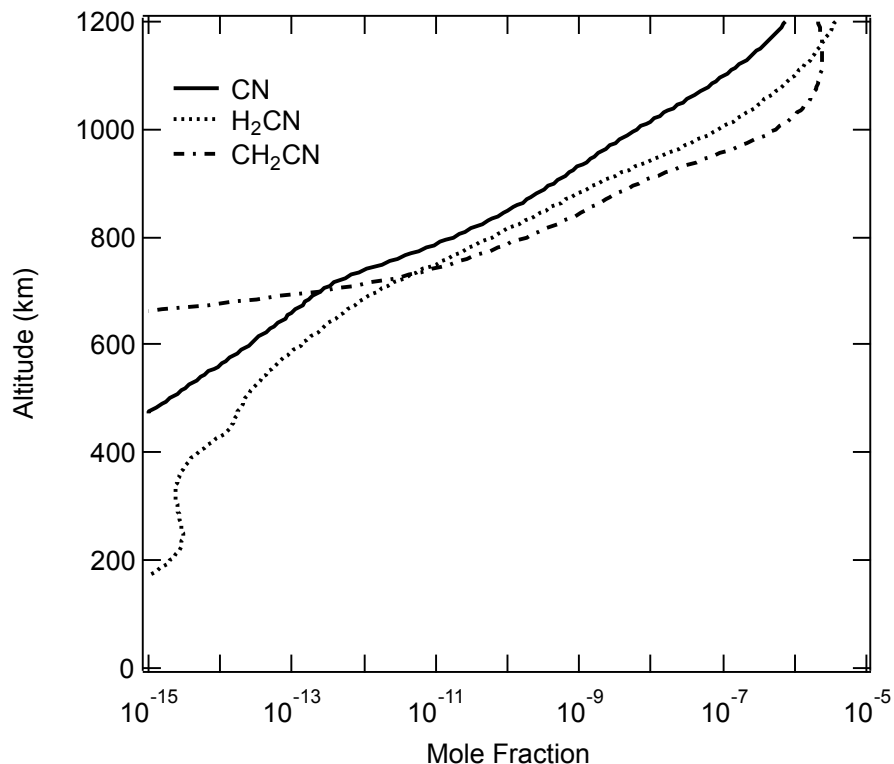
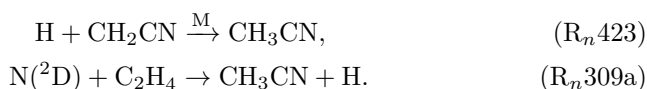


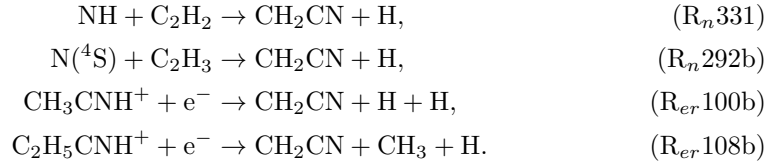
Figure 33: Model results for the mole fraction of the CN, H₂CN, and CH₂CN radicals.

2448 Acetonitrile is formed by two major channels:



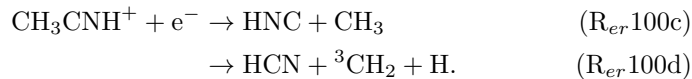
2449 It has been established that the C₂H₃N products formed in reaction (R_n309a)
 2450 are not CH₃CN but two other isomers, cyclic-CH₂NCH and CH₂(N)CH (Balu-
 2451 cani et al., 2012). Nevertheless, because the reactivity of these species is un-
 2452 known, we assume that they eventually rearrange to acetonitrile by collisions
 2453 with other species. We emphasize that this reaction represents ~30% of the
 2454 total acetonitrile production above 600 km and that setting this production to
 2455 zero would not drastically affect the CH₃CN profile.

2456 Cyanomethyl radicals (CH₂CN, cf. Figure 33) are formed through reaction
 2457 of imidogen radicals with acetylene, of nitrogen atoms with vinyl radicals and
 2458 through electron recombination of CH₃CNH⁺ and C₂H₅CNH⁺:



2459 The dissociative recombination of protonated propionitrile has been recently
2460 investigated at CRYRING (Vigren et al., 2010a, 2012a). Due to insufficient
2461 resolution of the detector, it was not possible to do a detailed investigation
2462 into the relative importance of the product channels; only the significance of
2463 different breakups or retention of the CCCN chain could be determined. In
2464 $\sim 43\%$ of the reactions the four heavy atoms (a C atom or an N atom, denoted
2465 X) remain in the same product fragment. An equal portion of the reactions
2466 leads to products where one of the heavy atoms is split off from the other three
2467 and $\sim 14\%$ result in a breakup into two heavy fragments containing two heavy
2468 atoms each. For the first channel leading to X_4 , the only energetically allowed
2469 channel is $\text{CH}_3\text{CH}_2\text{CN} + \text{H}$, while for the third channel giving $X_2 + X_2$, we prefer
2470 the fragmentation of one single C–C bond giving $\text{C}_2\text{H}_5 + \text{HNC}$. Finally, the
2471 authors believe that it is a fission of a C–C bond that dominates the $X_3 + X$
2472 type of fragmentations, possibly leading to the stable CH_3 and CH_2CN radicals
2473 alongside a hydrogen atom and we stick to this supposition.

2474 Acetonitrile is mostly lost by downward transport until it reaches the iono-
2475 spheric peak where its affinity for protons ($\text{R}_{cn} 713, \text{R}_{cn} 320$) becomes its promi-
2476 nent fate. Although most CH_3CNH^+ recycles back to CH_3CN through proton
2477 transfer reactions ($\text{R}_{cn} 775, \text{R}_{cn} 776$) and the two major electron recombination
2478 channels ($\text{R}_{er} 100\text{a}, \text{b}$), about 20% is lost through the two minor electron recom-
2479 bination channels:



2480 Below 700 km, the only source of acetonitrile is diffusion from the upper atmo-
2481 sphere and its major loss is photodissociation ($\text{J}_d 26$) and condensation near the
2482 tropopause (cf. Table 19).

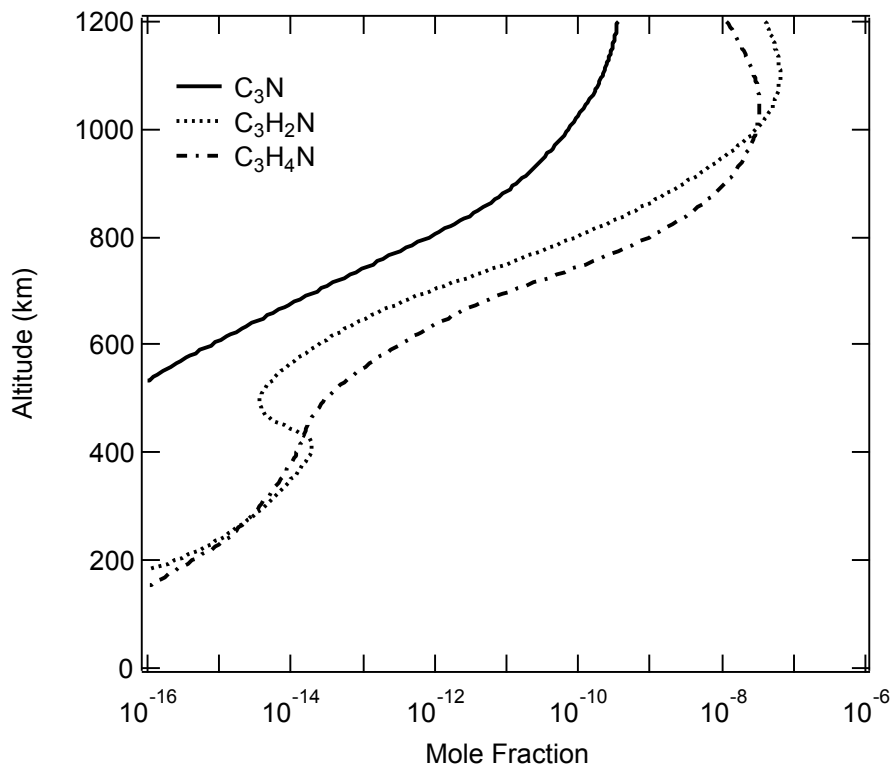
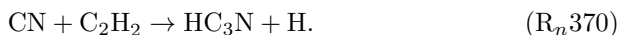
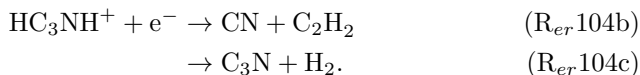


Figure 34: Model results for the mole fraction of the C_3N , H_2C_3N , and C_2H_4CN radicals.

2483 **Cyanoacetylene (HC_3N), Acrylonitrile (C_2H_3CN), Propionitrile**
 2484 **(C_2H_5CN).** Above 1000 km, cyanoacetylene is formed by the reaction be-
 2485 tween cyano radicals and acetylene:



2486 Like CH_3CN , it diffuses down to a level (~ 1000 km) where proton transfer
 2487 from $HCNH^+$ and $C_2H_5^+$ ($R_{cn}714, R_{cn}321$) followed by electron recombination
 2488 of HC_3NH^+ become its most important loss:



2489 Geppert et al. (2004b) and Vigren et al. (2012a) presented results on the elec-
 2490 tron recombination of protonated cyanoacetylene: the rate coefficient at elec-
 2491 tron temperatures relevant for Titan's upper atmosphere as well as the product
 2492 branching ratios. Instead of HC_3NH^+ , DC_3ND^+ was used for reasons concern-
 2493 ing the detection of the fragments, but previously measured branching ratios

2494 on other small polyatomic ions (Neau et al., 2000; Jensen et al., 2000; Geppert
 2495 et al., 2006; Kamińska et al., 2010) were similar for the deuterated and hydro-
 2496 genated species. The channels preserving the carbon chain ($D_xC_3N + (D)$) or
 2497 producing two fragments with a pair of heavy atoms each ($C_2D_x + CND_y +$
 2498 (D)) are detected with about equal fractions. Although the latter channel does
 2499 lead to a net loss of HC_3N , the first one essentially recycles back HC_3N through
 2500 reaction of C_3N (cf. Figure 34) with CH_4 (R_n438).

2501 Between 1000 and 700 km, photodissociation of acrylonitrile (J_d28a) be-
 2502 comes the major formation pathway of cyanoacetylene. It diffuses further down
 2503 where it is lost by photodissociation (J_d27) and addition of hydrogen atoms,
 2504 which subsequently leads to the production of acrylonitrile (see further below).
 2505 Less than 10% of HC_3N is lost by condensation (cf. Table 19).

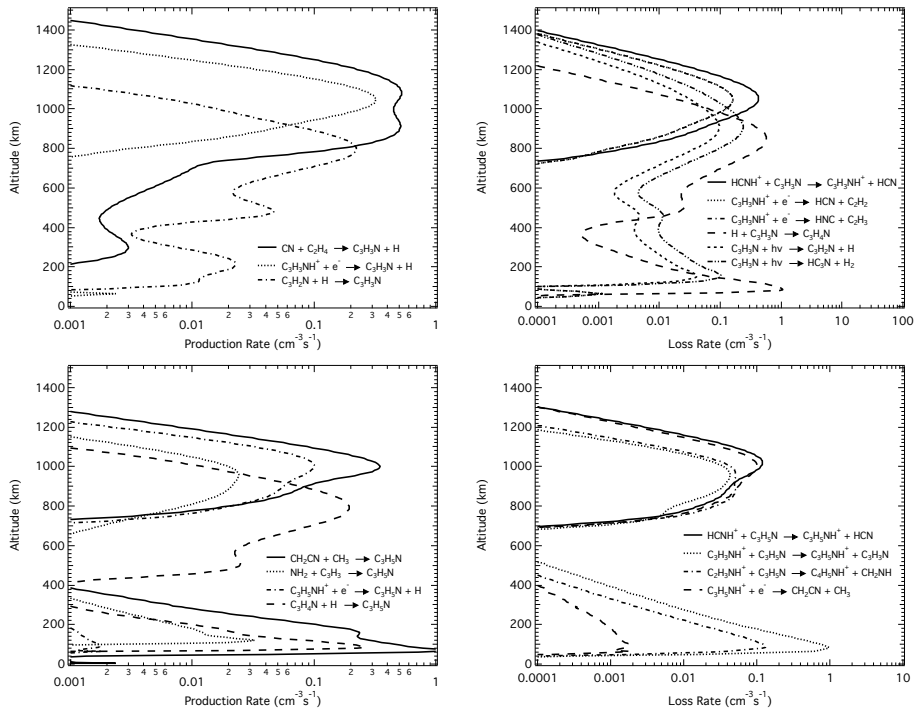
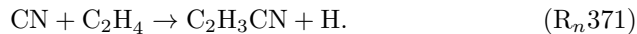


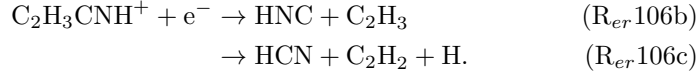
Figure 35: Production (left panels) and loss (right panels) rates of acrylonitrile (upper panels) and propionitrile (lower panels).

2506 Above 800 km, acrylonitrile is almost exclusively produced by the reaction
 2507 between cyano radicals and ethylene (cf. upper left panel of Figure 35):

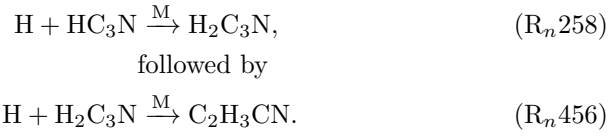


2508 It is lost essentially through downward transport with the exception of around
 2509 the ionospheric peak where, like the other nitriles, it is mostly destroyed by

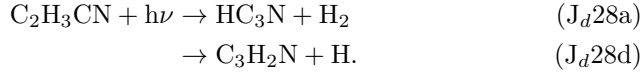
2510 proton transfer reactions from HCNH^+ and C_2H_5^+ ($\text{R}_{cn}715, \text{R}_{cn}322$), and sub-
 2511 sequent fragmentation of $\text{C}_2\text{H}_3\text{CNH}^+$ via electron recombination (cf. upper
 2512 right panel of Figure 35):



2513 Below 800 km, $\text{C}_2\text{H}_3\text{CN}$ is a secondary product of HC_3N through additions of
 2514 hydrogen atoms:



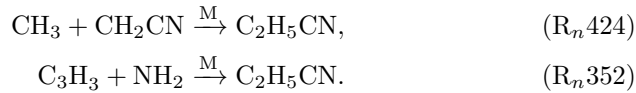
2515 Acrylonitrile is efficiently photodissociated but, with the main products being
 2516 HC_3N and $\text{C}_3\text{H}_2\text{N}$ (cf. Figure 34), this process does not result in a major sink
 2517 for $\text{C}_2\text{H}_3\text{CN}$:



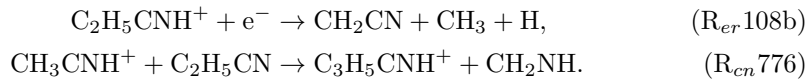
2518 Instead, it is mostly lost by addition of H atoms (R_n259).

2519 There are no reactions known to produce propionitrile in conditions relevant
 2520 to Titan. We therefore searched for radical associations that could reasonably
 2521 produce $\text{C}_2\text{H}_5\text{CN}$ and estimated their rate coefficient based on the number of
 2522 heavy atoms involved (section 2.7.3.1 and Vuitton et al. (2012)). The reaction of
 2523 excited nitrogen atoms with propylene (R_n313) is quite fast at room temperature
 2524 (Herron, 1999) and can also be reasonably expected to produce propionitrile.

2525 Within these assumptions, our model results indicate that above 900 km,
 2526 propionitrile is formed by addition of methyl and cyanomethyl radicals and to
 2527 a lower extent of propargyl with amino radicals (cf. lower left panel of Figure
 2528 35):



2529 In this region, it is almost exclusively lost via proton attachment ($\text{R}_{cn}716, \text{R}_{cn}323$)
 2530 followed by electron recombination of $\text{C}_2\text{H}_5\text{CNH}^+$, and ion-molecule reactions
 2531 (cf. lower right panel of Figure 35):



2532 Unlike for neutral chemistry, these reactions have been fairly well constrained
 2533 experimentally (Edwards et al., 2008; Vigren et al., 2010a). From 900 km down
 2534 to 400 km, propionitrile is found to be formed by a sequence of addition of hydro-
 2535 gen atoms to acrylonitrile and lost by transport downward ultimately reaching
 2536 the condensation level (cf. Table 19):



2537 **Cyanodiacetylene (HC_5N).** Similarly to cyanoacetylene, above 800 km,
 2538 cyanodiacetylene is formed by the reaction between cyanoethynyl radicals (C_3N)
 2539 and acetylene, and between cyano radicals and diacetylene:



2540 Cyanoethynyl radicals are formed in the electron recombination of protonated
 2541 cyanoacetylene above 1000 km and the photodissociation of cyanoacetylene
 2542 (J_d27a) below.

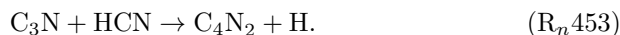
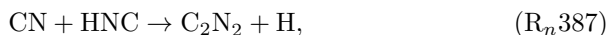
2543 The rate coefficients of reactions (R_n439) and (R_n377) have recently been
 2544 measured at low temperature by Sims et al. (Cheikh Sid Ely, 2012; Fournier,
 2545 2014). A common assumption in the literature is to assume that the rate co-
 2546 efficient for reaction (R_n439) is the same as that for $\text{C}_4\text{H} + \text{C}_2\text{H}_2$ (R_n195),
 2547 which proves to be a fairly valid assumption ($k(\text{R}_n439) = 3.4 \times 10^{-10}$ versus
 2548 $k(\text{R}_n195) = 2.4 \times 10^{-10} \text{ cm}^{-3} \text{ s}^{-1}$ at 150 K). Since the products have never been
 2549 investigated, we assume that the formation of HC_5N and a H atom, which is
 2550 more exothermic than the H abstraction and reformation of HC_3N , is the only
 2551 channel.

2552 The reactivity of the CN radical (cf. Figure 24) with C_4H_2 (R_n377) is found
 2553 to be very close to its reactivity with C_2H_2 (R_n370), with a mild negative
 2554 temperature dependence. It is worthwhile mentioning that the semi-empirical
 2555 capture model of Faure et al. (2009) reproduces extremely well the experimental
 2556 measurements. The products have never been investigated experimentally but
 2557 ab initio calculations demonstrate that the reactions of the CN radical with
 2558 polyynes lead to the formation of cyanopolyne chains HC_{2n}CN , here HC_5N
 2559 (Fukuzawa et al., 1998).

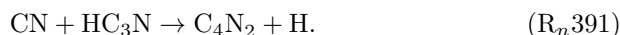
2560 Production of cyanodiacetylene is balanced by photolysis (J_d30) and ion
 2561 chemistry (proton exchange reactions and subsequent electron recombination)
 2562 in the upper atmosphere, as for HC_3N . The magnitude of these loss processes is
 2563 quite uncertain since data are neither available for the photodissociation branch-
 2564 ing ratios or electron recombination (both rate coefficient and products).

2565 **Cyanogen (C_2N_2) and dicyanoacetylene (C_4N_2).** From quantum
 2566 chemical calculations by Petrie and Osamura (2004), the main source of cyanogen

2567 and dicyanogen is, respectively:



2568 Dicyanoacetylene is also formed through CN addition and H atom elimination:



2569 The first experimental measurements of this reaction below room temperature
 2570 show only a slight increase in the rate coefficient from room temperature to 150
 2571 K (from 1.8×10^{-11} to 2.8×10^{-11} $\text{cm}^3 \text{s}^{-1}$) (Cheikh Sid Ely et al., 2013), falling
 2572 short of capture theory calculations, which predicted a value of 5.5×10^{-11} cm^3
 2573 s^{-1} at 150 K (Faure et al., 2009).

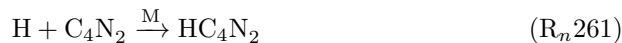
2574 Both C_2N_2 and C_4N_2 are lost by H atom addition and to a lower extent
 2575 photodissociation:



followed by



and



followed by



2576 3.2.3. O-bearing Species

2577 A crucial reaction for the distribution of O-bearing species is that between
 2578 OH and CH_3 ($\text{R}_n 526$) but the nature of the products has been a long standing
 2579 debate. For many years, $\text{CO} + 2\text{H}_2$ were thought to be the main products but
 2580 laboratory experiments performed in the 90's suggested that instead they were
 2581 $\text{H}_2\text{O} + {}^1\text{CH}_2$ in the bimolecular regime and CH_3OH in the termolecular regime
 2582 (Baulch et al., 1994; De Avillez Pereira et al., 1997). In Appendix A we present
 2583 calculations based on transition state theory that confirm that $\text{H}_2\text{O} + {}^1\text{CH}_2$ is
 2584 indeed an important channel but that the major products are actually CHOH
 2585 $+ \text{H}_2$, where CHOH is an isomer of formaldehyde (H_2CO) (cf. Figure A.4).

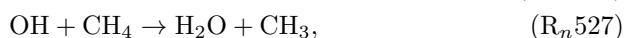
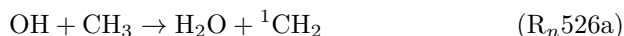
2586 With this scheme, the fate of an OH (hydroxy radicals) influx into Titan's
 2587 upper atmosphere can be divided into three basic pathways that are further
 2588 described below:

- 2589 • To restore H_2O in reactions with CH_3 , CH_4 , and C_2H_6 .
- 2590 • To form CO in reactions with CH_3 , C_2H_4 , and ${}^3\text{CH}_2$ because the products
 2591 in these reactions decompose further to CO.

2592 • To form CO₂ by removing CO.

2593 As a consequence, OH can lead to the formation of the three major O-bearing
2594 species (CO, H₂O and CO₂). This is fundamentally different than the Hörst
2595 et al. (2008) paper where both O and OH were required.

2596 The OH radicals deposited in the upper atmosphere are also quickly trans-
2597 formed to H₂O molecules by reaction with abundant species, such as CH₃ and
2598 CH₄:

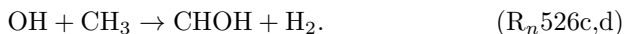


2599 but OH is rapidly recycled by photolysis:



2600 Water is ultimately lost by condensation near the tropopause.

2601 The OH flux ($10^7 \text{ cm}^{-2} \text{ s}^{-1}$) is mostly spent to form CO in reactions with
2602 CH₃:



2603 CHOH mainly reacts with H to form formaldehyde (H₂CO):



2604 Formaldehyde easily photodissociates forming CO either directly:



2605 or through a 2-step process involving HCO:



2606 CO is an extremely stable species in the conditions of the atmosphere of Titan,
2607 with the only loss mechanism being the reaction with OH radicals to produce
2608 CO₂:

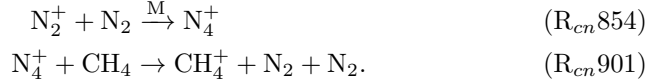


2609 CO₂ major loss is condensation near the tropopause.

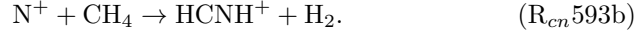
2610 Above ~800 km, proton transfer reactions are not a main loss for H₂O and
2611 CO as electron recombinations recycle them efficiently. The relevant ion-neutral
2612 chemistry is given in section 3.1.1.4. The coupled nitrogen-oxygen chemistry
2613 only impacts the density of the major O-bearing species to the 1% level at
2614 most.

2615 *3.3. The GCR Layer*

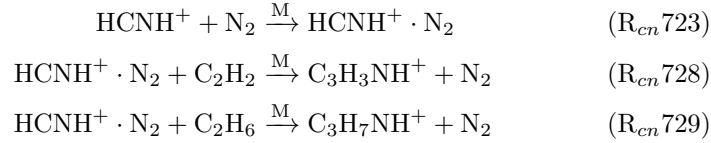
2616 GCR can penetrate to the deeper atmosphere to altitude levels where solar
 2617 radiation and saturnian electrons cannot reach and are the main ionization
 2618 source below 400 km. The main product following GCR impact is N_2^+ (cf.
 2619 Figure 18). Unlike in the upper ionosphere, it can efficiently add to N_2 by
 2620 three-body collisions to form N_4^+ (Anicich et al., 2000; McEwan and Anicich,
 2621 2007), which immediately reacts with methane:



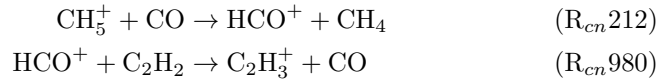
2622 This process rather than direct ionization is actually the main source of CH_4^+ .
 2623 CH_3^+ is a direct product of N_2^+ and CH_4 ($R_{cn}836a$) and the chemistry then
 2624 goes on to CH_5^+ ($R_{cn}162$), $C_2H_5^+$ ($R_{cn}132$) and $HCNH^+$ ($R_{cn}316$, $R_{cn}194$), as
 2625 in the upper ionosphere. Nevertheless, a third channel contributes as well to
 2626 the formation of $HCNH^+$ (Dutuit et al., 2013):



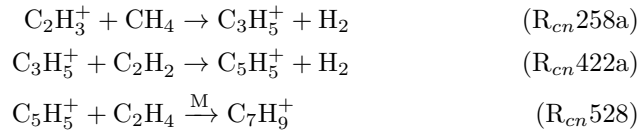
2627 Because of the high-pressure at low altitude, the main loss of $HCNH^+$ occurs
 2628 through a 3-body reaction with nitrogen (Capone et al., 1981) to form an adduct
 2629 that can subsequently react with acetylene (Capone et al., 1981) and ethane
 2630 (Vacher et al., 2000):



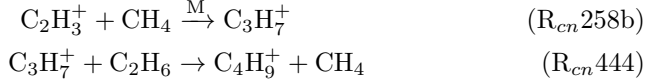
2631 CH_5^+ ions are at the origin of a suite of hydrocarbon ions, via HCO^+ :



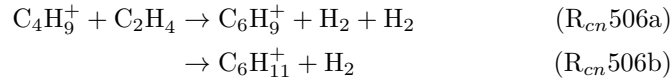
2632 After reacting with CH_4 , $C_2H_3^+$ can either lead to $C_7H_9^+$:



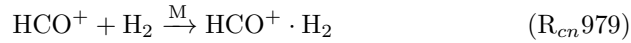
2633 or to $C_4H_9^+$:



2634 Then C_4H_9^+ can either lead to C_6H_9^+ or $\text{C}_6\text{H}_{11}^+$ (Burt et al., 1970):



2635 Nevertheless, the main loss of HCO^+ is not proton transfer to C_2H_2 but asso-
2636 ciation to H_2 (McEwan and Anicich, 2007; Molina-Cuberos et al., 1999a):



2637 As in the upper ionosphere, the presence of NH_3 leads to the formation of
2638 NH_4^+ , which is thus an intermediate in the chain of proton transfer reactions,
2639 eventually leading to heavier nitrogen-bearing ions with a large proton affinity.

2640 The chemistry induced by cosmic rays is also an important source of neu-
2641 tral species. It is well established that electron recombination of $\text{C}_3\text{H}_3\text{NH}^+$
2642 ($\text{R}_{er}106\text{a}$) leads to acrylonitrile. Similarly, some fraction of the electron recom-
2643 bination of $\text{C}_3\text{H}_7\text{NH}^+$ ($\text{R}_{er}109\text{c}$) may lead to ammonia.

2644 The photodissociation of ammonia (J_d20) as well as the reaction of NH
2645 radicals with ethane (Mullen and Smith, 2005) are the main sources of NH_2 :

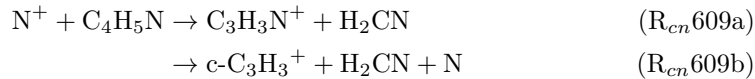


2646 NH_2 radicals are at the origin of methylamine (R_n349) and hydrazine (R_n361b).

2647 The photodissociation of CH_3NH_2 (J_d25a) and the reaction of excited nitro-
2648 gen atoms with methane (R_n307a) are the principal channels forming metha-
2649 nimine.

2650 The $\text{N}(^2\text{D})$ peak in the GCR layer is at the origin of the production of HCCN
2651 (R_n308), which by reaction with N atoms forms C_2N_2 (R_n300).

2652 The production of N^+ by GCR impact and the presence of heavy nitrogen
2653 bearing species (cf. Figure 55) lead to the formation of H_2CN (Stavish et al.,
2654 2009):



2655 As in the upper ionosphere, the formation of H_2CN and N atoms subsequently
2656 leads to the production of HNC (R_n298).

2657 4. Comparison to Observations and Other Models

2658 In this section, we compare the density profiles obtained with this latest
2659 update of our photochemical model to the available observations and to the
2660 models developed by other groups. We first focus on the positively charged hy-
2661 drocarbon ions and negatively charged species present in the upper ionosphere.
2662 In a second part, we discuss neutral species, including hydrocarbons, nitrogen
2663 (including ^{15}N) and oxygen bearing species. The protonated nitrogen species
2664 are also discussed here because their abundance is closely related to the pres-
2665 ence of the neutral form of those species. In addition to the nominal model
2666 discussed up to this point, we have run a number of additional models to test
2667 the sensitivity of certain molecules to various parameters. These models are
2668 shown in the relevant figures. Finally, we finish with a tentative composition
2669 for the GCR produced layer.

2670 4.1. The Upper Ionosphere

2671 4.1.1. Positive Ions

2672 4.1.1.1. *Previous Models.* Beside our own work, the groups of Cravens and that
2673 based at SwRI have been focusing extensively on the composition and density
2674 of ions in Titan's atmosphere (cf. Table 8 in Mandt et al. (2012a), and the
2675 reviews by Galand et al. (2014) and Vuitton et al. (2014)). Cravens et al.
2676 (2009) and Richard et al. (2015a) focus on the nightside ionosphere (T5, T21,
2677 T55-T59) while Robertson et al. (2009), Westlake et al. (2012), Mandt et al.
2678 (2012a) and Richard et al. (2015b) are interested in the dayside (T17, T18,
2679 T40, T48). These models use neutral background atmospheres usually based
2680 on the INMS observations available at that time or previous photochemical
2681 models. Cravens et al. (2009) and Richard et al. (2015a) used magnetospheric
2682 electron fluxes measured by CAPS ELS as boundary conditions at the top of the
2683 atmosphere for the downward electron flux in a two-stream model (Gan et al.,
2684 1992), the model of Robertson et al. (2009) includes ionization by solar radiation
2685 and photoelectrons, while in Westlake et al. (2012), the primary ionization is
2686 initiated by solar photons and magnetospheric electrons. Mandt et al. (2012a)
2687 improves on these models by including high resolution photoabsorption cross-
2688 sections for N_2 and $^{15}\text{N}^{14}\text{N}$, while Richard et al. (2015b) makes the simplified
2689 assumption that only 50% of the photons between 80 and 100 nm interact
2690 with N_2 . In all models, the chemical network relies heavily on the reaction
2691 list published in Vuitton et al. (2007). The models achieve somewhat different
2692 success in fitting various species in altitude regions of interest, but despite all
2693 differences in input parameters, one common conclusion to all these models is
2694 that CH_5^+ , C_2H_5^+ and HCNH^+ are overestimated by a factor of typically 2-4.
2695 We will return to this in section 5.1.

2696 4.1.1.2. *Observations.* INMS and CAPS performed the first and only ion den-
2697 sity measurements of Titan's upper atmosphere, most of which cannot be ob-
2698 tained with any other technique. INMS detected roughly 50 ions at or above the
2699 detection threshold in the mass range 1-100 u. Qualitatively the dayside and

2700 nightside ion composition are similar, but quantitative differences exist, partic-
2701 ularly for the species with a relatively short chemical lifetime (CH_5^+ , HCNH^+ ,
2702 C_2H_5^+) that are more abundant for the dayside than for the nightside. On
2703 the other hand, the day-to-night variations for terminal ion species with long
2704 lifetimes (NH_4^+ , C_6H_7^+ , $\text{C}_2\text{H}_3\text{CNH}^+$) are rather small (Cui et al., 2009a).

2705 The first ion observations by INMS were made deep into the nightside (solar
2706 zenith angle of 127° or more) during the outbound portion of the T5 flyby. It
2707 later appeared that they occurred during a strong precipitation event of mag-
2708 netospheric electrons and that the ionization rate exceeded the “typical” one
2709 by a factor of 10 (Ågren et al., 2007; Cravens et al., 2008). Therefore, although
2710 largely studied, T5 appears as a peculiar encounter with total ion densities
2711 somewhere in between that for a mean nightside ($400\text{-}1000\text{ cm}^{-3}$) and for a
2712 dayside pass ($2500\text{-}3500\text{ cm}^{-3}$) (Ågren et al., 2009).

2713 We choose to compare our ion density profiles to the T40 flyby because it
2714 is a dayside flyby (solar zenith angle of 65° at 1500 km inbound, 38° at closest
2715 approach and 14° at 1500 km outbound) that occurred at mid-latitudes (-21° at
2716 1500 km inbound, -12° at closest approach and 0° at 1500 km outbound) and in
2717 which high quality INMS and CAPS data were retrieved. The ion densities are
2718 obtained using the method described in Mandt et al. (2012a). Teolis et al. (2015)
2719 corrected the original INMS calibration model and accordingly, the previously
2720 published ion densities are revised upward by a correction factor of 1.55 ± 0.33 .

2721 *4.1.1.3. Density Profiles.* The calculated ion densities are given in Table 9 and
2722 the model spectrum is compared to the INMS spectrum obtained during the
2723 T40 flyby in Figure 36. For the ions that are closely related to a neutral (sec-
2724 tion 3), we discuss them in conjunction with the associated neutral in section
2725 4.2.3. Because our model corresponds to globally averaged conditions while T40
2726 is a dayside pass, we expect the predicted densities for the primary ions to un-
2727 derestimate the measured densities. We will see that this is indeed the case for
2728 the ionization products of N_2 and CH_4 , whose density is in agreement with the
2729 observations if multiplied by a factor of two. This does not support the idea
2730 that there is a problem with our understanding of the production of primary
2731 ions on the dayside. Because the model conveniently matches the primary ion
2732 densities, we expect that the subsequent chemistry should be well described.

Table 9: Calculated ion densities (cm^{-3}) at the peak of the ionosphere (1125 km). Only ions with a density above 10^{-1} cm^{-3} and major isotopologues are shown.

m/z	Species	Density	Species	Density	Species	Density	Species	Density
13	CH^+	1.2×10^{-1}						
14	CH_2^+	7.8×10^0	N^+	7.1×10^0				
15	CH_3^+	3.1×10^1						
16	CH_4^+	1.9×10^0						
17	CH_5^+	3.6×10^1						
18	NH_4^+	6.0×10^0						
19	H_3O^+	6.4×10^{-1}						
26	C_2H_2^+	1.2×10^0						
27	C_2H_3^+	1.4×10^1	HCN^+	8.8×10^{-1}				
28	HCNH^+	1.6×10^3	C_2H_4^+	1.2×10^2	N_2^+	3.7×10^1		
29	C_2H_5^+	4.2×10^2	$\text{HC}^{15}\text{NH}^+$	1.8×10^1	N_2H^+	6.3×10^0	HCO^+	9.8×10^{-1}
30	CH_2NH_2^+	7.6×10^1	C_2H_6^+	7.6×10^{-1}				
31	$\text{CH}_2^{15}\text{NH}_2^+$	2.0×10^0	C_2H_7^+	1.6×10^0	CH_2OH^+	2.9×10^{-1}		
32	CH_3NH_3^+	7.1×10^{-1}						
33	CH_3OH_2^+	6.0×10^{-1}						
38	CNC^+	2.8×10^{-1}						
39	$c\text{-C}_3\text{H}_3^+$	1.4×10^2	$l\text{-C}_3\text{H}_3^+$	8.5×10^0	HC_2N^+	2.1×10^0		
40	HC_2NH^+	1.3×10^1	C_3H_4^+	4.3×10^0				
41	C_3H_5^+	4.8×10^2						
42	CH_3CNH^+	1.8×10^2						
43	$\text{CH}_3\text{C}^{15}\text{NH}^+$	2.8×10^0	C_3H_7^+	2.5×10^0				
50	C_4H_2^+	1.1×10^{-1}						
51	C_4H_3^+	7.1×10^1						

Table 9 – Continued from previous page

m/z	Species	Density (cm ⁻³)	Species	Density (cm ⁻³)	Species	Density (cm ⁻³)	Species	Density (cm ⁻³)
52	HC ₃ NH ⁺	3.8 × 10 ¹	C ₄ H ₄ ⁺	2.1 × 10 ⁻¹				
53	C ₄ H ₅ ⁺	4.7 × 10 ¹	HC ₂ N ₂ ⁺	1.1 × 10 ⁻²				
54	C ₂ H ₃ CNH ⁺	8.4 × 10 ¹						
55	C ₄ H ₇ ⁺	9.3 × 10 ⁰	C ₂ H ₃ C ¹⁵ NH ⁺	1.0 × 10 ⁰	C ₂ H ₃ CO ⁺	5.1 × 10 ⁻¹		
56	C ₂ H ₅ CNH ⁺	1.7 × 10 ¹						
57	C ₄ H ₉ ⁺	1.2 × 10 ⁰						
58	C ₃ H ₅ NH ₃ ⁺	1.2 × 10 ⁰						
63	C ₅ H ₃ ⁺	1.6 × 10 ⁰						
65	C ₅ H ₅ ⁺	1.4 × 10 ²						
66	C ₄ H ₃ NH ⁺	4.2 × 10 ¹						
67	C ₅ H ₇ ⁺	7.6 × 10 ¹						
68	C ₄ H ₅ NH ⁺	6.5 × 10 ⁰						
70	C ₄ H ₇ NH ⁺	7.7 × 10 ⁰						
75	C ₆ H ₃ ⁺	1.7 × 10 ⁰						
76	HC ₅ NH ⁺	1.5 × 10 ⁰	C ₆ H ₄ ⁺	1.0 × 10 ⁰				
77	C ₆ H ₅ ⁺	5.9 × 10 ⁰	C ₅ H ₃ N ⁺	5.4 × 10 ⁻¹				
78	C ₅ H ₃ NH ⁺	4.4 × 10 ⁻¹						
79	C ₆ H ₇ ⁺	9.9 × 10 ⁰						
80	C ₅ H ₅ NH ⁺	4.4 × 10 ⁰						
81	C ₆ H ₉ ⁺	3.6 × 10 ⁻¹						
83	C ₆ H ₁₁ ⁺	3.6 × 10 ⁻¹						
89	C ₇ H ₅ ⁺	8.4 × 10 ⁻¹						
90	C ₆ H ₃ NH ⁺	3.3 × 10 ⁰						
91	C ₇ H ₇ ⁺	3.0 × 10 ¹						
92	C ₆ H ₅ NH ⁺	1.2 × 10 ⁰						

Table 9 – Continued from previous page

m/z	Species	Density (cm ⁻³)	Species	Density (cm ⁻³)	Species	Density (cm ⁻³)	Species	Density (cm ⁻³)
93	C ₇ H ₉ ⁺	2.0 × 10 ⁰						
94	C ₆ H ₇ NH ⁺	6.4 × 10 ⁻¹						
96	C ₆ H ₉ NH ⁺	1.4 × 10 ⁰						

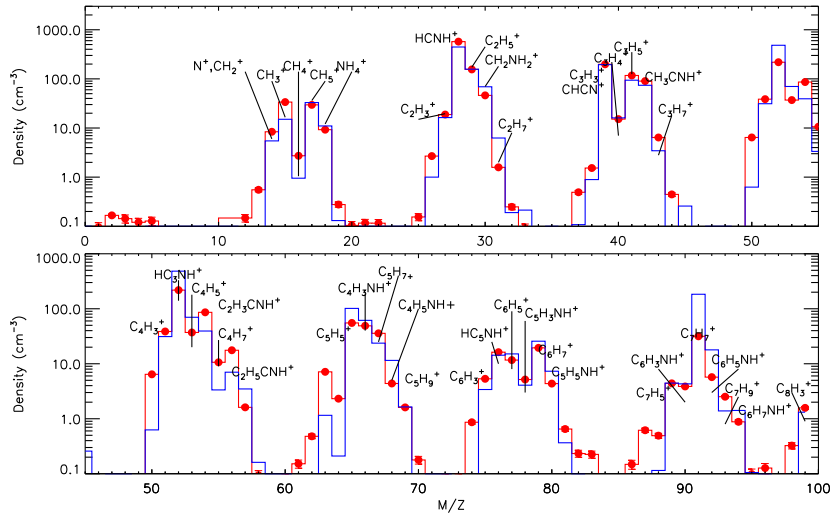


Figure 36: INMS observed during T40 (symbols) and modeled (lines) mass spectrum at 1100 km.

2733 $N^+/CH_2^+, CH_3^+, CH_4^+, CH_5^+$. The ion species in the model containing one carbon atom are $C^+, CH^+, CH_2^+, CH_3^+, CH_4^+$ and CH_5^+ . The
 2734 production rate of C^+ and CH^+ is too small for these ions to be detectable by
 2735 INMS. CH_2^+ at $m/z = 14$ has a similar abundance as N^+ , while CH_3^+, CH_4^+
 2736 and CH_5^+ can be constrained by the observations.
 2737

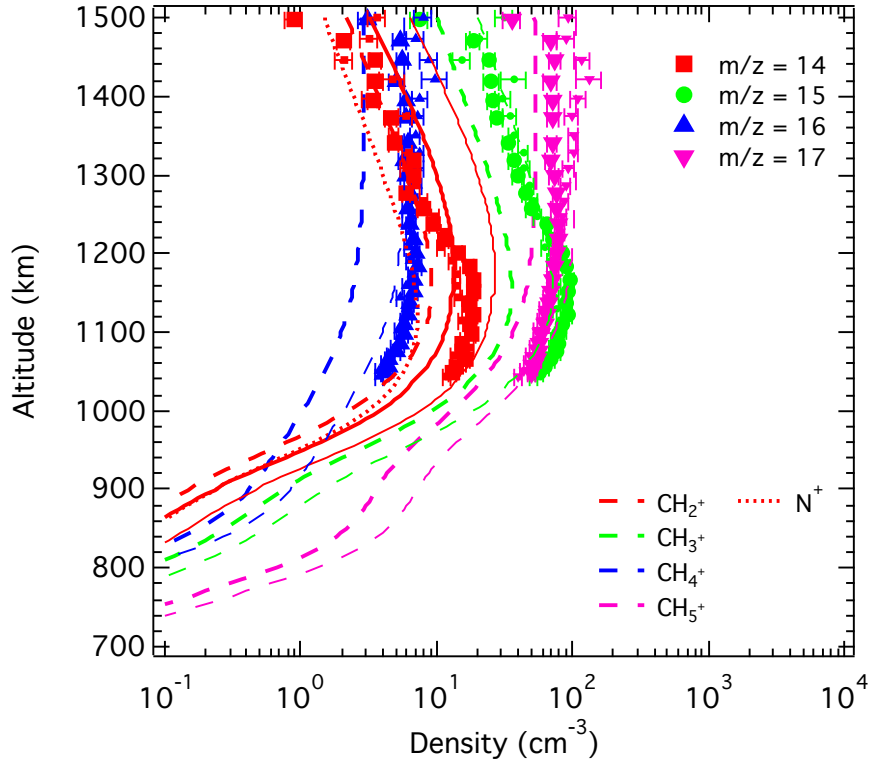


Figure 37: Model results for the density of N^+/CH_2^+ , CH_3^+ , CH_4^+ and CH_5^+ and comparison to the T40 INMS ion density measurements at m/z 14, 15, 16 and 17. The thin lines correspond to the model results multiplied by a factor of two, to approximate a daytime calculation.

2738 The simulated profiles for CH_2^+/N^+ , CH_3^+ , CH_4^+ and CH_5^+ are illustrated
 2739 in Figure 37. In order to compare the model with data we scale the model by
 2740 a factor of 2 to convert from global average to dayside values. The sum of the
 2741 N^+ and CH_2^+ profiles agrees roughly in magnitude and shape with the m/z
 2742 =14 densities in the vicinity of the peak with slightly worse agreement at high
 2743 altitudes. This could be due to the lack of diffusion or magnetic forces in the
 2744 model. "Dayside" CH_3^+ , CH_4^+ and CH_5^+ are within the INMS error bars for
 2745 $m/z = 15, 16$ and 17 , respectively.

2746 N^+ , N_2^+ and CH_4^+ are the direct ionization products of N_2 and CH_4 , re-
 2747 spectively. Since $HCNH^+$ is the dominant species at $m/z = 28$ (Cravens et al.
 2748 (2009) and section 4.2.3.2), CH_3^+ , the main product of the reaction of N_2^+
 2749 with CH_4 (section 3.1.1.2), is the best tracer of the N_2^+ density. The pro-
 2750 duction rates depend on both the CH_4 and N_2 ionizing schemes, through the
 2751 N_2 high-resolution cross-sections, as first suggested by Lavvas et al. (2011a).
 2752 Therefore, the perfect agreement between the observations and the simulated

2753 CH_4^+ and CH_3^+ densities when multiplied by a factor of 2 suggests that the
 2754 primary ionization products of N_2 are calculated accurately.

2755 The N^+ modeled densities of Mandt et al. (2012a) are a factor of ~ 5 too
 2756 high when compared to the data, while Westlake et al. (2012) and Dobrijevic
 2757 et al. (2016) do not overpredict this ion. The results for the hydrocarbon ions
 2758 in the simulations by Robertson et al. (2009), Mandt et al. (2012a), Westlake
 2759 et al. (2012), Richard et al. (2015b) and Dobrijevic et al. (2016) exhibit den-
 2760 sities close to the INMS measurements for CH_3^+ and CH_4^+ but densities too
 2761 high by a factor of 2-3 for CH_5^+ . Mandt et al. (2012a) emphasize that the
 2762 use of the Lavvas et al. (2011a) high-resolution cross-sections for the photodis-
 2763 sociation of N_2 (80-100 nm) produce better results for both CH_4^+ and CH_3^+ .
 2764 Although the strong effect that the high-resolution cross-sections have on the
 2765 CH_4^+ production rates has already been put forward and explained by Lavvas
 2766 et al. (2011a), it is unclear why they should have some impact on CH_3^+ as this
 2767 ion is mostly formed through the reaction of N_2^+ with CH_4 ($R_{cn}836a$) and not
 2768 through direct photoionization of CH_4 , which accounts only for 5% of the total
 2769 CH_3^+ production rate.

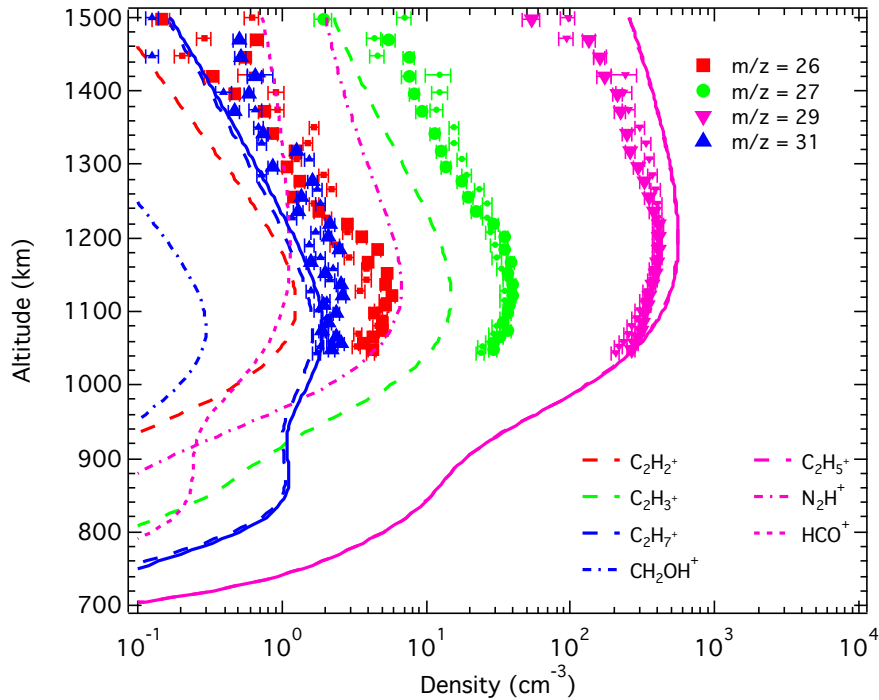


Figure 38: Model results for the density of C_2H_2^+ , C_2H_3^+ , $\text{C}_2\text{H}_5^+/\text{N}_2\text{H}^+/\text{HCO}^+$ and $\text{C}_2\text{H}_7^+/\text{CH}_2\text{OH}^+$ and comparison with the T40 INMS ion density measurements at $m/z = 26, 27, 29, 31$.

2770 C_2H_2^+ , C_2H_3^+ , C_2H_5^+ , C_2H_7^+ . The hydrocarbon ions containing two
 2771 carbon atoms are C_2H^+ , C_2H_2^+ , C_2H_3^+ , C_2H_4^+ , C_2H_5^+ , C_2H_6^+ and C_2H_7^+ .
 2772 C_2H^+ has too small a production rate ($10 \text{ cm}^{-2} \text{ s}^{-1}$) to be observable by INMS.
 2773 The open-shell ion C_2H_2^+ and the closed-shell ions C_2H_3^+ , C_2H_5^+ , and C_2H_7^+
 2774 are constrained by the INMS observations at $m/z = 26, 27, 29$ and 31 , respec-
 2775 tively. However, the open-shell ions C_2H_4^+ and C_2H_6^+ are not constrained by
 2776 INMS because N-bearing species are more abundant at their respective m/z
 2777 (section 4.2.3.2).

2778 Figure 38 shows the modeled C_2H_2^+ , C_2H_3^+ , C_2H_5^+ and C_2H_7^+ densities
 2779 and the INMS channels 26, 27, 29 and 31 densities for the T40 flyby. The
 2780 modeled densities of C_2H_2^+ and C_2H_3^+ are within a factor of two of the observed
 2781 ion densities at $m/z = 26$ and 27 , respectively. However, the model overestimates
 2782 the measured densities at $m/z = 29$. Although HCO^+ , N_2H^+ and C_2H_5^+ all
 2783 fall in this mass channel, C_2H_5^+ is far more abundant than HCO^+ and N_2H^+
 2784 and the small discrepancy between modeled and observed densities should be
 2785 attributed to C_2H_5^+ alone. This result is in line with previous models that
 2786 all predict C_2H_5^+ to be a factor of 2-4 higher than the measured densities at
 2787 $m/z = 29$ (Mandt et al., 2012a; Robertson et al., 2009; Westlake et al., 2012;
 2788 Dobrijevic et al., 2016). We will return to this issue in section 4.2.3.2. The
 2789 modeled density of C_2H_7^+ is in good agreement with the observations at $m/z =$
 2790 31 . CH_2OH^+ falls in this same mass channel but only contributes 15% at 1075
 2791 km, which is different from Dobrijevic et al. (2016) where CH_2OH^+ contributes
 2792 65% to the peak.

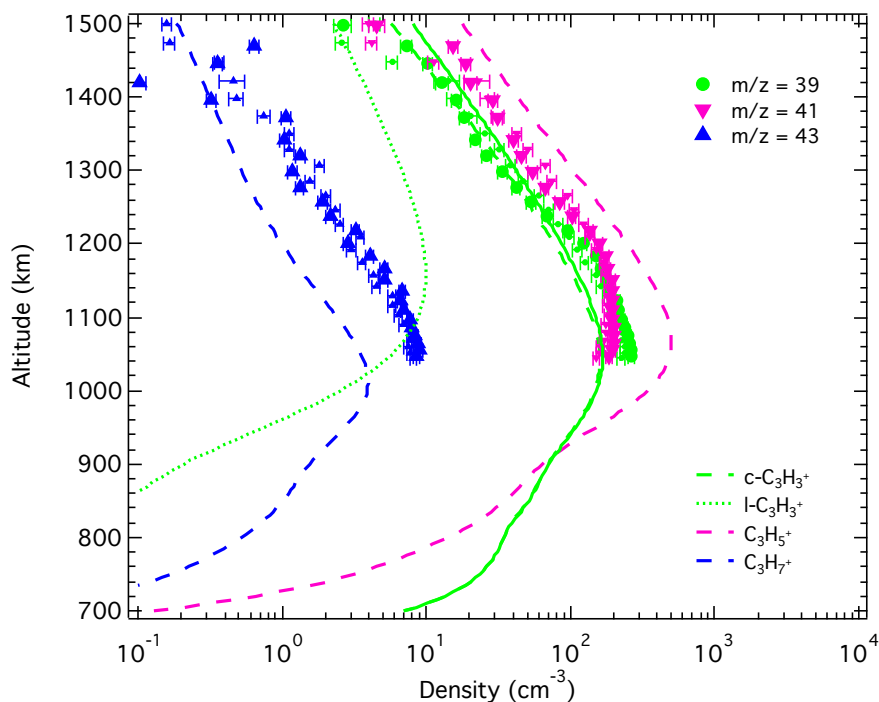
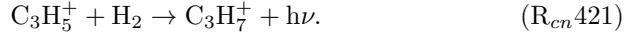


Figure 39: Model results for the density of c -, l - $C_3H_3^+$, $C_3H_5^+$ and $C_3H_7^+$ and comparison with the T40 INMS ion density measurements at $m/z = 39, 41, 43$.

2793 $C_3H_3^+$, $C_3H_5^+$, $C_3H_7^+$. The signal at $m/z = 39$ is attributed to $C_3H_3^+$
2794 and is well reproduced by the model (cf. Figure 39). At the top of the iono-
2795 sphere, the l - $C_3H_3^+$ / c - $C_3H_3^+$ ratio is about one but because of the high reac-
2796 tivity of l - $C_3H_3^+$ with hydrocarbons, the ratio drops significantly below 1400
2797 km to reach a value of $\sim 10\%$ at the c - $C_3H_3^+$ peak at 1050 km. Dobrijevic et al.
2798 (2016) slightly underestimates the $C_3H_3^+$ measured densities, which is consis-
2799 tent with the fact that they do not differentiate l - $C_3H_3^+$ and c - $C_3H_3^+$. Indeed,
2800 Carrasco et al. (2008) showed that the assumption that both isomers are iden-
2801 tically reactive leads to an under prediction of $C_3H_3^+$ of the same magnitude
2802 (cf. their Figure 4).

2803 The signal at $m/z = 41$ is attributed to $C_3H_5^+$ (cf. Figure 39). The INMS
2804 ion density is overestimated by the model by a factor of ~ 2 above 1200 km and
2805 a factor of ~ 4 at the peak at 1060 km. This can be partly explained by the
2806 overestimation of $C_2H_5^+$, which contributes to 30% of the $C_3H_5^+$ production
2807 through its reaction with C_2H_4 ($R_{cn}302a$).

2808 Finally, using the rate coefficient from Herbst et al. (2010), initial calcula-
2809 tions showed that the radiative association reaction involving $C_3H_5^+$ and H_2
2810 was an efficient source of protonated propene:



2811 This reaction lead to a large overestimation of the signal at $m/z = 43$. However,
 2812 a combination of experiments and more refined quantum chemical ab initio
 2813 calculations reported later on (Lin et al., 2013) does not corroborate the Herbst
 2814 et al. (2010) rate coefficient. Indeed, the latter approach shows that this reaction
 2815 does *not* occur efficiently at cold temperatures due to activation energy barriers.
 2816 Without this reaction, the signal at $m/z = 43$ is now well reproduced by the
 2817 model (cf. Figure 39).

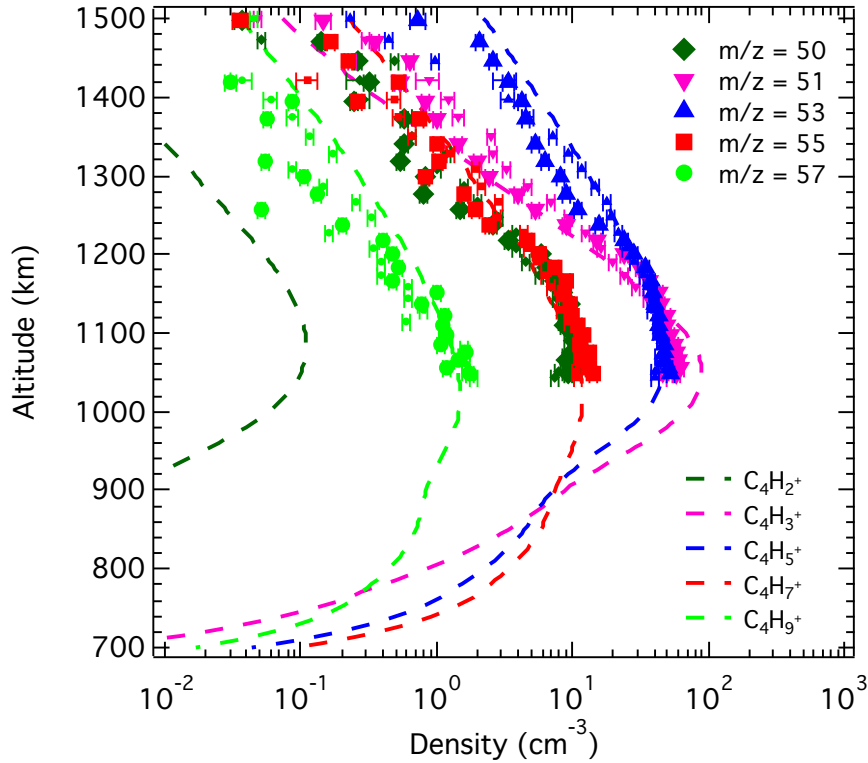


Figure 40: Model results for the density of C_4H_2^+ , C_4H_3^+ , C_4H_5^+ , C_4H_7^+ and C_4H_9^+ and comparison with the T40 INMS ion density measurements at $m/z = 50, 51, 53, 55, 57$.

2818 C_4H_2^+ , C_4H_3^+ , C_4H_5^+ , C_4H_7^+ , C_4H_9^+ . As already discussed in
 2819 Vuitton et al. (2007), our model cannot reproduce the observed ion density
 2820 at $m/z = 50$ (cf. Figure 40). The major ion at this channel is C_4H_2^+ but its
 2821 density at the peak is a factor of 45 lower than measured. C_4H_2^+ is formed by
 2822 charge transfer from C_2H_2 to C_4H_2 (McEwan and Anicich, 2007):



2823 As discussed above, the model underestimates C_4H_2 in the thermosphere, which
 2824 implies that the production rate of C_4H_2^+ through this reaction is underesti-
 2825 mated, as shown in Figure 40. However, this difference cannot account for the
 2826 factor of 40 between observed and modeled densities. In low-pressure plasma
 2827 conditions, reaction of C_2H^+ with C_2H_2 serves as one of the main routes to
 2828 formation of C_4H_2^+ , after a loss of H atom (Benedikt, 2010). An association
 2829 reaction of C_2^+ with C_2H_2 can also form some C_4H_2^+ as discussed in Bera et al.
 2830 (2015). But neither C_2H^+ or C_2^+ are detected by INMS (Vuitton et al., 2007)
 2831 and it is still unclear what production reaction(s) are missing for C_4H_2^+ .

2832 The signal at $m/z = 51$ is attributed to C_4H_3^+ and is well reproduced by
 2833 the model (cf. Figure 40). This might seem surprising since C_4H_3^+ is closely
 2834 related to C_4H_2 through proton transfer reactions ($\text{R}_{cn}700$, $\text{R}_{cn}308$) and since
 2835 the model profile of C_4H_2 is not in very good agreement with the observations
 2836 in the thermosphere. However, both HCNH^+ and C_2H_5^+ , the precursor ions of
 2837 C_4H_3^+ , are overestimated, which essentially compensates the underestimation
 2838 of C_4H_2 .

2839 The signals at $m/z = 53$, 55 and 57 are attributed to C_4H_5^+ , C_4H_7^+ and
 2840 C_4H_9^+ and are all very well reproduced by the model (cf. Figure 40).

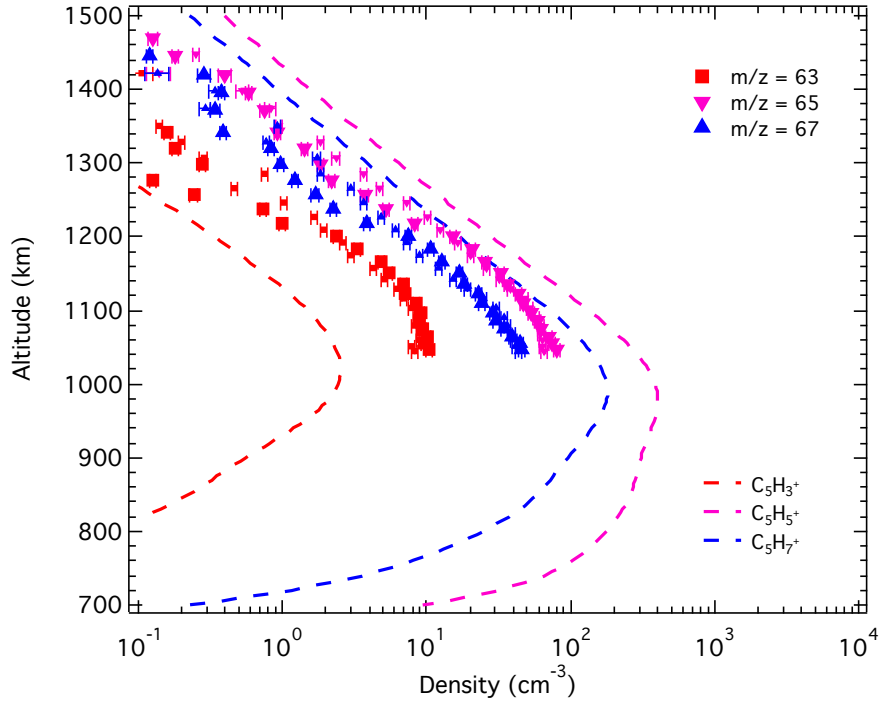


Figure 41: Model results for the density of $C_5H_3^+$, $C_5H_5^+$, and $C_5H_7^+$ and comparison with the T40 INMS ion density measurements at $m/z = 63, 65, 67$.

2841 $C_5H_3^+$, $C_5H_5^+$, $C_5H_7^+$. The signal at $m/z = 63$ is attributed to $C_5H_3^+$
 2842 but is underestimated in the model by a factor of about 5 (cf. Figure 41). $C_5H_3^+$
 2843 formation reactions all involve C_4H_2 ($R_{cn}287a, R_{cn}393b, R_{cn}138b$) and again its
 2844 underestimation can mostly explain the incapacity of the model to properly
 2845 predict the $C_5H_3^+$ density.

2846 The signals at $m/z = 65$ and 67 are attributed to $C_5H_5^+$ and $C_5H_7^+$, re-
 2847 spectively. They both are overestimated by the model by a factor of about 2
 2848 (cf. Figure 41), which is still a fair agreement since the rate coefficient for the
 2849 main loss processes, electron recombination ($R_{er}51, R_{er}53$), is an estimate.

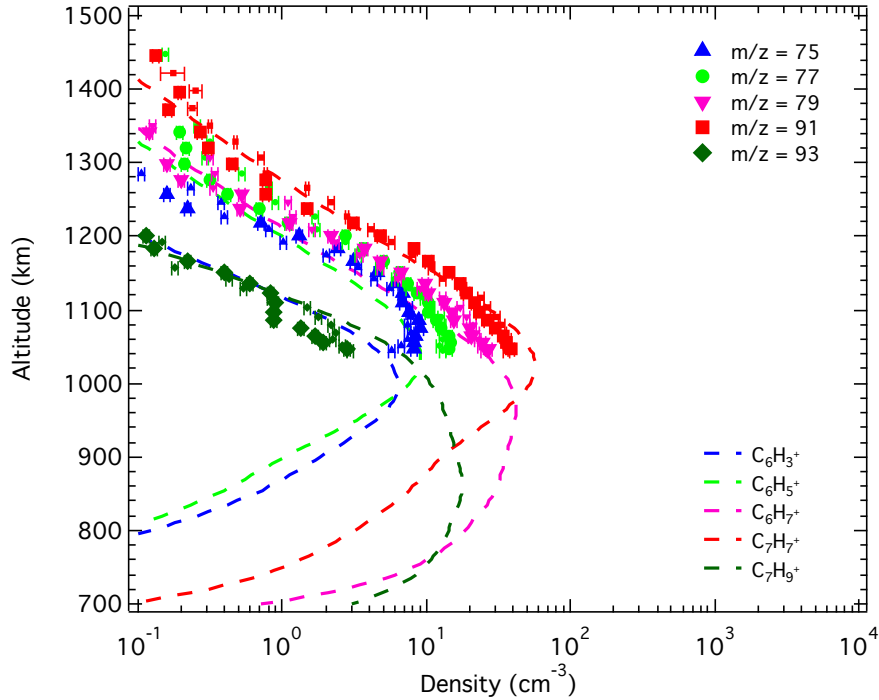


Figure 42: Model results for the density of $C_6H_3^+$, $C_6H_5^+$, $C_6H_7^+$, $C_7H_7^+$ and $C_7H_9^+$ and comparison with the T40 INMS ion density measurements at $m/z = 75, 77, 79, 91, 93$.

2850 $C_6H_3^+$, $C_6H_5^+$, $C_6H_7^+$, $C_7H_7^+$, $C_7H_9^+$. The signal at $m/z = 75$ is
 2851 attributed to $C_6H_3^+$ and is underestimated by the model by a factor of 4 (cf.
 2852 Figure 42). The production of $C_6H_3^+$ is directly related to the C_4H_2 density
 2853 through reaction ($R_{cn}481a$) and the underestimation of $C_6H_3^+$ may be inter-
 2854 preted as a consequence of the underestimation of C_4H_2 . Another possible
 2855 explanation relies on the observation that the loss processes for $C_6H_3^+$, reac-
 2856 tion with acetylene and electron recombination, both suffer from large errors.
 2857 Radiative association of $C_6H_3^+$ to C_2H_2 is reported in McEwan and Anicich
 2858 (2007) to be extremely efficient with a rate coefficient of $2.3 \times 10^{-10} \text{ cm}^3 \text{ s}^{-1}$.
 2859 However, two different structures of $C_6H_3^+$ are known to exist, one reactive
 2860 with C_2H_2 and one unreactive (Anicich et al., 2003, 2006). It is possible that
 2861 the isomer produced in reaction ($R_{cn}481a$) is mostly the unreactive one and that
 2862 the loss of $C_6H_3^+$ with acetylene is largely overestimated in the model. Also,
 2863 both rate coefficient and products of the $C_6H_3^+$ recombination with electrons
 2864 are unknown and have been estimated, and the actual reactivity may be lower.
 2865 The signals at $m/z = 77$ and 79 are attributed to $C_6H_5^+$ and $C_6H_7^+$, res-
 2866 pectively, and both channels are very well reproduced by the model and this
 2867 despite the fact that the model does not match the $C_4H_2^+$ densities (cf. Figure
 2868 42). In Vuitton et al. (2008), $C_4H_2^+$ was identified as the major precursor of

2869 $C_6H_5^+$ (through reaction (R_{cn}465c)) and had to be set to the observation values
 2870 for the model to reproduce the abundance of $C_6H_5^+$. Here, the model matches
 2871 the $C_6H_5^+$ observations, even though the $C_4H_2^+$ predictions are about one or-
 2872 der of magnitude off. This is particularly interesting because both species are
 2873 important intermediates in the production of C_6H_6 (section 3.1.1.2 and Vuitton
 2874 et al. (2008)).

2875 The signals at $m/z = 91$ and 93 are attributed to $C_7H_7^+$ and $C_7H_9^+$ and
 2876 are well reproduced by the model (cf. Figure 42).

2877 4.1.2. Negative Ions

2878 4.1.2.1. *Observations.* Although it was not designed to detect ions, CAPS-ELS
 2879 showed evidence for negatively charged ions up to $\sim 10,000$ u including three
 2880 distinct low mass peaks (Coates et al., 2007). Because of the poor energy resolu-
 2881 tion of the analyzer, the exact mass-to-charge ratio of the negative ions cannot
 2882 be retrieved and only broad mass ranges giving the approximate location of the
 2883 peaks can be determined. The mass range of the three first mass groups are
 2884 provided in Table 10. Wellbrock et al. (2013) presented, for 34 Titan encounters,
 2885 the negative ion density trend versus altitude for each mass group. They found
 2886 that the average peak altitude for the three low mass groups is about 1060 km
 2887 and that the peak density varies by about one order of magnitude from flyby
 2888 to flyby, with densities reaching up to 112, 92 and 36 cm^{-3} for mass group 1,
 2889 2 and 3, respectively. The total negative ion densities inferred from the Radio
 2890 and Plasma Wave Science (RPWS) Langmuir Probe for 47 flybys (Shebanits
 2891 et al., 2013) are in general agreement with the values retrieved by CAPS-ELS,
 2892 although a specific comparison of both datasets is still warranted.

Table 10: Negative ions mass groups.

Mass group	Mass range (u)	Negative ions
1	12-30	H^- , CH_2^- , CH_3^- , C_2H^- , CN^- , O^- , OH^-
2	30-55	C_4H^- , C_3N^-
3	55-95	C_6H^- , C_5N^-

2893 4.1.2.2. *Density Profiles.* The calculated densities of the 11 negative ion species
 2894 included in our model are given in Figure 43. The 7 ions falling into mass group
 2895 1 are shown in panel a, while the ions falling into mass groups 2 and 3 are
 2896 shown in panel b (cf. Table 10). As in Vuitton et al. (2009), CN^- is the most
 2897 prominent ion with a peak density of $\sim 1 \text{ cm}^{-3}$ at 1050 km and it contributes
 2898 almost entirely to the total density in mass group 1. H^- , CH_2^- and CH_3^- reach
 2899 peak densities of 10^{-1} (at 1345 km), 2×10^{-2} (at 1260 km) and 10^{-3} cm^{-3} (at
 2900 1165 km), respectively. This H^- density is a factor of about 200 higher than
 2901 that calculated in Vuitton et al. (2009), which is mostly explained by the much
 2902 higher CH_4 dissociative electron attachment cross-section used in the current
 2903 study (cf. section 2.7.3.3). The C_2H^- density reaches $3.6 \times 10^{-2} \text{ cm}^{-3}$ at 1270
 2904 km, which is higher by about one order of magnitude compared to Vuitton et al.

2905 (2009). Because C_2H^- originates mostly from H^- , the higher H^- density in this
2906 model compared to Vuitton et al. (2009) is directly responsible for the higher
2907 C_2H^- density. This is in line with the results of Dobrijevic et al. (2016). O^-
2908 and OH^- both reach a negligible peak density of about $7 \times 10^{-6} \text{ cm}^{-3}$ close to
2909 1200 km.

2910 Both C_4H^- and C_3N^- contribute to the density in mass group 2, with C_4H^-
2911 dominating above 1140 km and C_3N^- below, with peak densities of 5.7×10^{-2}
2912 cm^{-3} (at 1165 km) and $1.1 \times 10^{-1} \text{ cm}^{-3}$ (at 1050 km), respectively. For mass
2913 group 3, C_6H^- and C_5N^- are almost equally abundant below 1040 km but
2914 C_5N^- dominates in the upper ionosphere. Their peak density is 7.3×10^{-2}
2915 cm^{-3} (at 1065 km) and $2.7 \times 10^{-1} \text{ cm}^{-3}$ (at 1145 km), respectively. This is
2916 somewhat different from Vuitton et al. (2009), where the nitrile ions (C_3N^- ,
2917 C_5N^-) dominated over the hydrocarbon ions (C_4H^- , C_6H^-). Indeed, the C_6H^-
2918 densities are higher by about one order of magnitude in this model compared
2919 to Vuitton et al. (2009). It is the higher C_6H density in this model compared
2920 to Vuitton et al. (2009) that translates into a higher density for this ion. In
2921 Vuitton et al. (2009), the abundances of the neutral species originated from the
2922 Lavvas et al. (2008b) model scaled to match the INMS observations, while they
2923 are now calculated self-consistently. Desai et al. (2017) recently reported that
2924 the third peak appears compatible with C_5N^-/C_6H^- at higher altitudes but
2925 that at lower altitudes this peak widens, extending as high as ~ 94 u in some
2926 instances. This indicates the presence of anionic structures other than linear
2927 chains and Desai et al. (2017) suggest a number of possible anions in this range.

2928 The negative ion production is initiated by dissociative and radiative electron
2929 attachment, which depend on the energetic and thermal electron distributions,
2930 respectively. These distributions heavily depend on solar illumination conditions
2931 (Ågren et al., 2009), which probably explains at least some of the variability in
2932 density and altitude of the peaks observed in the CAPS-ELS data (cf. Figure 2
2933 of Wellbrock et al. (2013)). Our model is meant to reproduce globally averaged
2934 conditions and the calculated negative ion profiles should not be too far from
2935 the average altitudes and densities that can be retrieved from the observations.
2936 Indeed, the altitude of the calculated density peak for the three mass groups
2937 (cf. right panel in Figure 43) is in fair agreement with the CAPS-ELS data.
2938 However, as already observed at 1015 km for the T40 encounter, our calculated
2939 ion densities fall short by one to two orders of magnitude compared to the
2940 observations, a conclusion also shared by Dobrijevic et al. (2016).

2941 A first possibility is that we are missing a source of light negative ions in
2942 our models. It seems quite difficult to believe that our bottom-up approach to
2943 generate negative ions could be enhanced by such a large factor. However, it
2944 may be possible that once formed, heavy ions fragment back to light ions in
2945 a top-down process. Pirim et al. (2015) reported H^- desorption during low-
2946 energy (3-15 eV) electron irradiation of tholin materials maintained at 130 K.
2947 Another explanation is related to the fact that the efficiency of the CAPS-ELS
2948 microchannel plates was never tested using negative ions. A value of 5% was
2949 used based upon the extensive work by Fraser (2002) for species detected at >1
2950 keV. Studies have however shown that at energies of <1 keV this can be up to

2951 an order or magnitude larger for negative ions (Peko and Stephen, 2000), and
 2952 calibration studies should be performed to confirm the densities published so far.
 2953 Although the total ion densities inferred from RPWS-LP (Shebanits et al.,
 2954 2013) support those provided by CAPS-ELS, heavy ions dominate over light
 2955 ions at the ionospheric peak, which implies that the RPWS-LP dataset does
 2956 not provide any constrain for the light ions.

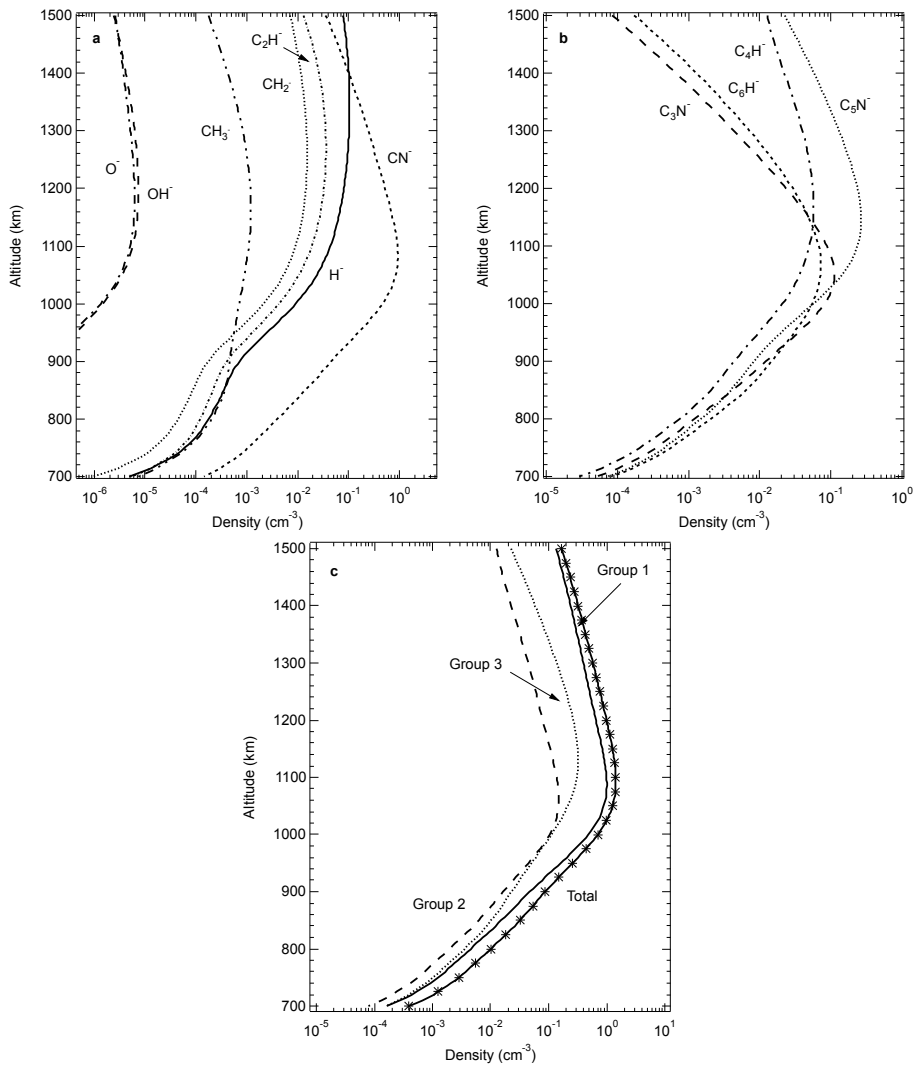


Figure 43: Calculated negative ion densities (upper left panel) H^- , CH_2^- , CH_3^- , O^- , OH^- , (upper right panel) C_2H^- , C_4H^- , C_6H^- , CN^- , C_3N^- , C_5N^- and (lower panel) sum of the ions constituting the three mass groups as defined in Table 10.

2957 *4.2. Neutral Atmosphere*

2958 *4.2.1. Previous Models*

2959 Four other teams have been working on the understanding of Titan’s neu-
2960 tral atmospheric chemistry through photochemical models: Krasnopolsky (2009,
2961 2010, 2012, 2014) constructed a model where the neutral and ion chemistry are
2962 fully coupled; the Bordeaux team (Hébrard et al., 2012, 2013; Dobrijevic et al.,
2963 2014; Loison et al., 2015; Dobrijevic et al., 2016) exhibited a model whose main
2964 specificity is its capacity to study the propagation of uncertainties; Lara (Moreno
2965 et al., 2012; Lara et al., 2014) updated an older neutral model first described
2966 in Lara et al. (1994) in support of the Herschel observations; the Caltech group
2967 revived the pioneering work of Yung et al. (1984) to study hydrocarbon and
2968 nitrogen (including isotopologues) chemistry (Liang et al., 2007; Li et al., 2014,
2969 2015; Willacy et al., 2016).

2970 Although Krasnopolsky (2009, 2010, 2014) and Dobrijevic et al. (2016) dis-
2971 cuss the chemistry as a whole, some of these models focus on a specific topic
2972 or class of molecules. For example, Hébrard et al. (2012) discuss the neutral
2973 production of hydrogen isocyanide (HNC) and hydrogen cyanide (HCN), while
2974 Loison et al. (2015) and Willacy et al. (2016) are mostly interested in N-bearing
2975 species. Hébrard et al. (2013) put the emphasis on C_3H_p hydrocarbons and
2976 Krasnopolsky (2012), Moreno et al. (2012), Dobrijevic et al. (2014) and Lara
2977 et al. (2014) on O-bearing species, especially H_2O .

2978 In general, these models take into account the same physical and chemical
2979 processes (dissociation of N_2 and CH_4 by photons and charged particles followed
2980 by a complex chemistry, transport by eddy mixing and molecular diffusion,
2981 condensation close to the tropopause, etc.) and only differ on the quantitative
2982 treatment of these processes, such as different rate coefficients, eddy mixing
2983 coefficients, saturation vapor pressure expressions, etc. Because of the large
2984 number of degrees of freedom, it is often extremely difficult to track down why
2985 the model outputs differ sometimes significantly from each other. Nevertheless,
2986 we will in the next section compare the results obtained by the different models
2987 and discuss these differences, when possible.

2988 *4.2.2. Observations*

2989 The abundant measurements from Cassini-Huygens and Earth-based efforts
2990 over the past 13 years have substantially increased the amount of information
2991 that we have about the composition of Titan’s atmosphere and its spatial and
2992 temporal variations. The completeness in observational coverage (both spa-
2993 tially and temporally) varies substantially by molecule. Rather than compare
2994 our model calculations to every observation, we have compiled a set of repre-
2995 sentative observations with a preference for measurements that provide altitude
2996 profiles from Cassini-Huygens when possible. There appears to be little, if any,
2997 inter-annual variability detected when comparing Voyager and Cassini observa-
2998 tions (Coustenis et al., 2013, 2016). For molecules where observations appear
2999 to disagree, as is the case for H_2O , we include them all. We also note that
3000 some measurements were published as a function of altitude, while others were

3001 published as a function of pressure. Although pressure (or number density) is
3002 the more relevant parameter, it was easier to provide a consistent comparison
3003 between observations using altitude. Representative values and references are
3004 listed in Table 11, which focuses on the equatorial and mid-latitudes as the
3005 observations allow. We include upper limit measurements, shown in Table 12,
3006 only when detections at a similar altitude have not been published and avoid
3007 disk-integrated measurements unless they are the only measurements available.

3008 At the surface and for most of the troposphere, composition measurements
3009 are limited exclusively to the Gas Chromatograph/Mass Spectrometer (GCMS)
3010 (Niemann et al., 2005, 2010). In the stratosphere and the mesosphere, observa-
3011 tions come from a combination of spacecraft measurements (Voyager, Cassini)
3012 and Earth-based observations (e.g., Infrared Space Observatory (ISO), Ata-
3013 cama Large Millimeter Array (ALMA), Institut de radioastronomie millimétrique
3014 (IRAM), Herschel). For Voyager, the measurements were obtained by the
3015 Infrared Interferometer Spectrometer (IRIS), which covered the upper tropo-
3016 sphere/stratosphere. Cassini remote sensing composition measurements cover
3017 the upper troposphere (Cassini Composite Infrared Spectrometer CIRS), strato-
3018 sphere (CIRS and Visible Infrared Mapping Spectrometer (VIMS)), and meso-
3019 sphere (VIMS and Ultraviolet Imaging Spectrograph UVIS) (cf. Figure 1 in
3020 Hörst (2017)). It is important to note that the altitude ranges covered by these
3021 instruments are not well-defined as the ability to observe molecules depends
3022 on their abundances, so observations of trace species are sometimes possible
3023 only for smaller altitude ranges (or limited to specific latitudes). The neutral
3024 ionospheric composition is provided by measurements from the closed source
3025 neutral mode (CSN) of the Ion and Neutral Mass Spectrometer (INMS) carried
3026 by Cassini. The CSN INMS measurements we use for comparison come from
3027 averaging a number of flybys to increase signal to noise; these measurements
3028 provide altitude profiles but average out any latitude variations.

3029 Due to the length of the mission, Cassini CIRS has provided substantial
3030 information about variations with latitude/season for a number of molecules.
3031 The model presented here is 1-D and therefore does not capture these types of
3032 variations. The strength of seasonal variations in Titan’s atmospheric composi-
3033 tion depends on the chemical lifetime of the species (c.f. Lavvas et al. (2008a)
3034 and section 5.4). Long-lived species (e.g., C_2H_2 , C_2H_6 , C_3H_8 , CO_2) exhibit
3035 very little seasonal (latitudinal) variation compared to short-lived species (e.g.,
3036 C_2H_4 , C_3H_4 , C_4H_2 , C_6H_6 , HC_3N). In assessing the performance of the model,
3037 we compare the model to the equatorial and mid-latitude observations where
3038 little to no seasonal variation is observed. However, as possible, we include ob-
3039 servations for a variety of latitudes to provide a sense of the variations that are
3040 observed for a given molecule when plotting the model output profiles compared
3041 to observations. For a small number of molecules (e.g., C_6H_6), the abundance
3042 is only sufficiently high to be detected by Cassini CIRS limb observations at the
3043 winter high latitudes where the stratosphere is enriched by downwelling from
3044 the descending branch of the global circulation. We do not expect to reproduce
3045 these observations, as we do not capture this type of dynamical behavior, but
3046 include the observations for completeness.

Table 11: Composition of Titan's neutral atmosphere

Formula	Stratosphere			Mesosphere	Thermosphere
	Ground Based ^(a)	ISO ^(g) /Herschel	CIRS ^(m)	UVIS ^(s)	INMS (CSN) ^(u)
H ₂			9.6±2.4×10 ⁻⁴⁽ⁿ⁾		3.9±0.01×10 ⁻³
⁴⁰ Ar					1.1±0.03×10 ⁻⁵
C ₂ H ₂		5.5±0.5×10 ⁻⁶	2.97×10 ⁻⁶	5.9±0.6×10 ⁻⁵	3.1±1.1×10 ⁻⁴
C ₂ H ₄		1.2±0.3×10 ⁻⁷	1.2×10 ⁻⁷	1.6±0.7×10 ⁻⁶	3.1±1.1×10 ⁻⁴
C ₂ H ₆		2.0±0.8×10 ⁻⁵	7.3×10 ⁻⁶		7.3±2.6×10 ⁻⁵
CH ₃ C ₂ H		1.2±0.4×10 ⁻⁸	4.8×10 ⁻⁹		1.4±0.9×10 ⁻⁴
C ₃ H ₆			2.6±1.6×10 ^{-9(o)}		2.3±0.2×10 ^{-6(v)}
C ₃ H ₈	6.2±1.2×10 ^{-7(b)}	2.0±1.0×10 ⁻⁷	4.5×10 ⁻⁷		<4.8×10 ⁻⁵
C ₄ H ₂		2.0±0.5×10 ⁻⁹	1.12×10 ⁻⁹	7.6±0.9×10 ⁻⁷	6.4±2.7×10 ⁻⁵
C ₆ H ₆		4.0±3.0×10 ⁻¹⁰	2.2×10 ⁻¹⁰	2.3±0.3×10 ⁻⁷	8.95±0.44×10 ⁻⁷
HCN	5×10 ⁻⁷	3.0±0.5×10 ⁻⁷	6.7×10 ⁻⁸	1.6±0.7×10 ⁻⁵	
HNC	4.9±0.3×10 ^{-9(c)}	4.5±1.2×10 ^{-9(h)}			
HC ₃ N	3×10 ⁻¹¹	5.0±3.5×10 ⁻¹⁰	2.8×10 ⁻¹⁰	2.4±0.3×10 ⁻⁶	3.2±0.7×10 ⁻⁵
CH ₃ CN	8×10 ⁻⁹		<1.1×10 ^{-7(p)}		3.1±0.7×10 ⁻⁵
C ₂ H ₃ CN	3.6×10 ^{-10(d)}				<1.8×10 ⁻⁵
C ₂ H ₅ CN	2.8×10 ^{-10(e)}				
C ₂ N ₂			9×10 ^{-10(q)}		4.8±0.8×10 ⁻⁵
NH ₃		<1.9×10 ⁻¹⁰⁽ⁱ⁾	<1.3×10 ^{-9(p)}		2.99±0.22×10 ⁻⁵
CO	5.1±0.4×10 ^{-5(f)}	4.0±5×10 ^{-5(j)}	4.7±0.8×10 ^{-5(r)}	5.4±3.2×10 ^{-5(t)}	
H ₂ O		8×10 ^{-9(k)} /7×10 ^{-10(l)}	4.5±1.5×10 ^{-10(r)}		<3.42×10 ⁻⁶
CO ₂		2.0±0.2×10 ⁻⁸	1.1×10 ⁻⁸		<8.49×10 ⁻⁷

Continued on next page

3048 (at 200 km) ^(b)Roe et al. (2003) ^(c)Cordiner et al. (2014) (constant profile at 400 km) ^(d)Palmer et al. (2017) (at 297 km, using
3049 fractional scale height model) ^(e)Cordiner et al. (2015b) (gradient profile at 200 km) ^(f)Gurwell (2004) ^(g)Coustenis et al. (2003)
3050 ^(h)Moreno et al. (2011) (constant profile at 400 km) ⁽ⁱ⁾Teanby et al. (2013) (3- σ upper limit, peak sensitivity at 75 km) ^(j)Courtin
3051 et al. (2011) ^(k)Coustenis et al. (1998) (at 400 km) ^(l)Moreno et al. (2012) (from the S_a profile at 400 km) ^(m)Coustenis et al. (2010)
3052 (at 5°S; HCN, C₆H₆, C₃H₈, C₄H₂, and HC₃N exhibit latitudinal variations (Coustenis et al., 2007)), values averaged over TB-T44
3053 assuming constant vertical profiles, for vertical variations see Vinatier et al. (2010)) ⁽ⁿ⁾Courtin et al. (2007) ^(o)Nixon et al. (2010)
3054 (3- σ upper limits at 25°S) ^(p)Teanby et al. (2006) (3- σ upper limit at 50°N) ^(q)Nixon et al. (2013) (at 225 km) ^(r)Cottini et al. (2012)
3055 (using constant VMR at 230 km) ^(s)Koskinen et al. (2011) (at ~600 km) ^(t)Fabiano et al. (2017) VIMS (at 450 km) ^(u)Cui et al.
3056 (2009b) (at 1077 km) from T5, 16, 18, 19, 21, 23, 25-30, 32, 36, 37 using INMS CSN mode, *italics* indicates corrected values, signals
3057 from C₂H₂ and C₂H₄ are difficult to separate so the reported value is for both species combined) ^(v)Magee et al. (2009) (global
3058 average at 1050 km).

Table 12: Upper limits on the composition of Titan’s neutral atmosphere

Formula	Stratosphere		Thermosphere INMS (CSN) ^(g)
	Voyager	ISO/Ground Based	
CH ₂ CCH ₂		<2×10 ^{-9(d)}	<9×10 ^{-10(f)}
C ₄ H ₆			<9.5×10 ⁻⁶
C ₆ H ₂	<6.0×10 ^{-10(a)}		
C ₇ H ₈			<1.32×10 ⁻⁷
C ₄ H ₃ N	<2.5×10 ^{-7(b)}		
C ₄ H ₅ N	<4.0×10 ^{-8(b)}		<3.0×10 ⁻⁷
C ₄ N ₂	<5.3×10 ^{-10(c)}		
HC ₅ N		<4×10 ^{-10(e)}	
H ₂ CO			<1.6×10 ^{-8(f)}

All values come from the work referenced in the table header unless otherwise noted in the table. ^(a)Delpech et al. (1994) ^(b)Cerceau et al. (1985) ^(c)Jolly et al. (2015) ^(d)Coustenis et al. (2003) ^(e)Marten et al. (2002) (at 200 km) ^(f)Nixon et al. (2010) (3- σ upper limits) ^(g)Cui et al. (2009b) (at 1077 km from T5, 16,18, 19, 21, 23, 25-30, 32, 36, 37 using INMS Closed Source Neutral mode).

3059 4.2.3. Density Profiles

3060 4.2.3.1. Hydrocarbons.

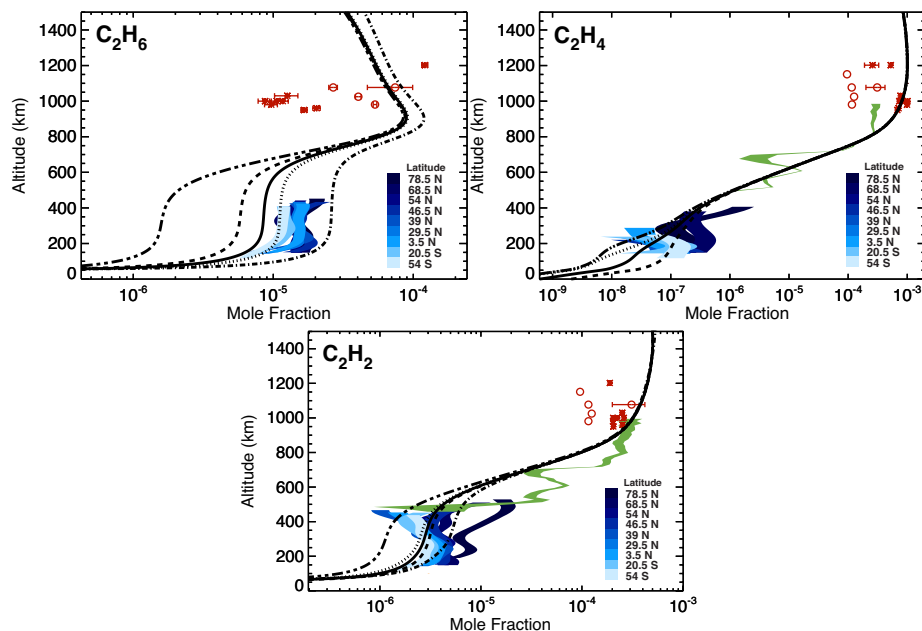


Figure 44: Calculated and observed mole fractions of C_2H_6 (upper left panel), C_2H_4 (upper right panel) and C_2H_2 (lower panel). Solid line: nominal; dash-dot and long dash - double short dash line: eddy mixing coefficient $K_0 = 10^2$ and 10^3 cm^{-2} , respectively, section 2.4; dotted and dashed lines: aerosol optical depth multiplied by 0.5 and 2, respectively, section 5.3.1; long dash-dot-dot line: no H heterogeneous loss, section 5.3.2. The data shown is from CIRS (Vinatier et al., 2010); UVIS (Koskinen et al., 2011); INMS (Cui et al., 2009b) (circles no error bars are uncorrected, circle with error bar is corrected) C_2H_2 joint with C_2H_4 , (Waite et al., 2007) asterisks.

3061 **Acetylene (C_2H_2), Ethylene (C_2H_4), Ethane (C_2H_6).** The model
 3062 profile of ethane resulting from the chemistry described in section 3.2.1, is presented
 3063 in the upper left panel of Figure 44. The C_2H_6 abundance at 1000-1100
 3064 km in the model falls in between the uncorrected and corrected mole fractions
 3065 retrieved from the INMS observations ($2 - 7 \times 10^{-5}$). CIRS limb observations
 3066 favor a constant ethane mole fraction of ~ 15 ppm from 150 to 400 km (cf.
 3067 Vinatier et al. (2010)) and the difference between these data and the model is
 3068 a factor of about 2.

3069 All the models (Lavvas et al., 2008b; Krasnopolsky, 2014; Li et al., 2015;
 3070 Dobrijevic et al., 2016) are in fairly good agreement with each other and with the
 3071 observations, despite using quite different rate coefficients for the recombination
 3072 of CH_3 radicals above 800 km (cf. Figure A.3c). We note that Dobrijevic et al.
 3073 (2016) mention that for INMS data they applied a correction factor of 2.2 ± 0.5
 3074 to the mixing ratios (cf. their Figure 7 for C_2H_6 but this applies to all their
 3075 figures). However, this correction applies to the absolute density of all molecules
 3076 and therefore cancels out for mixing ratios (Teolis et al., 2015).

3077 Ethylene and acetylene are amongst the best constrained species with the
 3078 combination of INMS, UVIS and CIRS observations providing an almost unin-

3079 interrupted profile from the thermosphere down to the troposphere (Cui et al.,
3080 2009b; Magee et al., 2009; Koskinen et al., 2011; Vinatier et al., 2010). The
3081 Krasnopolsky (2014) (their Figure 2) and Lavvas et al. (2008b) (their Figure
3082 4a) profiles agree with the INMS data but underestimate the C_2H_4 abundance
3083 by about one order of magnitude at 200 km, as do all previous photochemical
3084 models. In order to match the observations, Li et al. (2014) suggest a new ex-
3085 pression for the rate coefficient of the key reaction, $H + C_2H_4 + M \rightarrow C_2H_5 + M$.
3086 The new reaction rate coefficient is estimated to be ~ 10 times lower than that
3087 used by Moses et al. (2005) for giant planets (and by other Titan models), see
3088 Figure A.1b. Instead, our calculations yield a rate coefficient about one order
3089 of magnitude larger in the stratosphere (Vuitton et al., 2012). Nevertheless, the
3090 model simulation for C_2H_4 is in general agreement with the INMS and UVIS
3091 observations and provides values in good agreement with the CIRS retrieved
3092 mole fractions (cf. upper right panel of Figure 44). A possible explanation for
3093 the difference with our profile is the important production of ethylene below 400
3094 km via the photodissociation of butadiene in our model.

3095 Although our model as well as Dobrijevic et al. (2016) (their Figure 8) re-
3096 produce the observed C_2H_4 abundance, they do not capture the negative verti-
3097 cal gradient observed by CIRS at mid-latitudes. This peculiar behavior has
3098 been explained by the fact that ethylene does not condense, allowing the return
3099 branch of the global circulation cell to bring air enriched in C_2H_4 from the win-
3100 ter pole towards the equator, a circulation pattern that cannot be modeled with
3101 1-dimensional models (Crespin et al., 2008).

3102 Acetylene's vertical profile is presented in the lower panel of Figure 44. The
3103 observed acetylene mole fraction is near 3×10^{-4} at 1000 km and gradually
3104 decreases until reaching a constant value of 5×10^{-6} below 500 km. Hébrard
3105 et al. (2013) and Li et al. (2015) predict the right stratospheric abundance of
3106 C_2H_2 within a factor of about 2, while the profile of Krasnopolsky (2014) is too
3107 high by one order of magnitude at 600 km, probably because of his choice of
3108 eddy mixing coefficient. Other calculated C_2H_2 profiles (cf. Figure 4b in Lavvas
3109 et al. (2008b) and Figures 7 in Loison et al. (2015) and Dobrijevic et al. (2016)),
3110 including ours, agree very well with the INMS, UVIS and CIRS mid-latitude
3111 results.

3112 **Methylacetylene (CH_3CCH), Allene (CH_2CCH_2), Propylene (C_3H_6),**
3113 **Propane (C_3H_8).** The mole fractions of CH_3CCH , CH_2CCH_2 , C_3H_6 and
3114 C_3H_8 obtained with the current model are shown in Figure 45.

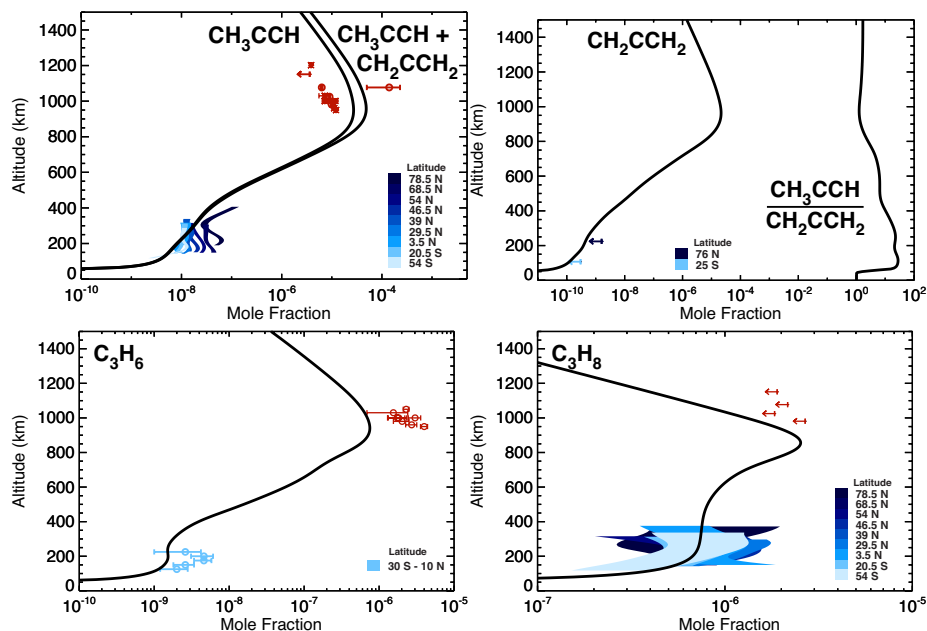


Figure 45: Calculated and observed mole fractions of CH_3CCH and CH_2CCH_2 (top panels), C_3H_6 (lower left panel), and C_3H_8 (lower right panel). The sum and ratio of CH_3CCH and CH_2CCH_2 are shown on panels (a) and (b), respectively. The data shown for CH_3CCH is from Vinatier et al. (2010), Cui et al. (2009b) (circles) and Waite et al. (2007) (asterisks), for CH_2CCH_2 from Nixon et al. (2010), for C_3H_6 from Nixon et al. (2013) (CIRS) and Waite et al. (2007) (circles) and for C_3H_8 from Vinatier et al. (2010) and Cui et al. (2009b).

3115 Methylacetylene (CH_3CCH) and its isomer allene (CH_2CCH_2) are presented
 3116 in the upper left panel of Figure 45. Because CIRS observations show evidence
 3117 for CH_3CCH (mole fraction of $\sim 10^{-8}$, Vinatier et al. (2010)) and not for
 3118 CH_2CCH_2 (upper limit of 3×10^{-10} at 107 km, Nixon et al. (2010)) and be-
 3119 cause CH_3CCH is more stable than CH_2CCH_2 , Cui et al. (2009b) only consider
 3120 CH_3CCH in their analysis of the INMS spectra. They provide uncorrected and
 3121 corrected mole fractions of $(6.31 \pm 0.24) \times 10^{-6}$ and $(1.4 \pm 0.9) \times 10^{-4}$ at 1077 km,
 3122 respectively (Cui et al., 2009b). However, they mention that strictly speaking,
 3123 the derived abundances of CH_3CCH should refer to the sum of CH_3CCH and
 3124 CH_2CCH_2 due to the similarity of their cracking patterns for mass channels 39
 3125 and 40 from which the CH_3CCH abundance is constrained.

3126 The current model indicates that in the upper atmosphere CH_3CCH and
 3127 CH_2CCH_2 have similar abundances, with mole fractions at 1075 km of 1.5×10^{-5}
 3128 and 1.8×10^{-5} for CH_3CCH and CH_2CCH_2 , respectively. Contrary to the
 3129 assumption made by Cui et al. (2009b), it therefore seems that both species
 3130 contribute to the INMS signal, a conclusion already reached by Lavvas et al.
 3131 (2008b). We plot the sum of the mole fractions of CH_3CCH and CH_2CCH_2
 3132 in the upper right panel of Figure 45. The combined contribution at 1075 km
 3133 (3.3×10^{-5}) falls in between the uncorrected and corrected mole fractions from

3134 INMS. In the lower atmosphere, the CH_3CCH model profile reproduces well
 3135 the CIRS mid-latitude abundance (Vinatier et al., 2010), while the modeled
 3136 CH_2CCH_2 mole fraction at 225 and 105 km is just in agreement with the CIRS
 3137 3σ upper limits (Nixon et al., 2010). These results are in line with previous
 3138 models, which with the exception of Lavvas et al. (2008b) in the stratosphere
 3139 (their Figure 5a), provide a good fit to both INMS and CIRS data (cf. Figure 3
 3140 in Krasnopolsky (2014), Figure 2 in Li et al. (2015) and Figure 8 in Dobrijevic
 3141 et al. (2016)).

3142 C_3H_6 has been tentatively detected in Titan's thermosphere by INMS with
 3143 a mole fraction of about 3×10^{-6} (Magee et al., 2009) and for the first time
 3144 in the stratosphere by CIRS with a mole fraction peaking at 5×10^{-9} at 200
 3145 km (Nixon et al., 2013). The profile of propylene from our model along with
 3146 the INMS and CIRS detections are shown in the lower left panel of Figure 45,
 3147 and the agreement of the prediction with the observations is within a factor
 3148 of two. Other models also reasonably match the C_3H_6 abundance in both the
 3149 thermosphere and stratosphere (cf. Figure 4 in Krasnopolsky (2014), Figures
 3150 2,3 and discussion in Li et al. (2015) and Figure 7 in Dobrijevic et al. (2016)).

3151 The modeled mole fraction of C_3H_8 around 1000 km is consistent with upper
 3152 limits from INMS ($< 5 \times 10^{-5}$). The CIRS stratospheric mole fraction is more
 3153 or less constant from 100 to 300 km with a value of 8×10^{-7} . Our model
 3154 reproduces a similar constant profile with a value of $\sim 5 \times 10^{-7}$ (cf. lower right
 3155 panel of Figure 45). While Lavvas et al. (cf. Figure 5b in Lavvas et al. (2008b))
 3156 overestimates the propane mole fraction in the stratosphere, Krasnopolsky (cf.
 3157 Figure 3 in Krasnopolsky (2014)), Yung et al. (cf. Figure 2 in Li et al. (2015))
 3158 and Dobrijevic et al. (cf. Figure 7 in Loison et al. (2015) and Figure 8 in
 3159 Dobrijevic et al. (2016)) obtain an almost perfect match with the observations.

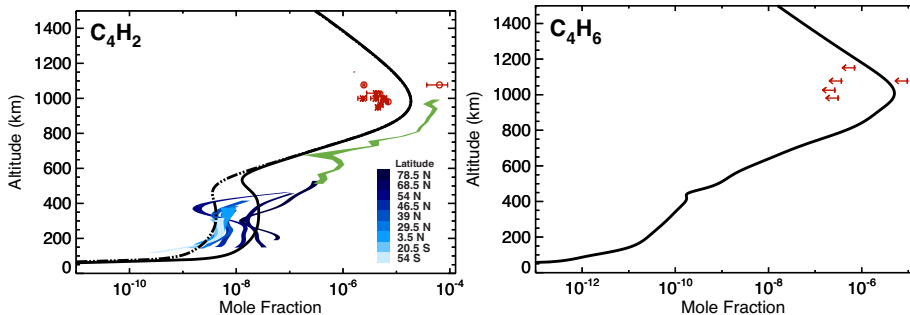


Figure 46: Calculated and observed mole fractions of C_4H_2 (left panel) and C_4H_6 (right panel). Solid line: nominal; long dash-dot-dot line: no H heterogeneous loss, section 5.3.2. The data shown for C_4H_2 is from CIRS (Vinatier et al., 2010); UVIS (Koskinen et al., 2011); INMS (Cui et al., 2009b) (circles no error bars are uncorrected, circle with error bar is corrected), (Waite et al., 2007) asterisks. The upper limits for C_4H_6 are from INMS (Cui et al., 2009b).

3160 **Diacetylene (C_4H_2), Butadiene (C_4H_6).** The calculated vertical profile
 3161 of diacetylene is compared to the INMS, UVIS and CIRS observations in
 3162 the left panel of Figure 46. The observed mole fractions are close to 6×10^{-5} at
 3163 1050 km (corrected INMS value from Cui et al. (2009b) that merges nicely with
 3164 the UVIS data at lower altitude) and decrease gradually to 3×10^{-9} at 200 km,
 3165 where they exhibit some strong latitudinal variations. Photochemical models
 3166 have never been fully successful at reproducing the diacetylene observations.
 3167 The Lavvas et al. (2008b) vertical profile (their Figure 5c) underestimates the
 3168 INMS observations by more than one order of magnitude, the Krasnopolsky
 3169 (2014) profile (his Figure 2) has a significantly different altitude variation than
 3170 the UVIS retrieved profile, while the Hébrard et al. (2013) profile (their Figure
 3171 1) underestimates the CIRS observations by a factor 10 or more. Only the Do-
 3172 brijevic et al. (2016) profile is in good agreement with the stratospheric data. It
 3173 is unclear to us what improvement lead to such a different profile from Hébrard
 3174 et al. (2013) to Dobrijevic et al. (2016). The reactions related to the production
 3175 and loss of C_4H_2 (according to our model) are mostly the same in both versions
 3176 of the Dobrijevic et al. model and a change in the chemistry cannot explain
 3177 the difference (unless some unexpected reaction controls the C_4H_2 abundance
 3178 in these models). Our calculated vertical profile of diacetylene falls short from
 3179 the INMS corrected values and the UVIS profile (Koskinen et al., 2011) by a
 3180 factor of a few and overestimates the mid-latitude CIRS data (Vinatier et al.,
 3181 2010) by a factor of about 5.

3182 C_4H_6 has neither been detected on Titan or described in previous photo-
 3183 chemical models, with the exception of the mole fraction profiles given in Figure
 3184 19 of Dobrijevic et al. (2016). Our model profile (cf. right panel of Figure 46)
 3185 agrees with the INMS upper limit of 10^{-5} (Cui et al., 2009b).

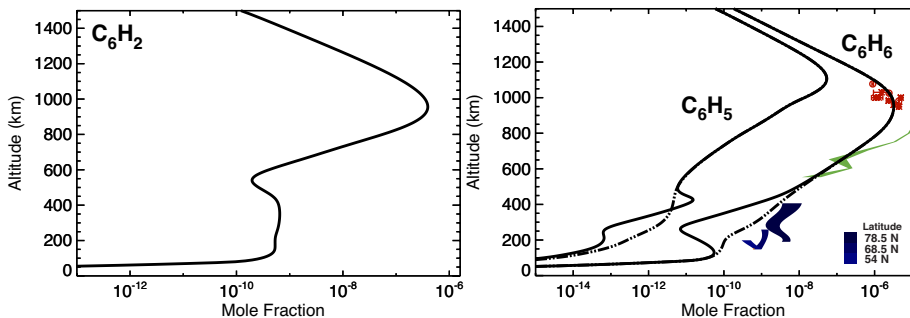


Figure 47: Calculated and observed mole fractions of C_6H_2 (left panel), and C_6H_6 and C_6H_5 (right panel). Solid line: nominal; long dash-dot-dot line: no H heterogeneous loss, section 5.3.2. The data shown for C_6H_6 is from CIRS (Vinatier et al., 2010); UVIS (Koskinen et al., 2011); INMS (Cui et al., 2009b) (circles no error bars are uncorrected, circle with error bar is corrected), (Waite et al., 2007) asterisks.

3186 **Triacetylene (C_6H_2), Benzene (C_6H_6).** Presented in the left panel of
 3187 Figure 47, is the vertical profile of triacetylene, which exhibits a sharp peak at

3188 950 km (mole fraction of 4×10^{-7}) and a broader one around 250 km (mole
3189 fraction of 6×10^{-10}). There are no observations available to constrain its
3190 altitude variation. In previous photochemical models, Lavvas et al. (2008b)
3191 has provided a vertical profile similar to ours, while Krasnopolsky (2012)'s high
3192 altitude peak is quite different with a mole fraction of $\sim 10^{-5}$.

3193 In Vuitton et al. (2008), we reported that the C_6H_6 signal measured by INMS
3194 (at $m/z=78$ and 77) exhibits a peculiar time dependence, peaking ~ 20 s after
3195 closest approach. We explained this behavior by recombination of C_6H_5 radicals
3196 with H atoms on the walls of the instrument and argued that the measured signal
3197 was a combination of (i) C_6H_6 from the atmosphere and (ii) C_6H_6 formed within
3198 the instrument. This interpretation was backed-up by our photochemical model,
3199 which predicted that C_6H_5 radicals were ~ 3 times as abundant as benzene.

3200 Unlike in our 2008 paper, our newest modeling results indicate that the
3201 abundance of phenyl radicals (C_6H_5) is small compared to that of benzene
3202 (cf. right panel of Figure 47). This is explained by the inclusion of radiative
3203 association in our chemical scheme (Vuitton et al., 2012). C_6H_5 does not react
3204 with closed-shell molecules and its main loss is addition to the most abundant
3205 radicals, such as H (R_n30) and CH_3 (R_n105). In 2008, we only considered three-
3206 body association reactions, (R_n30) and (R_n105) were inefficient in the upper
3207 atmosphere, leading to rather long chemical lifetime and therefore high density
3208 for C_6H_5 . Consideration of radiative association enhances the rate coefficient of
3209 reaction (R_n30) by seven orders of magnitude at 1000 km, resulting in the fast
3210 recycling of C_6H_5 into C_6H_6 even at high altitude, and as a consequence small
3211 C_6H_5 densities.

3212 Further analysis of the INMS data revealed that the C_6H_6 time behavior is
3213 actually observed for most species and that it is difficult to disentangle hetero-
3214 geneous surface chemistry of radicals from adsorption/desorption of the parent
3215 molecule (Cui et al., 2009b). The low radical abundance obtained with our
3216 improved chemical network tends to point towards the latter explanation. This
3217 implies that the densities inferred by our previous analyses of the INMS data
3218 should be attributed to C_6H_6 only and that the associated error bars are large.
3219 The UVIS mole fraction at 900 km is close to 10^{-5} , which is a factor of about two
3220 higher than the values retrieved from the INMS data at 950-1000 km (Koskinen
3221 et al., 2011). In the stratosphere, both CIRS limb and nadir data present some
3222 evidence for strong latitudinal variations, with mole fractions at mid-latitudes
3223 of about 2×10^{-10} at 150 km (Coustenis et al., 2010; Vinatier et al., 2010).

3224 Within this paradigm, the predicted C_6H_6 profile is in good agreement with
3225 the INMS data in the 950-1050 km altitude range and also with the UVIS data
3226 in the 550-900 km range. The benzene abundance in the Lavvas et al. (2008b)
3227 and Hébrard et al. (2013) models is significantly smaller than the INMS derived
3228 one, which is expected since C_6H_6 formation in the upper atmosphere is related
3229 to ion chemistry, which is not taken into account in these models.

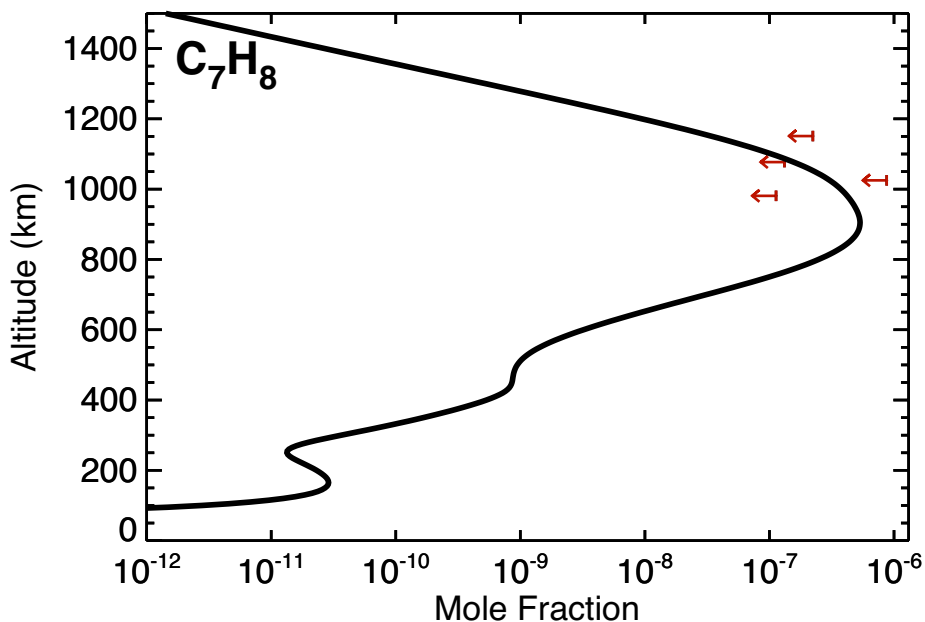


Figure 48: Calculated and observed mole fractions of C_7H_8 . The upper limits shown are from INMS (Cui et al., 2009b).

3230 **Toluene (C_7H_8).** We described explicitly chemical reactions and photol-
 3231 ysis of C_7H_8 in Vuitton et al. (2008) but no other photochemical model has
 3232 presented results for this molecule to date. C_7H_8 is not detected on Titan. Al-
 3233 though peaks at channels 91-92 in some of the INMS outbound spectra have
 3234 been attributed to C_7H_8 molecules, such a feature can be reasonably explained
 3235 by the wall effects in the INMS antechamber (Vuitton et al., 2008). C_7H_8 is not
 3236 detected at 3σ significance level in any individual inbound spectrum (Cui et al.,
 3237 2009b). Our current profile in the upper atmosphere is similar to that shown in
 3238 our previous paper with a peak mole fraction of 5×10^{-7} at 900 km (cf. Figure
 3239 48), which is in the ball park of the INMS upper limits.

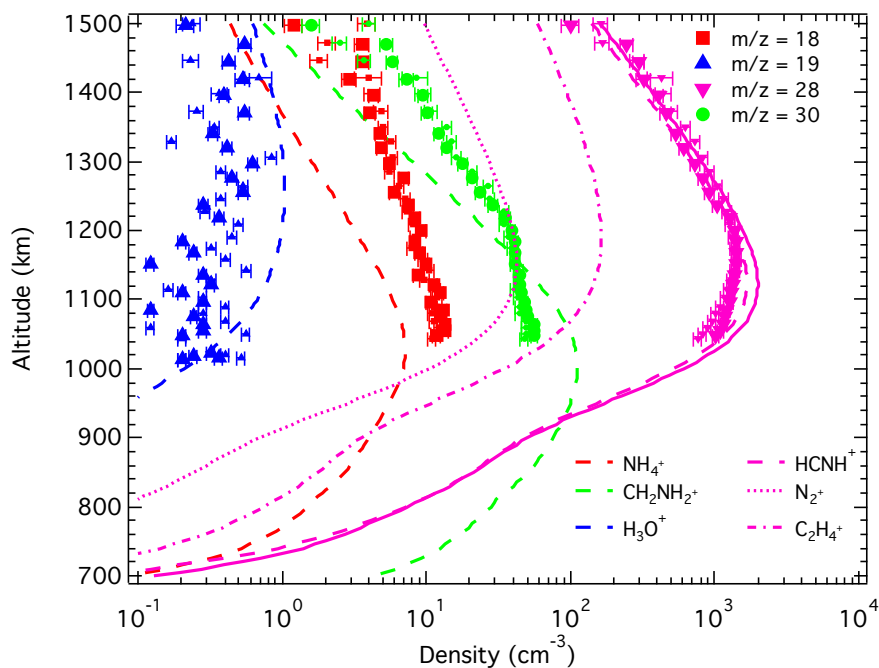


Figure 49: Model results for the density of NH_4^+ , H_3O^+ , $\text{HCNH}^+/\text{N}_2^+/\text{C}_2\text{H}_4^+$ and CH_2NH_2^+ , and comparison with the T40 INMS ion density measurements at $m/z = 18, 19, 28, 30$.

3240 4.2.3.2. Nitrogen-Bearing Species.

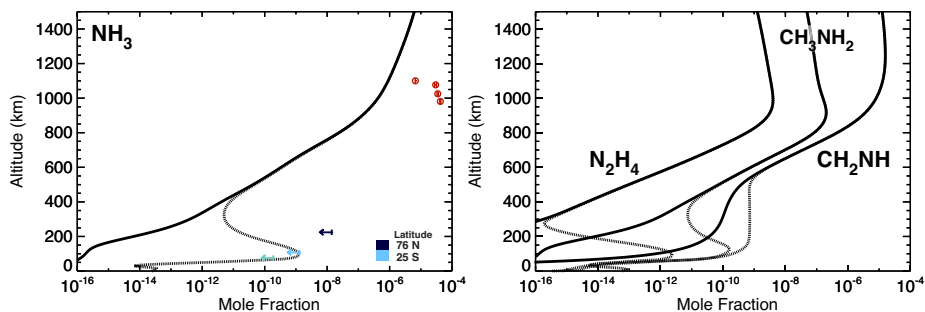


Figure 50: Calculated and observed mole fractions of NH_3 (left panel), and N_2H_4 , CH_2NH and CH_3NH_2 (right panel). Solid line: nominal; hair line: with GCR. The data shown for NH_3 is from CIRS 25S and 76N (Nixon et al., 2010) (blue), Herschel (Teunby et al., 2012) (green) and INMS (Cui et al., 2009b).

3241 **Ammonia ($\text{NH}_3 / \text{NH}_4^+$).** The presence of about 10 ppm of NH_3 in the
 3242 upper atmosphere (Vuitton et al., 2007; Cui et al., 2009b), is not reproduced by

3243 photochemical models (Lavvas et al., 2008b; Krasnopolsky, 2010; Loison et al.,
3244 2015; Dobrijevic et al., 2016; Willacy et al., 2016). Lavvas et al. (2008b) suggest
3245 that the photolysis of ethylenimine (C_2H_5N , produced from the reaction between
3246 $N(^2D)$ and C_2H_6) is the main source of NH_3 . However, this hypothesis implies
3247 densities of protonated ethylenimine ($C_2H_5NH^+$) that are incompatible with the
3248 small signal detected at $m/z = 44$ in the INMS ion spectra. The abundance of
3249 NH_3 in Figure 6 of Krasnopolsky (2010) is about one order of magnitude lower
3250 than the values retrieved from the INMS ion and neutral spectra. Although
3251 this model includes the new NH_3 production reaction suggested by Yelle et al.
3252 (2010), $NH_2 + H_2CN \rightarrow NH_3 + HCN$ (R_n362), the rate coefficient is taken equal
3253 to that of $N + H_2CN \rightarrow NH + HCN$, that is at 150 K, a factor of three lower
3254 than the rate calculated in Yelle et al. (2010), which probably partly explains
3255 the inability of the Krasnopolsky (2010) model to reproduce the observations.
3256 The Loison et al. (2015) NH_3 profile falls short of the INMS retrieved values by
3257 about two orders of magnitude (cf. their Figure 13), which they attribute to the
3258 lack of ion chemistry in their model to produce NH_2 , one of the major precursors
3259 of NH_3 , according to the chemical pathways described in Yelle et al. (2010) and
3260 section 3.2.2. This interpretation is supported by Willacy et al. (2016), whose
3261 model abundances in the upper atmosphere are a factor of 10 lower than the
3262 observations (their Figure 3).

3263 Our calculated NH_4^+ densities slightly underestimate the INMS ion spec-
3264 trum, as shown in Figure 49. This may be due to the fact that we do not
3265 consider the proton transfer reactions from $C_2H_5^+$ and $HCNH^+$ to NH_2 lead-
3266 ing to NH_3^+ and then to NH_4^+ , through the $NH_3^+ + CH_4$ reaction (Dobrijevic
3267 et al., 2016). However, our model underestimates the abundance of NH_3 by one
3268 to two orders of magnitude compared to the value inferred by Cui et al. (2009b),
3269 as illustrated in the left panel of Figure 50. The NH_4^+ and NH_3 densities found
3270 in the model of Dobrijevic et al. (2016) are similar to our simulations, which
3271 puts into question the validity of the INMS NH_3 detection. Actually, Dobrijevic
3272 et al. (2016) suggest that most of the NH_3 does not come from Titan's atmo-
3273 spheric chemistry but either from reaction of ambient N and H on the chamber
3274 walls or from spent hydrazine fuel (Cui et al., 2009b; Magee et al., 2009). In
3275 the stratosphere, the calculated NH_3 mole fraction is consistent with the upper
3276 limits from CIRS and Herschel (Nixon et al., 2010; Teanby et al., 2012).

3277 **Methanimine (CH_2NH / $CH_2NH_2^+$).** Methanimine is a particularly
3278 interesting molecule because, unlike all the other nitrogen-bearing species de-
3279 tected on Titan with the exception of ammonia, its nitrogen is not locked up in a
3280 triple bond and can therefore be more easily incorporated in prebiotic molecules,
3281 such as amino acids and nucleobases. Protonated methanimine ($CH_2NH_2^+$) has
3282 been identified in INMS ion spectra, resulting in a CH_2NH mole fraction of about
3283 10^{-5} at 1100 km (Vuitton et al., 2006b, 2007; Yelle et al., 2010).

3284 The chemical network of Lavvas et al. (2008a) was the first one to follow the
3285 destruction of CH_2NH . Yet their calculated CH_2NH abundance is larger than
3286 the one retrieved from the INMS measurements, which the authors attribute to

3287 the poor knowledge of photodissociation cross-sections and more generally of
 3288 loss processes for this species. However, it seems likely that the absence of ion
 3289 chemistry is responsible for the discrepancy between model and observations in
 3290 the upper atmosphere, as suggested by Dobrijevic et al. who face the same issue
 3291 with their own photochemical model (Loison et al., 2015).

3292 Calculated densities for CH_2NH_2^+ are shown in Figure 49, along with the
 3293 measured densities. CH_2NH mole fractions are presented in the right panel of
 3294 Figure 50. Their order of magnitude is adequate over most of the altitude range
 3295 but the shape of the profile is insufficient, especially below 1200 km. Although
 3296 the primary production and loss mechanisms for CH_2NH_2^+ and CH_2NH have
 3297 been identified in Yelle et al. (2010), we should keep in mind the large uncer-
 3298 tainties on the dissociative recombination reaction of CH_2NH_2^+ .

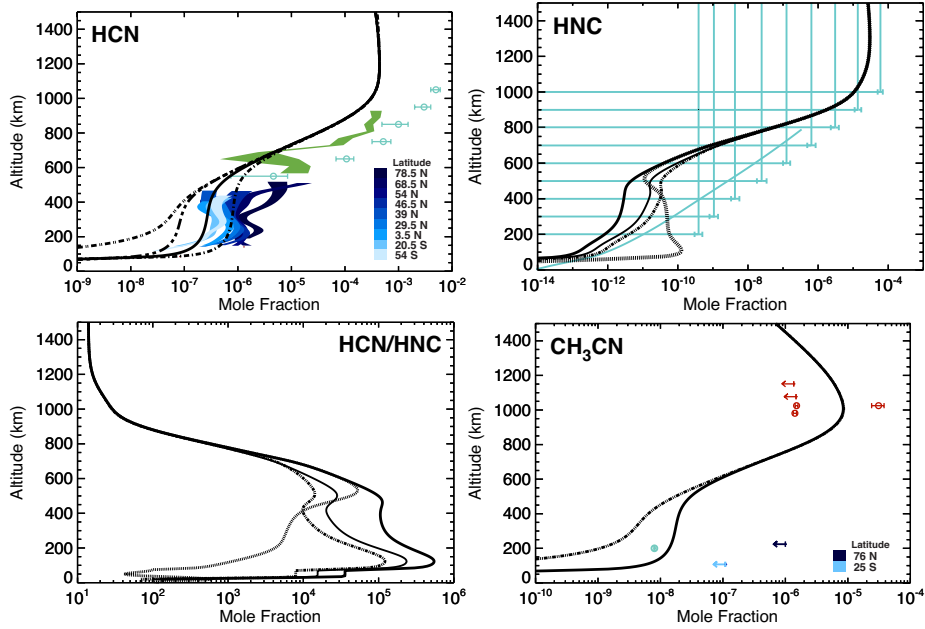


Figure 51: Calculated and observed mole fractions of HCN (upper left panel), HNC (upper right panel), HCN/HNC ratio (lower left panel), and CH_3CN (lower right panel). Solid line: nominal; short dash-dot-dot and thin lines: HC_3N sensitivity test, Table 13; dotted line: with GCR; dash-dot and long dash - double short dash line: eddy mixing coefficient $K_0 = 10^2$ and 10^3 cm^{-2} , respectively, section 2.4; dash-dot-dot line: with nitriles heterogeneous chemistry, section 5.3.3. Some of the lines are displayed in some plots and not in others. The data shown for HCN is from CIRS (Vinatier et al., 2010), UVIS (Koskinen et al., 2011), VIMS (Adriani et al., 2011); for HNC is from Herschel HIFI (Moreno et al., 2011) (lines that assume constant profiles), ALMA (Cordiner et al., 2014) (line is their gradient model); for CH_3CN is from IRAM (Marten et al., 2002) (green), CIRS (Nixon et al., 2010) (blue upper limits), INMS (Cui et al., 2009b).

3299 **Hydrogen (iso)cyanide (HCN, HNC / HCNH⁺).** Titan ionospheric
3300 models have long predicted that HCNH⁺ should be one of the most abundant
3301 ions with a peak density on the order of 1000 cm⁻³ around 1000-1200 km (Ip,
3302 1990; Keller et al., 1998). Nevertheless, it is a recurrent problem amongst Titan
3303 ionospheric models (from either the Cravens, Waite or Yelle groups) that they
3304 predict an HCNH⁺ density that is 2-3 times higher than observed by INMS. The
3305 Dobrijevic et al. (2016) model result agrees better with INMS data than those
3306 previous results. This would be explained by the introduction of the reaction
3307 N(²D) + HCN → CH + N₂ that would efficiently consume HCN, according to
3308 the authors. Despite including this reaction in our model with a similar rate
3309 coefficient, it turns out to only be a minor (< 5%) loss process for HCN in our
3310 model. Therefore, our current findings are in line with Westlake et al. (2012),
3311 Mandt et al. (2012a) and Richard et al. (2015a), as our calculated globally
3312 averaged HCNH⁺ profile overestimates the T40 observations by 1.4 at 1100
3313 km. This issue is probably related to the overproduction of electrons in dayside
3314 models, as discussed in Vigren et al. (2013) and Sagnières et al. (2015). We will
3315 return to this complicated topic in section 5.1.

3316 The HCN molecule is the main nitrile in Titan's atmosphere. There is a
3317 relatively wide consensus for its main formation and loss pathways despite the
3318 fact that most post-Cassini models tend to underestimate its abundance (Lavvas
3319 et al., 2008b; Krasnopolsky, 2014; Loison et al., 2015). One important differ-
3320 ence with the recent model of Dobrijevic et al. (Loison et al., 2015; Dobrijevic
3321 et al., 2016) is that we find that a large fraction of the CN radicals reacts with
3322 C₂H₄ and C₂H₂ leading to C₂H₃CN and HC₃N production, while only a small
3323 fraction (~10%) reacts with CH₄ and C₂H₆ leading back to HCN. Willacy et al.
3324 (2016) report that below 200 km, HCN destruction is by reaction with C₂H₃
3325 but calculations performed in the present work (cf. Appendix A) indicate that
3326 the rate coefficient of this reaction is extremely small (~ 10⁻²² cm³ s⁻¹ at 150
3327 K).

3328 Our model vertical profile of HCN is presented in the upper left panel of
3329 Figure 51. HCN being the major product of the photodissociation of N₂, it
3330 is a particularly good test for the N₂ dissociation scheme derived from Lavvas
3331 et al. (2011a). The model gives a simulated HCN abundance in good agreement
3332 with INMS in the thermosphere and CIRS in the stratosphere, but it is smaller
3333 than the abundance derived from UV absorption in the mesosphere. Despite the
3334 differences in formation and destruction processes mentioned above, the profiles
3335 obtained in the present work, Dobrijevic et al. (2016) and Willacy et al. (2016)
3336 are similar.

3337 After high-level ab initio quantum chemical investigations concurred that
3338 HNC is a major product of the dissociative recombination of HCNH⁺ (Talbi and
3339 Ellinger, 1998), it was soon recognized that HNC could have a significant den-
3340 sity in Titan's upper thermosphere (Petrie, 2001). Simple calculations assuming
3341 formation through electron recombination of HCNH⁺, loss through proton ex-
3342 change reactions, and using the atmospheric properties known at that time, lead
3343 to an HNC column density of 7.0 × 10¹¹ – 5.2 × 10¹² cm⁻², which is somewhat
3344 marginally consistent with a column density in the range (0.6 – 1.5) × 10¹³ cm⁻²

3345 from observations of the HIFI instrument on the Herschel Space Observatory
3346 (Moreno et al., 2011) and $(1.2 - 1.9) \times 10^{13} \text{ cm}^{-2}$ using ALMA (Cordiner et al.,
3347 2014).

3348 Our model vertical profile of HNC is presented in the upper right panel of
3349 Figure 51. With improved production and loss rates (Appendix A), we find that
3350 the bulk of the HNC is produced above 800 km, with a density profile reaching
3351 a peak of $\sim 10^5 \text{ cm}^{-3}$ at an altitude of 950-1000 km. This translates into a
3352 constant mole fraction of $\sim 2 \times 10^{-5}$ above 1050-1100 km (cf. lower left panel of
3353 Figure 51) and a total column density of $8.9 \times 10^{12} \text{ cm}^{-2}$, which is the column
3354 density retrieved from the observations assuming a constant mole fraction profile
3355 above 700 km. While the simple comparison of the column density can give us a
3356 feeling that our distribution is adequate overall, a definitive test of the modeling
3357 would require the computation of a synthetic spectrum based on our calculated
3358 mixing profile and comparison against the HIFI and ALMA data.

3359 Following its detection, Hébrard et al. (2012) investigated the production of
3360 HNC via neutral reactions. They find that HNC is mostly produced from H_2CN
3361 $+ \text{H} \rightarrow \text{HNC} + \text{H}$ and to a lesser extent from $\text{N}(^4\text{S}) + ^3\text{CH}_2 \rightarrow \text{HNC} + \text{H}$, which
3362 are also the two major processes involving neutrals in our model. It is mainly
3363 destroyed by its reaction with $\text{N}(^2\text{D})$ above 1000 km and H at lower altitude.
3364 We agree with the latter but find that the former process is a marginal loss.
3365 Since Hébrard et al. (2012) estimated the rate coefficient of this reaction to be
3366 about one order of magnitude faster than the rate coefficient that we calculated,
3367 their $\text{N}(^2\text{D})$ density must be about three orders of magnitude higher than ours,
3368 probably because of a different dissociation scheme for N_2 . The column density
3369 obtained is $3.4 \times 10^{13} \text{ cm}^{-2}$, which is about 3 times higher than the value derived
3370 from the observations.

3371 In Dobrijevic et al. (2016) where neutral and ion chemistries are coupled,
3372 the dissociative recombination of HCNH^+ now produces a significant fraction
3373 of HNC, in good agreement with our findings. Its relative abundance reaches a
3374 value of 7×10^{-5} above 1200 km. Although the authors claim that their HNC
3375 profile is in good agreement with the Herschel/HIFI observations, they do not
3376 provide the column density obtained and the mole fraction profile presented in
3377 their Figure 26 does not seem to match with Cordiner et al. (2014). Although
3378 the same main production and loss reactions are at play in both the present and
3379 Dobrijevic et al. (2016) models, different rate coefficients explain the distinct
3380 HNC profiles. Willacy et al. (2016) are only able to reasonably match the ALMA
3381 best-fit profile with a model where an extra loss leading to haze is applied to
3382 HNC at lower altitudes.

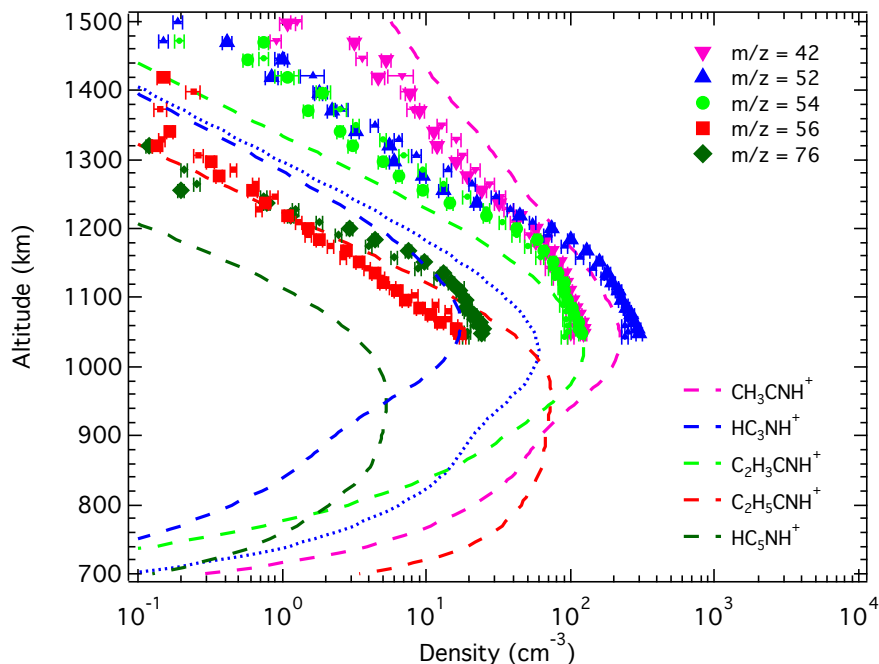


Figure 52: Model results for the density of CH_3CNH^+ , HC_3NH^+ , $\text{C}_2\text{H}_3\text{CNH}^+$, $\text{C}_2\text{H}_5\text{CNH}^+$ and HC_5NH^+ , and comparison with the T40 INMS ion density measurements at $m/z = 42, 52, 54, 56, 76$. The HC_3NH^+ dotted line corresponds to the sensitivity test described in the text.

3383 **Acetonitrile ($\text{CH}_3\text{CN} / \text{CH}_3\text{CNH}^+$).** Our model vertical profile of
 3384 acetonitrile is presented in the lower right panel of Figure 51. Like for all model
 3385 profiles (Krasnopolsky, 2014; Loison et al., 2015; Dobrijevic et al., 2016; Willacy
 3386 et al., 2016), the resulting CH_3CN abundance is slightly below the observed
 3387 values in the thermosphere (Vuitton et al., 2007; Cui et al., 2009b), while the
 3388 situation reverses in the stratosphere where our calculated abundance is slightly
 3389 above the the ground-based data (Marten et al., 2002). Our calculated profile
 3390 for CH_3CNH^+ (Figure 52) overestimates the INMS abundance by a factor of 3
 3391 at 1100 km. Since CH_3CNH^+ is mostly formed by reactions involving HCNH^+
 3392 ($R_{cn}692, R_{cn}713$), the overestimation of the latter directly translates into the
 3393 overestimation of the former. The situation is reversed in Dobrijevic et al.
 3394 (2016), where the CH_3CNH^+ ion is underestimated.

3395 Our main CH_3CN neutral production and loss pathways are similar to those
 3396 discussed in the models of Lavvas et al. (2008b), Krasnopolsky (2014), and
 3397 Loison et al. (2015). However, we find that ion chemistry also plays an important
 3398 role in the thermosphere through the production of CH_2CN , which further adds
 3399 to H atoms to form CH_3CN (R_n423) and through loss by proton transfer reaction
 3400 (cf. section 3.1.1.3).

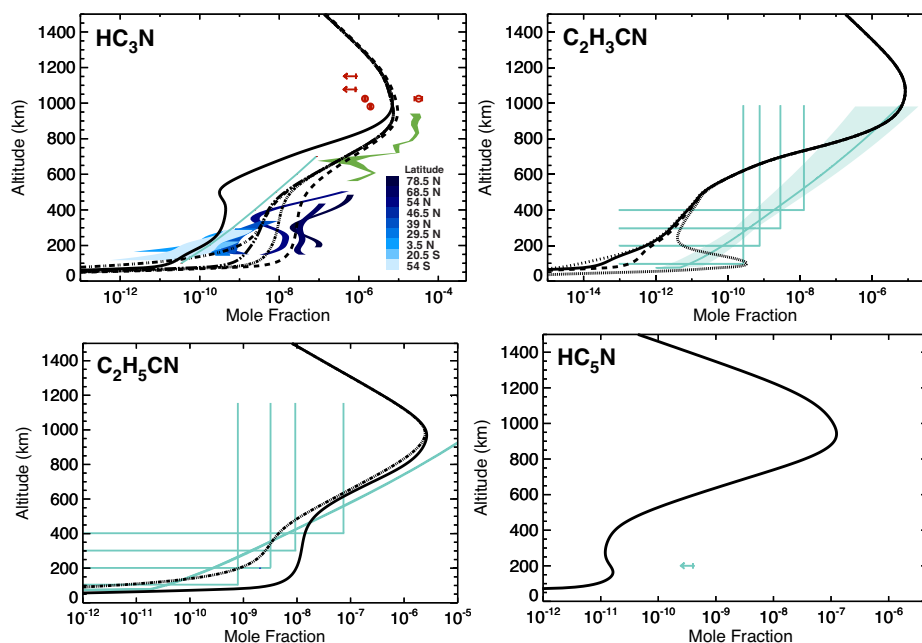


Figure 53: Calculated and observed mole fractions of HC_3N (upper left panel), $\text{C}_2\text{H}_3\text{CN}$ (upper right panel), $\text{C}_2\text{H}_5\text{CN}$ (lower left panel) and HC_5N (lower right panel). Solid line: nominal; thin line: HC_3N sensitivity test, Table 13; hair line: with GCR; dotted and dashed lines: aerosol optical depth multiplied by 0.5 and 2, respectively, section 5.3.1; long dash-dot-dot line: no H heterogeneous loss, section 5.3.2; dash-dot-dot line: with nitriles heterogeneous chemistry, section 5.3.3. The data shown for HC_3N is from ALMA (Cordiner et al., 2014) (green line, gradient model), CIRS (Vinatier et al., 2010); UVIS (Koskinen et al., 2011); INMS (Cui et al., 2009b) (circles no error bars are uncorrected, circle with error bar is corrected); for $\text{C}_2\text{H}_3\text{CN}$ is from ALMA (Palmer et al., 2017) (the line with error bars is their fractional scale height model. The other lines are just assuming a constant value above a certain height); for $\text{C}_2\text{H}_5\text{CN}$ is from ALMA (Cordiner et al., 2014) (line is gradient model, others are assuming constant with height); for HC_5N is from IRAM (Martens et al., 2002).

3401 **Cyanoacetylene (HC_3N / HC_3NH^+).** Like that of diacetylene, the
 3402 cyanoacetylene vertical profile is well constrained with available observations
 3403 from INMS, UVIS and CIRS. In the thermosphere, the UVIS data support the
 3404 corrected value from Cui et al. (2009b). In the stratosphere, the abundance
 3405 presents some drastic latitudinal variations, with polar abundances at 200 km
 3406 being three orders of magnitude higher than the equatorial ones.

Table 13: Parameters used in the nominal and HC₃N sensitivity test runs.

Reaction	Nominal Run	Test Run
$\text{HC}_3\text{NH}^+ + \text{C}_2\text{H}_4 \rightarrow \text{C}_5\text{H}_5\text{N}^+ + \text{H}$ ($R_{cn}790$)	Upper Limit	0
$\text{HC}_3\text{NH}^+ + \text{e}^- \rightarrow \text{HC}_3\text{N} + \text{H} / \text{C}_3\text{N} + \text{H}_2$ ($R_{er}104\text{a,c}$)	0.5 / 0.5	1 / 0
$\text{H} + \text{HC}_3\text{N} \rightarrow \text{H}_2\text{C}_3\text{N}$ (R_n258)	This Work	est.(H + C ₄ H ₂)

3407 Our model vertical profile of HC_3N and HC_3NH^+ are presented in Figures
3408 53 (upper left panel) and 52, respectively. In the upper atmosphere, both HC_3N
3409 and HC_3NH^+ are too low by a factor of about five and twenty, respectively. In
3410 the stratosphere, HC_3N is one to two orders of magnitude higher than CIRS
3411 mid-latitude observations. Therefore, we obtain a similar underestimation in
3412 the thermosphere / overestimation in the stratosphere for C_4H_2 and HC_3N .

3413 Our main HC_3N production and loss pathways are similar to those discussed
3414 in previous models (cf. section 3.2.2) but the chemistry of HC_3NH^+ is some-
3415 what uncertain. The reaction with C_2H_4 ($R_{cn}790$), which is its main loss, has a
3416 rate coefficient that is given as an upper limit in McEwan and Anicich (2007).
3417 The rate coefficient of its second main loss, recombination with electrons, is well
3418 constrained but the exact products are unknown with the channel preserving
3419 the carbon chain being either $\text{HC}_3\text{N} + \text{H}$ or $\text{C}_3\text{N} + \text{H}_2$ ($R_{er}104a,c$). We per-
3420 formed a sensitivity test (cf. Table 13), in which we attempted to increase the
3421 $\text{HC}_3\text{NH}^+/\text{HC}_3\text{N}$ density by (i) setting ($R_{cn}790$) to 0 and (ii) assuming that the
3422 electron recombination of HC_3NH^+ does not produce any $\text{C}_3\text{N} + \text{H}_2$ and that
3423 instead 100% of the products of the channel preserving the carbon chain are
3424 $\text{HC}_3\text{N} + \text{H}$ ($R_{er}104a$). With this new scheme, the HC_3NH^+ density increases
3425 by a factor of about three (thin line in Figure 52), which implies that it still
3426 falls short from the observations by a factor of ~ 5 . The impact on HC_3N is
3427 minor, as its density increases by only about 30%. This is due to the fact that
3428 ion chemistry is a minor player for HC_3N , as discussed in section 3.1.1.3.

3429 We actually realized that an older version of the model, where we had the rate
3430 coefficients of the main loss reaction along with photodissociation, $\text{H} + \text{HC}_3\text{N}$
3431 (R_n258), set equal to that of the $\text{H} + \text{C}_4\text{H}_2$ reaction (R_n21), provided quite a
3432 good fit below 300 km. This is reproduced here as the thin line in the upper
3433 left panel of Figure 53. However, our present calculations predict that the
3434 $\text{H} + \text{HC}_3\text{N}$ reaction is quite a bit slower than the $\text{H} + \text{C}_4\text{H}_2$ reaction, with the
3435 high pressure limits differing by a factor of 30 at 140 K (cf. Figure A.2d).
3436 Note, however, since the reaction is tunneling dominated, there is considerable
3437 uncertainty in the present rate estimates. For example, decreasing the imaginary
3438 frequency by 100 cm^{-1} lowers the rate constant by a factor of 2 at 140 K,
3439 as does increasing the barrier height by 0.2 kcal/mol. This strong sensitivity
3440 may be the cause of either the overprediction of the HC_3N concentration at
3441 low altitudes or the underprediction at high altitudes. However, it is difficult
3442 to see how the predicted rate can be both too low at low altitudes and too
3443 high at high altitudes, since we predict only a modest pressure dependence.
3444 It has been postulated that because of their polar nature, the nitriles present
3445 in the gas phase could efficiently stick to the aerosols present in particular in
3446 the stratosphere, adding an extra heterogeneous loss for these species. We will
3447 return to this in section 5.3.3.

3448 Earlier models have not been very successful at matching the cyanoacetylene
3449 mole fraction at all levels of the atmosphere. Both the Lavvas et al. and Loison
3450 et al. calculated profiles (cf. Figure 9c in Lavvas et al. (2008b) and top of Fig-
3451 ure 10 in Loison et al. (2015)) are below the retrieved abundance in the upper
3452 atmosphere, yet they are closer to the polar profiles retrieved from the CIRS ob-

3453 servations than from the mid-latitudes ones. The cyanoacetylene abundance in
 3454 the model from Krasnopolsky (cf. Figure 3 in Krasnopolsky (2014)) agrees with
 3455 that from INMS neutral and ion spectra but significantly exceeds both UVIS
 3456 and CIRS data. The Dobrijevic et al. (2016) model results in an overestimate of
 3457 the HC_3N abundance compared to the observations in all regions (their Figure
 3458 10), while their HC_3NH^+ profile is in fair agreement with INMS (their Figure
 3459 12). Finally, Willacy et al. (2016) tend to under predict the HC_3N abundance
 3460 above 700 km, while below 500 km, it is in agreement with the observations
 3461 (their Figure 3 bottom left) only if it is assumed that HC_3N forms aerosols and
 3462 thus is permanently removed from the gas.

3463 **Acrylonitrile ($\text{C}_2\text{H}_3\text{CN}$ / $\text{C}_2\text{H}_3\text{CNH}^+$).** Our calculated $\text{C}_2\text{H}_3\text{CNH}^+$
 3464 densities between 1000 and 1400 km altitude are in good agreement with the
 3465 INMS observations (cf. Figure 52). The abundance profile of the neutral from
 3466 our chemical model is shown in the upper right panel of Figure 53. Its over-
 3467 all shape is consistent with ALMA (the fractional scale height model, with a
 3468 smoothly varying altitude dependence), but its magnitude is slightly too low.
 3469 Indeed, the vertical column densities implied by the observations lie in the range
 3470 of $(0.37 - 1.4) \times 10^{14} \text{ cm}^{-2}$ (Palmer et al., 2017), while our nominal model gives a
 3471 value of $3 \times 10^{13} \text{ cm}^{-2}$. This is nevertheless better than the modeled abundance
 3472 profile of Dobrijevic et al. that is consistent with the observed line shapes, pro-
 3473 vided that it is scaled up by a constant factor of 4.7 (Palmer et al., 2017). Our
 3474 main neutral production and loss processes are mostly consistent with those dis-
 3475 cussed in (Loison et al., 2015). The need for an enhanced $\text{C}_2\text{H}_3\text{CN}$ production
 3476 may imply that the rate coefficient of the reaction $\text{CN} + \text{C}_2\text{H}_4 \rightarrow \text{C}_2\text{H}_3\text{CN} +$
 3477 H (R_n371) is underestimated in both models. It might also imply that there
 3478 is a polar enhancement for $\text{C}_2\text{H}_3\text{CN}$, which would result in the disc-averaged
 3479 measurement being higher than the equatorial models (Palmer et al., 2017).

3480 The models calculated profiles are generally in good agreement with the
 3481 observed abundance in the upper atmosphere (cf. Figure 9b in Lavvas et al.
 3482 (2008b), Figure 1d in Krasnopolsky (2012), Figure 11 in Loison et al. (2015) and
 3483 Figure 4 in Willacy et al. (2016)). There is more variability in the predicted pro-
 3484 files in the lower atmosphere, some of them (Krasnopolsky, 2012; Willacy et al.,
 3485 2016) being well above the detection limit placed by ground-based observations
 3486 ($\sim 2 \times 10^{-9}$, Marten et al. (2002)). Also, the Krasnopolsky profile produces
 3487 strong pressure-broadened line wings that do not match with the very recent
 3488 ALMA observations (Palmer et al., 2017). This is essentially because of the
 3489 reaction of hydrogen cyanide with vinyl radicals (C_2H_3), which was suggested
 3490 to lead to the formation of acrylonitrile, but whose suggested rate below room
 3491 temperature was too high ($2.7 \times 10^{-15} \text{ cm}^3 \text{ s}^{-1}$ instead of $1.4 \times 10^{-22} \text{ cm}^3 \text{ s}^{-1}$ at
 3492 150 K, see Appendix A). Actually, this reaction turns out to be negligible with
 3493 our newly calculated rate coefficient. In a few photochemical models (Lavvas
 3494 et al., 2008b; Willacy et al., 2016), some chemical loss to the haze counterbal-
 3495 anced the excessive production of acrylonitrile in the lower atmosphere through
 3496 this reaction.

3497 **Propionitrile ($C_2H_5CN / C_2H_5CNH^+$).** Our calculated densities for
3498 $C_2H_5CNH^+$ between 1000 and 1400 km altitude are in relatively good agree-
3499 ment with the INMS observations but the C_2H_5CN vertical profile (cf. lower left
3500 panel of Figure 53) leads to a column density of $1.6 \times 10^{16} \text{ cm}^{-2}$, which is about
3501 a factor of 50 higher than that deduced from the ALMA observations (Cordiner
3502 et al., 2015b). None of the photochemical models (Krasnopolsky, 2012; Loison
3503 et al., 2015; Dobrijevic et al., 2016; Willacy et al., 2016) that present predic-
3504 tions for C_2H_5CN are in agreement with the recent ALMA observations that
3505 imply a C_2H_5CN column density in the range $(2.1 - 5.1) \times 10^{14} \text{ cm}^{-2}$ (Cordiner
3506 et al., 2015b). The model from Krasnopolsky (2009), that produces C_2H_5CN
3507 through the reaction of excited nitrogen atoms with C_3H_6 , generates a strato-
3508 spheric abundance about two orders of magnitude too low, which indicates that
3509 (an)other production channel(s) is required. Conversely, the C_2H_5CN abun-
3510 dance calculated with the model from Dobrijevic et al. (Loison et al., 2015;
3511 Dobrijevic et al., 2016) are, between 100 and 300 km altitude, from one to three
3512 orders of magnitude higher than the observations. In this case, C_2H_5CN is
3513 produced by the ternary association of CH_2CN and CH_3 (R_n424), whose rate
3514 coefficient has never been measured. Only the model of Willacy et al. (2016)
3515 reaches an agreement with the ALMA data by including an additional sticking
3516 of C_2H_5CN to the aerosols. The trend is similar in the upper atmosphere, with
3517 the Krasnopolsky (2012) model underestimating the INMS data, while the Lo-
3518 ison et al. (2015) and Willacy et al. (2016) models overestimate the abundance
3519 of C_2H_5CN , probably because they do not include ion chemistry, a feature that
3520 was later added in Dobrijevic et al. (2016), providing a good agreement with
3521 the measurements.

3522 The main limitation of these models is a lack of knowledge of the production
3523 and loss mechanisms for C_2H_5CN . The only reactions that have been studied
3524 are $N(^2D) + C_3H_6 \rightarrow C_2H_5CN + H$ and the radiative association of CH_3CN
3525 with CH_3^+ . The latter reaction produces $C_2H_5CNH^+$ and this species being in
3526 equilibrium with C_2H_5CN through proton transfer reactions and the electronic
3527 recombination of $C_2H_5CNH^+$, the production of $C_2H_5CNH^+$ ultimately leads
3528 to some C_2H_5CN as well. However, our calculations show that, with our esti-
3529 mated rate coefficients, radical-radical reactions ($CH_2CN + CH_3$ (R_n424), NH_2
3530 + C_3H_3 (R_n352), etc.) are the main source of C_2H_5CN . Loss occurs mostly
3531 through proton transfer reactions above 700 km, by radical reactions below 400
3532 km, and by photodissociation in between (cf. section 3.2.2).

3533 **Cyanodiacetylene (HC_5N / HC_5NH^+).** We obtain a peak at $\sim 3 \times$
3534 10^{-7} in the thermosphere, associated to a HC_5NH^+ that underestimates the
3535 INMS signal at $m/z = 76$ by a factor of about 5. In the stratosphere, the
3536 modeled mole fraction decreases to reach a constant value of $\sim 10^{-11}$, in good
3537 agreement with the Marten et al. (2002) upper limit of 4×10^{-10} (cf. lower right
3538 panel of Figure 53). The Dobrijevic et al. model is the only one to present mole
3539 fraction profiles of HC_5N (top panel in Figure 14 from Loison et al. (2015)). It
3540 peaks with a similar magnitude as our model at 1000 km and in the stratosphere,

3541 it is one order of magnitude lower.

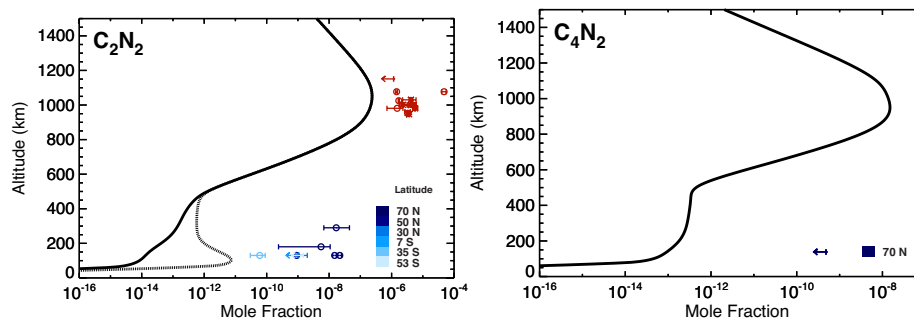


Figure 54: Calculated and observed mole fractions of C_2N_2 (left panel) and C_4N_2 (right panel). Solid line: nominal; hair line: with GCR. The data shown for C_2N_2 is from IRIS (Coustenis et al., 1991; Coustenis and Bézard, 1995), CIRS (Teanby et al., 2006; Teanby et al., 2009), INMS (Cui et al., 2009b) (circles no error bars are uncorrected, circle with error bar is corrected) (Waite et al., 2007) (asterisks); for C_4N_2 is from CIRS (Jolly et al., 2015).

3542 **Cyanogen (C_2N_2).** Our model under predicts the observations by one
3543 order of magnitude in the thermosphere and almost four orders of magnitude in
3544 the stratosphere (cf. left panel of Figure 54). Actually, the only CIRS detections
3545 are at pretty high latitudes, implying that C_2N_2 is probably enriched at the
3546 poles and that the values on the Figure are higher than what we expect at the
3547 equator. Also, the chemistry of C_2N_2 is poorly constrained and its principal
3548 production and loss reactions had to be estimated (cf. section 3.2.2).

3549 Most of the previous models underestimate the cyanogen abundance in the
3550 upper atmosphere as well. In the stratosphere, the Lavvas et al. profile is
3551 well below the CIRS observations for the low latitude regions (cf. Figure 9d in
3552 Lavvas et al. (2008b)) while both the Krasnopolsky and Dobrijevic et al. models
3553 overestimate them (cf. Figure 5 in Krasnopolsky (2014) and top panel of Figure
3554 12 in Loison et al. (2015)). Unlike them, the most recent model of the Yung et
3555 al. group is in very good agreement with both the INMS and CIRS datasets
3556 (cf. top left panel of Figure 4 in Willacy et al. (2016)). It is unfortunate that
3557 the values and origin of the rate coefficients used in this model are not clearly
3558 stated.

3559 **Dicyanogen (C_4N_2).** Our calculated profile for C_4N_2 and that from pre-
3560 vious models are all well below the upper limit retrieved close to 100 km. This
3561 is shown on the right panel of Figure 54 for this work but see also Figure 9d in
3562 Lavvas et al. (2008b), Figure 1d in Krasnopolsky (2012) and bottom panel of
3563 Figure 12 in Loison et al. (2015).

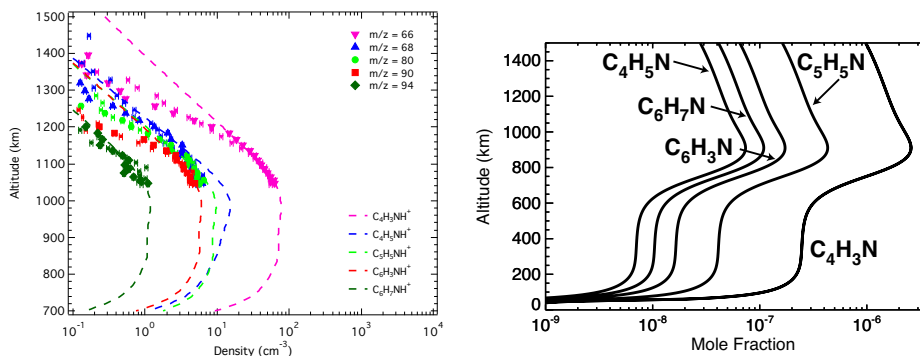


Figure 55: Model results for the density of $C_4H_3NH^+$, $C_4H_5NH^+$, $C_5H_5NH^+$, $C_6H_3NH^+$ and $C_6H_7NH^+$, and comparison with the T40 INMS ion density measurements at $m/z = 66, 68, 80, 90, 94$ (left panel). Inferred vertical profile for associated neutrals (right panel).

Table 14: Inferred neutrals mole fraction at 1100 km.

Species	Mixing Ratio	
	Vuitton et al. (2007)	This Work
C_4H_3N	4.0×10^{-6}	2.0×10^{-6}
C_4H_5N	$< 3.0 \times 10^{-7}$	5.0×10^{-8}
C_5H_5N	4.0×10^{-7}	3.0×10^{-7}
C_6H_3N	3.0×10^{-7}	1.0×10^{-7}
C_6H_7N	1.0×10^{-7}	8.0×10^{-8}

3564 **Heavies.** The nitrogen rule states that protonated organic compounds
 3565 with an even nominal mass have an odd number of nitrogen atoms. This general
 3566 principal allowed us to attribute the ions at $m/z = 66, 68, 80, 90$ and 94
 3567 to $C_4H_3NH^+$, $C_4H_5NH^+$, $C_5H_5NH^+$, $C_6H_3NH^+$ and $C_6H_7NH^+$. Moreover, we
 3568 showed that they depend closely on the composition of the neutral atmosphere
 3569 and that measurement of their density coupled with simple chemical schemes
 3570 provides a sensitive determination of the abundance of their associated neutral
 3571 species (Vuitton et al., 2007). Because the production and loss pathways for
 3572 C_4H_3N , C_4H_5N , C_5H_5N , C_6H_3N and C_6H_7N are largely undetermined, we do
 3573 not track them specifically but instead stick to our previous approach to estimate
 3574 their abundance in the upper atmosphere. Mixing ratios at 1100 km
 3575 inferred from the T40 ion densities (this model) are given in Table 14, along
 3576 with the values inferred from the T5 ion densities (Vuitton et al., 2007). Both
 3577 set of values are in good agreement although the T40 ones tend to be smaller
 3578 by a factor of about 2.

3579 **¹⁵N Isotopologues** The $^{14}N/^{15}N$ ratio in N_2 has been retrieved from
 3580 INMS and GCMS measurements (cf. Table 15). INMS gives a ratio of 172
 3581 to 215 from the analysis of an average spectrum for the altitude range of 1230

3582 to 1174 km during TA, which translates into an estimated value at the surface
3583 of 168-211 (Waite et al., 2005). A later fit of the INMS $^{14}\text{N}^{14}\text{N}$ and $^{14}\text{N}^{15}\text{N}$
3584 vertical profiles between 1100 and 1500 km averaged over 16 passes gives a
3585 $^{14}\text{N}/^{15}\text{N}$ ratio of 147.5 ± 7.5 below the homopause level (Mandt et al., 2009).
3586 GCMS measurements in the troposphere indicate a ratio of 167.7 ± 0.6 averaged
3587 through the entire altitude range 144-16 km (Niemann et al., 2010). (Niemann
3588 et al., 2010) is meant to supersede the earlier ratio of (Niemann et al., 2005)
3589 (183 ± 5) anywhere they disagree.

3590 The $^{14}\text{N}/^{15}\text{N}$ ratio in HCN has been determined from ground-based observa-
3591 tions (Marten et al., 2002; Gurwell, 2004), as well as from CIRS (Vinatier et al.,
3592 2007b) and Herschel (Courtin et al., 2011) data, which all probe the strato-
3593 sphere. The values are somewhat scattered, ranging from 56 ± 8 for CIRS to
3594 94 ± 13 for the Sub-Millimeter Array using the Lellouch (1990) temperature
3595 profile. The $^{14}\text{N}/^{15}\text{N}$ ratio in CH_3CN has been retrieved from ALMA data
3596 (Cordiner et al., 2015a) but it may be subject to revision based on more accu-
3597 rate observations and modeling. This preliminary ratio is in excellent agreement
3598 with the CIRS value for HCN. The HCN- and CH_3CN -derived values are there-
3599 fore a factor of 2-3 lower than the N_2 -derived values, showing enrichment of the
3600 heavier isotope of nitrogen in HCN and CH_3CN .

Table 15: Observed $^{14}\text{N}/^{15}\text{N}$ isotopic ratio in N_2 , HCN and CH_3CN .

N_2 (thermosphere)	$193.5 \pm 21.5^{(a)}$			
N_2 (troposphere)	$188 \pm 16^{(b)}$	$147.5 \pm 7.5^{(c)}$	$183 \pm 5^{(d)}$	$167.7 \pm 0.6^{(e)}$
HCN (stratosphere)	$65 \pm 5^{(f)}$	$72 \pm 9^*$; $94 \pm 13^{** (g)}$	$56 \pm 8^{(h)}$	$76 \pm 6^{(i)}$
CH_3CN (stratosphere)	$58 \pm 8^{(j)}$			

^(a)INMS (Waite et al., 2005); ^(b)INMS extrapolated to surface (Waite et al., 2005); ^(c)INMS extrapolated to surface (Mandt et al., 2009); ^(d)GCMS (Niemann et al., 2005); ^(e)GCMS (Niemann et al., 2010); ^(f)IRAM (Marten et al., 2002); ^(g)SMA (Gurwell, 2004) *assuming the temperature profile from (Lellouch, 1990), **assuming the temperature profile from (Coustenis and Bézard, 1995); ^(h)CIRS (Vinatier et al., 2007b); ⁽ⁱ⁾Herschel (Courtin et al., 2011); ^(j)ALMA (Cordiner et al., 2015a).

3601 Photo-induced isotopic fractionation has been put forward to explain the
 3602 ^{15}N enrichment in HC^{15}N (Liang et al., 2007; Mandt et al., 2012a). However,
 3603 the original calculations by Liang et al. (2007) required an additional source of
 3604 atomic nitrogen in the upper atmosphere to obtain the observed $\text{HC}^{14}\text{N}/\text{HC}^{15}\text{N}$
 3605 ratio. With a $^{14}\text{N}/^{15}\text{N} = 183 - 260$, the N input was constrained to be in the
 3606 range $(1-2) \times 10^9 \text{ cm}^{-2} \text{ s}^{-1}$. This value, in agreement with the understanding of
 3607 N_2 dissociation by Saturnian magnetospheric ion/electron impact at that time,
 3608 is now believed to be overestimated by about two orders of magnitude (Lavvas
 3609 et al., 2011a), which implies that the origin of the $^{14}\text{N}/^{15}\text{N}$ fractionation needs
 3610 to be reevaluated.

3611 As presented in section 2.6.3, photoabsorption cross sections for $^{28}\text{N}_2$ and
 3612 $^{29}\text{N}_2$ are highly structured in the 80-100 nm region and can induce some isotope-
 3613 selective shielding, resulting in a higher photolytic efficiency for $^{29}\text{N}_2$ than for
 3614 $^{28}\text{N}_2$, therefore leading to a higher HC^{15}N production rate. This is illustrated
 3615 in the left panel of Figure 56, which shows the profiles of the photodissociation
 3616 rate coefficients (J-value, defined in Eq. E8) for $^{28}\text{N}_2$ and $^{29}\text{N}_2$. Shifts in the
 3617 rovibrational transition energies associated with differences in line intensities
 3618 due to isotopic substitution and selective overlap with solar lines cause $J(^{29}\text{N}_2)$
 3619 to be larger than $J(^{28}\text{N}_2)$, the ratio reaching a maximum of 19 at 980 km.

3620 The calculated photodissociation rates for $^{28}\text{N}_2$ and $^{29}\text{N}_2$ are shown in the
 3621 right panel of Figure 56. Unlike $^{28}\text{N}_2$, where the rate peaks at 1130 km, the
 3622 isotope-selective photodissociation allows more dissociative photons for $^{29}\text{N}_2$ to
 3623 penetrate deeper into Titan's atmosphere and moves the $^{29}\text{N}_2$ maximum down
 3624 to 970 km.

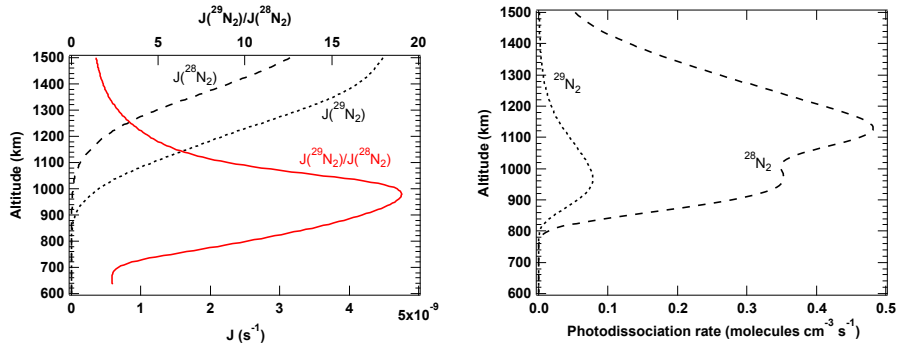


Figure 56: $^{28}\text{N}_2$ and $^{29}\text{N}_2$ photodissociation rate coefficient (left panel) and photodissociation rate (right panel).

3625 Higher photodissociation rate coefficients for $^{29}\text{N}_2$ than for $^{28}\text{N}_2$ translate
 3626 into the production of more ^{15}N than ^{14}N and therefore higher ^{15}N densities
 3627 (both $\text{N}(^2\text{D})$ and $\text{N}(^4\text{S})$), as illustrated in Figure 57.

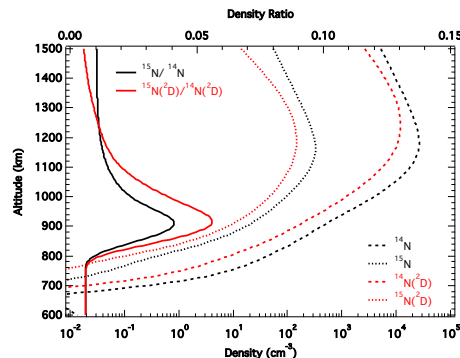


Figure 57: Model results for the density of nitrogen atoms.

3628 The subsequent nitrogen chemistry is described in section 3.2.2. The re-
 3629 sulting abundances of the ^{15}N isotopologues of HCN, CH_3CN and HC_3N are
 3630 presented in Figure 58. The $^{14}\text{N}/^{15}\text{N}$ ratio for those three species is shown in
 3631 those same plots and corresponding values at 1200 and 200 km are listed in Ta-
 3632 ble 16. For all three species, the $^{14}\text{N}/^{15}\text{N}$ ratio is constant above 1100 km and
 3633 then decreases to reach again a pretty constant value close to 55 below 800 km.
 3634 Because the $^{29}\text{N}_2$ photolysis peaks at lower altitude (cf. Figure 56), the ^{15}N
 3635 fraction increases with decreasing altitude eventually reaching a plateau near
 3636 800 km (cf. Figure 57). The $^{14}\text{N}/^{15}\text{N}$ ratio varies from 76 for CH_3CN to 103 for
 3637 HC_3N and is a direct consequence of the primary source of nitrogen leading to
 3638 the formation of the molecule. Since $\text{N}(^2\text{D})$ is more enriched in ^{15}N than $\text{N}(^4\text{S})$
 3639 (cf. Figure 57), the species originating from $\text{N}(^2\text{D})$, such as CH_3CN should
 3640 be more enriched in ^{15}N than the species originating from $\text{N}(^4\text{S})$, such as HCN.
 3641 This translates into a higher $^{14}\text{N}/^{15}\text{N}$ in HCN than in CH_3CN . As the molecules
 3642 diffuse downward, several recycling pathways and secondary production of (not
 3643 fractionated) reactive nitrogen by galactic cosmic rays tend to homogenize the
 3644 $^{14}\text{N}/^{15}\text{N}$ ratio. Therefore, the model predicts at 200 km a ratio of ~ 55 for all
 3645 three nitrile species, which is in good agreement with the CIRS and ALMA
 3646 value for HCN and CH_3CN , respectively. This provides an overall check on the
 3647 reaction network and its multiple inputs. We emphasize that our calculations
 3648 are self-consistent and do not require any additional source of atomic nitrogen
 3649 in the upper atmosphere, unlike Liang et al. (2007).

Table 16: Modeled $^{14}\text{N}/^{15}\text{N}$ isotopic ratio in HCN, CH_3CN and HC_3N at 1200 and 200 km.

	HCN	CH_3CN	HC_3N
at 1200 km	88	76	103
at 200 km	55	54	52

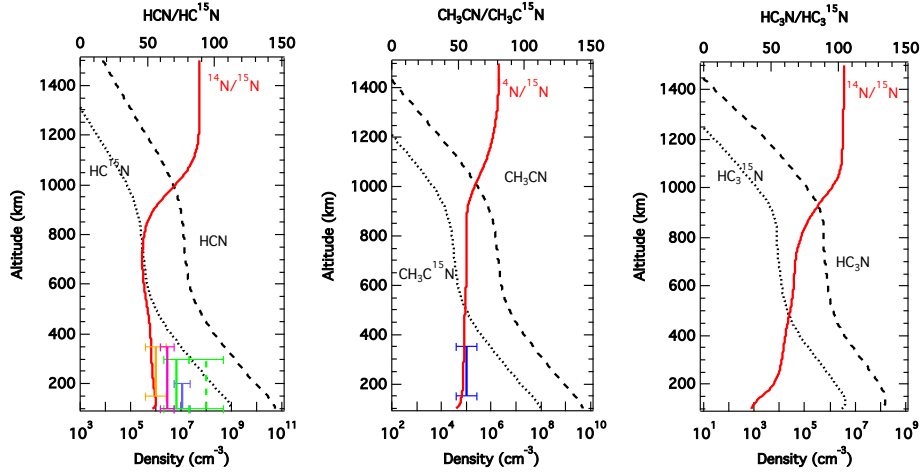


Figure 58: Modeled density of the three major nitrile species and their ^{15}N isotopologue versus altitude and associated observations as listed in Table 15. HCN, pink: Marten et al. (2002), green: Gurwell (2004), red: Vinatier et al. (2007b), blue: Courtin et al. (2011) (left panel); CH_3CN (middle panel); HC_3N (right panel).

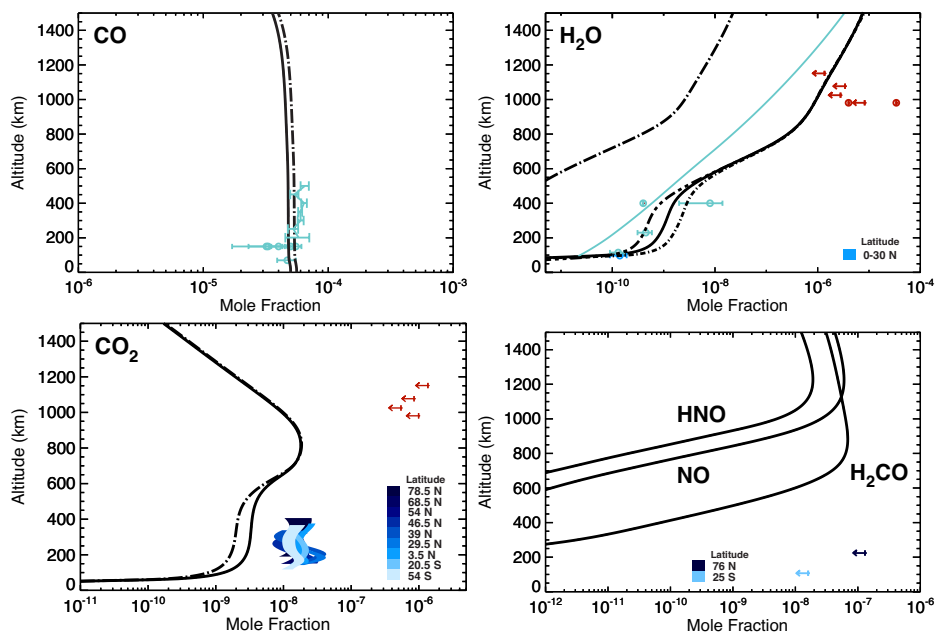


Figure 59: Calculated and observed mole fractions of CO (upper left panel), H₂O (upper right panel), CO₂ (lower left panel) and other minor oxygen-bearing species (lower right panel). Solid line: nominal (OH flux of $10^7 \text{ cm}^{-2} \text{ s}^{-1}$); dash-dot and long dash - double short dash line: eddy mixing coefficient $K_0 = 10^2$ and 10^3 cm^{-2} , respectively, section 2.4; long dashed dotted line: CO fixed, no external flux. The data shown for CO is from CIRS (De Kok et al., 2007; Teanby et al., 2010), VIMS (Baines et al., 2006; Bellucci et al., 2009; Fabiano et al., 2017), Herschel SPIRE (Courtin et al., 2011), Herschel PACS (Rengel et al., 2014); for H₂O is from ISO (Coustenis et al., 1998) (two circles at 400 km, one with small error bar is assuming constant profile, the one with large error bars is the scaled Lara profile), CIRS (Cottini et al., 2012) (lower 3 circles), INMS (Cui et al., 2009b) (upper limits are average of all the flybys, circles are individual detections from single flybys), Herschel (Moreno et al., 2012) (green line, SA profile); for CO₂ is from CIRS (Vinatier et al., 2010), INMS (Cui et al., 2009b); for H₂CO is from CIRS (Nixon et al., 2010).

3650 *4.2.3.3. Oxygen-Bearing Species.* Unlike N₂ and CH₄, which are at the origin of
 3651 all the minor nitriles and hydrocarbons detected on Titan, it became apparent
 3652 from early on that CO, the main reservoir of oxygen on Titan, cannot be the
 3653 single source of oxygen in this atmosphere. Specifically, an external flux of
 3654 oxygen is necessary to produce the OH atoms required for the CO₂ formation
 3655 (cf. section 3.2.3). This is illustrated in Figure 59, where a test run with CO
 3656 fixed and no external oxygen flux produces H₂O densities that underestimate
 3657 the observations by 4 orders of magnitude.

3658 Early investigations about external sources of oxygen suggested that CO₂
 3659 could be produced through a chemical reaction scheme that begins with an
 3660 influx of H₂O into the upper atmosphere from micrometeorite ablation (Lara
 3661 et al., 1996; Toublanc et al., 1995; Yung et al., 1984). However, these models
 3662 had some difficulty in reproducing the abundance of all three observed species
 3663 and a different approach for the origin of O on Titan was needed.

3664 The detection of O^+ precipitating into Titan's atmosphere by CAPS (Hartle
3665 et al., 2006) has offered a valid alternative to those suggestions. A photochem-
3666 ical model was presented by Hörst et al. (2008) in which the oxygen ions are
3667 incorporated into CO and CO_2 and the observed abundances of CO, CO_2 and
3668 H_2O are simultaneously reproduced using an oxygen flux of $\sim 10^6 \text{ cm}^{-2} \text{ s}^{-1}$
3669 consistent with the CAPS observations during TA and an OH flux in agreement
3670 with predicted production from micrometeorite ablation (cf. Figure 3 in Hörst
3671 et al. (2008)).

3672 The O^+ ions are stopped as neutral O atoms, in the ground state ($O(^3P)$)
3673 or in some excited state ($O(^1D)$, $O(^1S)$). H_2O can easily be converted (through
3674 photolysis or reactions with radicals) into OH radicals. Therefore, a steady state
3675 between OH and H_2O is established down to the stratosphere. In this model,
3676 the main production peak for CO occurs at ~ 1100 km, where $O(^3P)$ is primarily
3677 deposited. A second peak at ~ 200 km is, instead, due to the CO_2 photolysis.
3678 It is essential to have sources of both atomic oxygen and OH or H_2O : O alone
3679 would produce only CO, while input of OH or H_2O alone does not produce CO
3680 and leads only to the production of CO_2 if CO is already present.

3681 At that time, the only observation available for H_2O was that from ISO,
3682 which provided a fairly loose constraint with a mole fraction of $8_{-4}^{+6} \times 10^{-9}$ in
3683 the stratosphere, assuming a profile constant with height above the condensation
3684 level (Coustenis et al., 1998). More recent H_2O observations from CIRS and
3685 Herschel show that the H_2O relative abundance strongly increases with altitude
3686 with mole fractions of 4.5×10^{-10} at 230 km and 7×10^{-10} at 400 km (Cottini
3687 et al., 2012; Moreno et al., 2012). Both observations indicate that the Hörst
3688 et al. (2008) model is too "water-rich" with a too shallow slope over 100-300
3689 km.

3690 As a follow-up, Moreno et al. (2012) reconsidered the oxygen chemistry by
3691 updating the Lara et al. photochemical model. They fixed CO at the lower
3692 boundary but they were unable to match both H_2O and CO_2 with a given
3693 OH/ H_2O flux. Their OH flux required to match the Herschel H_2O observations
3694 is about $3 \times 10^5 \text{ cm}^{-2} \text{ s}^{-1}$ but this leads to a CO_2 mole fraction one order of
3695 magnitude short below the measured value. They observed that neither the OH
3696 versus H_2O form of the water input or the deposition profile is important. They
3697 envisaged a direct injection of CO_2 but the required CO_2/H_2O ratio is inconsis-
3698 tent with cometary composition. They also considered some additional chemical
3699 loss for H_2O but given that the formation of CO_2 occurs predominantly from
3700 OH, the associated CO_2 profile remained inadequate. Subsequently, Krasnopolsky
3701 (2012) did manage to match CO, CO_2 and H_2O pretty well (cf. Figure 3 in
3702 Krasnopolsky (2012)) with a H_2O and O^+ flux of 4.78×10^6 and $3.46 \times 10^6 \text{ cm}^{-2}$
3703 s^{-1} , respectively, albeit with the wrong chemistry as discussed in the following.

3704 In order to tackle this problem, we have calculated new rates for the OH +
3705 CH_3 reaction (cf. section 3.2.3). The main difference between our new scheme
3706 and the one in Hörst et al. (2008) is that it gives mostly CO in our case via
3707 CHOH, while it gives mostly H_2O in their case. As a matter of fact, we are
3708 essentially back to last century's models, where this reaction was considered to
3709 produce $CO + 2 H_2$ (Wong et al., 2002), and therefore to form a C-O bond

3710 instead of recycling back OH to H₂O.

3711 With the new reaction rates, it became virtually impossible to reproduce the
3712 observations with the previous O(³P)/OH fluxes. As a matter of fact, an O(³P)
3713 input is no longer required as OH alone can now lead to H₂O, CO and CO₂. The
3714 mole fractions of the most abundant oxygen-bearing species calculated with an
3715 OH/H₂O flux of 10⁷ cm⁻² s⁻¹ (and no atomic oxygen) are shown in Figure 59.
3716 Although H₂O and CO₂ are overestimated and underestimated, respectively by
3717 a factor of 10, this is the best fit that we could achieve with any combination of
3718 O(³P)/OH/H₂O/CO₂, irrespectively of observational constrains regarding the
3719 flux. This OH flux is consistent with the INMS observations of H₂O as well as
3720 H₃O⁺ (cf. Figure 49) in the upper atmosphere.

3721 Interestingly enough, recent studies (Sillanpää and Johnson, 2015; Snowden
3722 et al., 2018) seem to indicate that the O⁺ flux in Titan's plasma wake during
3723 TA was unusually high and that the average O⁺ flux is around 5 × 10⁴ cm⁻²
3724 s⁻¹, instead of 10⁶ cm⁻² s⁻¹ as reported in Hartle et al. (2006). Some test runs
3725 indicate that as long as the O⁺ flux stays below 10⁵ cm⁻² s⁻¹, it does not have
3726 any impact on the abundance of the major species. However, Hartogh et al.
3727 (2011) inferred that neither Enceladus' activity or micrometeorites are likely to
3728 provide a flux large enough for them to be the ultimate source of water in the
3729 upper atmosphere of Titan.

3730 The difficulty of finding the origin of Titan's water with the current known
3731 external sources supports the idea first put forward by Moreno et al. (2012) of a
3732 variable oxygen input. This hypothesis is based on the fact that CO, CO₂ and
3733 H₂O have very different lifetimes (in our model ~2 Myrs., ~2 kyrs., ~3 yrs.,
3734 Titan years). To follow on this idea, Lara et al. (2014) used a time-dependent
3735 model where they fixed CO at the lower boundary and initialized the oxygen
3736 compounds to the steady state solution profiles. Then, the oxygen sources were
3737 cut to zero and the oxygen species evolved over time according to $\phi(\text{OH}) =$
3738 $\phi_0(\text{OH}) \times \exp(-(t/\tau))$. They obtained a satisfactory set of solutions ($\phi(\text{OH}) =$
3739 $1 - 2 \times 10^7 \text{ cm}^{-2} \text{ s}^{-1}$, $t_0 = 290\text{-}360 \text{ yrs.}$, $\tau = 100 \text{ yrs.}$) if the targeted water
3740 profile was the one retrieved from CIRS, whereas the approach was unsuccessful
3741 if the targeted water profile was the one retrieved from Herschel, unless some
3742 additional loss to the haze was added.

3743 Subsequently, Dobrijevic et al. (2014) investigated two different scenarios,
3744 one where CO is from an internal source and one where it originates from
3745 external O and OH/H₂O. In the first case, they could match both H₂O and
3746 CO₂ with an OH flux of 2.6 × 10⁶ cm⁻² s⁻¹ and CO fixed at the lower boundary.
3747 In the second case, they could match everything with OH/O fluxes of 2.6 × 10⁶
3748 and 1.6 × 10⁶ cm⁻² s⁻¹, respectively and an integration time adjusted to 10¹⁶
3749 s to get to the agreement for CO. They concluded that the oxygen input (both
3750 OH from micrometeorites and O from Enceladus) must have started 300 Myrs.
3751 ago, a point already raised in Hörst et al. (2008).

3752 In order to definitively clarify the source of oxygen on Titan, future work
3753 includes:

- 3754 • Analysis of the CAPS and CDA data to better constrain the external

3755 sources of oxygen (OH_x^+ from Enceladus, H_2O from micrometeorites) in
3756 order to evaluate their average flux and variability with time.

3757 • Analysis of the INMS data to better constrain the density and variability
3758 of H_2O and H_3O^+ in the upper atmosphere, and new observations of
3759 H_2O in the lower atmosphere to clarify the discrepancy between CIRS
3760 and Herschel. The detection of a 4th oxygen species would also be a
3761 valuable asset. According to our model results, H_2CO appears as the best
3762 candidate.

3763 • Investigation of a range of possible chemical evolutionary tracks through
3764 the development of time dependent photochemical models with state-of-
3765 the-art chemistry.

3766 4.3. The GCR Layer

3767 The permittivity, waves and altimetry (PWA) experiment onboard the Huy-
3768 gens probe measured a peak electron density of $\sim 650 \text{ cm}^{-3}$ at 65 km (Hamelin
3769 et al., 2007; López-Moreno et al., 2008). In our study, the ion density peaks
3770 at 90 km, with a magnitude of $\sim 2000 \text{ cm}^{-3}$, which implies that it is not so
3771 consistent with the electron densities measured by Huygens. Our model does
3772 not take into account electron attachment onto aerosols or electrophilic species,
3773 which could reduce the electron densities by significant factors (Borucki et al.,
3774 1987; Borucki and Whitten, 2008). Molina-Cuberos et al. (1999a,b) calculated
3775 the vertical distributions of ions resulting from the impact of cosmic radiation
3776 and subsequent ion-neutral chemistry. The GCR ionization peak is similar in
3777 both altitude and magnitude with that obtained in our work.

3778 The chemistry resulting from GCR is essentially initiated by nitrogen atoms
3779 ($\text{N}(^4\text{S})$ and $\text{N}(^2\text{D})$) and to a lower extent ions (N_2^+ and N^+), the production
3780 of CH_4 fragments being lower by a factor of ~ 30 (cf. section 2.6). $\text{N}(^4\text{S})$ leads
3781 to HNC (R_n289b) and to the secondary formation of many nitrogen radicals,
3782 including NH (R_n293a) followed by NH_2 (R_n333), and H_2CN (R_n290a). NH_2
3783 radicals are responsible for the subsequent production of NH_3 (R_n350b), N_2H_4
3784 (R_n361b) and CH_3NH_2 (R_n349), and H_2CN for that of HNC (R_n395b). The
3785 production of $\text{N}(^2\text{D})$ leads directly to CH_2NH (R_n307a) and also to the for-
3786 mation of the HC_2N radicals (R_n308). The latter, in combination with $\text{N}(^4\text{S})$,
3787 produce C_2N_2 (R_n300).

3788 Our column-integrated abundances of some selected species with and with-
3789 out GCR impact are presented in Table 17. We do observe an impact around
3790 100 km on some minor nitrogen-bearing species such as NH_3 , HNC, CH_2NH ,
3791 CH_3NH_2 , N_2H_4 , $\text{C}_2\text{H}_3\text{CN}$ and C_2N_2 . C_6H_6 and C_4N_2 do not exhibit any sig-
3792 nificant change in their vertical profile, with a column-integrated abundance
3793 increase of about 30% only. The addition of GCR brings C_2N_2 in better agree-
3794 ment with the observations (see left panel of Figure 54) although as we men-
3795 tioned earlier, we do not have an appropriate observation to compare to. NH_3
3796 is very close to the available upper limits at low latitude (cf. left panel of Figure
3797 50), while the HNC column-integrated abundance exhibits a 50-fold increase

3798 and is therefore no longer in agreement with the observations (cf. Table 11).
 3799 This is linked to the presence of $C_4H_3NH^+$ that forms HNC through electron re-
 3800 combination ($R_{er,115c}$) but we highlight that both rate and products have been
 3801 estimated. The photodissociation cross sections of HNC have very recently been
 3802 calculated and it was found that HNC is photodissociated faster than HCN by
 3803 one order of magnitude for the solar radiation field, at 1 au (Aguado et al.,
 3804 2017). Future models should test these cross sections to check their impact on
 3805 the HNC abundance in the atmosphere of Titan. It is also possible that HNC
 3806 efficiently forms aggregates, a process that could lead to a significant decrease
 3807 of its density.

Table 17: Calculated column-integrated abundances (molecules cm^{-2}) of the species most affected by GCR.

Species	Model without GCR	Model with GCR
NH_3	8.9×10^{11}	5.1×10^{15}
HNC	8.9×10^{12}	4.5×10^{14}
CH_2NH	4.1×10^{13}	1.3×10^{15}
CH_3NH_2	1.7×10^{12}	4.9×10^{14}
N_2H_4	1.2×10^{10}	2.4×10^{13}
C_2H_3CN	3.2×10^{13}	9.6×10^{14}
C_2N_2	4.7×10^{11}	2.9×10^{13}

3808 In both the Lavvas et al. and Dobrijevic et al. models, the inclusion of
 3809 nitrogen atoms from GCR impact induces some drastic increase of the CH_2NH
 3810 mole fraction and to a lesser extent of C_4N_2 (cf. Figures 9d and 12a in Lavvas
 3811 et al. (2008b), Figure 16 in Loison et al. (2015)). Loison et al. (2015) also reports
 3812 the increase of several other nitrogen compounds, such as NH_3 , CH_3NH_2 , HNC,
 3813 C_2H_3CN , and C_2N_2 . Krasnopolsky (2014) observes a sharp peak in the C_6H_6
 3814 mole fraction at 50 km resulting from GCR.

3815 While the neutral pathways are fairly well constrained, the chemistry result-
 3816 ing from ion formation is very uncertain. As in the upper atmosphere, the ion
 3817 chemistry heavily depends on the presence of heavy nitrogen-bearing species,
 3818 whose profiles in the lower stratosphere cannot be constrained from observa-
 3819 tions and are therefore largely unknown (cf. section 4.2.3.2). With our current
 3820 chemical network and assumed vertical profiles, the density of NH_3 and HNC
 3821 relies on the abundance of C_3H_7N / C_5H_5N , and C_4H_3N , respectively.

3822 Figure 60 shows the predicted density of cations at the peak, with values
 3823 higher than $10^{-1} cm^{-3}$. The major species at the peak are the nitrogen-bearing
 3824 ions $C_3H_7NH^+$ ($m/z = 58$) and $C_5H_5NH^+$ ($m/z = 80$) and the hydrocarbon
 3825 ions $C_6H_9^+$ ($m/z = 81$), $C_6H_{11}^+$ ($m/z = 83$) and $C_7H_9^+$ ($m/z = 93$). Below the
 3826 peak, the cluster ion $HCO^+ \cdot H_2$ increases. In Molina-Cuberos et al. (1999a,b)
 3827 model, the most abundant ions above the peak are purely covalent hydrocarbon
 3828 ions with four or more carbon atoms and a few nitrogen-bearing ions. Below
 3829 the peak, the ionosphere is mainly composed of cluster ions such as $CH_5^+ \cdot CH_4$,
 3830 $HCO^+ \cdot H_2$, $HCNH^+ \cdot C_2H_4$ and $CH_4^+ \cdot N_2$, formed by three-body processes.

3831 Unfortunately, 3-body reaction rate coefficients are poorly known as well as loss
 3832 processes for adduct species. There are no observations that constrain the ion
 3833 composition in the lower atmosphere.

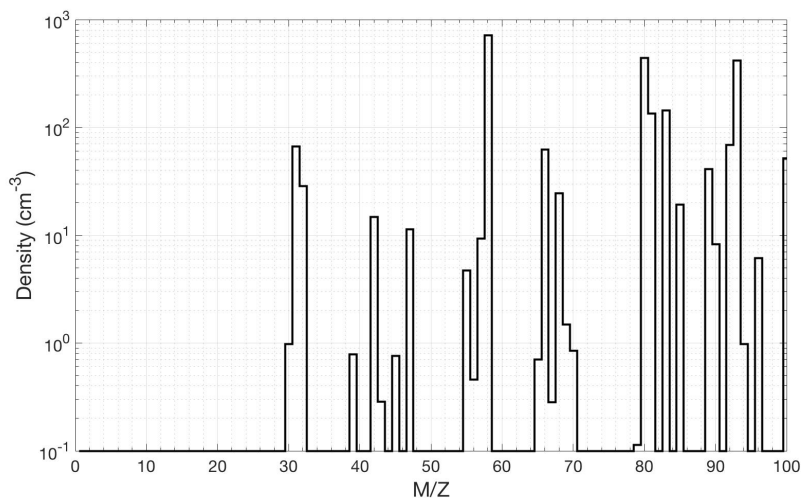


Figure 60: Calculated ion mass spectrum at 90 km.

3834 5. Discussion

3835 5.1. The Puzzle of the Overestimation of $C_2H_5^+$ and $HCNH^+$

3836 We return here to the results described in section 3.1.1.3, especially to those
 3837 ions whose density in Titan's upper atmosphere is smaller than predictions from
 3838 theoretical models, i.e. the dominant $HCNH^+$ ion but also $C_2H_5^+$. All other
 3839 studies do find the same discrepancy, thereby suggesting a lack in our under-
 3840 standing of the reactions that control the first steps of the chemistry (Robertson
 3841 et al., 2009; Mandt et al., 2012a; Westlake et al., 2012; Sagnières et al., 2015).

3842 A mechanism that would lead to a reduction of the electron density in Ti-
 3843 tan's ionosphere appears necessary as well. An analysis of Cassini observations
 3844 demonstrates that the observed electron densities are lower by a factor of 2 than
 3845 densities calculated with photochemical models under the conditions of the ob-
 3846 servations (Vigren et al., 2013). This problem seems to appear only during
 3847 the daytime where energy deposition is dominated by solar photons. During
 3848 night-time, the observed electron densities are found to be in good agreement
 3849 with predictions from models of magnetospheric electron ionization. Similarly,
 3850 on the night-side the densities of the primary ions are in agreement with the
 3851 INMS measurements (Vigren et al., 2015). LP data shows electrons soaked up
 3852 by aerosols and the negative charge on these exceed that of the ions. However,
 3853 electrons are preferentially soaked up in the nightside (Shebanits et al., 2016)
 3854 while electron densities are overestimated by models only on the dayside (Vigren

3855 et al., 2013, 2015). This therefore doesn't seem to be a possible explanation.
3856 Moreover, having electrons soaked up by aerosols on the dayside would actually
3857 worsen the model overestimation of the $C_2H_5^+$ and $HCNH^+$ densities because
3858 the recombination of positive ions with charged aerosols is not as efficient as
3859 with electrons (see e.g. Vigren et al. (2014)).

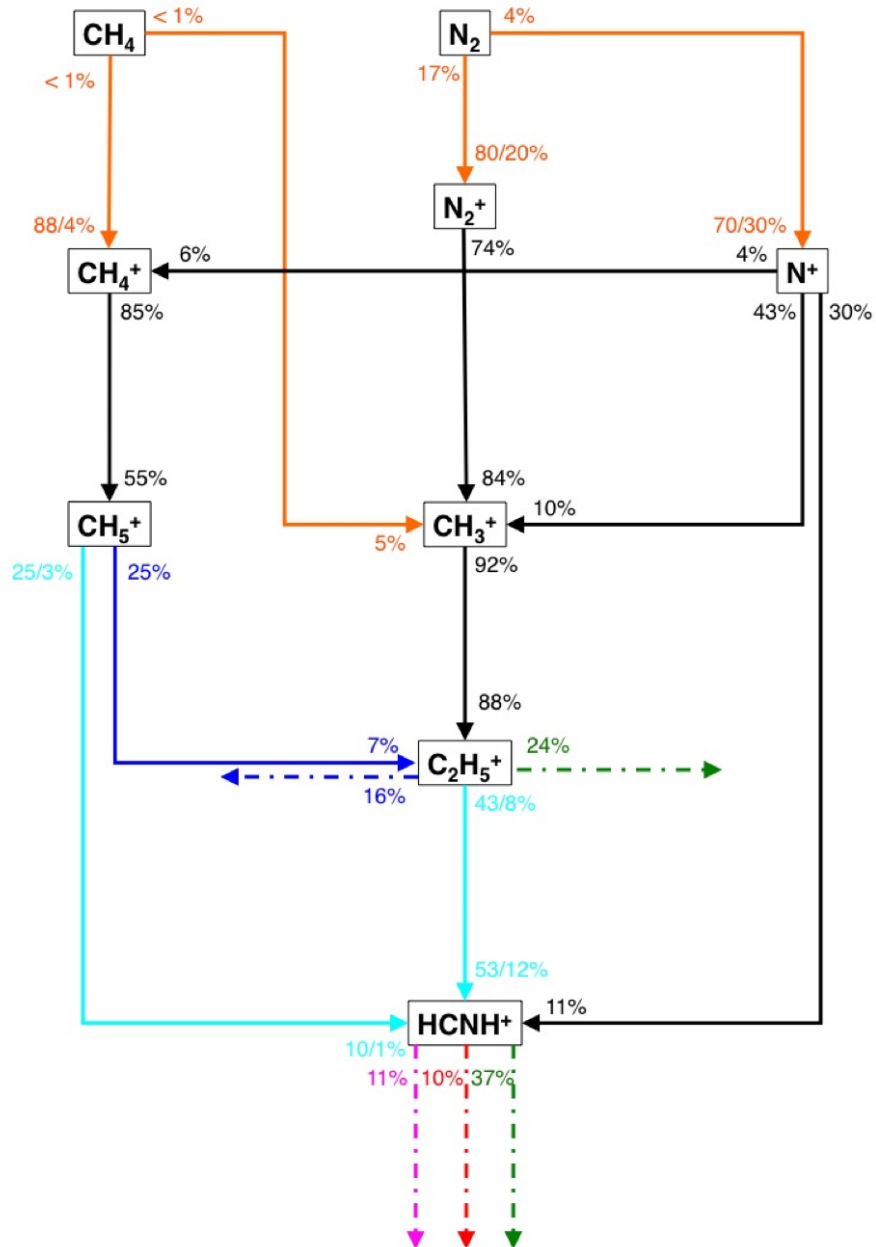


Figure 61: Flowchart highlighting the very first steps of the ionospheric chemistry. Orange: $h\nu/e_s^-$, green: e_T^- , black: CH₄, blue: C₂H₄, pink: C₄H₂, cyan: HCN/HNC, red: C₂H₃CN. The percentages represent the calculated contribution of the given channel to the total production/loss of the given species for a globally average model.

3860 *5.1.1. Reactivity and Nature of HCNH⁺*

3861 Westlake et al. (2012) analyzed the processes producing and consuming
3862 HCNH⁺ in order to determine the cause of the discrepancy between calcula-
3863 tions and observations. They identified four potential culprits for the model
3864 overestimation that are detailed below. We repeated numerical experiments
3865 (1)-(3) and essentially reached the same conclusions.

- 3866 1. Errors in the HCN atmospheric densities: The HCN mole fraction is poorly
3867 constrained by INMS and there is a large range of acceptable values ($3 \times$
3868 $10^{-4} - 3 \times 10^{-3}$). However, while decreasing the HCN density has the
3869 desired effect of decreasing the HCNH⁺ density, it does so at the expense of
3870 the CH₅⁺ and C₂H₅⁺ densities, which are as a consequence overestimated
3871 (cf. Figure 61 and section 3.1.1.2). Therefore, the HCN profile cannot be
3872 held responsible for the overestimation of the ionospheric densities.
- 3873 2. Errors in the electron density, electron temperature, or electron recombi-
3874 nation coefficients of HCNH⁺: Electron recombination is the major loss of
3875 HCNH⁺ (cf. Figure 61). The electron recombination rate depends on both
3876 the electron density and temperature (cf. section 3.1.1.2). Runs using dif-
3877 ferent realistic sets of values for the electron density (taken as either the
3878 LP total electron density or the INMS total ion density) and temperature
3879 (taken as either the measured LP electron temperature or the calculated
3880 electron temperature of Richard et al. (2011)) show that these paramet-
3881 ers have some effect on the HCNH⁺ density but cannot completely solve
3882 the problem. Both electron recombination rate constants available in the
3883 literature (cf. section 3.1.1.2) were also tested but none is fast enough to
3884 lead to a sufficient loss of HCNH⁺.
- 3885 3. Missing reactions with heavy neutrals or negative ions: Large amounts of
3886 heavy neutrals could lead to a significant loss of HCNH⁺ through proton
3887 exchange reactions. However, the expected scale height of such species
3888 is incompatible with the large excess of HCNH⁺ still observed at higher
3889 altitude. The positive - negative ion recombination rates and observed
3890 negative ion densities are too small to be competitive with ion - neutral
3891 reactions.
- 3892 4. Missing reactions with light species: The reaction of HCNH⁺ with H₂,
3893 CH₄, C₂H₂ or C₂H₄ would lead to enough destruction of HCNH⁺ were
3894 the rate constants fast enough. Although these reactions have all been in-
3895 vestigated experimentally or theoretically and have been found to be slow
3896 (typically $k < 5 \times 10^{-13} \text{ cm}^3 \text{ s}^{-1}$), Westlake et al. (2012) argue that the
3897 pressures and temperatures used were not relevant to the Titan's iono-
3898 sphere and that the rate constants could actually be much faster. They
3899 finally compute that rate constants equal to 6×10^{-11} , 1×10^{-11} , $2 \times$
3900 10^{-10} and $2 \times 10^{-10} \text{ cm}^3 \text{ s}^{-1}$ for H₂, CH₄, C₂H₂ or C₂H₄, respectively
3901 would solve the HCNH⁺ issue.

3902 In response to item (4), Demarais et al. (2013) investigated these reactions
3903 experimentally and theoretically to probe for the specific products suggested

3904 by Westlake et al. (2012). In all cases, the products were not observed experi-
3905 mentally, which is rationalized computationally by the presence of large energy
3906 barriers. However, association products for the reactions with C_2H_2 and C_2H_4
3907 have been found. In the experimental conditions, the adducts are stabilized by
3908 3-body collisions but in the Titan ionosphere, only radiative association could
3909 be efficient.

3910 Following this, we investigated theoretically the association rate for $HCNH^+ +$
3911 C_2H_4 (section 2.7.3.2) and found that k_R is only $4 \times 10^{-15} \text{ cm}^3 \text{ s}^{-1}$ at 150 K
3912 and this rate is too low for this reaction to be an efficient pathway for the loss
3913 of $HCNH^+$. The $HCNH^+$ addition to C_2H_2 (and HCN, another major neutral
3914 in the thermosphere) will certainly not be faster because the binding energy
3915 is much less and there are fewer vibrational modes. Therefore, we use a rate
3916 constant of $1.5 \times 10^{-15} \text{ cm}^3 \text{ s}^{-1}$ for both these reactions, based on Herbst et al.
3917 (1989). Again, this is too slow to significantly impact the $HCNH^+$ density.

3918 It is interesting to mention that the most stable form of this ion is the singlet
3919 linear $HCNH^+$ ($H-C^+=N-H$). The singlet methylenimine cation H_2CN^+ (H_2-
3920 $C=N^+$), which energetically lies 3.6 eV above $HCNH^+$, is inherently unstable.
3921 Four triplet isomers with stable geometries have been computed with energies at
3922 least 5.4 eV higher than the linear ion $HCNH^+$: H_2NC^+ , *cis*- $HCNH^+$, H_2CN^+
3923 and *trans*- $HCNH^+$ (Holzmeier et al., 2013). One could entertain the idea that
3924 the isomer formed in the ionosphere is not the one studied in the laboratory
3925 and that their different reactivity could explain the observed discrepancy.

3926 Semaniak et al. (2001) give an extensive discussion supported by theo-
3927 retical calculations on the nature of the $HCNH^+$ ions present in the storage
3928 ring for dissociative recombination measurements. The conclusion is that the
3929 formaldehyde-like H_2CN^+ ions cannot be present in the ion source for stability
3930 or thermodynamic reasons. However, a combined crossed-beam (at 2 collision
3931 energies close to 4 eV) and theoretical study suggests that reaction ($R_{cn,593c}$)
3932 leads preferentially ($\sim 70\%$) to the triplet H_2CN^+ isomer ($+ H_2$) over both sin-
3933 glet ($+ 2H$) and triplet ($+ H_2$) $HCNH^+$ isomers (Žabka et al., 2010). Clearly,
3934 new investigations are required to clarify the nature of the $HCNH^+$ isomers and
3935 their respective reactivity before any further conclusion can be made.

3936 Since it seems difficult to stretch the chemistry currently present in models
3937 by enough to achieve our purpose, i.e. decrease the predicted $HCNH^+$ densities
3938 by a significant factor, we turn to other chemical processes that are missing
3939 from the models but nonetheless could significantly alter the chemistry.

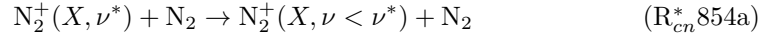
3940 5.1.2. *Vibrationally Excited Nitrogen*

3941 Lavvas et al. (2015) calculated the vibrational distribution of the ground
3942 state levels $N_2^+(X^2\Sigma_g^+)$ and $N_2^+(X^1\Sigma_g^+)$ and we use this investigation as a
3943 starting point to discuss the ramifications of vibrational excited nitrogen for
3944 the ionospheric densities.

3945 The $N_2^+(X, \nu^*)$ density demonstrates a rapid drop with increasing vibra-
3946 tional level. For example, at 1000 km only the $\nu = 1$ level has a fraction higher
3947 than 1% of the ground level. For any chemical reaction involving hot molecules

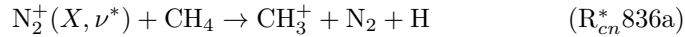
3948 to be competitive, the magnitude of the rate of the hot molecules should there-
 3949 fore be 100 times higher than that of the ground state.

3950 The main fate of $N_2^+(X, \nu^*)$ is to collide with N_2 and four possible outcomes
 3951 can be considered:



3952 Collisions of vibrationally excited N_2^+ ions ($\nu = 0-4$) can lead to vibrational
 3953 deactivation ($R_{cn}^* 854a$) as well as charge transfer ($R_{cn}^* 854b$), which essentially
 3954 only replenishes the N_2^+ ground state. The formation of N_3^+ ($R_{cn}^* 854c$) is
 3955 endothermic by 4.97 eV (Dutuit et al., 2013) and is inaccessible to levels with
 3956 moderate excitation. The formation of N_4^+ ($R_{cn}^* 854d$), even if fast enough (a
 3957 reaction rate of $10^{-11} \text{ cm}^3 \text{ s}^{-1}$ is required), is unlikely to affect the ionospheric
 3958 balance because its main fate will be reaction with methane to form CH_4^+ and
 3959 ultimately $HCNH^+$ (cf. Figure 61 and Lavvas et al. (2015)).

3960 The second major process defining the abundance of $N_2^+(X, \nu^*)$ is reaction
 3961 with methane:



3962 After taking into account the experimental uncertainties, the branching ratios
 3963 for the three channels are found to be independent of the ν state of reactant
 3964 N_2^+ for $\nu = 0-4$ (Dutuit et al., 2013; Xu et al., 2013) and this reaction cannot
 3965 differentially affect the ion densities.

3966 The variation of the recombination rate of N_2^+ with vibrational level has
 3967 also been considered in Lavvas et al. (2015) but this process is not efficient
 3968 either because the recombination rate of the hot ions is smaller than the rate
 3969 for the ground ion level (Bates and Mitchell, 1991). Therefore, a reduction of
 3970 the ionospheric densities due to loss of the primary N_2^+ ions seems unlikely
 3971 from the processes we have considered.

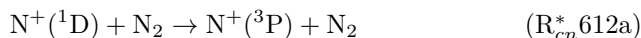
3972 A significant fraction of N_2 is in some vibrationally excited state of the
 3973 ground electronic state, about 10% for $\nu = 1,2$ and 1% for $\nu > 2$ (Lavvas et al.,
 3974 2015). These states have a lifetime of $10^7 - 10^{11} \text{ s}$ and are up to a few eV
 3975 above the ground state implying that some reactions considered endothermic
 3976 could actually occur with some fraction of the N_2 population. Lavvas et al.
 3977 (2015) considered the chemical reactivity of $C_2H_5^+$ and $HCNH^+$ with hot ni-
 3978 trogen molecules but the population of those having enough internal energy is

3979 too small to affect the overall abundance of these major ions. Vibrational en-
 3980 ergy transfer is another possible outcome of those collisions but for polyatomic
 3981 ions the recombination rate is not expected to be significantly affected by their
 3982 vibrational excitation and will not affect the ionospheric balance either.

3983 5.1.3. Electronically Excited Nitrogen

3984 The ionization cross sections of N_2 are well constrained but a key issue is
 3985 the description of the electronic state of the dissociation fragments (R. Thissen,
 3986 private communication, 2013). For example, the dissociative ionization of N_2
 3987 is known to lead to $N^+(^3P) + N(^4S)$, $N^+(^1D) + N(^4S)$ and $N^+(^3P) + N(^2D)$,
 3988 depending on the photon energy. However, our calculations only consider the
 3989 production in the $N^+(^3P) + N(^2D)$ states.

3990 The $N^+(^1D)$ state lies 1.9 eV above the $N^+(^3P)$ ground state and has a
 3991 lifetime of 258 s (Dutuit et al., 2013). If $N^+(^1D)$ is formed in sufficient amount
 3992 and its reactivity is significantly different from that of $N^+(^3P)$, its consideration
 3993 in the calculations could alter the N^+ density and have some impact on the
 3994 subsequent chemistry.



3995 The quenching of $N^+(^1D)$ by collisions with N_2 , channel ($R_{cn}^* 612a$), is negligible
 3996 due to its spin forbidden nature (Dutuit et al. (2013) after Freysinger et al.
 3997 (1994)). Channel ($R_{cn}^* 612b$) is exothermic by 0.9 eV but the first spin-allowed
 3998 channel is endothermic by 1.53 eV (Dutuit et al., 2013). One obvious possibility
 3999 is that it does react with $N_2(X, \nu^*)$ but the relevant hot states are not abundant
 4000 enough for this reaction to have an impact on N^+ (Lavvas et al., 2015).



4001 The total rate constant seems to be the same as for the $N^+(^3P)$ state, i.e. $1.2 \times$
 4002 $10^{-9} \text{ cm}^3 \text{ s}^{-1}$ at 300 K. The product branching ratios ($R_{cn}^* 593a$)/($R_{cn}^* 593b$)/($R_{cn}^* 593c$)/($R_{cn}^* 593d$)
 4003 are equal to 0.09/0.18/0.33/0.40. In comparison with the reactivity of $N^+(^3P)$,
 4004 the ratio $(CH_3^+ + CH_4^+)/(\text{HCN}^+ + \text{HCNH}^+)$ decreases from 1.6 to 0.96, cor-
 4005 responding to an increase in the yield of the nitrogen-containing compounds.
 4006 The strongest effect is a complete inversion of the ratio CH_3^+/CH_4^+ , from 4.4
 4007 to 0.22 (Dutuit et al. (2013) after Tichý et al. (1979) and Alcaraz et al. (2004)).
 4008 $N^+(^4S)$ also reacts with H_2 and all the major hydrocarbons but these are minor
 4009 loss processes for N^+ and these reactions cannot substantially affect its density.

4010 Carrasco et al. (2008) evaluated the effect on model predictions of the dif-
4011 ferent reactivity of $N^+(^1D)$ than $N^+(^3P)$ with methane. They made a test by
4012 considering the extreme scenario in which 100% of the N^+ ions would be in the
4013 excited state. The effect is globally weak, the biggest difference consisting in
4014 the increase of the CH_5^+ and $C_2H_3^+$ densities by tens of percent. N^+ is not
4015 affected (the total rate constant is identical for both states) while the effect on
4016 $HCNH^+$ is almost negligible (cf. their Figure 3).

4017 This result is consistent with our observation that the production of $HCNH^+$
4018 directly from channel (R_{cn}^* 593c) and indirectly from channel (R_{cn}^* 593d) followed
4019 by the reaction of HCN^+ with CH_4 is only 15%. Moreover, following the study
4020 of Nicolas et al. (2003a), Carrasco et al. (2008) estimate that the actual fraction
4021 of $N^+(^1D)$ produced in the photoionization of N_2 represents only about 15% of
4022 the N^+ population. Therefore, it appears that the $N^+(^1D)$ state has no relevant
4023 effect on $HCNH^+$ (and the model as a whole) and it seems reasonable to ignore
4024 it.

4025 Finally, the first two excited states of N_2^+ , ($A^2\Pi_u$) and ($B^2\Sigma_u^+$), have life-
4026 times of ~ 10 ms and ~ 70 ns, respectively (Dutuit et al., 2013) and cannot play
4027 any active role in the chemistry.

4028 5.2. Molecular Weight Growth

4029 There is much uncertainty in the growth mechanisms of Titan’s aerosols,
4030 particularly how simple precursors form larger molecules that ultimately seed
4031 haze particles. Generalized mechanisms focusing on radical chemistry have been
4032 put forward for four chemical families: polyynes, nitriles, copolymers (mixed
4033 hydrocarbons and nitriles), and aromatics (Lebonnois et al., 2002; Wilson and
4034 Atreya, 2003; Lavvas et al., 2008a).

4035 Wilson and Atreya (2003) and Lebonnois (2005) found that the aerosol pro-
4036 duction is concentrated around 200 km and that the main contribution comes
4037 from $C_6H_5 + C_2H_2$ and $H_2CN + HCN$. Note that the rate coefficient of both
4038 reactions was not available at the Titan temperatures and was extrapolated
4039 from combustion studies for the first reaction (Wang and Frenklach, 1994) and
4040 estimated for the second one. Our calculations show that the entrance barrier
4041 of these reactions is high and consequently the predicted rates are small (cf.
4042 Appendix A).

4043 Lavvas et al. (2008b) obtain a secondary aerosol production in the upper
4044 atmosphere dominated by copolymers ($C_3N + C_4H_2$, R_n 446) around 800 km and
4045 nitriles ($CN + C_2H_3CN$, R_n 392) above 1000 km. The existence of this secondary
4046 peak is supported by the Descent Imager/Spectral Radiometer (DISR) haze
4047 extinction profile (Tomasko et al., 2005) and the Huygens Atmosphere Structure
4048 Instrument (HASI) temperature profile (Fulchignoni et al., 2005). The total
4049 column production rate from both low and high altitude production is 1.3×10^{-14}
4050 $g\ cm^{-2}\ s^{-1}$ for monomers of 7.25 Å radius.

4051 The model of Krasnopolsky reproduces this high altitude peak, although in
4052 this case, reactions of C_6H and C_3N with C_4H_2 (R_n 236, R_n 446) are signifi-
4053 cant (cf. Figure 7 in Krasnopolsky (2014)), with a total production of 10^{-13}

4054 $\text{g cm}^{-2} \text{ s}^{-1}$. It also considers for the first time recombination of heavy ions
 4055 ($\text{C}_9\text{H}_{11}^+$, $\text{C}_{10}\text{H}_9^+$ and $\text{C}_{10}\text{H}_{11}^+$) as a source of haze, although this turns out to
 4056 be negligible (less than 1% of the neutral polymerization channels).

4057 Lavvas et al. (2011c) consider formation of polycyclic aromatic compounds
 4058 through neutral reactions starting from benzene and involving the CN, C_2H
 4059 and HCCN radicals. However, the main focus of this investigation is to identify
 4060 the main processes that can affect the aerosol evolution and these pathways are
 4061 mostly proxies for the possible contribution of radicals.

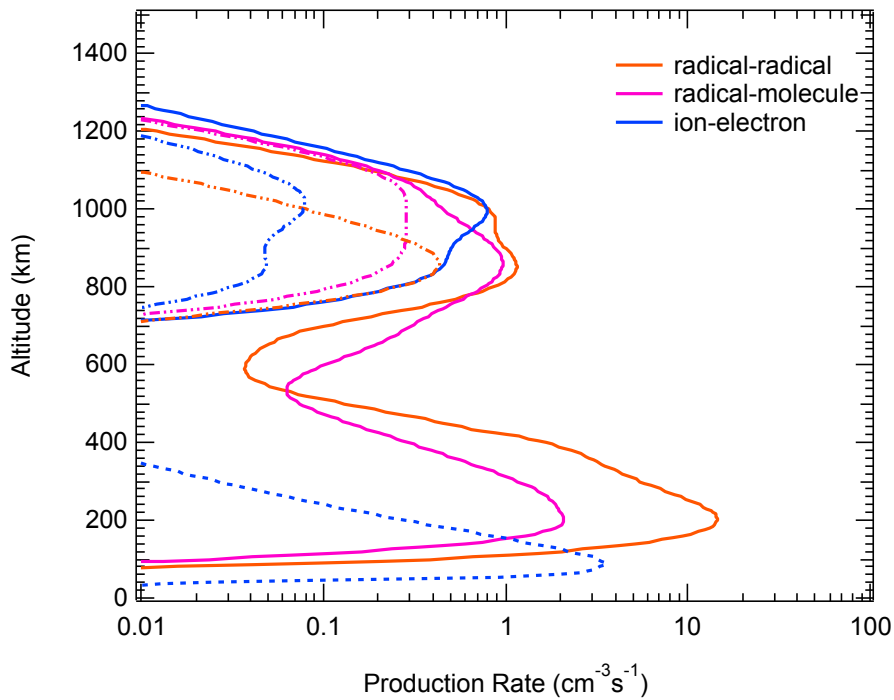


Figure 62: Calculated production rate of species that are considered as aerosol seeds. Dot-dashed lines represent the production rate of nitrogen-bearing species. The dotted line shows the production rate from the electron recombination of cluster ions resulting from GCR impact; they all contain nitrogen.

Table 18: Calculated column-integrated production rates ($\text{molecules cm}^{-2} \text{ s}^{-1}$) of the three generic channels.

Channels	Thermosphere	Stratosphere	Total
Radical-Radical	6.6×10^7	2.9×10^8	3.6×10^8
Radical-Molecule	4.6×10^7	4.4×10^7	9.0×10^7
Ion-Electron	3.6×10^7	4.1×10^6	4.0×10^7
Total	1.5×10^8	3.4×10^8	4.9×10^8

4062 Photochemical models as they currently exist are not well suited to predict-
4063 ing haze production rates. Our understanding of the pathways leading to the
4064 observed aerosols is still at a preliminary stage and it is likely that those pro-
4065 posed so far are only a small fraction of a multitude of chemical processes acting
4066 simultaneously. As a result, models can at best provide an upper limit from the
4067 sum of the production rate of all the species that do not have any loss process.
4068 Our total aerosol flux of $\sim 5 \times 10^8 \text{ cm}^{-2} \text{ s}^{-1}$ (cf. Table 18) translates to a mass
4069 production of $\sim 6 \times 10^{-14} \text{ g cm}^{-2} \text{ s}^{-1}$, if considering that the transition occurs
4070 at a mean molecular mass of 70-80 g mol^{-1} , which corresponds to a molecule
4071 having 5 or 6 carbon atoms. A total aerosol mass production of $3 \times 10^{-14} \text{ g}$
4072 $\text{cm}^{-2} \text{ s}^{-1}$ is required to match the haze optical properties retrieved by the DISR
4073 observations (Lavvas et al., 2010). This implies that about 50% of the species
4074 that we do not track should further decompose back to smaller molecules while
4075 50% should evolve to aerosol particles.

4076 We find that the copolymers and nitriles contribution to the radical-molecule
4077 channel is negligible, with a total rate of $\sim 3 \times 10^4 \text{ cm}^{-2} \text{ s}^{-1}$. The polyene type
4078 pathways are somewhat significant with $\text{C}_6\text{H} + \text{C}_2\text{H}_2$, ($\text{R}_n 229$) and $\text{C}_4\text{H} + \text{C}_2\text{H}_4$,
4079 ($\text{R}_n 196$) representing $\sim 15\%$ of the total production. Electron recombination of
4080 nitrogen-bearing cluster ions formed in the GCR layer leads to the production
4081 of many nitrile species with a total integrated production rate of $3 \times 10^{-7} \text{ cm}^{-2}$
4082 s^{-1} , which is similar to the value calculated by Molina-Cuberos et al. (2002).
4083 To summarize, although our total aerosol mass production is of the same order
4084 of magnitude as previous models (Lavvas et al., 2008b; Krasnopolsky, 2014),
4085 the specific molecular growth reactions are very different.

4086 Instead of discussing further specific reaction pathways, we adopt an alterna-
4087 tive approach consisting in grouping reactions in three generic channels: radical-
4088 radical, radical-molecule and ion-electron (cf. Figure 62). Not surprisingly, pro-
4089 duction rates peak where the energy deposition is maximum, i.e. around 900
4090 and 200 km. Our major source of aerosols in the stratosphere originates from
4091 the recombination of hydrocarbon radicals (amongst which the most efficient are
4092 $\text{CH}_3 + \text{C}_4\text{H}_n$), a process that had never been put forward. The unprecedented
4093 efficiency of this process in our model ($2.9 \times 10^8 \text{ cm}^{-2} \text{ s}^{-1}$) is attributed to the
4094 consideration of radiative association reactions that become extremely efficient
4095 ($k = 8 \times 10^{-11} \text{ cm}^3 \text{ s}^{-1}$) when the number of carbon atoms involved reaches
4096 4 or 5 (Vuitton et al., 2012). In the thermosphere, all three channels have a
4097 similar contribution to the total production, values are given in Table 18.

4098 5.3. Effects of Stratospheric Aerosols

4099 The aerosols in the stratosphere of Titan have four important roles on the
4100 (photo)chemistry: (1) shielding of the UV flux, (2) recombination of H atoms on
4101 their surface, (3) heterogeneous removal of polar species, and (4) condensation
4102 nuclei.

4103 5.3.1. UV Shielding

4104 Aerosols are the dominant source of opacity for wavelengths $\geq 180 \text{ nm}$ in
4105 the stratosphere (cf. Figure 14) and aerosol shielding has a profound impact on

4106 the photochemistry. In our nominal model, aerosol opacities are derived from
4107 the single scattering albedo and extinction retrieved by DISR (Lavvas et al.,
4108 2010). However, a newer analysis of DISR data (Doose et al., 2016) implies a
4109 different aerosol scale height above 80 km. The impact of this recent study on
4110 the aerosol opacity has not been investigated yet. Can lack of fits for HC_3N
4111 and $\text{C}_2\text{H}_5\text{CN}$, i.e. species that are mostly lost by photodissociation, be resolved
4112 with small adjustments in aerosol opacity?

4113 To answer this question, we performed two model runs where the nominal
4114 aerosol opacity was either multiplied or divided by a factor of 2. Figures 44
4115 and 53 show the sensitivity for C2 hydrocarbons and some nitriles ($\text{C}_2\text{H}_3\text{CN}$
4116 and $\text{C}_2\text{H}_5\text{CN}$), respectively. The different choices of opacity do not significantly
4117 change the results. The mole fraction of C_2H_2 , C_2H_4 and the nitriles (not
4118 shown for HC_3N to avoid overcrowding the plot) increases by a few tens of
4119 percent from the low to high opacity run because of the increase in aerosol
4120 shielding and subsequent decrease in photodissociation rate for these species.
4121 Not surprisingly, the most sensitive species is C_2H_6 , which can be explained by
4122 the less effective photodissociation of C_2H_2 leading to a lower abundance of C_2H
4123 radicals and subsequently of CH_3 radicals, the precursors of C_2H_6 , as detailed
4124 in section 3.2.1.

4125 5.3.2. Atomic and Molecular Hydrogen Budget

4126 Since CH_4 is the ultimate source of all carbon atoms, the production of the
4127 more complex carbon species must be accompanied by comparable quantities
4128 of H or H_2 . Indeed, molecular hydrogen is the third most abundant species in
4129 Titan’s atmosphere, with a mole fraction of 10^{-3} at the tropopause (cf. Table
4130 11).

4131 Sekine et al. (2008b) introduced heterogeneous chemistry of hydrogen atoms
4132 in the model of Lebonnois (2005) and observed dramatic impacts on atomic
4133 hydrogen and heavy hydrocarbon profiles, as expected from the high reaction
4134 probabilities inferred in the laboratory (Sekine et al. (2008a), see section 2.7.5).
4135 According to their calculations, heterogeneous reactions increase the mole frac-
4136 tions of C_4H_2 and C_6H_5 by more than 2 orders of magnitude around 400 km.
4137 Although they did not perform a thorough comparison of their computed pro-
4138 files with available observations, they mention that the C_4H_2 profile obtained
4139 with heterogeneous processes is in better agreement with the CIRS observa-
4140 tions (Vinatier et al., 2007a), a conclusion also shared by Lavvas et al. (2008b).
4141 Krasnopolsky (2009) considers the same processes as Sekine et al. (2008b) and
4142 finds that formation of H_2 in the heterogeneous recombination of H with the
4143 haze is insignificant.

4144 In our model, the H production in the upper atmosphere peaks around 800
4145 km and occurs through direct photodissociation of CH_4 (J_d2a,c,d) and CH_3
4146 (J_d38), and reaction of CH with CH_4 (R_n47). H_2 is mostly produced by reaction
4147 of H with $^3\text{CH}_2$ (R_n3) and photodissociation of CH_4 (J_d2b). In the stratosphere,
4148 a secondary production of hydrogen atoms occurs through photodissociation of
4149 abundant unsaturated species such as C_2H_2 (J_d5), C_2H_4 (J_d6b), C_4H_2 (J_d12a)

4150 and C_6H_2 (J_d17a). Molecular hydrogen is essentially formed by photodissociation of C_2H_4 (J_d6a) and C_4H_4 (J_d13c), and reaction of H with C_2H_3 (R_n8b) and C_2H_5 (R_n10b). All the H_2 produced eventually escapes hydrodynamically from the exosphere (Strobel, 2010). Similarly, the hydrogen atoms formed in the thermosphere subsequently flow upward and escape the atmosphere at a rate of $3.0 \times 10^9 \text{ cm}^{-2} \text{ s}^{-1}$.

4156 Below 500 km, the heterogeneous reactions of atomic hydrogen atoms on the surface of aerosol particles become their dominant removal process and a sharp decrease in the atomic hydrogen density in the region centered around 400 km is evident as shown in the left panel of Figure 63. About 60% of the total H produced ends up adsorbed onto aerosols, a conclusion also shared by Sekine et al. (2008b). Here, hydrogen atoms are not recycled back to the gas phase and therefore, this process represents a net loss for hydrogen in the model and as a consequence, a decrease in the H_2 mole fraction is observed (cf. right panel of Figure 63). This is the opposite effect as reported in Lavvas et al. (2008b) because the latter include recombination of H atoms on the aerosols but not their hydrogenation. However, because H_2 is practically inert in the atmosphere, the actual fate of hydrogen atoms (sequestration at the surface of the aerosols or release in the atmosphere as H_2) has little impact on the chemistry, including haze formation, the essential point being their removal from the gas phase.

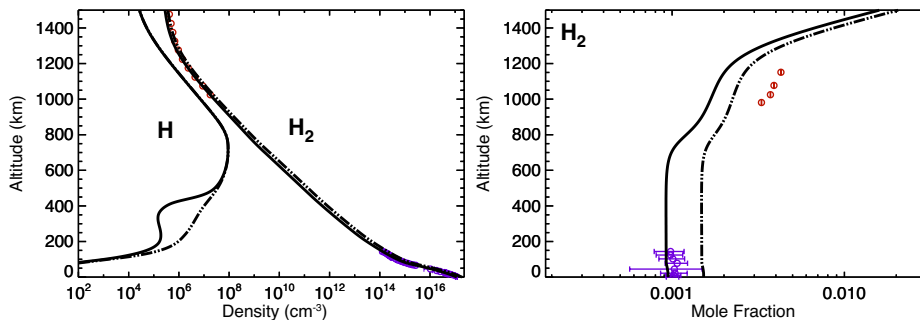


Figure 63: Calculated densities of H and H_2 (left panel). Calculated and observed mole fractions of H_2 with (solid line) and without (long dash-dot-dot line) atomic hydrogen heterogeneous loss (right panel).

4170 Combination of H with C_2H_2 , C_2H_4 , C_4H_2 and HC_3N (R_n7a , R_n9a , R_n21 ,
 4171 R_n258) are critical loss reactions for these species (section 2.7.3.1) and therefore
 4172 removal of H atoms strongly raises their stratospheric abundance. The vertical
 4173 profiles of C_2H_2 and C_2H_4 with and without the atomic hydrogen heterogeneous
 4174 loss process are shown in Figure 44. Their mole fractions increase by a factor
 4175 of ~ 2 and ~ 5 , respectively and are found to be closer to that of the CIRS mid-
 4176 latitude profiles when this heterogeneous chemistry is included. However, the
 4177 decrease in the atomic hydrogen population, allows for more diacetylene and
 4178 cyanoacetylene, with the simulated profiles (solid lines in Figure 47 (left panel)
 4179 and 53 (upper left panel)) being in worse agreement with the CIRS retrieved

4180 vertical profiles. Benzene is decreased by a factor of ~ 20 at 300 km (cf. right
4181 panel of Figure 47) because combination of H with C_6H_5 (R_n30), its main
4182 recycling reaction, has been reduced.

4183 It is interesting that the $H + C_2H_2$ (R_n7b) and $H + C_2H_4$ (R_n9b) hydrogen
4184 abstractions do not efficiently convert hydrogen atoms into molecular hydrogen,
4185 unlike stated in previous models. We note that the $H + C_4H_2$ and $H + HC_3N$
4186 abstraction reactions are endothermic.

4187 5.3.3. Nitriles Heterogeneous Chemistry

4188 Lara et al. (1999) reported difficulties in matching with their photochemical
4189 model the observed nitrile and hydrocarbon profiles and suggested that an ad-
4190 ditional chemical loss to the aerosols is required for HCN. Our nominal model
4191 does not include the heterogeneous reactions of molecules onto aerosols, with
4192 the exception of hydrogen atoms. Sticking should apply to polar molecules, such
4193 as nitriles and water. We performed a sensitivity test on putative adsorption
4194 reactions for HCN, HNC, CH_3CN , HC_3N , C_2H_3CN , C_2H_5CN , HC_5N and H_2O .
4195 The adsorption rates are assumed to be proportional to the physical collision
4196 rate between molecules and aerosols; the aerosol radius and density are from
4197 Figure 22. The efficiency for this absolute loss is taken as 10^{-7} .

4198 The densities of HCN, CH_3CN , HC_3N and C_2H_5CN with the heterogeneous
4199 loss process described above are shown in Figures 51 and 53. This brings
4200 the model abundances of HC_3N and C_2H_5CN (column-integrated density of
4201 $5.7 \times 10^{14} \text{ cm}^{-2} \text{ s}^{-1}$) into better conformance with the observations but HCN
4202 and CH_3CN are now largely underestimated. CH_3CN , HC_3N , C_2H_3CN and
4203 C_2H_5CN all have a similar dipole moment (3.7-4.1 D) and there is no obvious
4204 reason suggesting that their sticking efficiency should differ significantly. There
4205 is no impact on HNC because of its very large reactivity with H atoms. The
4206 contribution of this process to aerosol mass loading comes essentially from HCN
4207 with an adsorption rate of $6 \times 10^{-15} \text{ g cm}^{-2} \text{ s}^{-1}$. This is to be compared to the
4208 aerosol mass flux from the upper atmosphere of $3 \times 10^{-14} \text{ g cm}^{-2} \text{ s}^{-1}$ (Lavvas
4209 et al., 2010).

4210 Even with a conservatively small adsorption probability to the aerosols, the
4211 implied loss for the species considered is enough to drastically affect their abun-
4212 dance. We emphasize that there are significant uncertainties on adsorption rates
4213 and that stronger constraints are needed to know if heterogeneous chemistry can
4214 resolve the issues we are encountering for some nitriles. Laboratory measure-
4215 ments and/or theoretical computations for the sticking efficiency of molecules
4216 onto tholins are required to verify this process and to provide a better constraint
4217 on its impact in Titan's stratosphere.

4218 5.3.4. Condensation

4219 As mentioned previously, all the minor species (with the exception of C_2H_4)
4220 are subject to condensation near the tropopause followed by precipitation to the
4221 surface. Willacy et al. (2016) investigated the condensation and sublimation
4222 with treatments of the sedimentation of the aerosols and their condensates,
4223 and the formation of haze particles. They found that these processes do affect

4224 the abundances of nitrogen-bearing species, particularly HCN, HNC, HC₃N,
 4225 C₂H₃CN and C₂H₅CN. Lavvas et al. (2011b) had followed a similar approach
 4226 but only considered the effects of the condensation of methane, ethane and
 4227 hydrogen cyanide and found that the latter one followed its saturation mole
 4228 fraction.

4229 The column integrated mass fluxes for the six species that are the major
 4230 sources of condensates are presented in Table 19. The major liquid condensate
 4231 is C₂H₆ with a precipitation flux of $3.5 \times 10^9 \text{ cm}^{-2} \text{ s}^{-1}$ (or $1.7 \times 10^{-13} \text{ g cm}^{-2}$
 4232 s^{-1}), while the major solid condensate is C₂H₂ with a precipitation flux of
 4233 $1.1 \times 10^9 \text{ cm}^{-2} \text{ s}^{-1}$ (or $4.6 \times 10^{-14} \text{ g cm}^{-2} \text{ s}^{-1}$). In general, the values from
 4234 our model are similar to that in previous models (cf. Table 7.6 in Vuitton et al.
 4235 (2014) and Table 4 in Willacy et al. (2016)).

Table 19: Calculated condensation flux of major species. For each species, the fraction of its condensation rate to its total loss rate as well as the associated deposition rate of material on the surface are given.

Species	Flux ^(a) (g cm ⁻² s ⁻¹)	Fraction of the total loss	Depth (mm Myr ⁻¹)
Liquids			
C ₂ H ₆	1.7×10^{-13}	88%	55
C ₃ H ₈	2.6×10^{-14}	81%	8.1
C ₄ H ₁₀	2.7×10^{-15}	71%	0.85
Total	2.0×10^{-13}	-	64
Solids			
C ₂ H ₂	4.6×10^{-14}	11%	14
HCN	5.9×10^{-15}	41%	1.9
HC ₃ N	9.8×10^{-16}	8%	0.31
Total	5.3×10^{-14}	-	17
Aerosols^(b)			
	3.0×10^{-14}	-	10

^(a)The density of all compounds is taken as 1 g cm^{-3} .

^(b)From Lavvas et al. (2010).

4236 The above fluxes can be used to calculate the depth of material accumulated
 4237 on the surface of Titan over a given period of time. This is presented in Table 19
 4238 in mm Myr⁻¹. The mass flux of the solid condensates is equivalent to 5.3×10^{-14}
 4239 $\text{g cm}^{-2} \text{ s}^{-1}$, which is about twice as much as the aerosol mass flux. Liquids
 4240 (C₂H₆, C₃H₈, C₄H₁₀) dominate over solid deposits (condensates + aerosols) by
 4241 a factor of ~ 2 , with a deposition rate of 6.4 cm Myr^{-1} . If this deposition rate has
 4242 been constant over the age of the solar system, the equivalent of 290 m of liquid
 4243 material and 120 m of solid material should have accumulated on the surface.
 4244 This is to be compared to the 0.2-2.0 m equivalent depth of liquid currently
 4245 present in the lakes, while dunes are consistent with an organic component that
 4246 would be 2 to 8 m thick if evenly spread on the surface, as inferred from Cassini
 4247 RADAR observations (Lorenz et al., 2008). These values support the ideas

4248 that: (i) the concentration of atmospheric methane has varied over the age of
4249 the solar system and may be a recent addition to the atmosphere (Tobie et al.,
4250 2006), 75-300 Myrs being enough to produce some 2-8 m thick dune material,
4251 (ii) C_2H_6 is lost to the crust or deeper interior in the form of clathrates (Lunine,
4252 2010).

4253 *5.4. Lifetimes*

4254 Minor species have a large range of lifetimes, from days to several thousand
4255 years, which means that they are sensitive to atmospheric motions over a range
4256 of timescales and different gases can be used to study different aspects of the dy-
4257 namics. If the only processes occurring are photochemical reactions and vertical
4258 atmospheric motion, the polar enrichment observed in the stratosphere during
4259 winter should be proportional to the species vertical gradient, i.e. inversely pro-
4260 portional to its lifetime. This is explained by the presence of a circulation cell
4261 with downwelling in the polar regions, which causes the lower stratosphere to
4262 be greatly enriched in short lifetime species compared to the equator.

4263 Figure 64 shows the lifetime of several compounds as a function of altitude.
4264 The species lifetime is the shortest of their chemical and transport time constant,
4265 as defined in section 2.4. The diurnal/ annual time constants are equal to the
4266 length of a day/ year (in seconds) divided by 2π . The solar time constant
4267 corresponds to the solar cycle of 11 Earth years (cf. next section).

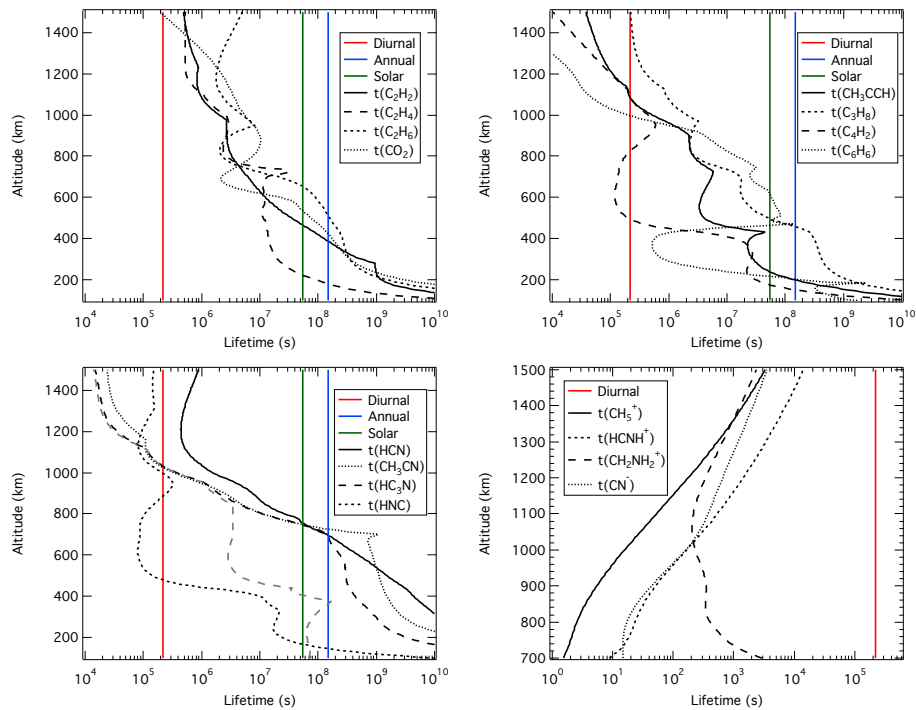


Figure 64: Calculated lifetime of C_2H_2 , C_2H_4 , C_2H_6 , and CO_2 (upper left panel), CH_3CCH , C_3H_8 , C_4H_2 and C_6H_6 (upper right panel), HCN , HNC , CH_3CN and HC_3N (lower left panel), CH_5^+ , HCNH^+ , CH_2NH_2^+ and CN^- (lower right panel). Characteristic diurnal/annual/solar times are also presented.

Table 20: Calculated chemical (t_C) and transport (t_K) lifetime of various species at 300 km.

Species	t_C (s)	t_K (s)
C_2H_2	9.1×10^8	5.6×10^8
C_2H_4	2.0×10^8	2.0×10^7
C_2H_6	4.0×10^9	3.5×10^8
CH_3CCH	1.9×10^8	2.8×10^7
C_3H_8	1.9×10^9	4.2×10^8
C_4H_2	2.6×10^7	6.2×10^7
C_6H_6	6.2×10^8	8.2×10^5
HCN	3.8×10^{11}	1.1×10^{10}
HNC	2.0×10^7	4.9×10^7
CH_3CN	8.9×10^{11}	2.9×10^9
$HC_3N^{(a)}$	8.2×10^7	9.2×10^7
C_2N_2	3.6×10^7	4.6×10^7
H_2O	3.7×10^{10}	1.1×10^8
CO_2	6.9×10^{15}	3.5×10^8

^(a)Values obtained with the nitriles heterogeneous chemistry turned on, see section 5.3.3.

4268 Generally, as species settle towards the surface, their lifetime increases from
 4269 typically one Titan day in the thermosphere to one Titan year in the strato-
 4270 sphere. Nevertheless, there is some large variability between species, with HCN
 4271 having a lifetime of ~ 200 Titan yrs. and C_6H_6 of ~ 4 days at 300 km (cf. Table
 4272 20). In the ionosphere, the nitriles are efficiently lost by ion chemistry. Be-
 4273 cause the reaction rates are all fast and quite similar, the chemical lifetime of
 4274 all species is about the same. It is a different story in the stratosphere. For
 4275 example, HNC isomerizes very quickly to HCN by collision with H atoms and
 4276 its lifetime is quite short. However, the nitriles do not react efficiently with any
 4277 of the radicals present there and their main chemical loss is photodissociation.
 4278 Because HC_3N absorbs to much longer wavelengths (where there are more pho-
 4279 tons available) than CH_3CN , its loss rate is higher and therefore its chemical
 4280 lifetime shorter. Actually, the chemical loss for CH_3CN is so inefficient that its
 4281 main actual loss is vertical transport (downwelling) to the tropopause where it
 4282 condenses (cf. Table 20). In fact, for most species, depending on the altitude,
 4283 regions dominated by photochemical equilibrium alternate with regions domi-
 4284 nated by dynamical equilibrium. At 300 km, the lifetime of most species is
 4285 dominated by transport, with the exception of the few having a short chemical
 4286 time constant, such as C_4H_2 , HNC and C_2N_2 .

4287 CIRS shows that north-polar C_4H_2 and HC_3N enrichment is much greater
 4288 than that of HCN (Teany et al., 2008b). This is consistent with the much
 4289 shorter photochemical lifetime of C_4H_2 and HC_3N (~ 1 yr.) compared to HCN
 4290 (~ 1000 yrs.), which prevents them from mixing with air at lower latitude (cf.
 4291 Figure 4 in (Teany et al., 2008b)). However, nitriles appear to be anomalously
 4292 enriched compared to hydrocarbons (cf. Figure 8 in Teany et al. (2010)).
 4293 Teany et al. (2010) suggests that an additional loss mechanism is required for

4294 nitrile species. However, our stratospheric HCN profile is already on the lower
4295 edge of the observations and any additional loss would lead to an inconsistent
4296 HCN abundance (unless the production rate is somehow increased as well). For
4297 HC_3N , adding some heterogeneous loss to the aerosols in order to match the
4298 observations leads to a decrease of its chemical lifetime from 1.6×10^9 to 8.2×10^7
4299 s.

4300 At the ionospheric peak, the lifetime of ions is typically 10^2 - 10^3 s. It is
4301 largely dominated by their chemical loss as their reactivity is high and generally
4302 increases with decreasing altitude, therefore leading to a decreasing lifetime, as
4303 shown in the bottom right panel of Figure 64.

4304 5.5. Solar Cycle

4305 11-year variations in the Sun's magnetic field significantly affect the shorter
4306 EUV/UV range of the solar output, making these changes directly relevant to
4307 Titan's photochemistry. The Cassini prime mission encountered an extended
4308 solar minimum, with a rising phase of solar activity starting in 2011. As shown
4309 in Figure 64, lifetimes of most constituents are considerably shorter than one
4310 solar cycle above the stratosphere and are thus sensitive to the changes in solar
4311 flux over the course of that cycle in that region.

4312 In Titan's atmosphere, constituents above 500 km are typically destroyed
4313 chemically within one solar cycle, while for certain stable constituents, like
4314 C_4H_2 , their relatively short lifetimes may allow changes in solar output to affect
4315 their lower stratospheric abundances, as well. With this in mind, it is construc-
4316 tive to analyze the effect of variations in solar flux on the distribution of various
4317 key constituents in Titan's atmosphere.

4318 Westlake et al. (2014) and Madanian et al. (2016) studied the effects of the
4319 solar cycle based on a total of twelve years (2004-2015) of measurements by
4320 INMS. They reported a declining trend in the CH_4 , N_2 and C2 hydrocarbon
4321 abundance during solar maximum. For ions, the solar maximum densities are
4322 significantly greater than their solar minimum counterparts (at similar solar
4323 zenith angles), with a decrease in altitude of the ionospheric peak.

4324 Combining these data with modeling, Westlake et al. (2014) relate the
4325 diminution of CH_4 during high solar activity periods to an increased CH_4 pho-
4326 todestruction because of the increased photon flux. They also suggested that
4327 ion-molecule reactions producing large hydrocarbons are responsible for an en-
4328 hanced loss of C2 hydrocarbons during solar maximum and therefore declining
4329 mole fractions in the thermosphere. Luspay-Kuti et al. (2016) investigated as
4330 well the influence on minor hydrocarbons of variations in the solar photons in
4331 response to the solar cycle. Their calculations indicate a decrease of CH_3 , C_2H_6
4332 and C_3H_8 above ~ 900 - 950 km during solar maximum, which they explain by
4333 the role of $\text{N}(^4\text{S})$. Higher abundance of $\text{N}(^4\text{S})$ would increase the importance
4334 of the $\text{CH}_3 + \text{N}(^4\text{S})$ reaction, decreasing the CH_3 abundance and affecting the
4335 overall hydrocarbon chemistry.

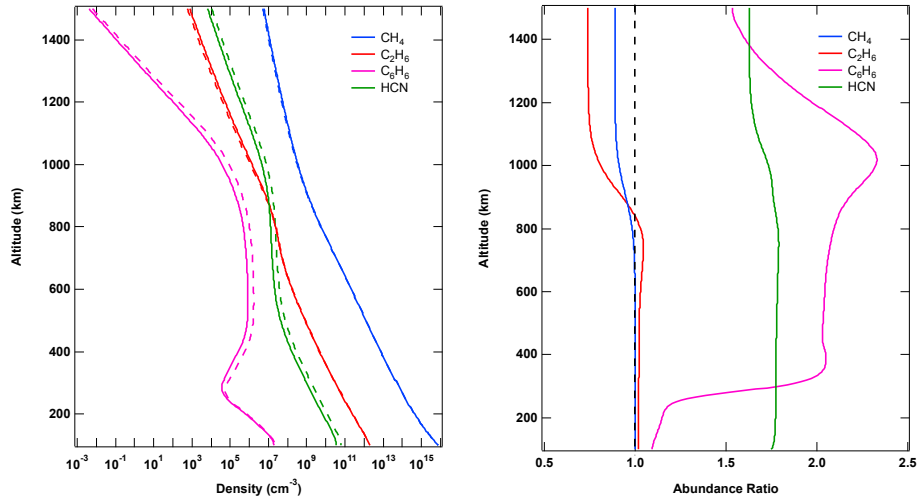


Figure 65: Calculated CH_4 , C_2H_6 , C_6H_6 , HCN density (left panel) at solar maximum (dashed) / solar minimum (solid) and abundance ratio (right panel).

4336 A comparison between our solar maximum and solar minimum profiles (ab-
 4337 solute and relative abundances) of selected neutrals is shown in Figure 65.
 4338 Methane and ethane show a reduction in density above ~ 900 km during solar
 4339 maximum compared to solar minimum conditions. C_6H_6 and HCN show
 4340 increased densities during solar maximum over the entire altitude range. The
 4341 magnitude of the variation varies among species from about 10% (CH_4) to as
 4342 much as a factor of more than 2 (C_6H_6). C_2H_2 and C_2H_4 exhibit a very moder-
 4343 erate increase of 20% and 5%, respectively (not shown).

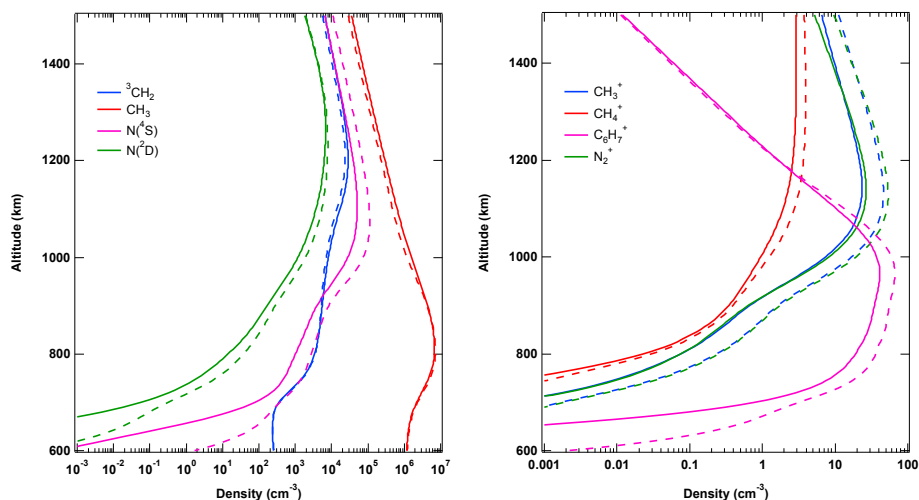


Figure 66: Calculated solar maximum (dashed) / solar minimum (solid) abundance of ${}^3\text{CH}_2$, CH_3 , $\text{N}(^4\text{S})$, $\text{N}(^2\text{D})$ (left panel) and CH_3^+ , CH_4^+ , N_2^+ , HCNH^+ (right panel).

4344 The observed solar maximum depletion in CH_4 is in agreement with its in-
 4345 creased photodestruction (11%) during solar maximum conditions in response to
 4346 the increased photon flux. Since CH_3 is a primary product of CH_4 photodissocia-
 4347 tion (J_d38a), a higher peak abundance (6%) is observed during solar maximum
 4348 as a result of increased production (cf. left panel of Figure 66). Similarly, the
 4349 peak abundance of $\text{N}(^4\text{S})$ increases at solar maximum (factor of ~ 2). A drop
 4350 in peak altitude (30 km) is due to the relative enhancement of the photon flux
 4351 at shorter wavelengths (cf. Figure 16), where the N_2 cross-sections decrease
 4352 sharply. The higher $\text{N}(^4\text{S})$ abundance during solar maximum boosts reactions
 4353 between $\text{N}(^4\text{S})$ and CH_3 , resulting in higher CH_3 loss rates and a lower CH_3
 4354 abundance during solar maximum than during solar minimum above 880 km.
 4355 This general trend is the same as observed by Luspay-Kuti et al. (2016), al-
 4356 though their very small CH_3 abundance ratio above 1000 km in their Figure 1
 4357 does not seem realistic to us, especially looking at their C_2H_6 profile. CH_3 plays
 4358 a lead role in the photochemistry of Titan's upper atmosphere, and is especially
 4359 important for the production of C_2H_6 and HCN (R_n90, R_n290b). Hence, the
 4360 enriched solar maximum C_2H_6 abundance below 850 km and depleted above.
 4361 The effect of $\text{N}(^4\text{S})$ is observed on the density of HCN , which is higher by up to
 4362 about 80% during solar maximum because of increasing production.

4363 Ion-molecule chemistry becomes enhanced during solar maximum compared
 4364 with solar minimum due to the increased EUV flux that initiates ion produc-
 4365 tion (cf. right panel of Figure 66). The density enhancement is best seen in
 4366 the primary ion species N_2^+ and CH_3^+ that increase by a factor of about 2.
 4367 The density of CH_4^+ exhibits a smaller increase of $\sim 40\%$ between high and low
 4368 solar activity, while that of HCNH^+ increases by $\sim 60\%$. The ion peak altitudes
 4369 are slightly lower (10-15 km) for higher activity, again because of the relative

4370 increase in solar flux at shorter wavelengths. Since ion-molecule chemistry dom-
4371 inates the production of C_6H_6 at high altitudes, its higher density is primarily
4372 due to the increased reaction rates. Although we do observe an enhanced loss
4373 of C_2H_2 and C_2H_4 from ion-molecule reactions, this process is not competitive
4374 and does not support the conclusion of Westlake et al. (2014).

4375 6. Conclusions and Perspectives

4376 We developed and improved a photochemical model extending from Titan's
4377 surface to the exobase. Solar EUV/UV, photoelectrons and cosmic rays are
4378 considered as energy sources. The chemical network includes hydrocarbons,
4379 nitrogen and oxygen-bearing species, in the form of neutrals as well as positive
4380 and negative ions. It has become apparent that:

- 4381 • New constraints from Cassini on the background atmosphere, eddy diffu-
4382 sion coefficient and haze opacity significantly reduce uncertainties in the
4383 photochemical model.
- 4384 • The neutral composition is fairly well understood, with the notable excep-
4385 tion of oxygen-bearing species. Neutral and ion chemistry are intimately
4386 coupled and the latter is a substantial source of neutral species through
4387 electron recombination reactions.
- 4388 • The model provides assignments for the complex positive and negative
4389 ions present in the thermosphere, up to $m/z \sim 100$. We notably infer that
4390 ions are nitrogen rich. Reproducing the measured density of major ions
4391 (both positive and negative) with photochemical models remains an issue.
- 4392 • Reaction pathways leading to the macromolecules constituting the aerosols
4393 as well as the impact of heterogeneous reactions are largely unknown but
4394 likely involve ion as well as neutral species.

4395 Investigations into the nature of Titan's chemistry can be extended in several
4396 ways:

- 4397 • Analysis of more Cassini data, to further characterize temporal (solar
4398 zenith angle, season) and spatial (altitude, latitude, magnetospheric inter-
4399 action geometry) variations. Neutral mole fractions are well constrained
4400 by CIRS in the stratosphere but extensive analysis of the UVIS occulta-
4401 tion data and INMS data are necessary to constrain neutral abundances
4402 in the upper atmosphere. INMS and CAPS positive and negative ion mass
4403 spectra should be interpreted for a large number of flybys.
- 4404 • Diurnal variations as well as transport based on realistic general circula-
4405 tion models should be included in photochemical models. A time-variable
4406 model may be required to solve the oxygen photochemistry discrepancy.

- 4407 • Collection of more chemical data, from both experimental and theoretical
4408 investigations, at the temperature and pressure conditions relevant for Ti-
4409 tan, with emphasis on nitrogen-bearing species. Special attention should
4410 be paid to product branching ratios at low temperature and isomers iden-
4411 tification. Of highest interest are electron recombination and association
4412 (both collisional and radiative) reactions as well as negative ion chemistry
4413 in general. Radical-radical and ion-radical reactions should be given the
4414 highest priority. Laboratory investigations of heterogeneous processes on
4415 tholins should also be developed.
- 4416 • Construction of state-of-the-art laboratory experiments in order to get
4417 some insight into the intermediate steps involved in molecular growth
4418 (from $m/z = 100$ to 1000). Detection should be performed in situ and
4419 allow probing intermediate species such as radicals and ions as a function of
4420 time. EUV/UV light should be preferred and ultra-high vacuum reactors
4421 should be used to limit atmospheric contamination. Temperature and
4422 pressure should be representative of Titan as far as possible.
- 4423 • Remote sensing (ALMA, Herschel, JWST, etc.) observational campaigns
4424 should target more complex molecules (nitriles, aromatics, oxygen species,
4425 including ^{15}N and ^{18}O isotopes) not detected by Cassini. The mystery of
4426 the aerosol composition will not be conclusively resolved, however, until
4427 next generation space instruments are sent to the Saturn system. Very
4428 high-resolution mass spectrometers optimized for the detection of complex
4429 organics, both in the volatile and solid phases, should be developed for that
4430 critical endeavor.

4431 Acknowledgements

4432 VV acknowledges support from the French space agency (CNES) through a
4433 Cassini Participating Scientist grant. The contribution from SJK is based upon
4434 work supported through NASA Planetary Atmospheres Program grant number
4435 NNH09AK24I and by the U.S. Department of Energy, Office of Science, Office
4436 of Basic Energy Sciences, Division of Chemical Sciences, Geosciences, and Bio-
4437 sciences under Contract No. DE-AC02-06CH11357 (BES Gas Phase Chemical
4438 Physics Core Program). PL acknowledges support from the PNP under program
4439 AMG and from the CNRS PICS program TAC. The authors thank Alexandre
4440 Faure, Wolf Geppert, Murray McEwan, Darci Snowden, Roland Thissen and
4441 Erik Vigren for useful discussions.

4442 References

- 4443 Abouelaziz, H., Gomet, J., Pasquerault, D., Rowe, B., Mitchell, J., 1993. Mea-
4444 surements of C_3H_3^+ , C_5H_3^+ , C_6H_6^+ , C_7H_5^+ , and $\text{C}_{10}\text{H}_8^+$ dissociative re-
4445 combination rate coefficients. *J. Chem. Phys.* 99, 237–243.

- 4446 Adachi, H., Basco, N., James, D., 1981. The acetyl radicals CH_3CO and CD_3CO
4447 studied by flash photolysis and kinetic spectroscopy. *Int. J. Chem. Kin.* 13,
4448 1251–1276.
- 4449 Adam, L., Hack, W., Zhu, H., Qu, Z., Schinke, R., 2005. Experimental and
4450 theoretical investigation of the reaction $\text{NH}(\text{X}^3\Sigma^-) + \text{H}(\text{2S}) \rightarrow \text{N}(\text{4S}) +$
4451 $\text{H}_2(\text{X}^1\Sigma_g^+)$. *J. Chem. Phys.* 122, 114301–114307.
- 4452 Adams, N., 1996. Gas phase ionic reactions, in: Drake, G. (Ed.), *Atomic, molec-*
4453 *ular & optical physics handbook*. American Institute of Physics, Woodbury,
4454 New York, pp. 441–451.
- 4455 Adams, N., Herd, C., Geoghegan, M., Smith, D., Canosa, A., Gomet, J., Rowe,
4456 B., Queffelec, J., Morlais, M., 1991. Laser induced fluorescence and vacuum
4457 ultraviolet spectroscopic studies of H-atom production in the dissociative re-
4458 combination of some protonated ions. *J. Chem. Phys.* 94, 4852–4857.
- 4459 Adams, N., Mathews, L., Osborne Jr., D., 2010. Laboratory chemistry relevant
4460 to understanding and modeling the ionosphere of Titan. *Faraday Discuss.*
4461 147, 323–335.
- 4462 Adams, N., Molek, C., McLain, J., 2009. New flowing afterglow technique for
4463 determining products of dissociative recombination: CH_5^+ and N_2H^+ . *J.*
4464 *Phys.: Conf. Ser.* 192, #012004.
- 4465 Adams, N., Smith, D., 1978. Reactions of CH_n^+ ions with molecules at 300 K.
4466 *Chem. Phys. Lett.* 54, 530–534.
- 4467 Adams, N., Smith, D., 1988a. Laboratory studies of dissociative recombination
4468 and mutual neutralization and their relevance to interstellar chemistry, in:
4469 Millar, T., Williams, D. (Eds.), *Rate coefficients in astrochemistry*. Kluwer
4470 Academic Publishers, pp. 173–192.
- 4471 Adams, N., Smith, D., 1988b. Measurements of the dissociative recombination
4472 coefficients for several polyatomic ion species at 300 K. *Chem. Phys. Lett.*
4473 144, 11–14.
- 4474 Adams, N., Smith, D., Paulson, J., 1980. An experimental survey of the reac-
4475 tions of NH_n^+ ions ($n = 0$ to 4) with several diatomic and polyatomic molecules
4476 at 300 K. *J. Chem. Phys.* 72, 288–297.
- 4477 Adriani, A., Dinelli, B., López-Puertas, M., García-Comas, M., Moriconi, M.,
4478 D’Aversa, E., Funke, B., Coradini, A., 2011. Distribution of HCN in Titan’s
4479 upper atmosphere from Cassini/VIMS observations at 3 μm . *Icarus* 214, 584–
4480 595.
- 4481 Ågren, K., Wahlund, J.E., Garnier, P., Modolo, R., Cui, J., Galand, M., Müller-
4482 Wodarg, I., 2009. On the ionospheric structure of Titan. *Planet. Space Sci.*
4483 57, 1821–1827.

- 4484 Ågren, K., Wahlund, J.E., Modolo, R., Lummerzheim, D., Galand, M., Müller-
4485 Wodarg, I., Canu, P., Kurth, W., Cravens, T., Yelle, R., Waite Jr., J., Coates,
4486 A., Lewis, G., Young, D., Bertucci, C., Dougherty, M., 2007. On magneto-
4487 spheric electron impact ionisation and dynamics in Titan's ram-side and polar
4488 ionosphere - a Cassini case study. *Ann. Geophys.* 25, 2359–2369.
- 4489 Aguado, A., Roncero, O., Zanchet, A., Agúndez, M., Cernicharo, J., 2017. The
4490 photodissociation of HCN and HNC: Effects on the HNC/HCN abundance
4491 ratio in the interstellar medium. *Astrophys. J.* 838, #33.
- 4492 Ahmed, M., Peterka, D., Suits, A., 1999. The photodissociation of the vinyl
4493 radical (C_2H_3) at 243 nm studied by velocity map imaging. *J. Chem. Phys.*
4494 110, 4248–4253.
- 4495 Ajello, J., Stevens, M., Stewart, I., Larsen, K., Esposito, L., Coldwell, J., Mc-
4496 Clintock, W., Holsclaw, G., Gustin, J., Pryor, W., 2007. Titan airglow spectra
4497 from Cassini Ultraviolet Imaging spectrograph (UVIS): EUV analysis. *Geo-
4498 phys. Res. Lett.* 34, #L24202.
- 4499 Akimoto, H., Obi, K., Tanaka, I., 1965. Primary process in the photolysis of
4500 ethane at 1236 Å. *J. Chem. Phys.* 42, 3864–3868.
- 4501 Albritton, D., 1978. Ion-neutral reaction rate constants measured in flow reac-
4502 tors through 1977. *At. Data Nucl. Data Tables* 22, 1–101.
- 4503 Alcaraz, C., Nicolas, C., Thissen, R., Žabka, J., Dutuit, O., 2004. $^{15}N^+ +$
4504 CD_4 and $O^+ + ^{13}CO_2$ state-selected ion-molecule reactions relevant to the
4505 chemistry of planetary ionospheres. *J. Phys. Chem. A* 108, 9998–10009.
- 4506 Alge, E., Adams, N., Smith, D., 1983. Measurements of the dissociative re-
4507 combination coefficients of O_2^+ , NO^+ and NH_4^+ in the temperature range
4508 200–600 K. *J. Phys. B: At. Mol. Phys.* 16, 1433–1444.
- 4509 Allen, M., Pinto, J., Yung, Y., 1980. Titan: Aerosol photochemistry and varia-
4510 tions related to the sunspot cycle. *Astrophys. J.* 242, L125–L128.
- 4511 Alnama, K., Boyé-Péronne, S., Douin, S., Innocenti, F., O'Reilly, J., Roche,
4512 A.L., Shafizadeh, N., Zuin, L., Gauyacq, D., 2007. Photolysis of allene and
4513 propyne in the 7–30 eV region probed by the visible fluorescence of their
4514 fragments. *J. Chem. Phys.* 126, #044304.
- 4515 Amitay, Z., Zajfman, D., Forck, P., Hechtfisher, U., Seidel, B., Grieser, M.,
4516 Habs, D., Repnow, R., Schwalm, D., Wolf, A., 1996. Dissociative recombina-
4517 tion of CH^+ : Cross section and final states. *Phys. Rev. A* 54, 4032–4050.
- 4518 Angelova, G., Novotny, O., Mitchell, J., Rebrion-Rowe, C., Le Garrec, J.,
4519 Bluhme, H., Seiersen, K., Andersen, L., 2004a. Branching ratios for the
4520 dissociative recombinaion of hydrocarbon ions II. The cases of $C_4H_n^+$ ($n =$
4521 1–9). *Int. J. Mass Spectrom.* 232, 195–203.

- 4522 Angelova, G., Novotny, O., Mitchell, J., Rebrion-Rowe, C., Le Garrec, J.,
4523 Bluhme, H., Svendsen, A., Andersen, L., 2004b. Branching ratios for the
4524 dissociative recombination of hydrocarbon ions III: the cases of $C_3H_n^+$ ($n =$
4525 1-8). *Int. J. Mass Spectrom.* 235, 7–13.
- 4526 Anicich, V., 1993. Evaluated bimolecular ion-molecule gas phase kinetics of
4527 positive ions for use in modeling planetary atmospheres, cometary comae,
4528 and interstellar clouds. *J. Phys. Chem. Ref. Data* 22, 1469–1569.
- 4529 Anicich, V., McEwan, M., 1997. Ion-molecule chemistry in Titan’s ionosphere.
4530 *Planet. Space Sci.* 45, 897–921.
- 4531 Anicich, V., Milligan, D., Fairley, D., McEwan, M., 2000. Termolecular ion-
4532 molecule reactions in Titan’s atmosphere. I: Principal ions with principal
4533 neutrals. *Icarus* 146, 118–124.
- 4534 Anicich, V., Wilson, P., McEwan, M., 2003. Termolecular ion-molecule reac-
4535 tions in Titan’s atmosphere. IV: A search made at up to 1 micron in pure
4536 hydrocarbons. *J. Am. Soc. Mass Spectrom.* 14, 900–915.
- 4537 Anicich, V., Wilson, P., McEwan, M., 2004. A SIFT ion-molecule study of some
4538 reactions in Titan’s atmosphere. Reactions of N^+ , N_2^+ , and HCN^+ with CH_4 ,
4539 C_2H_2 , and C_2H_4 . *J. Am. Soc. Mass Spectrom.* 15, 1148–1155.
- 4540 Anicich, V., Wilson, P., McEwan, M., 2006. An ICR study of ion-molecules reac-
4541 tions in Titan’s atmosphere: An investigation of binary hydrocarbon mixtures
4542 up to 1 micron. *J. Am. Soc. Mass Spectrom.* 17, 544–561.
- 4543 Aoto, T., Ito, K., Hikosaka, Y., Shibasaki, A., Hirayama, R., Yamamoto, N.,
4544 Miyoshi, E., 2006. Inner-valence states of N_2^+ and the dissociation dynamics
4545 studied by threshold photoelectron spectroscopy and configuration interaction
4546 calculation. *J. Chem. Phys.* 124, 6.
- 4547 Arnold, S., Dotan, I., Williams, S., Viggiano, A., Morris, R., 2000. Selected ion
4548 flow tube studies of air plasma cations reacting with alkylbenzenes. *J. Phys.*
4549 *Chem. A* 104, 928–934.
- 4550 Arnold, S., Williams, S., Dotan, I., Midey, A., Morris, R., Viggiano, A., 1999.
4551 Flow tube studies of benzene charge transfer reactions from 250 to 1400 K.
4552 *J. Phys. Chem. A* 103, 8421–8432.
- 4553 Ashfold, M., Dixon, R., Kono, M., Mordaunt, D., Reed, C., 1997. Near ultra-
4554 violet photolysis of ammonia and methylamine studied by H Rydberg atom
4555 photofragment translational spectroscopy. *Phil. Trans. Roy. Soc. London A*
4556 355, 1659–1676.
- 4557 Asvany, O., Savić, I., Schlemmer, S., Gerlich, D., 2004. Variable temperature
4558 ion trap studies of $CH_4^+ + H_2$, HD and D_2 : negative temperature dependence
4559 and significant isotope effect. *Chem. Phys.* 298, 97–105.

- 4560 Atkinson, D., Hudgens, J., 1999. Rate coefficients for the propargyl radical
4561 self-reaction and oxygen addition reaction measured using ultraviolet cavity
4562 ring-down spectroscopy. *J. Phys. Chem. A* 103, 4242–4252.
- 4563 Atreya, S., 1986. Atmospheres and ionospheres of the outer planets and their
4564 satellites. volume 15 of *Physics and Chemistry in Space*. Springer-Verlag, New
4565 York.
- 4566 Au, J., Cooper, G., Burton, G., Olney, T., Brion, C., 1993. The valence shell
4567 photoabsorption of the linear alkanes C_nH_{2n+2} ($n=1-8$): Absolute oscillator
4568 strengths (7-220 eV). *Chem. Phys.* 173, 209–239.
- 4569 Ausloos, P., 1982. Structure and isomerization of $C_7H_7^+$ ions formed in the
4570 charge-transfer-induced fragmentation of ethylbenzene, toluene, and norbor-
4571 nadiene. *J. Am. Chem. Soc.* 104, 5259–5265.
- 4572 Ausloos, P., Jackson, J.A., Lias, S., 1980. Reactions of benzyl ions with alkanes,
4573 alkenes, and aromatic compounds. *Int. J. Mass Spectrom. Ion Processes* 33,
4574 269–283.
- 4575 Ausloos, P., Lias, S., Buckley, T., Rogers, E., 1989. Concerning the formation
4576 and the kinetics of phenylium ions. *Int. J. Mass Spectrom.* 92, 65–77.
- 4577 Baines, K., Drossart, P., Lopez-Valverde, M., Atreya, S., Sotin, C., Momary,
4578 T., Brown, R., Buratti, B., Clark, R., Nicholson, P., 2006. On the discovery
4579 of CO nighttime emissions on Titan by Cassini/VIMS: Derived stratospheric
4580 abundances and geological implications. *Planet. Space Sci.* 54, 1552–1562.
- 4581 Balko, B.A., Zhang, J., Lee, Y.T., 1992. Photodissociation of ethylene at 193
4582 nm. *J. Chem. Phys.* 97, 935–942.
- 4583 Balucani, N., Asvany, O., Kaiser, R., Osamura, Y., 2002. Formation of three
4584 C_4H_3N isomers from the reaction of CN ($X^2\Sigma^+$) with allene, H_2CCCH_2
4585 (X^1A_1), and methylacetylene, CH_3CCH (X^1A_1): A combined crossed beam
4586 and ab initio study. *J. Phys. Chem. A* 106, 4301–4311.
- 4587 Balucani, N., Leonori, F., Petrucci, R., Stazi, M., Skouteris, D., Rosi, M.,
4588 Casavecchia, P., 2010. Formation of nitriles and imines in the atmosphere
4589 of Titan: Combined crossed-beam and theoretical studies on the reaction dy-
4590 namics of excited nitrogen atoms $N(^2D)$ with ethane. *Faraday Discuss.* 147,
4591 1–28.
- 4592 Balucani, N., Skouteris, D., Leonori, F., Petrucci, R., Hamberg, M., Geppert,
4593 W., Casavecchia, P., 2012. Combined crossed beam and theoretical studies
4594 of the $N(^2D) + C_2H_4$ reaction and implications for atmospheric models of
4595 Titan. *J. Phys. Chem. A* 116, 10467–10479.
- 4596 Bampasidis, G., Coustenis, A., Achterberg, R., Vinatier, S., Lavvas, P., Nixon,
4597 C., Jennings, D., Teanby, N., Flasar, F., Carlson, R., Moussas, X., Preka-
4598 Papadema, P., Romani, P., Guandique, E., Stamogiorgos, S., 2012. Thermal

- 4599 and chemical structure variations in Titan's stratosphere during the Cassini
4600 mission. *Astrophys. J.* 760, #144.
- 4601 Banaszekiewicz, M., Lara, L., Rodrigo, R., López-Moreno, J., Molina-Cuberos,
4602 G., 2000. A coupled model of Titan's atmosphere and ionosphere. *Icarus* 147,
4603 386–404.
- 4604 Barckholtz, C., Snow, T., Bierbaum, V., 2001. Reactions of C_n^- and C_nH^- with
4605 atomic and molecular hydrogen. *Astrophys. J.* 547, L171–L174.
- 4606 Bartels, M., Edelbuttel-Einhaus, J., Hoyerermann, K., 1991. The detection of
4607 CH_3CO , C_2H_5 , and CH_3CHO by REMPI/mass spectrometry and the appli-
4608 cation to the study of the reactions $H + CH_3CO$ and $O + CH_3CO$. *Symp. Int.*
4609 *Combust. Proc.* 23, 131–138.
- 4610 Bartels, M., Hoyerermann, K., Sievert, R., 1982. Elementary reactions in the
4611 oxidation of ethylene: the reaction of OH radicals with ethylene and the
4612 reaction of C_2H_4OH radicals with H atoms. *Symp. Int. Combust. Proc.* 19,
4613 61.
- 4614 Bartmess, J., 1982. Gas-phase ion chemistry of 5-methylene-1,3-cyclohexadiene
4615 (o-isotoluene) and 3-methylene-1,4-cyclohexadiene (p-isotoluene). *J. Am.*
4616 *Chem. Soc.* 104, 335–337.
- 4617 Bastian, M., Dressler, R., Murad, E., Arnold, S., Viggiano, A., 1996. Detailed
4618 study of the dynamics of the $O^+(^4S) + HCN$ reaction: a case study of ion-
4619 molecule reactions in the spacecraft environment. *J. Chem. Soc., Faraday*
4620 *Trans.* 92, 2659–2670.
- 4621 Bates, D., Mitchell, J., 1991. Rate coefficients for N_2^+ (ν) dissociative recom-
4622 bination. *Planet. Space Sci.* 39, 1297–1300.
- 4623 Baulch, D., Bowman, C., Cobos, C., Cox, R., Just, T., Kerr, J., Pilling, M.,
4624 Stocker, D., Troe, J., Tsang, W., Walker, R., Warnatz, J., 2005. Evaluated
4625 kinetic data for combustion modeling: Supplement II. *J. Phys. Chem. Ref.*
4626 *Data* 34, 757–1397.
- 4627 Baulch, D., Cobos, C., Cox, R., Esser, C., Frank, P., Just, T., Kerr, J., Pilling,
4628 M., Troe, J., Walker, R., Warnatz, J., 1992. Evaluated kinetic data for com-
4629 bustion modeling. *J. Phys. Chem. Ref. Data* 21, 411–734.
- 4630 Baulch, D., Cobos, C., Cox, R., Frank, P., Hayman, G., Just, T., Kerr, J.,
4631 Murrells, T., Pilling, M., Troe, J., Walker, R., Warnatz, J., 1994. Evaluated
4632 kinetic data for combustion modeling: Supplement I. *J. Phys. Chem. Ref.*
4633 *Data* 23, 847–1033.
- 4634 Becke, A., 1993. Density-functional thermochemistry. 3. The role of exact ex-
4635 change. *J. Chem. Phys.* 98, 5648–5652.

- 4636 Bell, J., Bougher, S., Waite Jr., J., Ridley, A., Magee, B., Mandt, K., Westlake,
4637 J., DeJong, A., Bar-Nun, A., Jacovi, R., Toth, G., De La Haye, V., Gell, D.,
4638 Fletcher, G., 2011. Simulating the one-dimensional structure of Titan's upper
4639 atmosphere: 3. Mechanisms determining methane escape. *J. Geophys. Res.*
4640 116, #E11002.
- 4641 Bellucci, A., Sicardy, B., Drossart, P., Rannou, P., Nicholson, P., Hedman,
4642 M., Baines, K., Burrati, B., 2009. Titan solar occultation observed by
4643 Cassini/VIMS: Gas absorption and constraints on aerosol composition. *Icarus*
4644 201, 198–216.
- 4645 Benedikt, J., 2010. Plasma-chemical reactions: low pressure acetylene plasmas.
4646 *J. Phys. D: Appl. Phys.* 43, #043001.
- 4647 Bénilan, Y., Bruston, P., Raulin, F., Cossart-Magos, C., Guillemin, J.C., 1994.
4648 Mid-UV spectroscopy of propynenitrile at low temperature: Consequences on
4649 expected results from observations of Titan's atmosphere. *J. Geophys. Res.*
4650 99, 17069–17074.
- 4651 Bénilan, Y., Jolly, A., Raulin, F., 1999. Comparative IR and UV spectroscopic
4652 studies of allene and methylacetylene: Implication for observation and mod-
4653 eling of Titan atmosphere. *Bull. Am. Astron. Soc.* 31, #1169.
- 4654 Bénilan, Y., Smith, N., Jolly, A., Raulin, F., 2000. The long wavelength range
4655 temperature variations of the mid-UV acetylene absorption coefficient. *Planet.*
4656 *Space Sci.* 48, 463–471.
- 4657 Bera, P., Head-Gordon, M., Lee, T., 2011. Initiating molecular growth in the
4658 interstellar medium via dimeric complexes of observed ions and molecules.
4659 *A&A* 535, #A74.
- 4660 Bera, P., Peverati, R., Head-Gordon, M., Lee, T., 2015. Hydrocarbon growth
4661 *via* ion-molecule reactions: computational studies of the isomers of $C_4H_2^+$,
4662 $C_6H_2^+$ and $C_6H_4^+$ and their formation paths from acetylene and its frag-
4663 ments. *Phys. Chem. Chem. Phys.* 17, 1859–1869.
- 4664 Bergeat, A., Hickson, K., Daugey, N., Caubet, P., Costes, M., 2009. A low
4665 temperature investigation of the $N(4S^{\circ}) + NO$ reaction. *Phys. Chem. Chem.*
4666 *Phys.* 11, 8149–8155.
- 4667 Bergeat, A., Loison, J., 2001. Reaction of carbon atoms, $C(2p^2, ^3P)$ with
4668 C_2H_2 , C_2H_4 and C_6H_6 : Overall rate constant and relative atomic hydrogen
4669 production. *Phys. Chem. Chem. Phys.* 3, 2038–2042.
- 4670 Berkowitz, J., 1996. Photoion-pair formation, in: Becker, U., Shirley, D. (Eds.),
4671 VUV and soft X-ray photoionization. Plenum Press, New York. *Physics of*
4672 *atoms and molecules*, pp. 263–289.
- 4673 Berkowitz, J., Chupka, W., Walter, T., 1969. Photoionization of HCN: The
4674 electron affinity and heat of formation of CN. *J. Chem. Phys.* 50, 1497–1500.

- 4675 Bernard, E., Strazisar, B., Davis, H., 1999. Excited state dynamics of H_2CN
4676 radicals. *Chem. Phys. Lett.* 313, 461–466.
- 4677 Berteloite, C., Le Picard, S., Balucani, N., Canosa, A., Sims, I., 2010a. Low
4678 temperature rate coefficients for reactions of the butadiynyl radical, C_4H ,
4679 with various hydrocarbons. Part I: reactions with alkanes (CH_4 , C_2H_6 , C_3H_8 ,
4680 C_4H_{10}). *Phys. Chem. Chem. Phys.* 12, 3666–3676.
- 4681 Berteloite, C., Le Picard, S., Balucani, N., Canosa, A., Sims, I., 2010b. Low
4682 temperature rate coefficients for reactions of the butadiynyl radical, C_4H , with
4683 various hydrocarbons. Part II: reactions with alkenes (ethylene, propene, 1-
4684 butene), dienes (allene, 1,3-butadiene) and alkynes (acetylene, propyne and
4685 1-butyne). *Phys. Chem. Chem. Phys.* 12, 3677–3689.
- 4686 Berteloite, C., Le Picard, S., Birza, P., Gazeau, M.C., Canosa, A., Bénilan, Y.,
4687 Sims, I., 2008. Low temperature (39–298 K) kinetics study of the reactions of
4688 the C_4H radical with various hydrocarbons observed in Titan’s atmosphere.
4689 *Icarus* 194, 746–757.
- 4690 Best, T., Otto, R., Trippel, S., Hlavenka, P., von Zastrow, A., Eisenbach, S.,
4691 Jézouin, S., Wester, R., Vigren, E., Hamberg, M., Geppert, W., 2011. Ab-
4692 solute photodetachment cross-section measurements for hydrocarbon chain
4693 anions. *Astrophys. J.* 742, #63.
- 4694 Bézard, B., 2014. The methane mole fraction in Titan’s stratosphere from DISR
4695 measurements during the Huygens probe’s descent. *Icarus* 242, 64–73.
- 4696 Biennier, L., Carles, S., Cordier, D., Guillemin, J.C., Le Picard, S., Faure, A.,
4697 2014. Low temperature reaction kinetics of $\text{CN}^- + \text{HC}_3\text{N}$ and implications
4698 for the growth of anions in Titan’s atmosphere. *Icarus* 227, 123–131.
- 4699 Blackman, G., Brown, R., Godfrey, P., Gunn, H., 1976. The microwave spec-
4700 trum of HNC: Identification of U90.7. *Nature* 261, 395–396.
- 4701 Blair, A., Harrison, A., 1973. Bimolecular reactions of trapped ions. VI. Ion-
4702 molecule reactions involving CH_5^+ and C_2H_5^+ . *Can. J. Chem.* 51, 1645–
4703 1654.
- 4704 Blank, D., Suits, A., Lee, Y., North, S., Hall, G., 1998. Photodissociation of
4705 acrylonitrile at 193 nm: A photofragment translational spectroscopy study
4706 using synchrotron radiation for product photoionization. *J. Chem. Phys.* 108,
4707 5784–5794.
- 4708 Bocherel, P., Herbert, L., Rowe, B., Sims, I., Smith, I., Travers, D., 1996.
4709 Ultralow-temperature kinetics of $\text{CH}(X^2\Pi)$ reactions: Rate coefficients for
4710 reactions with O_2 and NO ($T = 13\text{--}708\text{ K}$), and with NH_3 ($T = 23\text{--}295\text{ K}$).
4711 *J. Phys. Chem.* 100, 3063–3069.

- 4712 Bohme, D., 1975. The kinetics and energetics of proton transfer, in: Ausloos,
4713 P. (Ed.), Interaction between ions and molecules. Plenum Press, New York,
4714 N.Y. USA, pp. 489–504.
- 4715 Bohme, D., Fehsenfeld, F., 1969. Thermal reactions of O⁻ ions with saturated
4716 hydrocarbon molecules. *Can. J. Chem.* 47, 2717–2719.
- 4717 Bohme, D., Raksit, A., Schiff, H., 1982. Reactions of ¹²C⁺ with hydrocarbons
4718 at 296 K: carbon-carbon bond formation. *Chem. Phys. Lett.* 93, 592–597.
- 4719 Bomble, Y., Vázquez, J., Kállay, M., Michauk, C., Szalay, P., Császár, A.,
4720 Gauss, J., Stanton, J., 2006. High-accuracy extrapolated ab initio thermo-
4721 chemistry. II. Minor improvements to the protocol and a vital simplification.
4722 *J. Chem. Phys.* 125, #064108.
- 4723 Borrell, P., Cervenka, A., Turner, J.W., 1971. Pressure effects and quantum
4724 yields in the photolysis of ethylene and propene at 185 nm. *J. Chem. Soc. B*
4725 2, 2293–2298.
- 4726 Borucki, W., Levin, Z., Whitten, R., Keesee, R., Capone, L., Summers, A.,
4727 Toon, O., Dubach, J., 1987. Predictions of the electrical conductivity and
4728 charging of the aerosols in Titan’s atmosphere. *Icarus* 72, 604–622.
- 4729 Borucki, W., Whitten, R., 2008. Influence of high abundances of aerosols on the
4730 electrical conductivity of the Titan atmosphere. *Planet. Space Sci.* 56, 19–26.
- 4731 Bouwman, J., Fournier, M., Sims, I., Leone, S., Wilson, K., 2013. Reaction
4732 rate and isomer-specific product branching ratios of C₂H + C₄H₈: 1-butene,
4733 *cis*-2-butene, *trans*-2-butene, and isobutene at 79 K. *J. Phys. Chem. A* 117,
4734 5093–5105.
- 4735 Bouwman, J., Goulay, F., Leone, S., Wilson, K., 2012. Bimolecular rate constant
4736 and product branching ratio measurements for the reaction of C₂H with ethene
4737 and propene at 79 K. *J. Phys. Chem. A* 116, 3907–3917.
- 4738 Bowers, M., Neilson, P., Kemper, P., Wren, A., 1977. Temperature dependence
4739 of ion-molecule collision phenomena: An application of ion cyclotron reso-
4740 nance spectroscopy to the determination of reactive and momentum transfer
4741 rate constants. *Int. J. Mass Spectrom.* 25, 103–116.
- 4742 Boyé, S., Campos, A., Douin, S., Fellows, C., Gauyacq, D., Shafizadeh, N.,
4743 Halvick, P., Boggio-Pasqua, M., 2002. Visible emission from the vibrationally
4744 hot C₂H radical following vacuum-ultraviolet photolysis of acetylene: Exper-
4745 iment and theory. *J. Chem. Phys.* 116, 8843–8855.
- 4746 Bradforth, S., Kim, E., Arnold, D., Neumark, D., 1993. Photoelectron spec-
4747 troscopy of CN⁻, NCO⁻, and NCS⁻. *J. Chem. Phys.* 98, 800–810.
- 4748 Brown, R., 1973. A measurement of the rate of the reaction N + H + M → NH
4749 + M. *Int. J. Chem. Kinet.* 5, 663–667.

- 4750 Brownsword, R., Canosa, A., Rowe, B., Sims, I., Smith, I., Stewart, D.,
4751 Symonds, A., Travers, D., 1997a. Kinetics over a wide range of tempera-
4752 ture (13-744 K): Rate constants for the reactions of CH($\Sigma=0$) with H₂ and
4753 D₂ and for the removal of CH($\Sigma=1$) by H₂ and D₂. *J. Chem. Phys.* 106,
4754 7662–7677.
- 4755 Brownsword, R., Sims, I., Smith, I., Stewart, D., Canosa, A., Rowe, B., 1997b.
4756 The radiative association of CH with H₂: A mechanism for formation of CH₃
4757 in interstellar clouds. *Astrophys. J.* 485, 195.
- 4758 Burt, J., Dunn, J., McEwan, M., Sutton, M., Roche, A., Schiff, H., 1970. Some
4759 ion-molecule reactions of H₃⁺ and the proton affinity of H₂. *J. Chem. Phys.*
4760 52, 6062–6075.
- 4761 Burton, C., Noyes, W., 1968. Electronic energy relaxation in toluene vapor. *J.*
4762 *Chem. Phys.* 49, 1705–1714.
- 4763 Butterfield, M., Yu, T., Lin, M., 1993. Kinetics of CN reactions with allene,
4764 butadiene, propylene and acrylonitrile. *Chem. Phys.* 169, 129–134.
- 4765 Cameron, M., Sivakumaran, V., Dillon, T., Crowley, J., 2002. Reaction between
4766 OH and CH₃CHO Part 1. Primary product yields of CH₃ (296 K), CH₃CO
4767 (296 K), and H (237-296 K). *Phys. Chem. Chem. Phys.* 4, 3628–3638.
- 4768 Campbell, I., Gray, C., 1973. Rate constants for O(³P) recombination and
4769 association with N(⁴S). *Chem. Phys. Lett.* 18, 607–609.
- 4770 Canosa, A., Sims, I., Travers, D., Smith, I., Rowe, B., 1997. Reactions of the
4771 methylidene radical with CH₄, C₂H₂, C₂H₄, C₂H₆, and but-1-ene studied
4772 between 23 and 295 K with a CRESU apparatus. *Astron. Astrophys.* 323,
4773 644–651.
- 4774 Capalbo, F., Bénilan, Y., Fray, N., Schwell, M., Champion, N., Es-sebbar, E.,
4775 Koskinen, T., Lehocki, I., Yelle, R., 2016. New benzene absorption cross
4776 sections in the VUV, relevance for Titan’s upper atmosphere. *Icarus* 265,
4777 95–109.
- 4778 Capone, L., Dubach, J., Prasad, S., Whitten, R., 1983. Galactic cosmic rays
4779 and N₂ dissociation on Titan. *Icarus* 55, 73–82.
- 4780 Capone, L., Dubach, J., Whitten, R., Prasad, S., 1979. Cosmic ray ionization
4781 of the Jovian atmosphere. *Icarus* 39, 433–449.
- 4782 Capone, L., Dubach, J., Whitten, R., Prasad, S., Santhanam, K., 1980. Cosmic
4783 ray synthesis of organic molecules in Titan’s atmosphere. *Icarus* 44, 72–84.
- 4784 Capone, L., Prasad, S., Huntress, W., Whitten, R., Dubach, J., Santhanam, K.,
4785 1981. Formation of organic molecules on Titan. *Nature* 293, 45–46.
- 4786 Capone, L., Whitten, R., Dubach, J., Prasad, S., Huntress Jr., W., 1976. The
4787 lower ionosphere of Titan. *Icarus* 28, 367–378.

- 4788 Carelli, F., Satta, M., Grassi, T., Gianturco, F., 2013. Carbon-rich molecular
4789 chains in protoplanetary and planetary atmospheres: Quantum mechanisms
4790 and electron attachment rates for anion formation. *Astrophys J.* 774, #97.
- 4791 Carrasco, N., Alcaraz, C., Dutuit, O., Plessis, S., Thissen, R., Vuitton, V.,
4792 Yelle, R., Pernot, P., 2008. Sensitivity of a Titan ionospheric model to the
4793 ion-molecule reaction parameters. *Planet. Space Sci.* 56, 1644–1657.
- 4794 Carty, D., Le Page, V., Sims, I., Smith, I., 2001. Low temperature rate co-
4795 efficients for the reactions of CN and C₂H radicals with allene and methyl
4796 acetylene. *Chem. Phys. Lett.* 344, 310–316.
- 4797 Cerceau, F., Raulin, F., Courtin, R., Gautier, D., 1985. Infrared spectra of
4798 gaseous mononitriles - Application to the atmosphere of Titan. *Icarus* 62,
4799 207–220.
- 4800 Chabot, M., Béroff, K., Gratier, P., Jallat, A., Wakelam, V., 2013. Reactions
4801 forming C_{n=2,10}^(0,+), C_{n=2,4}H^(0,+), and C₃H₂^(0,+) in the gas phase: Semiempirical
4802 branching ratios. *Astrophys. J.* 771, #90.
- 4803 Chamot-Rooke, J., Mourgues, P., van der Rest, G., Audier, H., 2003. Am-
4804 bident reactivity and characterization of small ionized carbenes. *Int. J. Mass*
4805 *Spectrom.* 226, 249–269.
- 4806 Chan, W., Cooper, G., Brion, C., 1993a. Absolute optical oscillator strengths
4807 for discrete and continuum photoabsorption of carbon monoxide (7-200 eV)
4808 and transition moments for the X 1 Σ^+ + \tilde{U} A 1 Σ^+ system. *Chem. Phys.* 170,
4809 123–138.
- 4810 Chan, W., Cooper, G., Brion, C., 1993b. The electronic spectrum of carbon
4811 dioxide. Discrete and continuum photoabsorption oscillator strengths (6-203
4812 eV). *Chem. Phys.* 178, 401–413.
- 4813 Chan, W., Cooper, G., Brion, C., 1993c. The electronic spectrum of water in
4814 the discrete and continuum regions. Absolute optical oscillator strengths for
4815 photoabsorption (6-200 eV). *Chem. Phys.* 178, 387–401.
- 4816 Chastaing, D., James, P., Sims, I., Smith, I., 1998. Neutral-neutral reactions at
4817 the temperatures of interstellar clouds. Rate coefficients for reactions of C₂H
4818 radicals with O₂, C₂H₂, C₂H₄ and C₃H₆ down to 15 K. *Faraday Discuss.* 109,
4819 165–181.
- 4820 Chastaing, D., James, P., Sims, I., Smith, I., 1999. Neutral-neutral reactions
4821 at the temperatures of interstellar clouds: Rate coefficients for reactions of
4822 atomic carbon C(³P), with O₂, C₂H₂, C₂H₄ and C₃H₆ down to 15 K. *Phys.*
4823 *Chem. Chem. Phys.* 1, 2247–2256.
- 4824 Chastaing, D., Le Picard, S., Sims, I., Smith, I., 2001. Rate coefficients for the
4825 reactions of C(³P_J) atoms with C₂H₂, C₂H₄, CH₃C \equiv CH and H₂C=C=CH₂
4826 at temperatures down to 15 K. *Astron. Astrophys.* 365, 241–247.

- 4827 Cheikh Sid Ely, S., 2012. Réactivité des molécules organiques à très basses
4828 températures (22 - 300 K) pour la modélisation des milieux extra-terrestres
4829 froids. Ph.D. thesis. Université de Rennes 1.
- 4830 Cheikh Sid Ely, S., Morales, S., Guillemin, J.C., Klippenstein, S., Sims, I., 2013.
4831 Low temperature rate coefficients for the reaction $\text{CN} + \text{HC}_3\text{N}$. *J. Phys. Chem.*
4832 *A* 117, 12155–12164.
- 4833 Chen, F., Judge, D., Wu, C., 2000. Temperature dependent photoabsorption
4834 cross sections of allene and methylacetylene in the VUV-UV region. *Chem.*
4835 *Phys.* 260, 215–223.
- 4836 Chen, F., Judge, D., Wu, C., Caldwell, J., 1999. Low and room temperature
4837 photoabsorption cross sections of NH_3 in the UV region. *Planet. Space Sci.*
4838 47, 261–266.
- 4839 Chen, F., Wu, C., 2004. Temperature-dependent photoabsorption cross sections
4840 in the VUV-UV region. I. Methane and ethane. *J. Quant. Spectrosc. Radiat.*
4841 *Transfer* 85, 195–209.
- 4842 Cheng, B.M., Lu, H.C., Chen, H.K., Bahou, M., Lee, Y.P., Mebel, A., Lee, L.,
4843 Liang, M.C., Yung, Y., 2006. Absorption cross sections of NH_3 , NH_2D , NHD_2 ,
4844 and ND_3 in the spectral range 140–220 nm and implications for planetary
4845 isotopic fractionation. *Astrophys. J.* 647, 1535–1542.
- 4846 Choi, Y., Lin, M., 2005. Kinetics and mechanisms for reactions of HNO with
4847 CH_3 and C_6H_5 studied by quantum-chemical and statistical-theory calcula-
4848 tions. *Inter. J. Chem. Kin.* 37, 261–274.
- 4849 Chourou, S., Orel, A., 2009. Dissociative electron attachment to HCN and HNC.
4850 *Phys. Rev. A* 80, #032709.
- 4851 Chupka, W., Dehmer, P., Jivery, W., 1975. High resolution photoionization
4852 study of ion-pair formation in H_2 , HD, and D_2 . *J. Chem. Phys.* 63, 3929–
4853 3944.
- 4854 Clarke, D., Ferris, J., 1995. Photodissociation of cyanoacetylene: application to
4855 the atmospheric chemistry of Titan. *Icarus* 115, 119–125.
- 4856 Clyne, M., Stedman, D., 1967. Rate of recombination of nitrogen atoms. *J.*
4857 *Phys. Chem.* 71, 3071–3073.
- 4858 Coates, A., Crary, F., Lewis, G., Young, D., Waite Jr., J., Sittler Jr., E., 2007.
4859 Discovery of heavy negative ions in Titan’s ionosphere. *Geophys. Res. Lett.*
4860 34, #L22103.
- 4861 Coates, A., Wellbrock, A., Lewis, G., Jones, G., Young, D., Crary, F., Waite Jr.,
4862 J., 2009. Heavy negative ions in Titan’s ionosphere: altitude and latitude
4863 dependence. *Planet. Space Sci.* 57, 1866–1871.

- 4864 Coates, A., Wellbrock, A., Lewis, G., Jones, G., Young, D., Crary, F., Waite Jr.,
4865 J., Johnson, R., Hill, T., Sittler Jr., E., 2010. Negative ions at Titan and
4866 Enceladus: recent results. *Faraday Discuss.* 147, 293–305.
- 4867 Collin, G., 1988. Photochemistry of simple olefins: Chemistry of electronic
4868 excited states or hot ground state? *Adv. Photochem.* 14, 135–176.
- 4869 Collin, G., Deslauriers, H., Deschenes, J., 1979. Photolyse du propène et du
4870 méthyl-2-butène vers 174 et à 163 nm. *Can. J. Chem.* 57, 870–875.
- 4871 Collin, G., Perrin, P., 1972. Photolyse dans l’ultraviolet à vide du *Cis*- et du
4872 *trans*-butène-2. *Can. J. Chem.* 50, 2823–2832.
- 4873 Colombatti, G., Withers, P., Ferri, F., Aboudan, A., Ball, A.J., Bettanini,
4874 C., Gaborit, V., Harri, A.M., Hathi, B., Leese, M.R., Makinen, T., Stop-
4875 pato, P.L., Towner, M.C., Zarnecki, J.C., Angrilli, F., Fulchignoni, M., 2008.
4876 Reconstruction of the trajectory of the Huygens probe using the Huygens
4877 Atmospheric Structure Instrument (HASI). *Planet. Space Sci.* 56, 586–600.
- 4878 Connors, R., Roebber, J., Weiss, K., 1974. Vacuum ultraviolet spectroscopy of
4879 cyanogen and cyanoacetylenes. *J. Chem. Phys.* 60, 5011–5024.
- 4880 Cook, G., Metzger, P., Ogawa, M., 1965. Photoionization and absorption coef-
4881 ficients of CO in the 600 to 1000 Å region. *Can. J. Chem.* 43, 1706–1722.
- 4882 Cooper, G., Anderson, J., Brion, C., 1996. Absolute photoabsorption and pho-
4883 toionization of formaldehyde in the VUV and soft X-ray regions (3–200 eV).
4884 *Chem. Phys.* 209, 61–77.
- 4885 Cooper, G., Burton, G., Brion, C., 1995. Absolute UV and soft X-ray photoab-
4886 sorption of acetylene by high resolution dipole (e,e) spectroscopy. *J. Electron*
4887 *Spectrosc. Rel. Phenomena* 73, 139–148.
- 4888 Cordiner, M., Nixon, C., Charnley, S., Mumma, M., Serigano, J., Palmer, M.,
4889 Irwin, P., Teanby, N., Kisiel, Z., 2015a. ALMA spectroscopy of Titan’s atmo-
4890 sphere: First detections of vinyl cyanide and acetonitrile isotopologues. *Bull.*
4891 *Am. Astron. Soc.* 46, #205.03.
- 4892 Cordiner, M., Palmer, M., Nixon, C., Irwin, P., Teanby, N., Charnley, S.,
4893 Mumma, M., Kisiel, Z., Serigano, J., Kuan, Y.J., Chuang, Y.L., Wang, K.S.,
4894 2015b. Ethyl cyanide on Titan: Spectroscopic detection and mapping using
4895 ALMA. *Astrophys. J.* 800, #L14.
- 4896 Cordiner, M.A., Nixon, C.A., Teanby, N.A., Irwin, P.G.J., Serigano, J., Charn-
4897 ley, S.B., Milam, S.N., Mumma, M.J., Lis, D.C., Villanueva, G., Paganini,
4898 L., Kuan, Y.J., Remijan, A.J., 2014. ALMA Measurements of the HNC and
4899 HC₃N Distributions in Titan’s Atmosphere. *Astrophys. J.* 795, #L30.
- 4900 Costes, M., Halvick, P., Hickson, K., Daugey, N., Naulin, C., 2009. Non-
4901 threshold, threshold, and nonadiabatic behavior of the key interstellar C +
4902 C₂H₂ reaction. *Astrophys. J.* 703, 1179–1187.

- 4903 Cottini, V., Nixon, C., Jennings, D., Anderson, C., Gorius, N., Bjoraker, G.,
4904 Coustenis, A., Teanby, N., Achterberg, R., Bézard, B., de Kok, R., Lellouch,
4905 E., Irwin, P., Flasar, F., Bampasidis, G., 2012. Water vapor in Titan's strato-
4906 sphere from Cassini CIRS far-infrared spectra. *Icarus* 220, 855–862.
- 4907 Cotton, C., Francisco, J., Klemperer, W., 2013. Computational study of the
4908 linear proton bound ion-molecule complexes of HCNH^+ with HCN and HNC.
4909 *J. Chem. Phys.* 139, #014304.
- 4910 Courtin, R., Swinyard, B., Moreno, R., Fulton, T., Lellouch, E., Rengel, M.,
4911 Hartogh, P., 2011. First results of *Herschel*-SPIRE observations of Titan.
4912 *Astron. Astrophys.* 536, #L2.
- 4913 Courtin, R.D., Sim, C.K., Kim, S.J., Gautier, D., 2007. The tropospheric abun-
4914 dance of H_2 on Titan from the Cassini CIRS investigation. *Bull. Am. Astron.*
4915 *Soc.* 39, #56.05.
- 4916 Coustenis, A., Achterberg, R., Conrath, B., Jennings, D., Marten, A., Gautier,
4917 D., Nixon, C., Flasar, F., Teanby, N., Bézard, B., Samuelson, R., Carlson,
4918 R., Lellouch, E., Bjoraker, G., Romani, P., Taylor, F., Irwin, P., Fouchet,
4919 T., Hubert, A., Orton, G., Kunde, V., Vinatier, S., Mondellini, J., Ab-
4920 bas, M., Courtin, R., 2007. The composition of Titan's stratosphere from
4921 Cassini/CIRS mid-infrared spectra. *Icarus* 189, 35–62.
- 4922 Coustenis, A., Bampasidis, G., Achterberg, R., Lavvas, P., Jennings, D., Nixon,
4923 C., Teanby, N., Vinatier, S., Flasar, F., Carlson, R., Orton, G., Romani,
4924 P., Guandique, E., Stamogiorgos, S., 2013. Evolution of the stratospheric
4925 temperature and chemical composition over one Titanian year. *Astrophys. J.*
4926 779, #177.
- 4927 Coustenis, A., Bézard, B., 1995. Titan's atmosphere from Voyager infrared ob-
4928 servations IV. Latitudinal variations of temperature and composition. *Icarus*
4929 115, 126–140.
- 4930 Coustenis, A., Bézard, B., Gautier, D., Marten, A., Samuelson, R., 1991. Titan's
4931 atmosphere from Voyager infrared observations III. Vertical distributions of
4932 hydrocarbons and nitriles near Titan's north pole. *Icarus* 89, 152–167.
- 4933 Coustenis, A., Jennings, D., Nixon, C., Achterberg, R., Lavvas, P., Vinatier, S.,
4934 Teanby, N., Bjoraker, G., Carlson, R., Piani, L., Bampasidis, G., Flasar, F.,
4935 Romani, P., 2010. Titan trace gaseous composition from CIRS at the end of
4936 the Cassini-Huygens prime mission. *Icarus* 207, 461–476.
- 4937 Coustenis, A., Jennings, D.E., Achterberg, R.K., Bampasidis, G., Lavvas, P.,
4938 Nixon, C.A., Teanby, N.A., Anderson, C., Cottini, V., Flasar, F.M., 2016.
4939 Titan's temporal evolution in stratospheric trace gases near the poles. *Icarus*
4940 270, 409–420.

- 4941 Coustenis, A., Salama, A., Lellouch, E., Encrenaz, T., Bjoraker, G., Samuelson,
4942 R., de Graauw, T., Feuchtgruber, H., Kessler, M., 1998. Evidence for water
4943 vapor in Titan's atmosphere from ISO/SWS data. *Astron. Astrophys.* 336,
4944 L85–L89.
- 4945 Coustenis, A., Salama, A., Schulz, B., Ott, S., Lellouch, E., Encrenaz, T.,
4946 Gautier, D., Feuchtgruber, H., 2003. Titan's atmosphere from ISO mid-
4947 infrared spectroscopy. *Icarus* 161, 383–403.
- 4948 Crary, F., Magee, B., Mandt, K., Waite Jr., J., Westlake, J., Young, D., 2009.
4949 Heavy ions, temperatures and winds in Titan's ionosphere: Combined Cassini
4950 CAPS and INMS observations. *Planet. Space Sci.* 57, 1847–1856.
- 4951 Cravens, T., Robertson, I., Ledvina, S., Mitchell, D., Krimigis, S., Waite Jr., J.,
4952 2008. Energetic ion precipitation at Titan. *Geophys. Res. Lett.* 35, #L03103.
- 4953 Cravens, T., Robertson, I., Waite Jr., J., Yelle, R., Vuitton, V., Coates, A.,
4954 Wahlund, J.E., Agren, K., Richard, M., De La Haye, V., Wellbrock, A.,
4955 Neubauer, F., 2009. Model-data comparisons for Titan's nightside ionosphere.
4956 *Icarus* 199, 174–188.
- 4957 Cressin, A., Lebonnois, S., Vinatier, S., Bézard, B., Coustenis, A., Teanby,
4958 N., Achterberg, R., Rannou, P., Hourdin, F., 2008. Diagnostics of Titan's
4959 stratospheric dynamics using the Cassini/CIRS data and the 2-dimensional
4960 IPSL circulation model. *Icarus* 197, 556–571.
- 4961 Cui, J., Galand, M., Yelle, R., Vuitton, V., Wahlund, J.E., Lavvas, P., Müller-
4962 Wodarg, I., Cravens, T., Kasprzak, W., Waite Jr., J., 2009a. Diurnal varia-
4963 tions of Titan's ionosphere. *J. Geophys. Res.* 114, #A06310.
- 4964 Cui, J., Yelle, R., Strobel, D., Müller-Wodarg, I., Snowden, D., Koskinen, T.,
4965 Galand, M., 2012. The CH₄ structure in Titan's upper atmosphere revisited.
4966 *J. Geophys. Res.* 117, #E11006.
- 4967 Cui, J., Yelle, R., Vuitton, V., Waite Jr., J., Kasprzak, W., Gell, D., Niemann,
4968 H., Müller-Wodarg, I., Borggren, N., Fletcher, G., Patrick, E., Raaen, E.,
4969 Magee, B., 2009b. Analysis of Titan's neutral upper atmosphere from Cassini
4970 Ion Neutral Mass Spectrometer measurements. *Icarus* 200, 581–615.
- 4971 Curdt, W., Germerott, D., Wilhelm, K., Schühle, U., Teriaca, L., Innes, D.,
4972 Bocchialini, K., Lemaire, P., 2013. The SUMER data in the SOHO archive.
4973 *Solar Phys.* 289, 2345–2376.
- 4974 Dalgarno, A., Degges, T., Williams, D.A., 1967. Dipole properties of molecular
4975 nitrogen. *Proc. Phys. Soc.* 92, 291–295.
- 4976 Dangi, B., Maity, S., Kaiser, R., Mebel, A., 2013. A combined crossed beam and
4977 ab initio investigation of the gas phase reaction of dicarbon molecules (C₂;
4978 X¹Σ_g⁺/a³Π_u) with propene (C₃H₆; X¹A') : Identification of the resonantly
4979 stabilized free radicals 1- and 3-vinylpropargyl. *J. Phys. Chem. A* 117, 11783–
4980 11793.

- 4981 Danielsson, M., Hamberg, M., Zhaunerchyk, V., Ehlerding, A., Kamińska, M.,
4982 Hellberg, F., Thomas, R., Österdahl, F., af Ugglas, M., Källberg, A., Simon-
4983 sson, A., Paál, A., Larsson, M., Geppert, W., 2008. The cross-section and
4984 branching fractions for dissociative recombination of the diacetylene cation
4985 $C_4D_2^+$. *Int. J. Mass Spectrom.* 273, 111–116.
- 4986 Daranlot, J., Hincelin, U., Bergeat, A., Costes, M., Loison, J.C., Wakelam,
4987 V., Hickson, K., 2012. Elemental nitrogen partitioning in dense interstellar
4988 clouds. *PNAS* 109, 10233–10238.
- 4989 Daugey, N., Caubet, P., Bergeat, A., Costes, M., Hickson, K., 2008. Reaction
4990 kinetics to low temperatures. Dicarbon + acetylene, methylacetylene, allene
4991 and propene from $77 \leq T \leq 296$ K. *Phys. Chem. Chem. Phys.* 10, 729–737.
- 4992 Daugey, N., Caubet, P., Retail, B., Costes, M., Bergeat, A., Dorthe, G., 2005.
4993 Kinetic measurements on methylidyne radical reactions with several hydro-
4994 carbons at low temperatures. *Phys. Chem. Chem. Phys.* 7, 2921–2927.
- 4995 Davidson, J., Schiff, H., Brown, T., Howard, C., 1978. Temperature dependence
4996 of the deactivation of O(1D) by CO from 113–333 K. *J. Chem. Phys.* 69, 1216–
4997 1217.
- 4998 De Avillez Pereira, R., Baulch, D., Pilling, M., Robertson, S., Zeng, G., 1997.
4999 Temperature and pressure dependence of the multichannel rate coefficients
5000 for the $CH_3 + OH$ system. *J. Phys. Chem. A* 101, 9681–9693.
- 5001 De Bleeker, K., Bogaerts, A., Goedheer, W., 2006. Detailed modeling of hy-
5002 drocarbon nanoparticle nucleation in acetylene discharges. *Phys. Rev. E* 73,
5003 026405.
- 5004 De Kok, R., Irwin, P., Teanby, N., Lellouch, E., Bézard, B., Vinatier, S., Nixon,
5005 C., Fletcher, L., Howett, C., Calcutt, S., Bowles, N., Flasar, F., Taylor, F.,
5006 2007. Oxygen compounds in Titan’s stratosphere as observed by Cassini
5007 CIRS. *Icarus* 186, 354–363.
- 5008 De La Haye, V., Waite Jr., J., Cravens, T., Robertson, I., Lebonnois, S., 2008.
5009 Coupled ion and neutral rotating model of Titan’s upper atmosphere. *Icarus*
5010 197, 110–136.
- 5011 Deakyne, C., Meot-Ner, M., Buckley, T., Metz, R., 1987. Proton affinities of
5012 diacetylene, cyanoacetylene, and cyanogen. *J. Chem. Phys.* 86, 2334–2342.
- 5013 Delpech, C., Guillemin, J., Paillous, P., Khlifi, M., Bruston, P., Raulin, F., 1994.
5014 Infrared spectra of triacetylene in the 4000–220 cm^{-1} region: Absolute band
5015 intensity and implications for the atmosphere of Titan. *Spectrochim. Acta* 50
5016 A, 1095–1100.
- 5017 Demarais, N., Yang, Z., Snow, T., Bierbaum, V., 2013. Chemistry of $HCNH^+$:
5018 mechanisms, structures, and relevance to Titan’s atmosphere. *Struct. Chem.*
5019 24, 1957–1963.

- 5020 Derecskei-Kovacs, A., North, S., 1999. The unimolecular dissociation of vinyl-
5021 cyanide: A theoretical investigation of a complex multichannel reaction. J.
5022 Chem. Phys. 110, 2862–2871.
- 5023 Derkatch, A., Al-Khalili, A., Vikor, L., Neau, A., Shi, W., Danared, H., af Ug-
5024 glas, M., Larsson, M., 1999. Branching ratios in dissociative recombination
5025 of the $C_2H_2^+$ molecular ion. J. Phys. B: At. Mol. Opt. Phys. 32, 3391–3398.
- 5026 Desai, R.T., Coates, A.J., Wellbrock, A., Vuitton, V., Crary, F., González-
5027 Caniulef, D., Shebanits, O., Jones, G.H., Lewis, G.R., Waite, J.H., Taylor,
5028 S.A., Kataria, D.O., Wahlund, J.E., Edberg, N.J.T., Sittler, E.C., 2017. Car-
5029 bon chain anions and the growth of complex organic molecules in Titan’s
5030 ionosphere. Astrophys. J. 844, #L18.
- 5031 DeSain, J., Taatjes, C., 2003. Infrared laser absorption measurements of the ki-
5032 netics of propargyl radical self-reaction and the 193 nm photolysis of propyne.
5033 J. Phys. Chem. A 107, 4843–4850.
- 5034 Deslauriers, H., Makulski, W., Collin, G., 1987. The $\alpha(C-C)/\beta(C-H)$ ratio
5035 of the primary processes in the 184.9 nm photolysis of gaseous *cis*- and
5036 *trans*-2-butene. Can. J. Chem. 65, 1631–1638.
- 5037 Deyerl, H.J., Fischer, I., Chen, P., 1999. Photodissociation dynamics of the allyl
5038 radical. J. Chem. Phys. 110, 1450–1462.
- 5039 Deyerl, H.J., Gilbert, T., Fischer, I., Chen, P., 1997. Kinetics and dynamics in
5040 the photodissociation of the allyl radical. J. Chem. Phys. 107, 3329–3332.
- 5041 Dheandhanoo, S., Forte, L., Fox, A., Bohme, D., 1986. Ion-molecule reactions
5042 with carbon chain molecules: reactions with diacetylene and the diacetylene
5043 cation. Can. J. Chem. 64, 641–648.
- 5044 Dheandhanoo, S., Johnsen, R., Biondi, M., 1984. Measured ion-molecule reac-
5045 tion rates for modelling Titan’s atmosphere. Planet. Space Sci. 32, 1301–1305.
- 5046 Dibeler, V., Reese, R., Franklin, J., 1961. Mass spectrometric study of cyanogen
5047 and cyanoacetylenes. J. Am. Chem. Soc. 83, 1813–1818.
- 5048 Dobrijevic, M., Hébrard, E., Loison, J., Hickson, K., 2014. Coupling of oxygen,
5049 nitrogen, and hydrocarbon species in the photochemistry of Titan’s atmo-
5050 sphere. Icarus 228, 324–346.
- 5051 Dobrijevic, M., Loison, J., Hickson, K., Gronoff, G., 2016. 1D-coupled photo-
5052 chemical model of neutrals, cations and anions in the atmosphere of Titan.
5053 Icarus 268, 313–339.
- 5054 Dong, H., Ding, Y.H., Sun, C.C., 2005. C_2H+H_2CO : A new route for formalde-
5055 hyde removal. J. Chem. Phys. 122, #204321.

- 5056 Doose, L., Karkoschka, E., Tomasko, M., Anderson, C., 2016. Vertical structure
5057 and optical properties of Titan's aerosols from radiance measurements made
5058 inside and outside the atmosphere. *Icarus* 270, 355–375.
- 5059 Dryahina, K., Cunha de Miranda, B., Španěl, P., Žabka, J., Alcaraz, C., Her-
5060 man, Z., 2011. Selected ion flow tube study of ion-molecule reactions of
5061 $\text{N}^+(\text{}^3\text{P})$ and Kr^+ with C_3 hydrocarbons propane, propene, and propyne. *J.*
5062 *Phys. Chem. A* 115, 7310–7315.
- 5063 Dulaney, J., Biondi, M., Johnsen, R., 1987. Electron temperature dependence of
5064 the recombination of electrons with NO^+ ions. *Phys. Rev. A* 36, 1342–1350.
- 5065 Dunning, T., 1989. Gaussian-basis sets for use in correlated molecular calcula-
5066 tions. 1. The atoms boron through neon and hydrogen. *J. Chem. Phys.* 90,
5067 1007–1023.
- 5068 Dutuit, O., Carrasco, N., Thissen, R., Vuitton, V., Alcaraz, C., Pernot, P.,
5069 Balucani, N., Casavecchia, P., Canosa, A., Le Picard, S., Loison, J.C., Her-
5070 man, Z., Žabka, J., Ascenzi, D., Tosi, P., Franceschi, P., Price, S., Lavvas, P.,
5071 2013. Critical review of N , N^+ , N_2^+ , N^{++} and N_2^{++} main production pro-
5072 cesses and reactions of relevance to Titan's atmosphere. *Astrophys. J. Suppl.*
5073 *Ser.* 204, #20.
- 5074 Eden, S., Limão-Vieira, P., Kendall, P., Mason, N., Hoffmann, S., Spyrou, S.,
5075 2003. High resolution photo-absorption studies of acrylonitrile, $\text{C}_2\text{H}_3\text{CN}$, and
5076 acetonitrile, CH_3CN . *Eur. Phys. J. D* 26, 201–210.
- 5077 Edwards, S., Freeman, C., McEwan, M., 2008. The ion chemistry of methylen-
5078 imine and propionitrile and their relevance to Titan. *Int. J. Mass Spectrom.*
5079 272, 86–90.
- 5080 Edwards, S., Freeman, C., McEwan, M., 2009. Some ion chemistry of HC_5N .
5081 *Int. J. Mass Spectrom.* 279, 82–86.
- 5082 Ehlerding, A., Arnold, S., Viggiano, A., Kalhori, S., Semaniak, J., Derkatch,
5083 A., Rosén, S., af Ugglas, M., Larsson, M., 2003. Rates and products of the
5084 dissociative recombination of C_3H_7^+ in low-energy electron collisions. *J. Phys.*
5085 *Chem. A* 107, 2179–2184.
- 5086 Ehlerding, A., Hellberg, F., Thomas, R., Kalhori, S., Viggiano, A., Arnold, S.,
5087 Larsson, M., af Ugglas, M., 2004. Dissociative recombination of C_2H^+ and
5088 C_2H_4^+ : Absolute cross sections and product branching ratios. *Phys. Chem.*
5089 *Chem. Phys.* 6, 949–954.
- 5090 Eichelberger, B., Snow, T., Barckholtz, C., Bierbaum, V., 2007. Reactions
5091 of H, N, and O atoms with carbon chain anions of interstellar interest: An
5092 experimental study. *Astrophys. J.* 667, 1283–1289.

- 5093 Ellison, G., Engelking, P., Lineberger, W., 1978. An experimental determination
5094 of the geometry and electron affinity of methyl radical. *J. Am. Chem. Soc.*
5095 100, 2556–2558.
- 5096 English, M., Lara, L., Lorenz, R., Ratcliff, P., Rodrigo, R., 1996. Ablation and
5097 chemistry of meteoric materials in the atmosphere of Titan. *Adv. Space. Res.*
5098 17, 157–160.
- 5099 Erwin, D., Kunc, J., 2005. Electron-impact dissociation of the methane molecule
5100 into neutral fragments. *Phys. Rev. A* 72, 052719–052724.
- 5101 Erwin, D., Kunc, J., 2008. Dissociation and ionization of the methane molecule
5102 by nonrelativistic electrons including the near threshold region. *J. Appl. Phys.*
5103 103, #064906.
- 5104 Es-sebbar, E., Benilan, Y., Farooq, A., 2013. Temperature-dependent absorp-
5105 tion cross-section measurements of 1-butene (1-C₄H₈) in VUV and IR. *J.*
5106 *Quant. Spectrosc. Radiat. Transfer* 115, 1–12.
- 5107 Espinosa-Garcia, J., Corchado, J., 1994. Variational transition-state theory
5108 calculation using the direct dynamics method: NH₃+H → NH₂+H₂ reaction.
5109 *J. Chem. Phys.* 101, 1333–1342.
- 5110 Fabiano, F., López Puertas, M., Adriani, A., Moriconi, M.L., D’Aversa, E.,
5111 Funke, B., López-Valverde, M.A., Ridolfi, M., Dinelli, B.M., 2017. CO con-
5112 centration in the upper stratosphere and mesosphere of Titan from VIMS
5113 dayside limb observations at 4.7 μm. *Icarus* 293, 119–131.
- 5114 Fagerström, K., Lund, A., Mahmoud, G., Jodkowski, J., Ratajczak, E., 1993.
5115 Kinetics of the gas-phase reaction between ethyl and hydroxyl radicals. *Chem.*
5116 *Phys. Lett.* 208, 321–327.
- 5117 Fahr, A., Hassanzadeh, P., Atkinson, D., 1998. Ultraviolet absorption spectrum
5118 and cross-sections of vinyl (C₂H₃) radical in the 225-238 nm region. *Chem.*
5119 *Phys.* 236, 43–51.
- 5120 Fahr, A., Hassanzadeh, P., Laszlo, B., Huie, R., 1997. Ultraviolet absorption
5121 and cross sections of propargyl (C₃H₃) radicals in the 230-300 nm region.
5122 *Chem. Phys.* 215, 59–66.
- 5123 Fahr, A., Laufer, A., 1988. Ultraviolet absorption of the vinyl radical and
5124 reaction with oxygen. *J. Phys. Chem.* 92, 7229–7232.
- 5125 Fahr, A., Laufer, A., 1992. The 1,1-elimination of hydrogen cyanide and forma-
5126 tion of triplet vinylidene from the photolysis of acrylonitrile. *J. Phys. Chem.*
5127 96, 4217–4219.
- 5128 Fahr, A., Laufer, A., Klein, R., Braun, W., 1991. Reaction rate determinations
5129 of vinyl radical reactions with vinyl, methyl, and hydrogen atoms. *J. Phys.*
5130 *Chem.* 95, 3218–3224.

- 5131 Fahr, A., Nayak, A., 1994. Temperature dependant ultraviolet absorption cross
5132 sections of 1.3-butadiene and butadiyne. *Chem. Phys.* 189, 725–731.
- 5133 Fahr, A., Nayak, A., 1996. Temperature dependant ultraviolet absorption cross
5134 sections of propylene, methylacetylene and vinylacetylene. *Chem. Phys.* 203,
5135 351–358.
- 5136 Faure, A., Vuitton, V., Thissen, R., Wiesenfeld, L., 2009. A semiempirical
5137 capture model for fast neutral reactions at low temperature. *J. Phys. Chem.*
5138 *A* 113, 13694–13699.
- 5139 Fedor, J., Cicman, P., Coupier, B., Feil, S., Winkler, M., Gluch, K., Husarik,
5140 J., Jaksch, D., Farizon, B., Mason, N., Scheier, P., Märk, T., 2006. Frag-
5141 mentation of transient water anions following low-energy electron capture by
5142 $\text{H}_2\text{O}/\text{D}_2\text{O}$. *J. Phys. B: At. Mol. Opt. Phys.* 39, 3935–3944.
- 5143 Fehsenfeld, F., 1975. Interaction between ions and molecules, in: Ausloos,
5144 P. (Ed.), NATO advanced study institutes series. Series B, Physics. Plenum
5145 Press, New York. volume 6, p. 387.
- 5146 Fehsenfeld, F., Howard, C., Ferguson, E., 1973. Thermal energy reactions of
5147 negative ions with H atoms in the gas phase. *J. Chem. Phys.* 58, 5841–5842.
- 5148 Feng, W., Hershberger, J., 2013. Experimental and theoretical study of the
5149 product channels of the $\text{C}_2\text{H} + \text{NO}$ reaction. *J. Phys. Chem. A* 117, 3585–
5150 3592.
- 5151 Fennelly, J., Torr, D., 1992. Photoionization and photoabsorption cross sections
5152 of O, N_2 , O_2 , and N for aeronomic calculations. *At. Data Nucl. Data Tables*
5153 51, 321–363.
- 5154 Ferguson, E., 1973. Rate constants of thermal energy binary ion-molecule reac-
5155 tions of aeronomic interest. *At. Data Nucl. Data Tables* 12, 159–178.
- 5156 Fiaux, A., Smith, D., Futrell, J., 1974. Reaction of CH_5^+ with C_2H_2 , C_2H_4 ,
5157 C_3H_6 and $c\text{-C}_3\text{H}_6$. *Int. J. Mass Spectrom.* 15, 9–21.
- 5158 Fisher, J., McMahon, T., 1990. Determination of rate constants for low pressure
5159 association reactions by Fourier transform-ion cyclotron resonance spectrom-
5160 etry. *Int. J. Mass Spectrom. Ion Processes* 100, 701–717.
- 5161 Flad, J., Brown, S., Burkholder, J., Stark, H., Ravishankara, A., 2006. Absorp-
5162 tion cross sections for the $\text{A } 2\text{A}''(0,90,0) \leftarrow \text{X } 2\text{A}'(0,01,0)$ band of the HCO
5163 radical. *Phys. Chem. Chem. Phys.* 8, 3636–3642.
- 5164 Fondren, L., Adams, N., Stavish, L., 2009. Gas phase reactions of CH_3^+ with a
5165 series of homo- and heterocyclic molecules. *J. Phys. Chem. A* 113, 592–598.
- 5166 Fondren, L., McLain, J., Jackson, D., Adams, N., Babcock, L., 2007. Studies of
5167 reactions of a series of ions with nitrogen containing heterocyclic molecules
5168 using a selected ion flow tube. *Int. J. Mass Spectrom.* 265, 60–67.

- 5169 Fournier, J., Shuman, N., Melko, J., Ard, S., Viggiano, A., 2013. A novel
5170 technique for measurement of thermal rate constants and temperature depen-
5171 dences of dissociative recombination: CO_2^+ , CF_3^+ , N_2O^+ , C_7H_8^+ , C_7H_7^+ ,
5172 C_6H_6^+ , C_6H_5^+ , C_5H_6^+ , C_4H_4^+ , and C_3H_3^+ . *J. Chem. Phys.* 138, #154201.
- 5173 Fournier, M., 2014. Reactivity of C_3N and C_2H at low temperature: applications
5174 for the Interstellar Medium and Titan. Ph.D. thesis. Université de Rennes 1.
- 5175 Fox, J., Yelle, R., 1997. Hydrocarbon ions in the ionosphere of Titan. *Geophys.*
5176 *Res. Lett.* 24, 2179–2182.
- 5177 Franklin, J., Wada, Y., Natalis, P., Hierl, P., 1966. Ion-molecule reactions in
5178 acetonitrile and propionitrile. *J. Phys. Chem.* 70, 2353–2361.
- 5179 Fraser, G., 2002. The ion detection efficiency of microchannel plates (MCPs).
5180 *Int. J. Mass Spectrom.* 215, 13–30.
- 5181 Fray, N., Bénilan, Y., Gazeau, M.C., Jolly, A., Schwell, M., Arzoumanian, E.,
5182 Ferradaz, T., Es-Sebbar, E., Guillemin, J.C., 2010. Temperature-dependent
5183 photoabsorption cross section of cyanodiacetylene in the vacuum UV. *J.*
5184 *Geophys. Res.* 115, #E06010.
- 5185 Fray, N., Schmitt, B., 2009. Sublimation of ices of astrophysical interest: A
5186 bibliographic review. *Planet. Space Sci.* 57, 2053–2080.
- 5187 Freysinger, W., Khan, F., Armentrout, P., Tosi, P., Dimitrev, O., Bassi, D.,
5188 1994. Charge-transfer reaction of $^{14,15}\text{N}^+(\text{}^3\text{P}_J) + \text{N}_2(\text{}^1\Sigma_g^+)$ from thermal to
5189 100 eV. Crossed-beam and scattering-cell guided-ion beam experiments. *J.*
5190 *Chem. Phys.* 101, 3688–3695.
- 5191 Frisch, M., Trucks, G., Schlegel, H., Scuseria, G., Robb, M., Cheeseman, J.,
5192 Scalmani, G., Barone, V., Mennucci, B., Petersson, G., et al., 2009. Gaussian
5193 09, Revision D.01. Gaussian, Inc., Wallingford CT.
- 5194 Fröchtenicht, R., 1995. The photodissociation of toluene studied by forward
5195 photofragment translational spectroscopy. *J. Chem. Phys.* 102, 4850–4859.
- 5196 Fukuzawa, K., Matsushita, T., Morokuma, K., Levandier, D., Chiu, Y., Dressler,
5197 R., Murad, E., Midey, A., Williams, S., Viggiano, A., 2001. An ab initio and
5198 experimental study of vibrational effects in low energy $\text{O}^+ + \text{C}_2\text{H}_2$ charge-
5199 transfer collisions. *J. Chem. Phys.* 115, 3184–3194.
- 5200 Fukuzawa, K., Osamura, Y., Schaefer, H.I., 1998. Are neutral-neutral reactions
5201 effective for the carbon-chain growth of cyanopolynes and polyacetylenes in
5202 interstellar space? *Astrophys. J.* 505, 278–285.
- 5203 Fulchignoni, M., Ferri, F., Angrilli, F., Ball, A., Bar-Nun, A., Barucci, M.,
5204 Bettanini, C., Bianchini, G., Borucki, W., Colombatti, G., Coradini, M.,
5205 Coustenis, A., Debei, S., Falkner, P., Fanti, G., Flamini, E., Gaborit, V.,
5206 Gard, R., Hamelin, M., Harri, A., Hathi, B., Jernej, I., Leese, M., Lehto, A.,

- 5207 Lion Stoppato, P., López-Moreno, J., Mäkinen, T., McDonnell, J., McKay,
5208 C., Molina-Cuberos, G., Neubauer, F., Pirronello, V., Rodrigo, R., Saggin, B.,
5209 Schwingenschuh, K., Seiff, A., Simões, F., Svedhem, H., Tokano, T., Towner,
5210 M., Trautner, R., Withers, P., Zarnecki, J., 2005. In situ measurements of
5211 the physical characteristics of Titan's environment. *Nature* 438, 785–791.
- 5212 Fulle, D., Hippler, H., 1997. The temperature and pressure dependence of the
5213 reaction $\text{CH} + \text{H}_2 \rightleftharpoons \text{CH}_3 \rightleftharpoons \text{CH}_2 + \text{H}$. *J. Chem. Phys.* 106, 8691–8698.
- 5214 Galand, M., Coates, A., Cravens, T., Wahlund, J.E., 2014. Titan's ionosphere,
5215 in: Müller-Wodarg, I., Griffith, C., Lellouch, E., Cravens, T. (Eds.), *Titan:*
5216 *Interior, Surface, Atmosphere and Space Environment*. Cambridge University
5217 Press, New York. chapter 11, pp. 376–418.
- 5218 Galand, M., Lilensten, J., Toubanc, D., Maurice, S., 1999. The ionosphere of
5219 Titan: Ideal diurnal and nocturnal cases. *Icarus* 140, 92–105.
- 5220 Galand, M., Yelle, R., Cui, J., Wahlund, J.E., Vuitton, V., Wellbrock, A.,
5221 Coates, A., 2010. Ionization sources in Titan's deep ionosphere. *J. Geophys.*
5222 *Res.* 115, #A07312.
- 5223 Gan, L., Keller, C., Cravens, T., 1992. Electrons in the ionosphere of Titan. *J.*
5224 *Geophys. Res.* 97, 12137–12151.
- 5225 Gannon, K., Blitz, M., Liang, C., Pilling, M., Seakins, P., Glowacki, D., 2010a.
5226 Temperature dependent kinetics (195–798 K) and H atom yields (298–498 K)
5227 from reactions of $^1\text{CH}_2$ with acetylene, ethene, and propene. *J. Phys. Chem.*
5228 *A* 114, 9413–9424.
- 5229 Gannon, K., Blitz, M., Liang, C.H., Pilling, M., Seakins, P., Glowacki, D.,
5230 Harvey, J., 2010b. An experimental and theoretical investigation of the com-
5231 petition between chemical reaction and relaxation for the reactions of $^1\text{CH}_2$
5232 with acetylene and ethene: implications for the chemistry of the giant planets.
5233 *Faraday Discuss.* 147, 173–188.
- 5234 Gannon, K., Blitz, M., Pilling, M., Seakins, P., Klippenstein, S., Harding, L.,
5235 2008. Kinetics and product branching ratios of the reaction of $^1\text{CH}_2$ with H_2
5236 and D_2 . *J. Phys. Chem. A* 112, 9575–9583.
- 5237 Gannon, K., Glowacki, D., Blitz, M., Hughes, K., Pilling, M., Seakins, P., 2007.
5238 H atom yields from the reactions of CN radicals with C_2H_2 , C_2H_4 , C_3H_6 ,
5239 *trans*- C_4H_8 , and *iso*- C_4H_8 . *J. Phys. Chem. A* 111, 6679–6692.
- 5240 Gans, B., Boyé-Péronne, S., Broquier, M., Delsaut, M., Douin, S., Fellows,
5241 C., Halvick, P., Loison, J.C., Lucchese, R., Gauyacq, D., 2011. Photolysis
5242 of methane revisited at 121.6 nm and at 118.2 nm: quantum yields of the
5243 primary products, measured by mass spectrometry. *Phys. Chem. Chem. Phys.*
5244 13, 8140–8152.

- 5245 Gans, B., Peng, Z., Carrasco, N., Gauyacq, D., Lebonnois, S., Pernot, P., 2013.
5246 Impact of a new wavelength-dependent representation of methane photoly-
5247 sis branching ratios on the modeling of Titan's atmospheric photochemistry.
5248 *Icarus* 223, 330–343.
- 5249 Gardner, E., McNesby, J., 1982. Vacuum-ultraviolet photolysis of methylamine.
5250 *J. Phys. Chem.* 86, 2646–2651.
- 5251 Gehring, M., Hoyermann, K., Wagner, H., Wolfrum, J., 1971. Reaction of
5252 atomic hydrogen with hydrazine. *Ber. Bunsenges. Phys. Chem.* 75.
- 5253 Georgievskii, Y., Harding, L., Klippenstein, S., 2016. VaReCoF: Variable Reac-
5254 tion Coordinate Flux. <http://tcg.cse.anl.gov/papr/codes/varecof.html> .
- 5255 Georgievskii, Y., Klippenstein, S., 2003. Transition state theory for multichannel
5256 addition reactions: Multifaceted dividing surfaces. *J. Phys. Chem. A* 107,
5257 9776–9781.
- 5258 Georgievskii, Y., Klippenstein, S., 2005. Long-range transition state theory. *J.*
5259 *Chem. Phys.* 122, #194103.
- 5260 Georgievskii, Y., Klippenstein, S., 2016. MESS: Master Equation System Solver.
5261 <http://tcg.cse.anl.gov/papr/codes/mess.html> .
- 5262 Georgievskii, Y., Miller, J., Burke, M., Klippenstein, S., 2013. Reformulation
5263 and solution of the master equation for multiple-well chemical reactions. *J.*
5264 *Phys. Chem. A* 117, 12146–12154.
- 5265 Geppert, W., Ehlerding, A., Hellberg, F., Kalhori, S., Thomas, R., Novotny, O.,
5266 Arnold, S., Miller, T., Viggiano, A., Larsson, M., 2004a. First observation of
5267 four-body breakup in electron recombination: $C_2D_5^+$. *Phys. Rev. Lett.* 93,
5268 #153201.
- 5269 Geppert, W., Ehlerding, A., Hellberg, F., Semaniak, J., Österdahl, F.,
5270 Kamińska, M., Al-Khalili, A., Zhaunerchyk, V., Thomas, R., af Ugglas, M.,
5271 Källberg, A., Simonsson, A., Larsson, M., 2004b. Dissociative recombination
5272 of nitrile ions: $DCCCN^+$ and $DCCND^+$. *Astrophys. J.* 613, 1302–1309.
- 5273 Geppert, W., Hamberg, M., Thomas, R., Österdahl, F., Hellberg, F., Zhauner-
5274 chyk, V., Ehlerding, A., Millar, T., Roberts, H., Semaniak, J., af Ugglas, M.,
5275 Källberg, A., Simonsson, A., Kamińska, M., Larsson, M., 2006. Dissociative
5276 recombination of protonated methanol. *Faraday Discuss.* 133, 177–190.
- 5277 Geppert, W., Thomas, R., Ehlerding, A., Hellberg, F., Österdahl, F., Hamberg,
5278 M., Semaniak, J., Zhaunerchyk, V., Kamińska, M., Källberg, A., Paál, A.,
5279 Larsson, M., 2005. Dissociative recombination branching ratios and their
5280 influence on interstellar clouds. *J. Phys.: Conf. Ser.* 4, 26–31.
- 5281 Geppert, W., Thomas, R., Ehlerding, A., Hellberg, F., Österdahl, F., af Ugglas,
5282 M., Larsson, M., 2004c. Dissociative recombination of $C_3H_4^+$: preferential
5283 formation of the C_3H_3 radical. *Int. J. Mass Spectrom.* 237, 25–32.

- 5284 Geppert, W., Thomas, R., Ehlerding, A., Semaniak, J., Österdahl, F., af Ugglas,
5285 M., Djurić, N., Paál, A., Larsson, M., 2004d. Extraordinary branching ratios
5286 in astrophysically important dissociative recombination reactions. *Faraday*
5287 *Discuss.* 127, 425–437.
- 5288 Geppert, W., Vigren, E., Hamberg, M., Zhaumerchyk, V., Thomas, R.,
5289 Kamińska, M., Millar, T., Semaniak, J., Roberts, H., Hellberg, F., Österdahl,
5290 F., Ehlerding, A., Larsson, M., 2007. Formation of biomolecule precursors in
5291 space. *J. Phys.: Conf. Ser.* 88, #012068.
- 5292 Gerlich, D., Borodi, G., 2009. Buffer gas cooling of polyatomic ions in rf multi-
5293 electrode traps. *Faraday Discuss.* 142, 57–72.
- 5294 Gerlich, D., Borodi, G., Luca, A., Mogo, C., Smith, M., 2011. Reactions between
5295 cold CH_x^+ and slow H and H_2 . *Z. Phys. Chem.* 225, 475–492.
- 5296 Gerlich, D., Jusku, P., Roučka, Š., Zymak, I., Plašil, R., Glosík, J., 2012. Ion
5297 trap studies of $\text{H}^- + \text{H} \rightarrow \text{H}_2 + \text{e}^-$ between 10 and 135 K. *Astrophys. J.*
5298 749, #22.
- 5299 Gerlich, D., Smith, M., 2006. Laboratory astrochemistry: Studying molecules
5300 under inter- and circumstellar conditions. *Phys. Scr.* 73, C25–C31.
- 5301 Gichuhi, W., Suits, A., 2011. Primary branching ratios for the low-temperature
5302 reaction of state-prepared N_2^+ with CH_4 , C_2H_2 , and C_2H_4 . *J. Phys. Chem.*
5303 *A* 115, 7105–7111.
- 5304 Gierczak, T., Gawłowski, J., Niedzielski, J., 1988. Reactions of excited C_3H_5
5305 radicals: Implications for the photolysis of propylene at 8.4 eV. *J. Photochem.*
5306 *Photobiol. A* 43, 1–9.
- 5307 Gilbert, R., Luther, K., Troe, J., 1983. Theory of thermal unimolecular reactions
5308 in the fall-off range. II. Weak collision rate constants. *Ber. Bunsenges. Phys.*
5309 *Chem.* 87, 169–177.
- 5310 Gladstone, G., Allen, M., Yung, Y., 1996. Hydrocarbon photochemistry in the
5311 upper atmosphere of Jupiter. *Icarus* 119, 1–52.
- 5312 Glicker, S., Okabe, H., 1987. Photochemistry of diacetylene. *J. Phys. Chem.*
5313 91, 437–440.
- 5314 Glicker, S., Stief, L., 1971. Photolysis of formaldehyde at 1470 and 1236 Å. *J.*
5315 *Chem. Phys.* 54, 2852–2857.
- 5316 Glosík, J., Smith, D., Spanel, P., Freysinger, W., Lindinger, W., 1993. SIFDT
5317 studies of the reactions of C^+ , CH^+ and CH_2^+ with HCl and CO_2 , and CH_3^+
5318 with HCl. *Int. J. Mass Spectrom. Ion Processes* 129, 131–143.
- 5319 Goldfarb, F., Drag, C., Chaibi, W., Kröger, S., Blondel, C., Delsart, C., 2005.
5320 Photodetachment microscopy of the *P*, *Q*, and *R* branches of the $\text{OH}^-(v=0)$
5321 to $\text{OH}(v=0)$ detachment threshold. *J. Chem. Phys.* 122, #014308.

- 5322 Goncher, S., Moore, D., Sveum, N., Neumark, D., 2008. Photofragment trans-
5323 lational spectroscopy of propargyl radicals at 248 nm. *J. Chem. Phys.* 128,
5324 #114303.
- 5325 Gougousi, T., Golde, M., Johnsen, R., 1997. Electron-ion recombination rate
5326 coefficient measurements in a flowing afterglow plasma. *Chem. Phys. Lett.*
5327 265, 399–403.
- 5328 Goulay, F., Leone, S., 2006. Low-temperature rate coefficients for the reaction
5329 of ethynyl radical (C_2H) with benzene. *J. Phys. Chem. A* 110, 1875–1880.
- 5330 Goulay, F., Osborn, D., Taatjes, C., Zou, P., Meloni, G., Leone, S., 2007. Direct
5331 detection of polyynes formation from the reaction of ethynyl radical (C_2H)
5332 with propyne ($CH_3-C\equiv CH$) and allene ($CH_2=C=CH_2$). *Phys. Chem. Chem.*
5333 *Phys.* 9, 4291–4300.
- 5334 Goulay, F., Soorkia, S., Meloni, G., Osborn, D., Taatjes, C., Leone, S., 2011.
5335 Detection of pentatetraene by reaction of the ethynyl radical (C_2H) with
5336 allene ($CH_2=C=CH_2$) at room temperature. *Phys. Chem. Chem. Phys.* 13,
5337 20820–20827.
- 5338 Goulay, F., Trevitt, A., Meloni, G., Selby, T., Osborn, D., Taatjes, C.,
5339 Vereecken, L., Leone, S., 2009. Cyclic versus linear isomers produced by reac-
5340 tion of the methylidyne radical (CH) with small unsaturated hydrocarbons.
5341 *J. Am. Chem. Soc.* 131, 993–1005.
- 5342 Graupner, K., Field, T., Saunders, G., 2008. Experimental evidence for ra-
5343 diative attachment in astrochemistry from electron attachment to NCCCCN.
5344 *Astrophys. J.* 685, L95–L98.
- 5345 Greenwald, E., North, S., Klippenstein, S., 2005. A two transition state model
5346 for radical-molecule reactions: A case study of the addition of OH to C_2H_4 .
5347 *J. Phys. Chem. A* 109, 6031–6044.
- 5348 Gronoff, G., Lilensten, J., Desorgher, L., Flückiger, E., 2009. Ionization pro-
5349 cesses in the atmosphere of Titan I. Ionization in the whole atmosphere.
5350 *Astron. Astrophys.* 506, 955–964.
- 5351 Gronoff, G., Mertens, C., Lilensten, J., Desorgher, L., Flückiger, E., Velinov,
5352 P., 2011. Ionization processes in the atmosphere of Titan III. Ionization by
5353 high-Z nuclei cosmic rays. *Astron. Astrophys.* 529, #A143.
- 5354 Gu, X., Guo, Y., Mebel, A., Kaiser, R., 2006. Chemical dynamics of the forma-
5355 tion of the 1,3-butadiynyl radical ($C_4H(X^2\Sigma^+)$) and its isotopomers. *J. Phys.*
5356 *Chem. A* 110, 11265–11278.
- 5357 Gu, X., Guo, Y., Zhang, F., Mebel, A., Kaiser, R., 2007. A crossed molecular
5358 beams study on the formation and energetics of the resonantly stabilized free
5359 $i-C_4H_3(X^2A')$ radical and its isotopomers. *Chem. Phys.* 335, 95–108.

- 5360 Gu, X., Kaiser, R., Mebel, A., Kislov, V., Klippenstein, S., Harding, L., Liang,
5361 M.C., Yung, Y., 2009a. A crossed molecular beams study on the formation
5362 of the exotic cyanoethynyl radical in Titan's atmosphere. *Astrophys. J.* 701,
5363 1797–1803.
- 5364 Gu, X., Kim, Y., Kaiser, R., Mebel, A., Liang, M.C., Yung, Y., 2009b. Chem-
5365 ical dynamics of triacetylene formation and implications to the synthesis of
5366 polyynes in Titan's atmosphere. *PNAS* 106, 16078–16083.
- 5367 Guo, J., Carrington, T., Filseth, S., 2001. Energy disposal in $CN(X^2\Sigma^+)$ pro-
5368 duced in the 157 nm photodissociation of acrylonitrile. *J. Chem. Phys.* 115,
5369 8411–8417.
- 5370 Guo, Y., Gu, X., Balucani, N., Kaiser, R., 2006a. Formation of the 2,4-
5371 pentadiynyl-1 radical ($H_2CCCCCH$, X^2B_1) in the crossed beams reaction of
5372 dicarbon molecules with methylacetylene. *J. Phys. Chem. A* 110, 6245–6249.
- 5373 Guo, Y., Gu, X., Zhang, F., Mebel, A., Kaiser, R., 2006b. Unimolecular decom-
5374 position of chemically activated pentatetraene ($H_2CCCCCH_2$) intermediates:
5375 A crossed beams study of dicarbon molecule reactions with allene. *J. Phys.*
5376 *Chem. A* 110, 10699–10707.
- 5377 Gupta, S., Jones, E., Harrison, A., Myher, J.J., 1967. Reactions of ther-
5378 mal energy ions. VI. Hydrogen-transfer ion-molecule reactions involving polar
5379 molecules. *Can. J. Chem.* 45, 3107–3117.
- 5380 Gurwell, M., 2004. Submillimeter observations of Titan: Global measures of
5381 stratospheric temperature, CO, HCN, HC_3N , and the isotopic ratios $^{12}C/^{13}C$
5382 and $^{14}N/^{15}N$. *Astrophys. J.* 616, L7–L10.
- 5383 Hahndorf, I., Lee, H., Mebel, A., Lin, S., Lee, Y., Kaiser, R., 2000. A combined
5384 crossed beam and ab initio investigation on the reaction of carbon species
5385 with C_4H_6 isomers. I. The 1,3-butadiene molecule, $H_2CCHCHCH_2$ (X^1A').
5386 *J. Chem. Phys.* 113, 9622–9636.
- 5387 Haider, N., Husain, D., 1993. Absolute rate data for the reactions of ground-
5388 state atomic carbon, $C[{}^2P_2({}^3P_J)]$, with alkenes investigated by time-resolved
5389 atomic resonance absorption spectroscopy in the vacuum ultraviolet. *J. Chem.*
5390 *Soc., Faraday Trans.* 89, 7–14.
- 5391 Halpern, J., Huang, Y., 1997. Radiative lifetimes, fluorescence quantum yields
5392 and photodissociation of the C_2N_2 ($A^1\Sigma_u^-$) and ($B^1\Delta_u$) states: Evidence for
5393 sterically hindered, triplet mediated crossings to the ($X^1\Sigma_g^+$) ground state.
5394 *Chem. Phys.* 222, 71–86.
- 5395 Halpern, J., Miller, G., Okabe, H., Nottingham, W., 1988. The UV photochem-
5396 istry of cyanoacetylene. *J. Photochem. Photobiol. A* 42, 63–72.

- 5397 Halpern, J., Petway, L., Lu, R., Jackson, W., McCrary, V., Nottingham, W.,
5398 1990. Photochemistry of cyano- and dicyanoacetylene at 193 nm. *J. Phys.*
5399 *Chem.* 94, 1869–1873.
- 5400 Halpern, J., Tang, X., 1985. Production of cyanogen ($A^2\Pi$) in the photolysis of
5401 acetonitrile at 158 nm. *Chem. Phys. Lett.* 122, 294–299.
- 5402 Hamberg, M., Geppert, W., Thomas, R., Zhaunerchyk, V., Österdahl, F.,
5403 Ehlerding, A., Kamińska, M., Semaniak, J., af Ugglas, M., Källberg, A., Paál,
5404 A., Simonsson, A., Larsson, M., 2007. Experimental determination of disso-
5405 ciative recombination reaction pathways and absolute reaction cross-sections
5406 of CH_2OH^+ , CD_2OD^+ and CD_2OD_2^+ . *Mol. Phys.* 105, 899–906.
- 5407 Hamberg, M., Vigren, E., Thomas, R., Zhaunerchyk, V., Zhang, M., Trippel,
5408 S., Kamińska, M., Kashperka, I., af Ugglas, M., Källberg, A., Simonsson, A.,
5409 Paál, A., Semaniak, J., Larsson, M., Geppert, W., 2011. Experimental studies
5410 of the dissociative recombination processes for the C_6D_6^+ and C_6D_7^+ ions,
5411 in: Joblin, C., Tielens, A. (Eds.), *PAHs and the Universe*. EAS Publications
5412 Series. volume 46, pp. 241–249.
- 5413 Hamelin, M., Béghin, C., Grard, R., López-Moreno, J., Schwingenschuh, K.,
5414 Simões, F., Trautner, R., Berthelier, J., Brown, V., Chabassière, M., Falkner,
5415 P., Ferri, F., Fulchignoni, M., Jernej, I., Jeronimo, J., Molina-Cuberos, G.,
5416 Rodrigo, R., Tokano, T., 2007. Electron conductivity and density profiles
5417 derived from the mutual impedance probe measurements performed during
5418 the descent of Huygens through the atmosphere of Titan. *Planet. Space Sci.*
5419 55, 1964–1977.
- 5420 Hampson, J.R., McNesby, J., 1965. Vacuum-ultraviolet photolysis of ethane at
5421 high temperature. *J. Chem. Phys.* 42, 2200–2208.
- 5422 Harding, L., Georgievskii, Y., Klippenstein, S., 2005. Predictive theory for
5423 hydrogen atoms - Hydrocarbon radical association kinetics. *J. Phys. Chem.*
5424 *A* 109, 4646–4656.
- 5425 Harding, L., Guadagnini, R., Schatz, G., 1993. Theoretical studies of the re-
5426 actions $\text{H} + \text{CH} \rightarrow \text{C} + \text{H}_2$ and $\text{C} + \text{H}_2 \rightarrow \text{CH}_2$ using an ab initio global
5427 ground-state potential surface for CH_2 . *J. Phys. Chem.* 97, 5472–5481.
- 5428 Harding, L., Klippenstein, S., Georgievskii, Y., 2007. On the combination re-
5429 actions of hydrogen atoms with resonance-stabilized hydrocarbon radicals. *J.*
5430 *Phys. Chem. A* 111, 3789–3801.
- 5431 Harding, L., Klippenstein, S., Miller, J., 2008. Kinetics of $\text{CH} + \text{N}_2$ revisited
5432 with multireference methods. *J. Phys. Chem. A* 112, 522–532.
- 5433 Harich, S., Lee, Y., Yang, X., 2000. Photodissociation dynamics of allene at 157
5434 nm. *Phys. Chem. Chem. Phys.* 2, 1187–1191.

- 5435 van Harrevelt, R., van Hemert, M., Schatz, G., 2002. The CH + H reaction
5436 studied with quantum-mechanical and classical trajectory calculations. *J.*
5437 *Chem. Phys.* 116, 6002–6011.
- 5438 Hartle, R., Sittler Jr., E., Neubauer, F., Johnson, R., Smith, H., Crary, F.,
5439 McComas, D., Young, D., Coates, A., Simpson, D., Bolton, S., Reisenfeld,
5440 D., Szego, K., Berthelier, J.J., Rymer, A., Vilppola, J., Steinberg, J., Andre,
5441 N., 2006. Initial interpretation of Titan plasma interactions as observed by the
5442 Cassini Plasma Spectrometer: Comparisons with Voyager 1. *Planet. Space*
5443 *Sci.* 54, 1211–1224.
- 5444 Hartogh, P., Lellouch, E., Moreno, R., Bockelée-Morvan, D., Biver, N., Cassidy,
5445 T., Rengel, M., Jarchow, C., Cavalié, T., Crovisier, J., Helmich, F., Kidger,
5446 M., 2011. Direct detection of the Enceladus water torus with *Herschel*.
5447 *Astron. Astrophys.* 532.
- 5448 Hassinen, E., Kalliorinne, K., Koskikallio, J., 1990. Kinetics of reactions between
5449 methyl and acetyl radicals in gas phase produced by flash photolysis of acetic
5450 anhydride. *Int. J. Chem. Kin.* 22, 741–745.
- 5451 Haxton, D., Rescigno, T., McCurdy, C., 2007. Dissociative electron attachment
5452 to the H₂O molecule. II. Nuclear dynamics on coupled electronic surfaces
5453 within the local complex potential model. *Phys. Rev. A* 75, #012711.
- 5454 Hayden, C., Neumark, D., Shobatake, K., Sparks, R., Lee, Y., 1982. Methylene
5455 singlet-triplet energy splitting by molecular beam photodissociation of ketene.
5456 *J. Chem. Phys.* 76, 3607–3613.
- 5457 Hayes, F., Gutsche, G., Lawrance, W., Staker, W., King, K., 1995. Singlet
5458 methylene removal by saturated and unsaturated hydrocarbons. *Combust.*
5459 *Flame* 100, 653–660.
- 5460 Heays, A., Dickenson, G., Salumbides, E., de Oliveira, N., Joyeux, D., Nahon,
5461 L., Lewis, B., Ubachs, W., 2011. High-resolution Fourier-transform extreme
5462 ultraviolet photoabsorption spectroscopy of ¹⁴N¹⁵N. *J. Chem. Phys.* 135,
5463 #244301.
- 5464 Heber, O., Seiersen, K., Bluhme, H., Svendsen, A., Andersen, L., Maunoury, L.,
5465 2006. Dissociative recombination of small carbon cluster cations. *Phys. Rev.*
5466 *A* 73, 022712.
- 5467 Hébrard, E., Dobrijevic, M., Bénilan, Y., Raulin, F., 2006. Photochemical kinet-
5468 ics uncertainties in modeling Titan’s atmosphere: A review. *J. Photochem.*
5469 *Photobiol. C: Photochem. Rev.* 7, 211–230.
- 5470 Hébrard, E., Dobrijevic, M., Loison, J., Bergeat, A., Hickson, K., 2012. Neutral
5471 production of hydrogen isocyanide (HNC) and hydrogen cyanide (HCN) in
5472 Titan’s upper atmosphere. *Astron. Astrophys.* 541, #A21.

- 5473 Hébrard, E., Dobrijevic, M., Loison, J., Bergeat, A., Hickson, K., Caralp, F.,
5474 2013. Photochemistry of C₃H_p hydrocarbons in Titan's stratosphere revisited.
5475 *Astron. Astrophys.* 552, #A132.
- 5476 Hébrard, E., Dobrijevic, M., Pernot, P., Carrasco, N., Bergeat, A., Hickson, K.,
5477 Canosa, A., Le Picard, S., Sims, I., 2009. How measurements of rate coeffi-
5478 cients at low temperature increase the predictivity of photochemical models
5479 of Titan's atmosphere. *J. Phys. Chem. A* 113, 11227–11237.
- 5480 Hemsworth, R., Payzant, J., Schiff, H., Bohme, D., 1974. Rate constants at
5481 297°K for proton transfer reactions with NH₃. Comparisons with classical
5482 theories and exothermicity. *Chem. Phys. Lett.* 26, 417–421.
- 5483 Herbst, E., Leung, C., 1989. Gas phase production of complex hydrocarbons,
5484 cyanopolyynes, and related compounds in dense interstellar clouds. *Astro-*
5485 *phys. J. Suppl. Ser.* 69, 271–300.
- 5486 Herbst, E., Osamura, Y., 2008. Calculations of the formation rates and mech-
5487 anisms for C_nH anions in interstellar and circumstellar media. *Astrophys. J.*
5488 679, 1670–1679.
- 5489 Herbst, E., Roueff, E., Talbi, D., 2010. Radiative association and the formation
5490 of interstellar propylene. *Mol. Phys.* 108, 2171–2177.
- 5491 Herbst, E., Smith, D., Adams, N., McIntosh, B., 1989. Association reactions.
5492 Theoretical shortcomings. *J. Chem. Soc., Faraday Trans. 2* 85, 1655–1664.
- 5493 Herbst, E., Terzieva, R., Talbi, D., 2000. Calculations on the rates, mechanisms,
5494 and interstellar importance of the reactions between C and NH₂ and between
5495 N and CH₂. *Mon. Not. R. Astron. Soc.* 311, 869–876.
- 5496 Herron, J.T., 1999. Evaluated chemical kinetics data for reactions of N(²D),
5497 N(²P) and N₂(A ³Σ_v⁺) in the gas phase. *J. Phys. Chem. Ref. Data* 28, 1453–
5498 1483.
- 5499 Hickman, A., 1979. Approximate scaling formula for ion-ion mutual neutraliza-
5500 tion rates. *J. Chem. Phys.* 70, 4872–4878.
- 5501 Hickman, A., Miles, R., Hayden, C., Talbi, D., 2005. Dissociative recombination
5502 of e + HCNH⁺: Diabatic potential curves and dynamics calculations. *Astron.*
5503 *Astrophys.* 438, 31–37.
- 5504 Hickson, K., Loison, J., Cavalié, T., Hébrard, E., Dobrijevic, M., 2014. The
5505 evolution of infalling sulfur species in Titan's atmosphere. *Astron. Astrophys.*
5506 572, #A58.
- 5507 Hickson, K., Loison, J.C., Caubet, P., 2013. Unusual Low Temperature Reactiv-
5508 ity of Water. The CH H₂O Reaction as a Source of Interstellar Formaldehyde?
5509 *J. Phys. Chem. Lett.* 4, 2843.

- 5510 Hippler, H., Troe, J., Wendelken, H., 1983. UV absorption spectra of vibra-
5511 tionally highly excited toluene molecules. *J. Chem. Phys.* 78, 5351–5357.
- 5512 Hiraoka, K., Shoda, T., Kudaka, I., Fujimaki, S., Mizuse, S., Yamabe, S.,
5513 Wasada, H., Wasada-Tsutsui, Y., 2003. Gas phase study of the clustering
5514 reactions of $C_2H_5^+$, $s-C_3H_7^+$, and $t-C_4H_9^+$ with CO_2 and N_2O : Isomeric
5515 structure of $C_2H_5^+$, $C_2H_5^+(CO_2)_n$, and $C_2H_5^+(N_2O)_n$. *J. Phys. Chem. A*
5516 107, 775–781.
- 5517 Hlavenka, P., Otto, R., Trippel, S., Mikosch, J., Weidemüller, M., Wester, R.,
5518 2009. Absolute photodetachment cross section measurements of the O^- and
5519 OH^- anion. *J. Chem. Phys.* 130, #061105.
- 5520 Ho, G., Lin, M., Wang, Y., Chang, T., 1998. Photoabsorption and photoioniza-
5521 tion of propyne. *J. Chem. Phys.* 109, 5868–5879.
- 5522 Holland, D., Shaw, D., Hayes, M., Shpinkova, L., Rennie, E., Karlsson, L.,
5523 Baltzer, P., Wannberg, B., 1997. A photoabsorption, photodissociation and
5524 photoelectron spectroscopy study of C_2H_4 and C_2D_4 . *Chem. Phys.* 219, 91–
5525 116.
- 5526 Holzmeier, F., Lang, M., Hader, K., Hemberger, P., Fischer, I., 2013. H_2CN^+
5527 and H_2CNH^+ : New insight into the structure and dynamics from mass-
5528 selected threshold photoelectron spectra. *J. Chem. Phys.* 138, #214310.
- 5529 Homayoon, Z., Vázquez, S., Rodríguez-Fernández, R., Martínez-Núñez, E.,
5530 2011. Ab initio and RRKM study of the HCN/HNC elimination channels
5531 from vinyl cyanide. *J. Phys. Chem. A* 115, 979–985.
- 5532 Hoobler, R., Leone, S., 1997. Rate coefficients for reactions of ethynyl radical
5533 (C_2H) with HCN and CH_3CN : Implications for the formation of complex
5534 nitriles on Titan. *J. Geophys. Res.* 102, 28717–28723.
- 5535 Hörst, S., Vuitton, V., Yelle, R., 2008. The origin of oxygen species in Titan’s
5536 atmosphere. *J. Geophys. Res.* 113, #E10006.
- 5537 Hörst, S., Yelle, R., Buch, A., Carrasco, N., Cernogora, G., Dutuit, O., Quirico,
5538 E., Sciamma-O’Brien, E., Smith, M., Somogyi, Á., Szopa, C., Thissen, R.,
5539 Vuitton, V., 2012. Formation of amino acids and nucleotide bases in a Titan
5540 atmosphere simulation experiment. *Astrobiology* 12, 809–817.
- 5541 Hörst, S.M., 2017. Titan’s atmosphere and climate. *J. Geophys. Res. Planets*
5542 122, doi:10.1002/2016JE005240.
- 5543 Hotop, H., Lineberger, W., 1985. Binding energies in atomic negative ions: II.
5544 *J. Phys. Chem. Ref. Data* 14, 731–750.
- 5545 Houriet, R., Elwood, T., Futrell, J., 1978. A tandem ion cyclotron resonance
5546 study of the reactions of allyl ions with benzene and substituted benzene. *J.*
5547 *Am. Chem. Soc.* 100, 2320–2324.

- 5548 Howard, C., Fehsenfeld, F., McFarland, M., 1974. Negative ion-molecule reac-
5549 tions with atomic hydrogen in the gas phase at 296 K. *J. Chem. Phys.* 60,
5550 5086–5089.
- 5551 Howling, A., Sansonnens, L., Dorier, J.L., Hollenstein, C., 1994. Time-resolved
5552 measurements of highly polymerized negative ions in radio frequency silane
5553 plasma deposition experiments. *J. Appl. Phys.* 75, 1340–1353.
- 5554 Hubin-Franskin, M.J., Delwiche, J., Giuliani, A., Ska, M.P., Motte-Tollet, F.,
5555 Walker, I., Mason, N., Gingell, J., Jones, N., 2002. Electronic excitation and
5556 optical cross sections of methylamine and ethylamine in the UV-VUV spectral
5557 region. *J. Chem. Phys.* 116, 9261–9268.
- 5558 Huntress, W.T., J., Pinizzotto, R.F., J., 1973. Product distributions and rate
5559 constants for ion-molecule reactions in water, hydrogen sulfide, ammonia, and
5560 methane. *J. Chem. Phys.* 59, 4742–4756.
- 5561 Huntress, W., 1977. Laboratory studies of bimolecular reactions of positive ions
5562 in interstellar clouds, in comets, and in planetary atmospheres of reducing
5563 composition. *Astrophys. J. Suppl. Ser.* 33, 495–514.
- 5564 Hunziker, H., Knepp, H., McLean, A., Siegbahn, P., Wendt, H., 1983. Visible
5565 electronic absorption-spectrum of vinyl radical. *Can. J. Chem.* 61, 993–995.
- 5566 Husain, D., Ioannou, A., 1997. Reactions of ground-state atomic carbon, C[2p²
5567 (³P_J)], with dienes and diynes by time-resolved atomic resonance absorption
5568 spectroscopy in the vacuum ultraviolet. *J. Chem. Soc. Faraday Trans.* 93,
5569 3625–3629.
- 5570 Ikeda, N., Nakashima, N., Yoshihara, K., 1984. Formation and relaxation of hot
5571 benzyl radicals in the gas phase. *J. Phys. Chem. A* 88, 5803–5806.
- 5572 Inoue, M., 1966. Ions négatifs formés dans le cyanogène et l’acide cyanhydrique.
5573 *J. Chim. Phys. PCB* 63, 1061–1071.
- 5574 Ip, W., 1990. Titan’s upper ionosphere. *Astrophys. J.* 362, 354–363.
- 5575 Iraqi, M., Lifshitz, C., Reuben, B., 1991. Reaction of ketene ions with ammonia.
5576 *J. Phys. Chem.* 95, 7742–7746.
- 5577 Ismail, H., Abel, P., Green, W., Fahr, A., Jusinski, L., Knepp, A., Zádor, J.,
5578 Meloni, G., Selby, T., Osborn, D., Taatjes, C., 2009. Temperature-dependent
5579 kinetics of the vinyl radical (C₂H₃) self-reaction. *J. Phys. Chem. A* 113,
5580 1278–1286.
- 5581 Itikawa, Y., 2006. Cross Sections for electron collisions with nitrogen molecules.
5582 *J. Phys. Chem. Ref. Data* 35, #31.
- 5583 Jackson, D., Stibrich, N., Adams, N., Babcock, L., 2005. A selected ion flow
5584 tube study of the reactions of a sequence of ions with amines. *Int. J. Mass*
5585 *Spectrom.* 243, 115–120.

- 5586 Jackson, J.A.A., Lias, S., 1974. Primary processes in the photolysis of n-butane
5587 with 8.4 and 10.0 eV photons. *J. Photochem.* 3, 151–162.
- 5588 Jackson, W., Anex, D., Continetti, R., Balko, B., Lee, Y., 1991. Molecular
5589 beam studies of the photolysis of allene and the secondary photodissociation
5590 of the C_3H_x fragments. *J. Chem. Phys.* 95, 7327–7336.
- 5591 Jacox, M., 2003. Vibrational and electronic energy levels of polyatomic transient
5592 molecules. Supplement B. *J. Phys. Chem. Ref. Data* 32, #1.
- 5593 Janečková, R., May, O., Fedor, J., 2012. Dissociative electron attachment to
5594 methylacetylene and dimethylacetylene: Symmetry versus proximity. *Phys.*
5595 *Rev. A* 86, #052702.
- 5596 Janev, R., Reiter, D., 2004. Collision processes of $C_{2,3}H_y$ and $C_{2,3}H_y^+$ hydro-
5597 carbons with electrons and protons. *Phys. Plasmas* 11, 780–829.
- 5598 Jasper, A., Klippenstein, S., Harding, L., 2007. Secondary kinetics of methanol
5599 decomposition: Theoretical rate coefficients for ${}^3CH_2 + OH$, ${}^3CH_2 + {}^3CH_2$,
5600 and ${}^3CH_2 + CH_3$. *J. Phys. Chem. A* 111, 8699–8707.
- 5601 Jasper, A., Miller, J., 2011. Theoretical unimolecular kinetics for $CH_4 + M =$
5602 $CH_3 + H + M$ in eight baths, $M = He, Ne, Ar, Kr, H_2, N_2, CO,$ and CH_4 . *J.*
5603 *Phys. Chem. A* 115, 6438–6455.
- 5604 Jasper, A., Oana, C., Miller, J., 2015. "Third-body" collision efficiencies for
5605 combustion modeling: Hydrocarbons in atomic and diatomic baths. *Proc.*
5606 *Comb. Inst.* 35, 197–204.
- 5607 Jenkin, M., Murrells, T., Shalliker, S., Hayman, G., 1993. Kinetics and product
5608 study of the self-reactions of allyl and allyl peroxy radicals at 296 K. *J. Chem.*
5609 *Soc. Faraday Trans.* 89, 433–446.
- 5610 Jensen, M., Bilodeau, R., Safvan, C., Seiersen, K., Andersen, L., Pedersen, H.,
5611 Heber, O., 2000. Dissociative recombination and excitation of H_3O^+ , HD_2O^+ ,
5612 and D_3O^+ . *Astrophys. J.* 543, 764–774.
- 5613 Jiao, C., DeJoseph, C.J., Lee, R., Garscadden, A., 2006. Kinetics of electron im-
5614 pact ionization and ion-molecule reactions of pyridine. *Int. J. Mass Spectrom.*
5615 257, 34–40.
- 5616 Jodkowski, J., Ratajczak, E., Fagerström, K., Lund, A., Stothard, N., Humpfer,
5617 R., Grotheer, H.H., 1995. Kinetics of the cross reaction between amidogen
5618 and methyl radicals. *Chem. Phys. Lett.* 240, 63–71.
- 5619 Johnsen, R., Biondi, M., 1974. Measurements of positive ion conversion and
5620 removal reactions relating to the Jovian ionosphere. *Icarus* 23, 139–143.
- 5621 Jolly, A., Bénilan, Y., 2008. Review of quantitative spectroscopy of polyynes.
5622 *J. Quant. Spectrosc. Radiat. Transfer* 109, 963–973.

- 5623 Jolly, A., Cottini, V., Fayt, A., Manceron, L., Kwabia-Tchana, F., Benilan,
5624 Y., Guillemin, J.C., Nixon, C., Irwin, P., 2015. Gas phase dicyanoacety-
5625 lene (C_4N_2) on Titan: New experimental and theoretical spectroscopy results
5626 applied to Cassini CIRS data. *Icarus* 248, 340–346.
- 5627 Jones, B., Zhang, F., Kaiser, R., Jamal, A., Mebel, A., Cordiner, M., Charnley,
5628 S., 2011. Formation of benzene in the interstellar medium. *P. Natl. Acad.*
5629 *Sci. USA* 108, 452–457.
- 5630 Jones, B., Zhang, F., Maksyutenko, P., Mebel, A., Kaiser, R., 2010. Crossed
5631 molecular beam study on the formation of phenylacetylene and its relevance
5632 to Titan’s atmosphere. *J. Phys. Chem. A* 114, 5256–5262.
- 5633 Kajimoto, O., Fueno, T., 1979. Relative rate constants of O(1D2)-olefin reac-
5634 tions. *Chem. Phys. Lett.* 64, 445–447.
- 5635 Kalhori, S., Viggiano, A., Arnold, S., Rosén, S., Semaniak, J., Derkach, A.,
5636 af Ugglas, M., Larsson, M., 2002. Dissociative recombination of $C_2H_3^+$. *Astron.*
5637 *Astrophys.* 391, 1159–1165.
- 5638 Kállay, M., Surján, P., 2001. Higher excitations in coupled-cluster theory. *J.*
5639 *Chem. Phys.* 115, 2945–2954.
- 5640 Kameta, K., Machida, S., Kitajima, M., Ukai, M., Kouchi, N., Hatano, Y., Ito,
5641 K., 1996. Photoabsorption, photoionization, and neutral-dissociation cross
5642 sections of C_2H_6 and C_3H_8 in the extreme-uv region. *J. Electron Spectrosc.*
5643 *Relat. Phenom.* 79, 391–393.
- 5644 Kamińska, M., Zhaunerchyk, V., Vigren, E., Danielsson, M., Hamberg, M.,
5645 Geppert, W., Larsson, M., Rosén, S., Thomas, R., Semaniak, J., 2010. Dis-
5646 sociative recombination of CH_5^+ and CD_5^+ : Measurement of the product
5647 branching fractions and the absolute cross sections, and the breakup dynam-
5648 ics in the $CH_3 + H + H$ product channel. *Phys. Rev. A* 81, #062701.
- 5649 Kanda, K., Nagata, T., Ibuki, T., 1999. Photodissociation of some simple nitriles
5650 in the extreme vacuum ultraviolet region. *Chem. Phys.* 243, 89–96.
- 5651 Karpas, Z., Huntress, W.T., J., 1978. Reactions of OH+ and H₂O+ ions with
5652 some diatomic and simple polyatomic molecules. *Chem. Phys. Lett.* 59, 87–89.
- 5653 Karton, A., Rabinovich, E., Martin, J., Ruscic, B., 2006. W4 theory for com-
5654 putational thermochemistry: In pursuit of confident sub-kJ/mol predictions.
5655 *J. Chem. Phys.* 125, #144108.
- 5656 Keller, C., Anicich, V., Cravens, T., 1998. Model of Titan’s ionosphere with
5657 detailed hydrocarbon ion chemistry. *Planet. Space Sci.* 46, 1157–1174.
- 5658 Keller, C., Cravens, T., Gan, L., 1992. A model of the ionosphere of Titan. *J.*
5659 *Geophys. Res.* 97, 12117–12135.

- 5660 Kirby, K., Constantinides, E., Babeu, S., Oppenheimer, M., Victor, G., 1979.
5661 Photoionization and photoabsorption cross sections of He, O, N₂ and O₂ for
5662 aeronomic calculations. *At. Data Nucl. Data Tables* 23, 63–81.
- 5663 Kislov, V., Nguyen, T., Mebel, A., Lin, S., Smith, S., 2004. Photodissociation
5664 of benzene under collision-free conditions: An ab initio/Rice-Ramsperger-
5665 Kassel-Marcus study. *J. Chem. Phys.* 120, 7008–7017.
- 5666 Kley, D., Lawrence, G., Stone, E., 1977. The yield of N(²D) atoms in the
5667 dissociative recombination of NO⁺. *J. Chem. Phys.* 66, 4157–4165.
- 5668 Klippenstein, S., 1992. Variational optimizations in the Rice-Ramsperger-
5669 Kassel-Marcus theory calculations for unimolecular dissociations with no re-
5670 verse barrier. *J. Chem. Phys.* 96, 367–371.
- 5671 Klippenstein, S., 2017. From theoretical reaction dynamics to chemical modeling
5672 of combustion. *Proc. Comb. Inst.* 36, 77–111.
- 5673 Klippenstein, S., Georgievskii, Y., Harding, L., 2002. A theoretical analysis of
5674 the CH₃ + H reaction: Isotope effects, the high-pressure limit, and transition
5675 state recrossing. *Proc. Comb. Inst.* 29, 1229–1236.
- 5676 Klippenstein, S., Georgievskii, Y., Harding, L., 2006. Predictive theory for
5677 the combination kinetics of two alkyl radicals. *Phys. Chem. Chem. Phys.* 8,
5678 1133–1147.
- 5679 Klippenstein, S., Harding, L., 1999. A direct transition state theory based study
5680 of methyl radical recombination kinetics. *J. Phys. Chem. A* 103, 9388–9398.
- 5681 Klippenstein, S., Harding, L., Georgievskii, Y., 2007. On the formation and
5682 decomposition of C₇H₈. *Proc. Comb. Inst.* 31, 221–229.
- 5683 Klippenstein, S., Harding, L., Ruscic, B., Sivaramakrishnan, R., Srinivasan,
5684 N., Su, M.C., Michael, J., 2009. Thermal decomposition of NH₂OH and
5685 subsequent reactions: Ab initio transition state theory and reflected shock
5686 tube experiments. *J. Phys. Chem. A* 113, 10241–10259.
- 5687 Klippenstein, S., Miller, J., 2005. The addition of hydrogen atoms to diacetylene
5688 and the heats of formation of i-C₄H₃ and n-C₄H₃. *J. Phys. Chem. A* 109,
5689 4285–4295.
- 5690 Klippenstein, S., Ruscic, B., Harding, L., 2017. Ab initio computations and
5691 active thermochemical tables hand in hand: Heats of formation of core com-
5692 bustion species. *J. Phys. Chem. A* 121, 6580–6602.
- 5693 Klippenstein, S., Wagner, A., Dunbar, R., Wardlaw, D., Roberston, S., Miller,
5694 J., 2011. VariFlex: Version 2.04m. Argonne National Laboratory, Argonne,
5695 IL .

- 5696 Klippenstein, S., Yang, Y.C., Ryzhov, V., Dunbar, R., 1996. Theory and mod-
5697 eling of ion-molecule radiative association kinetics. *J. Chem. Phys.* 104, 4502–
5698 4516.
- 5699 Kloster-Jensen, E., Haink, H., Christen, H., 1974. The electronic spectra of
5700 unsubstituted mono- to penta- acetylene in the gas phase and in solution in
5701 the range 1100 to 4000 Å. *Helv. Chim. Acta* 57, 1731–1744.
- 5702 Knyazev, V., Slagle, I., 2001. Kinetics of the reactions of allyl and propargyl
5703 radicals with CH₃. *J. Phys. Chem. A* 105, 3196–3204.
- 5704 Koch, E., Otto, A., 1972. Optical absorption of benzene vapour for photon
5705 energies from 6 eV to 35 eV. *Chem. Phys. Lett.* 12, 476–480.
- 5706 Koizumi, H., Yoshimi, T., Shinsaka, K., Ukai, M., Morita, M., Hatano, Y., 1985.
5707 VUV-optical oscillator strength distributions of C₃H₆ and C₄H₈ isomers. *J.*
5708 *Chem. Phys.* 82, 4856–4861.
- 5709 Koskinen, T., Yelle, R., Snowden, D., Lavvas, P., Sandel, B., Capalbo, F.,
5710 Bénilan, Y., West, R., 2011. The mesosphere and thermosphere of Titan
5711 revealed by Cassini/UVIS stellar occultations. *Icarus* 216, 507–534.
- 5712 Kovács, T., Blitz, M., Seakins, P., 2010. H-atom yields from the photolysis of
5713 acetylene and from the reaction of C₂H with H₂, C₂H₂, and C₂H₄. *J. Phys.*
5714 *Chem. A* 114, 4735–4741.
- 5715 Koyano, I., Wauchop, T., Welge, K., 1975. Relative efficiencies of O(¹S) pro-
5716 duction from photodissociation of CO₂ between 1080 and 1160 Å. *J. Chem.*
5717 *Phys.* 63, 110–112.
- 5718 Krasnopolsky, V., 2009. A photochemical model of Titan’s atmosphere and
5719 ionosphere. *Icarus* 201, 226–256.
- 5720 Krasnopolsky, V., 2010. The photochemical model of Titan’s atmosphere and
5721 ionosphere: A version without hydrodynamic escape. *Planet. Space Sci.* 58,
5722 1507–1515.
- 5723 Krasnopolsky, V., 2012. Titan’s photochemical model: Further update, oxygen
5724 species, and comparison with Triton and Pluto. *Planet. Space Sci.* 73, 318–
5725 326.
- 5726 Krasnopolsky, V., 2014. Chemical composition of Titan’s atmosphere: Obser-
5727 vations and the photochemical model. *Icarus* 236, 83–91.
- 5728 Krishnakumar, E., Denifl, S., Čadež, I., Markelj, S., Mason, N., 2011. Dissocia-
5729 tive electron attachment cross sections for H₂ and D₂. *Phys. Rev. Lett.* 106,
5730 #243201.
- 5731 Krummacher, S., Schmidt, V., Wulleumier, F., 1980. Inner-shell photoionisa-
5732 tion in molecules: the nitrogen case. *J. Phys. B: Atom. Molec. Phys.* 13,
5733 3993–4005.

- 5734 Kuga, M., Carrasco, N., Marty, B., Marrocchi, Y., Bernard, S., Rigaudier, T.,
5735 Fleury, B., Tissandier, L., 2014. Nitrogen isotopic fractionation during abiotic
5736 synthesis of organic solid particles. *Earth Planet. Sc. Lett.* 393, 2–13.
- 5737 Kumar, S., Hauser, D., Jindra, R., Best, T., Roučka, Š., Geppert, W., Millar,
5738 T., Wester, R., 2013. Photodetachment as a destruction mechanism for CN^-
5739 and C_3N^- anions in circumstellar envelopes. *Astrophys. J.* 776, #25.
- 5740 Landera, A., Krishtal, S., Kislov, V., Mebel, A., Kaiser, R., 2008. Theoretical
5741 study of the C_6H_3 potential energy surface and rate constants and product
5742 branching ratios of the $\text{C}_2\text{H}(^2\Sigma^+) + \text{C}_4\text{H}_2(^1\Sigma_g^+)$ and $\text{C}_4\text{H}(^2\Sigma^+) + \text{C}_2\text{H}_2(^1\Sigma_g^+)$
5743 reactions. *J. Chem. Phys.* 128, #214301.
- 5744 Langford, A., Petek, H., Moore, C., 1983. Collisional removal of $\text{CH}_2(^1\text{A}_1)$:
5745 Absolute rate constants for atomic and molecular collisional partners at 295
5746 K. *J. Chem. Phys.* 78, 6650–6659.
- 5747 Lara, L., Lellouch, E., González, M., Moreno, R., Rengel, M., 2014. A time-
5748 dependent photochemical model for Titan’s atmosphere and the origin of
5749 H_2O . *Astron. Astrophys.* 566, #A143.
- 5750 Lara, L., Lellouch, E., Shematovich, V., 1999. Titan’s atmospheric haze: The
5751 case for HCN incorporation. *Astron. Astrophys.* 341, 312–317.
- 5752 Lara, L.M., Lellouch, E., López-Moreno, J.J., Rodrigo, R., 1996. Vertical dis-
5753 tribution of Titan’s atmospheric neutral constituents. *J. Geophys. Res.* 101,
5754 23261–23283.
- 5755 Lara, L.M., Lorenz, R.D., Rodrigo, R., 1994. Liquids and solids on the surface
5756 of Titan: Results of a new photochemical model. *Planet. Space Sci.* 42, 5–14.
- 5757 Larson, Å., Le Padellec, A., Semaniak, J., Strömholm, C., Larsson, M., Rosén,
5758 S., Peverall, R., Danared, H., Djuric, N., Dunn, G., Datz, S., 1998. Branching
5759 fractions in dissociative recombination of CH_2^+ . *Astrophys. J.* 505, 459–465.
- 5760 Larsson, M., Ehlerding, A., Geppert, W., Hellberg, F., Kalhori, S., Thomas, R.,
5761 Djuric, N., Österdahl, F., Angelova, G., Semaniak, J., Novotny, O., Arnold,
5762 S., Viggiano, A., 2005. Rate constants and branching ratios for the dissociative
5763 recombination of C_3D_7^+ and C_4D_9^+ . *J. Chem. Phys.* 122, 156101–156103.
- 5764 Laufer, A., Fahr, A., 2004. Reactions and kinetics of unsaturated C_2 hydrocar-
5765 bon radicals. *Chem. Rev.* 104, 2813–2832.
- 5766 Laufer, A., Keller, R., 1971. Lowest excited states of ketene. *J. Am. Chem. Soc.*
5767 93, 61–63.
- 5768 Laufer, A., McNesby, J., 1966. The chain decomposition of propane initiated
5769 by vacuum ultraviolet photolysis. *J. Phys. Chem.* 70, 4094–4096.

- 5770 Lauter, A., Lee, K., Jung, K., Vatsa, R., Mittal, J., Volpp, H.R., 2002. Absolute
5771 primary H atom quantum yield measurements in the 193.3 and 121.6 nm
5772 photodissociation of acetylene. *Chem. Phys. Lett.* 358, 314–319.
- 5773 Lavvas, P., Coustenis, A., Vardavas, I., 2008a. Coupling photochemistry with
5774 haze formation in Titan’s atmosphere. Part I: Model description. *Planet.*
5775 *Space Sci.* 56, 27–66.
- 5776 Lavvas, P., Coustenis, A., Vardavas, I., 2008b. Coupling photochemistry with
5777 haze formation in Titan’s atmosphere. Part II: Results and validation with
5778 Cassini/Huygens data. *Planet. Space Sci.* 56, 67–99.
- 5779 Lavvas, P., Galand, M., Yelle, R., Heays, A., Lewis, B., Lewis, G., Coates, A.,
5780 2011a. Energy deposition and primary chemical products in Titan’s upper
5781 atmosphere. *Icarus* 213, 233–251.
- 5782 Lavvas, P., Griffith, C., Yelle, R., 2011b. Condensation in Titan’s atmosphere
5783 at the Huygens landing site. *Icarus* 215, 732–750.
- 5784 Lavvas, P., Sander, M., Kraft, M., Imanaka, H., 2011c. Surface chemistry and
5785 particle shape. Processes for the evolution of aerosols in Titan’s atmosphere.
5786 *Astrophys. J.* 728, 80–90.
- 5787 Lavvas, P., West, R., Gronoff, G., Rannou, P., 2014. Titan’s emission processes
5788 during eclipse. *Icarus* 241, 397–408.
- 5789 Lavvas, P., Yelle, R., Griffith, C., 2010. Titan’s vertical aerosol structure at
5790 the Huygens landing site: Constraints on particle size, density, charge, and
5791 refractive index. *Icarus* 210, 832–842.
- 5792 Lavvas, P., Yelle, R., Heays, A., Campbell, L., Brunger, M., Galand, M., Vuit-
5793 ton, V., 2015. N₂ state population in Titan’s atmosphere. *Icarus* 260, 29–59.
- 5794 Lawrence, G., 1972. Production of O(¹S) from photodissociation of CO₂. *J.*
5795 *Chem. Phys.* 57, 5616–5617.
- 5796 Le Garrec, J.L., Carles, S., Speck, T., Mitchell, J., Rowe, B., Ferguson, E., 2003.
5797 The ion-molecule reaction of O⁺ with N₂ measured down to 23 K. *Chem.*
5798 *Phys. Lett.* 372, 485–488.
- 5799 Le Padellec, A., Mitchell, J., Al-Khalili, A., Danared, H., Kallberg, A., Larson,
5800 A., Rosen, S., af Ugglas, M., Viktor, L., Larsson, M., 1999. Storage ring mea-
5801 surements of the dissociative recombination and excitation of the cyanogen
5802 ion CN⁺ (X ¹Σ⁺ and a ³Π, ν=0). *J. Chem. Phys.* 110, 890–901.
- 5803 Le Padellec, A., Sheehan, C., Talbi, D., Mitchell, J., 1997. A merged-beam
5804 study of the dissociative recombination of HCO⁺. *J. Phys. B: At. Mol. Opt.*
5805 *Phys.* 30, 319–327.
- 5806 Lebonnois, S., 2005. Benzene and aerosol production in Titan and Jupiter’s
5807 atmospheres: A sensitivity study. *Planet. Space Sci.* 53, 486–497.

- 5808 Lebonnois, S., Bakes, E., McKay, C., 2002. Transition from gaseous compounds
5809 to aerosols in Titan's atmosphere. *Icarus* 159, 505–517.
- 5810 Lebonnois, S., Toubanc, D., Hourdin, F., Rannou, P., 2001. Seasonal variations
5811 of Titan's atmospheric composition. *Icarus* 152, 384–406.
- 5812 Lee, A., Yung, Y., Cheng, B.M., Bahou, M., Chung, C.Y., Lee, Y.P., 2001.
5813 Enhancement of deuterated ethane on Jupiter. *Astrophys. J.* 551, L93–L96.
- 5814 Lee, L., 1980. $\text{CN}(A \ ^2\Pi \rightarrow X \ ^2\Sigma^+)$ and $\text{CN}(B \ ^2\Sigma^+ \rightarrow X \ ^2\Sigma^+)$ yields from HCN
5815 photodissociation. *J. Chem. Phys.* 72, 6414–6421.
- 5816 Lee, L., Chiang, C., 1983. Fluorescence yield from photodissociation of CH_4 at
5817 1060–1420 Å. *J. Chem. Phys.* 78, 688–691.
- 5818 Lee, S.H., Lee, Y., Yang, X., 2004. Dynamics of photodissociation of ethylene
5819 and its isotopomers at 157 nm: Branching ratios and kinetic-energy distribu-
5820 tions. *J. Chem. Phys.* 120, 10983–10991.
- 5821 LeGarrec, J., Lepage, V., Rowe, B., Ferguson, E., 1997. The temperature de-
5822 pendence of the rate constant for $\text{O}^+ + \text{NO} \rightarrow \text{NO}^+ + \text{O}$ from 23 to 3000 K.
5823 *Chem. Phys. Lett.* 270, 66–70.
- 5824 Lehfaoui, L., Rebrion-Rowe, C., Laubé, S., Mitchell, J., Rowe, B., 1997. The
5825 dissociative recombination of hydrocarbon ions. I. Light alkanes. *J. Chem.*
5826 *Phys.* 106, 5406–5412.
- 5827 Lellouch, E., 1990. Atmospheric models of Titan and Triton. *Ann. Geophys.* 8,
5828 653–660.
- 5829 Lellouch, E., Bézard, B., Flasar, F., Vinatier, S., Achterberg, R., Nixon, C.,
5830 Bjoraker, G., Gorius, N., 2014. The distribution of methane in Titan's strato-
5831 sphere from Cassini/CIRS observations. *Icarus* 231, 323–337.
- 5832 Leonori, F., Petrucci, R., Hickson, K., Segoloni, E., Balucani, N., Le Picard,
5833 S., Foggi, P., Casavecchia, P., 2008. Crossed molecular beam study of gas
5834 phase reactions relevant to the chemistry of planetary atmospheres: the case
5835 of $\text{C}_2 + \text{C}_2\text{H}_2$. *Planet. Space Sci.* 56, 1658–1673.
- 5836 Leopold, D., Murray, K., Stevens Miller, A., Lineberger, W., 1985. Methylene:
5837 A study of the $X \ ^3B_1$ and $\tilde{a} \ ^1A_1$ states by photoelectron spectroscopy of CH_2^-
5838 and CD_2^- . *J. Chem. Phys.* 83, 4849–4865.
- 5839 Lewis, B., Gibson, S., Zhang, W., Lefebvre-Brion, H., Robbe, J.M., 2005. Pre-
5840 dissociation mechanism for the lowest $^1\Pi_u$ states of N_2 . *J. Chem. Phys.* 122,
5841 #144302.
- 5842 Li, C., Zhang, X., Gao, P., Yung, Y., 2015. Vertical distribution of C_3 -
5843 hydrocarbons in the stratosphere of Titan. *Astrophys. J.* 803, #L19.

- 5844 Li, C., Zhang, X., Kammer, J., Liang, M.C., Shia, R.L., Yung, Y., 2014. A non-
5845 monotonic eddy diffusivity profile of Titan's atmosphere revealed by Cassini
5846 observations. *Planet. Space Sci.* 104, 48–58.
- 5847 Li, Q., Zhang, X., 2006. Direct dynamics study on the hydrogen abstraction re-
5848 actions $\text{N}_2\text{H}_4 + R \rightarrow \text{N}_2\text{H}_3 + RH$ ($R = \text{NH}_2, \text{CH}_3$). *J. Chem. Phys.* 125, #064304.
- 5849 Liang, M.C., Heays, A., Lewis, B., Gibson, S., Yung, Y., 2007. Source of
5850 nitrogen isotope anomaly in HCN in the atmosphere of Titan. *Astrophys. J.*
5851 664, L115–L118.
- 5852 Lias, S., Ausloos, P., 1985. Structures of C_6H_7^+ ions formed in unimolecular
5853 and bimolecular reactions. *J. Chem. Phys.* 82, 3613–3624.
- 5854 Lias, S., Bartmess, J., Liebman, J., Holmes, J., Levin, R., Mallard, W., 1988.
5855 Gas-phase ion and neutral thermochemistry. *J. Phys. Chem. Ref. Data* 17,
5856 Suppl 1.
- 5857 Lias, S., Buckley, T., 1984. Structures and reactions of C_3H_6^+ ions generated
5858 in cyclopropane. *Int. J. Mass Spectrom. Ion Processes* 56, 123–137.
- 5859 Lias, S., Collin, G., Rebert, R., Ausloos, P., 1970. Photolysis of ethane at
5860 11.6–11.8 eV. *J. Chem. Phys.* 52, 1841–1851.
- 5861 Lifshitz, C., Gibson, D., Levsen, K., 1980. Structure of the gas-phase ion
5862 C_6H_5^+ . *International Journal of Mass Spectrometry and Ion Processes* 35,
5863 365–370.
- 5864 Lifshitz, C., Gibson, D., Levsen, K., Dotan, I., 1981. The gas-phase chemistry
5865 of C_4H_4^+ . *International Journal of Mass Spectrometry and Ion Processes* 40,
5866 157–165.
- 5867 Lifshitz, C., Reuben, B., 1969. Ion-molecule reactions in aromatic systems. I.
5868 Secondary ions and reaction rates in benzene. *J. Chem. Phys.* 50, 951–960.
- 5869 Lifshitz, C., Weiss, M., 1980a. Ion-molecule reactions in alkynes. Trapped-ion
5870 mass spectrometry of 1,5-hexadiyne. *International Journal of Mass Spectrom-*
5871 *etry and Ion Processes* 35, 73–81.
- 5872 Lifshitz, C., Weiss, M., 1980b. Ion-molecule reactions in aromatic systems.
5873 II. Trapped ion mass spectrometry of benzene. *Int. J. Mass Spectrom. Ion*
5874 *Processes* 34, 311–315.
- 5875 Lilensten, J., Witasse, O., Simon, C., Soldi-Lose, H., Dutuit, O., Thissen, R.,
5876 Alcaraz, C., 2005. Prediction of a N_2^{++} layer in the upper atmosphere of
5877 Titan. *Geophys. Res. Lett.* 32, #L03202.
- 5878 Limão-Vieira, P., Eden, S., Mason, N., Hoffmann, S., 2003. Electronic state
5879 spectroscopy of acetaldehyde, CH_3CHO , by high-resolution VUV photoab-
5880 sorption. *Chem. Phys. Lett.* 376, 737–747.

- 5881 Lin, Z., Talbi, D., Roueff, E., Herbst, E., Wehres, N., Cole, C., Yang, Z., Snow,
5882 T., Bierbaum, V., 2013. Can interstellar propene (CH_3CHCH_2) be formed
5883 via gas-phase reactions? *Astrophys. J.* 765, #80.
- 5884 Lindinger, W., Hansel, A., Herman, Z., 2000. Ion-molecule reactions. *Adv. At.*
5885 *Mol. Opt. Phys.* 43, 243–294.
- 5886 Liu, X., Shemansky, D., 2006. Analysis of electron impact ionization properties
5887 of methane. *J. Geophys. Res.* 111, A04303–A04319.
- 5888 Loison, J., Hébrard, E., Dobrijevic, M., Hickson, K., Caralp, F., Hue, V.,
5889 Gronoff, G., Venot, O., Benilan, Y., 2015. The neutral photochemistry of
5890 nitriles, amines and imines in the atmosphere of Titan. *Icarus* 247, 218–247.
- 5891 Loison, J.C., Bergeat, A., 2004. Reaction of carbon atoms, $\text{C}(2\text{p}^2, ^3\text{P})$ with
5892 C_3H_4 (allene and methylacetylene), C_3H_6 (propylene) and C_4H_8 (trans-
5893 butene): Overall rate constants and atomic hydrogen branching ratios. *Phys.*
5894 *Chem. Chem. Phys.* 6, 5396–5401.
- 5895 Loison, J.C., Bergeat, A., 2009. Rate constants and the H atom branch-
5896 ing ratio of the reactions of the methylidyne $\text{CH}(X^2\Pi)$ radical with C_2H_2 ,
5897 C_2H_4 , C_3H_4 (methylacetylene and allene), C_3H_6 (propene) and C_4H_8 (trans-
5898 butene). *Phys. Chem. Chem. Phys.* 11, 655–664.
- 5899 Loison, J.C., Bergeat, A., Caralp, F., Hannachi, Y., 2006. Rate constants and
5900 H atom branching ratios of the gas-phase reactions of methylidyne $\text{CH}(X^2\Pi)$
5901 radical with a series of alkanes. *J. Phys. Chem. A* 110, 13500–13506.
- 5902 López-Moreno, J., Molina-Cuberos, G., Hamelin, M., Grard, R., Simões, F., Go-
5903 dard, R., Schwingenschuh, K., Béghin, C., Berthelier, J., Brown, V., Falkner,
5904 P., Ferri, F., Fulchignoni, M., Jernej, I., Jerónimo, J., Rodrigo, R., Trautner,
5905 R., 2008. Structure of Titan’s low altitude ionized layer from the Relaxation
5906 Probe onboard HUYGENS. *Geophys. Res. Lett.* 35, #L22104.
- 5907 Lorenz, R., Mitchell, K., Kirk, R., Hayes, A., Aharonson, O., Zebker, H., Paillou,
5908 P., Radebaugh, J., Lunine, J., Janssen, M., Wall, S., Lopes, R., Stiles, B.,
5909 Ostro, S., Mitri, G., Stofan, E., 2008. Titan’s inventory of organic surface
5910 materials. *Geophys. Res. Lett.* 35, #L02206.
- 5911 Lunine, J., 2010. Titan and habitable planets around M-dwarfs. *Faraday Dis-*
5912 *cuss.* 147, 405–418.
- 5913 Luspay-Kuti, A., Mandt, K., Plessis, S., Greathouse, T., 2015. Effects of nitro-
5914 gen photoabsorption cross section resolution on minor species vertical profiles
5915 in Titan’s upper atmosphere. *Astrophys. J.* 801, #L14.
- 5916 Luspay-Kuti, A., Mandt, K., Westlake, J., Plessis, S., Greathouse, T., 2016. The
5917 role of nitrogen in Titan’s upper atmospheric hydrocarbon chemistry over the
5918 solar cycle. *Astrophys. J.* 823, #163.

- 5919 Luther, K., Oum, K., Sekiguchi, K., Troe, J., 2004. Recombination of benzyl
5920 radicals: dependence on the bath gas, temperature, and pressure. *Phys.*
5921 *Chem. Chem. Phys.* 6, 4133–4141.
- 5922 Luther, K., Troe, J., Weitzel, K.M., 1990. C-C and C-H bond splits of laser-
5923 excited aromatic molecules. 2. In situ measurements of branching ratios. *J.*
5924 *Phys. Chem.* 94, 6316–6320.
- 5925 Mackay, G., Betowski, D., Payzant, J., Schiff, H., Bohme, D., 1976. Rate con-
5926 stants at 297 K for proton-transfer reactions with HCN and CH₃CN. Compar-
5927 isons with classical theories and exothermicity. *J. Phys. Chem.* 80, 2919–2922.
- 5928 Mackay, G., Schiff, H., Bohme, D., 1981. A room-temperature study of the
5929 kinetics and energetics for the protonation of ethane. *Can. J. Chem.* 59,
5930 1771–1778.
- 5931 Mackay, G., Tanaka, K., Bohme, D., 1977. Rate constants at 297 K for proton-
5932 transfer reactions with C₂H₂: An assessment of the average quadrupole ori-
5933 entation theory. *Int. J. Mass Spectrom.* 24, 125–136.
- 5934 Mackay, G., Vlachos, G., Bohme, D., Schiff, H., 1980. Studies of reactions
5935 involving C₂H_x⁺ ions with HCN using a modified selected ion flow tube. *Int.*
5936 *J. Mass Spectrom.* 36, 259–270.
- 5937 Madanian, H., Cravens, T., Richard, M., Waite Jr., J., Edberg, N., West-
5938 lake, J., Wahlund, J.E., 2016. Solar cycle variations in ion composition
5939 in the dayside ionosphere of Titan. *J. Geophys. Res. Space Physics* 121,
5940 doi:10.1002/2015JA022274.
- 5941 Magee, B., Waite Jr., J., Mandt, K., Westlake, J., Bell, J., Gell, D., 2009.
5942 INMS-derived composition of Titan’s upper atmosphere: Analysis methods
5943 and model comparison. *Planet. Space Sci.* 57, 1895–1916.
- 5944 Maltagliati, L., Bézard, B., Vinatier, S. and Hedman, M., Lellouch, E., Nichol-
5945 son, P., Sotin, C., de Kok, R., Sicardy, B., 2015. Titan’s atmosphere as
5946 observed by Cassini/VIMS solar occultations: CH₄, CO and evidence for
5947 C₂H₆ absorption. *Icarus* 248, 1–24.
- 5948 Mandt, K., Gell, D., Perry, M., Waite Jr., J., Crary, F., Young, D., Magee, B.,
5949 Westlake, J., Cravens, T., Kasprzak, W., Miller, G., Wahlund, J.E., Ågren,
5950 K., Edberg, N., Heays, A., Lewis, B., Gibson, S., de la Haye, V., Liang,
5951 M.C., 2012a. Ion densities and composition of Titan’s upper atmosphere de-
5952 rived from the Cassini Ion Neutral Mass Spectrometer: Analysis methods and
5953 comparison of measured ion densities to photochemical model simulations. *J.*
5954 *Geophys. Res.* 117, #E10006.
- 5955 Mandt, K., Waite Jr., J., Lewis, W., Magee, B., Bell, J., Lunine, J., Mousis,
5956 O., Cordier, D., 2009. Isotopic evolution of the major constituents of Titan’s
5957 atmosphere based on Cassini data. *Planet. Space Sci.* 57, 1917–1930.

- 5958 Mandt, K., Waite Jr., J., Teolis, B., Magee, B., Bell, J., Westlake, J., Nixon,
5959 C., Mousis, O., Lunine, J., 2012b. The $^{12}\text{C}/^{13}\text{C}$ ratio on Titan from *Cassini*
5960 INMS measurements and implications for the evolution of methane. *Astro-*
5961 *phys. J.* 749, #160.
- 5962 Marquette, J.B., Rebrion, C., Rowe, B.R., 1988. Reactions of $\text{N}^+(^3\text{P})$ ions with
5963 normal, para, and deuterated hydrogens at low temperatures. *J. Chem. Phys.*
5964 89, 2041–2047.
- 5965 Marston, G., Nesbitt, F., Nava, D., Payne, W., Stief, L., 1989a. Temperature
5966 dependence of the reaction of nitrogen atoms with methyl radicals. *J. Phys.*
5967 *Chem.* 93, 5769–5774.
- 5968 Marston, G., Nesbitt, F., Stief, L., 1989b. Branching ratios in the atomic nitro-
5969 gen + methyl reaction: formation of the methylene amidogen (H_2CN) radical.
5970 *J. Chem. Phys.* 91, 3483–3491.
- 5971 Marston, G., Stief, L., 1989. Structure, spectroscopy and kinetics of the methy-
5972 lene amidogen (H_2CN) radical. *Research on Chemical Intermediates* 12, 161–
5973 186.
- 5974 Marten, A., Hidayat, T., Biraud, Y., Moreno, R., 2002. New millimeter hetero-
5975 dyne observations of Titan: Vertical distributions of HCN HC_3N , CH_3CN ,
5976 and the isotopic ratio $^{15}\text{N}/^{14}\text{N}$ in its atmosphere. *Icarus* 158, 532 – 544.
- 5977 Martin, T., Melton, C., 1960. Hydrogen atom abstraction reactions by cyanide
5978 ion-radicals. *J. Chem. Phys.* 32, 700–704.
- 5979 Martinez, O., Yang, Z., Demarais, N., Snow, T., Bierbaum, V., 2010. Gas-phase
5980 reactions of hydride anion, H^- . *Astrophys. J.* 720, 173–177.
- 5981 Mason, E., Marrero, T., 1970. The diffusion of atoms and molecules, in: Bates,
5982 D., Esterman, I. (Eds.), *Advances in Atomic and Molecular Physics*. Academic
5983 Press, New York. volume 6, pp. 155–232.
- 5984 Mathews, L., Adams, N., 2011. Experimental study of the gas phase chemistry
5985 of C_3H_3^+ with several cyclic molecules. *Int. J. Mass Spectrom.* 299, 139–144.
- 5986 May, O., Fedor, J., Allan, M., 2009. Isotope effect in dissociative electron
5987 attachment to acetylene. *Phys. Rev. A* 80, #012706.
- 5988 May, O., Fedor, J., Ibănescu, C., Allan, M., 2008. Absolute cross sections for
5989 dissociative electron attachment to acetylene and diacetylene. *Phys. Rev. A*
5990 77, #040701.
- 5991 May, O., Kubala, D., Allan, M., 2010. Absolute cross sections for dissociative
5992 electron attachment to HCN and DCN. *Phys. Rev. A* 82, #010701(R).
- 5993 McEwan, M., Anicich, V., 1995. A low-pressure study of C_2N_2 ion chemistry.
5994 *J. Phys. Chem.* 99, 12204–12208.

- 5995 McEwan, M., Anicich, V., 2007. Titan's ion chemistry: A laboratory perspec-
5996 tive. *Mass Spectrom. Rev.* 26, 281–319.
- 5997 McEwan, M., Anicich, V., Huntress, W.T., J., 1981. An ICR investigation of
5998 ion-molecule reactions of HCN. *Int. J. Mass Spectrom. Ion Processes* 37,
5999 273–281.
- 6000 McEwan, M., Scott, G., Anicich, V., 1998. Ion-molecule reactions relevant to
6001 Titan's ionosphere. *Int. J. Mass Spectrom.* 172, 209–219.
- 6002 McKee, K., Blitz, M., Hughes, K., Pilling, M., Qian, H.B., Taylor, A., Seakins,
6003 P.W., 2003. H atom branching ratios from the reactions of CH with C₂H₂,
6004 C₂H₄, C₂H₆, and *neo*-C₅H₁₂ at room temperature and 25 Torr. *J. Phys.*
6005 *Chem. A* 107, 5710–5716.
- 6006 McLain, J., Adams, N., 2009. Flowing afterglow studies of temperature depen-
6007 dencies for electron dissociative recombination of HCNH⁺, CH₃CNH⁺ and
6008 CH₃CH₂CNH⁺ and their symmetrical proton-bound dimers. *Planet. Space*
6009 *Sci.* 57, 1642–1647.
- 6010 McLain, J., Molek, C., Osborne Jr., D., Adams, N., 2009. Flowing afterglow
6011 studies of the electron recombination of protonated cyanides (RCN)H⁺ and
6012 their proton-bound dimer ions (RCN)₂H⁺ where R is H, CH₃, and CH₃CH₂.
6013 *Int. J. Mass Spectrom.* 282, 85–90.
- 6014 McLain, J., Poterya, V., Molek, C., Babcock, L., Adams, N., 2004. Flowing
6015 afterglow studies of the temperature dependencies for dissociative recombina-
6016 tion of O₂⁺, CH₅⁺, C₂H₅⁺, and C₆H₇⁺ with electrons. *J. Phys. Chem. A*
6017 108, 6704–6708.
- 6018 McLain, J., Poterya, V., Molek, C., Jackson, D., Babcock, L., Adams, N., 2005.
6019 C₃H₃⁺ isomers: Temperature dependencies of production in the H₃⁺ reaction
6020 with allene and loss by dissociative recombination with electrons. *J. Phys.*
6021 *Chem. A* 109, 5119–5123.
- 6022 Mebel, A., Diau, E., Lin, M., Morokuma, K., 1996. Theoretical rate constants
6023 for the NH₃ + NO_x → NH₂ + HNO_x (x = 1, 2) reactions by ab initio
6024 MO/VTST calculations. *J. Phys. Chem.* 100, 7517–7525.
- 6025 Mebel, A., Georgievskii, Y., Jasper, A., Klippenstein, S., 2017. Tem-
6026 perature and pressure-dependent rate coefficients for the HACA
6027 pathways from benzene to naphthalene. *Proc. Comb. Inst.*
6028 <http://dx.doi.org/10.1016/j.proci.2016.07.013>.
- 6029 Mebel, A., Kislov, V., Kaiser, R., 2006a. Ab initio/Rice-Ramsperger-Kassel-
6030 Marcus study of the singlet C₄H₄ potential energy surface and of the re-
6031 actions of C₂(X¹Σ_g⁺) with C₂H₄(X¹A_g¹) and C(¹D) with C₃H₄ (allene and
6032 methylacetylene). *J. Phys. Chem. A* 125, 133113.

- 6033 Mebel, A., Kislov, V., Kaiser, R., 2006b. Potential energy surface and product
6034 branching ratios for the reaction of dicarbon $C_2(X^1\Sigma_g^+)$, with methylacety-
6035 lene, $CH_3CCH(X^1A_1)$: an ab initio/RRKM study. *J. Phys. Chem. A* 110,
6036 2421–2433.
- 6037 Melko, J., Ard, S., Johnson, R., Shuman, N., Guo, H., Viggiano, A., 2014.
6038 Temperature-dependent kinetics of charge transfer, hydrogen-atom transfer,
6039 and hydrogen-atom expulsion in the reaction of CO^+ with CH_4 and CD_4 . *J.*
6040 *Phys. Chem. A* 118, 8141–8146.
- 6041 Meller, R., Moortgat, G.K., 2000. Temperature dependence of the absorption
6042 cross sections of formaldehyde between 223 and 323 K in the wavelength range
6043 225–375 nm. *J. Geophys. Res.* 105, 7089–7102.
- 6044 Mendes, M., Buhr, H., Berg, M., Froese, M., Grieser, M., Heber, O., Jordon-
6045 Thaden, B., Krantz, C., Novotný, O., Novotny, S., Orlov, D., Petrigiani,
6046 A., Rappaport, M., Repnow, R., Schwalm, D., Shornikov, A., Stützel, J.,
6047 Zajfman, D., Wolf, A., 2012. Cold electron reactions producing the energetic
6048 isomer of hydrogen cyanide in interstellar clouds. *Astrophys. J.* 746, #L8.
- 6049 Millar, T., Walsh, C., Cordiner, M., Chuimín, R., Herbst, E., 2007. Hydrocarbon
6050 anions in interstellar clouds and circumstellar envelopes. *Astrophys. J.* 662,
6051 L87–L90.
- 6052 Miller, J., Klippenstein, S., 2002. Solution of some one- and two-dimensional
6053 master equation models for thermal dissociation: The dissociation of methane
6054 in the low-pressure limit. *J. Phys. Chem. A* 106, 4904–4913.
- 6055 Miller, J., Klippenstein, S., 2003. The recombination of propargyl radicals and
6056 other reactions on a C_6H_6 potential. *J. Phys. Chem. A* 107, 7783–7799.
- 6057 Miller, J., Klippenstein, S., 2004. The $H+C_2H_2 (+M) \rightleftharpoons C_2H_3 (+M)$ and
6058 $H+C_2H_4 (+M) \rightleftharpoons C_2H_5 (+M)$ reactions: Electronic structure, variational
6059 transition-state theory, and solutions to a two-dimensional master equation.
6060 *Phys. Chem. Chem. Phys.* 6, 1192–1202.
- 6061 Miller, J., Klippenstein, S., 2006. Master equation methods in gas phase chem-
6062 ical kinetics. *J. Phys. Chem. A* 110, 10528–10544.
- 6063 Miller, J., Klippenstein, S., 2013. Dissociation of propyl radicals and other
6064 reactions on a C_3H_7 potential. *J. Phys. Chem. A* 117, 2718–2727.
- 6065 Miller, J., Klippenstein, S., Robertson, S., 2000. A theoretical analysis of the
6066 reaction between vinyl and acetylene: Quantum chemistry and solution of the
6067 master equation. *J. Phys. Chem. A* 104, 7525–7536.
- 6068 Miller, J., Senosiain, J., Klippenstein, S., Georgievskii, Y., 2008. Reactions
6069 over multiple, interconnected potential wells: Unimolecular and bimolecular
6070 reactions on a C_3H_5 potential. *J. Phys. Chem. A* 112, 9429–9438.

- 6071 Miller, T., Shuman, N., Viggiano, A., 2012. Behavior of rate coefficients for
6072 ion-ion mutual neutralization, 300-550 K. *J. Chem. Phys.* 136, #204306.
- 6073 Milligan, D., Fairley, D., Meot-Ner, M., McEwan, M., 1998. Proton affinity of
6074 cyanogen and association reactions of $C_2N_2H^+$ and $C_2N_2CH_3^+$. *Int. J. Mass*
6075 *Spectrom. Ion Processes* 179/180, 285–291.
- 6076 Milligan, D., Freeman, C., Maclagan, R., McEwan, M., Wilson, P., Anicich,
6077 V., 2001. Termolecular ion-molecule reactions in Titan’s atmosphere. II: The
6078 structure of the associato adducts of $HCNH^+$ with C_2H_2 and C_2H_4 . *J. Am.*
6079 *Soc. Mass Spectrom.* 12, 557–564.
- 6080 Milligan, D., McEwan, M., 2000. $H_3^+ + O$: an experimental study. *Chemical*
6081 *Physics Letters* 319, 482–485.
- 6082 Milligan, D., Wilson, P., Freeman, C., Meot-Ner, M., McEwan, M., 2002. Dis-
6083 sociative proton transfer reactions of H_3^+ , N_2H^+ , and H_3O^+ with acyclic,
6084 cyclic, and aromatic hydrocarbons and nitrogen compounds, and astrochem-
6085 ical implications. *J. Phys. Chem. A* 106, 9745–9755.
- 6086 Mitchell, J., 1990. The dissociative recombination of molecular ions. *Phys. Rep.*
6087 186, 215–248.
- 6088 Mitsuke, K., Suzuki, S., Imamura, T., Koyano, I., 1991. Negative-ion mass
6089 spectrometric study of ion-pair formation in the vacuum ultraviolet. IV. CH_4
6090 $\rightarrow H^- + CH_3^+$ and $CD_4 \rightarrow D^- + CD_3^+$. *J. Chem. Phys.* 94, 6003–6006.
- 6091 Molek, C., Poterya, V., Adams, N., McLain, J., 2009. Development of a novel
6092 technique for quantitatively determining the products of electron-ion disso-
6093 ciative recombination. *Int. J. Mass Spectrom.* 285, 1–11.
- 6094 Molina-Cuberos, G., Lammer, H., Stumtner, W., Schwingenschuh, K., Rucker,
6095 H., López-Moreno, J., Rodrigo, R., Tokano, T., 2001. Ionospheric layer in-
6096 duced by meteoric ionization in Titan’s atmosphere. *Planet. Space Sci.* 49,
6097 143–153.
- 6098 Molina-Cuberos, G., López-Moreno, J., Rodrigo, R., 2000. Influence of elec-
6099 trophilic species on the lower ionosphere of Titan. *Geophys. Res. Lett.* 27,
6100 1351–1354.
- 6101 Molina-Cuberos, G., López-Moreno, J., Rodrigo, R., Lara, L., 1999a. Chemistry
6102 of the galactic cosmic ray induced ionosphere of Titan. *J. Geophys. Res.* 104,
6103 21997–22024.
- 6104 Molina-Cuberos, G., Schwingenschuh, K., López-Moreno, J., Rodrigo, R., Lara,
6105 L., Anicich, V., 2002. Nitriles produced by ion chemistry in the lower iono-
6106 sphere of Titan. *J. Geophys. Res.* 107, #5099.
- 6107 Molina-Cuberos, G.J., López-Moreno, J.J., Rodrigo, R., Lara, L.M., O’Brien,
6108 K., 1999b. Ionization by cosmic rays of the atmosphere of Titan. *Planet.*
6109 *Space Sci.* 47, 1347–1354.

- 6110 Morales, S., Bennett, C., Le Picard, S., Canosa, A., Sims, I., Sun, B., Chen, P.,
6111 Chang, A., Kislov, V., Mebel, A., Gu, X., Zhang, F., Maksyutenko, P., Kaiser,
6112 R., 2011. A crossed molecular beam, low-temperature kinetics, and theoretical
6113 investigation of the reaction of the cyano radical (CN) with 1,3-butadiene
6114 (C_4H_6). A route to complex nitrogen-bearing molecules in low-temperature
6115 extraterrestrial environments. *Astrophys. J.* 742, 26.
- 6116 Morales, S., Le Picard, S., Canosa, A., Sims, I., 2010. Experimental measure-
6117 ments of low temperature rate coefficients for neutral-neutral reactions of
6118 interest for atmospheric chemistry of Titan, Pluto and Triton: Reactions of
6119 the CN radical. *Faraday Discuss.* 147, 155–171.
- 6120 Mordaunt, D.H., Ashfold, M.N.R., Dixon, R.N., 1994. Dissociation dynamics of
6121 $H_2O(D_2O)$ following photoexcitation at the Lyman- α wavelength (121.6 nm).
6122 *J. Chem. Phys.* 100, 7360–7375.
- 6123 Moreno, R., Lellouch, E., Lara, L., Courtin, R., Bockelée-Morvan, D., Hartogh,
6124 P., Rengel, M., Biver, N., Banaszkiwicz, M., González, A., 2011. First detec-
6125 tion of hydrogen isocyanide (HNC) in Titan’s atmosphere. *Astron. Astrophys.*
6126 536, #L12.
- 6127 Moreno, R., Lellouch, E., Lara, L., Feuchtgruber, H., Rengel, M., Hartogh, P.,
6128 Courtin, R., 2012. The abundance, vertical distribution and origin of H_2O
6129 in Titan’s atmosphere: Herschel observations and photochemical modelling.
6130 *Icarus* 221, 753–767.
- 6131 Morgan, C., Drabbers, M., Wodtke, A., 1996. The correlated product state
6132 distribution of ketene photodissociation at 308 nm. *J. Chem. Phys.* 104,
6133 7460–7474.
- 6134 Moses, J., Allen, M., Yung, Y., 1992. Hydrocarbon nucleation and aerosol
6135 formation in Neptune’s atmosphere. *Icarus* 99, 318–346.
- 6136 Moses, J.I., Fouchet, T., Bézard, B., Gladstone, G., Lellouch, E., Feuchtgruber,
6137 H., 2005. Photochemistry and diffusion in Jupiter’s stratosphere: Constraints
6138 from ISO observations and comparisons with other giant planets. *J. Geophys.*
6139 *Res.* 110, #E08001.
- 6140 Mota, R., Parafita, R., Giuliani, A., Hubin-Franskin, M.J., Lourenço, J., Garcia,
6141 G., Hoffmann, S., Mason, M., Ribeiro, P., Raposo, M., Limão-Vieira, P., 2005.
6142 Water VUV electronic state spectroscopy by synchrotron radiation. *Chem.*
6143 *Phys. Lett.* 416, 152–159.
- 6144 Mount, G.H., Warden, E.S., Moos, H.W., 1977. Photoabsorption cross sections
6145 of methane from 1400 to 1850 Å. *Astrophys. J.* 214, L47–L49.
- 6146 Mul, P., McGowan, J., Defrance, P., Mitchell, J., 1983. Merged electron-ion
6147 beam experiments: V. Dissociative recombination of OH^+ , H_2O^+ , H_3O^+ and
6148 D_3O^+ . *J. Phys. B: At. Mol. Phys.* 16, 3099–3107.

- 6149 Mullen, C., Smith, M., 2005. Low temperature $\text{NH}(X^3\Sigma^-)$ radical reactions with
6150 NO, saturated, and unsaturated hydrocarbons studied in a pulsed supersonic
6151 Laval nozzle flow reactor between 53 and 188 K. *J. Phys. Chem. A* 109,
6152 1391–1399.
- 6153 Murphy, J., Vakhtin, A., Leone, S., 2003. Laboratory kinetics of C_2H radical
6154 reactions with ethane, propane, and n-butane at $T = 96\text{--}296$ K: Implications
6155 for Titan. *Icarus* 163, 175–181.
- 6156 Nahar, S., 1999. Electron-ion recombination rate coefficients, photoionization
6157 cross sections, and ionization fractions for astrophysically abundant elements.
6158 II. Oxygen ions. *Astrophys. J. Suppl. Ser.* 120, 131–145.
- 6159 Nahar, S., Pradhan, A., 1997. Electron-ion recombination rate coefficients, pho-
6160 toionization cross sections, and ionization fractions for astrophysically abun-
6161 dant elements. I. Carbon and nitrogen. *Astrophys. J. Suppl. Ser.* 111, 339–355.
- 6162 Nakajima, M., Matsugi, A., Miyoshi, A., 2009. Mechanism and kinetic isotope
6163 effect of the reaction of $\text{C}_2(X^1\Sigma_g^+)$ radicals with H_2 and D_2 . *J. Phys. Chem.*
6164 *A* 113, 8963–8970.
- 6165 Nakayama, T., Watanabe, K., 1964. Absorption and photoionization coefficients
6166 of acetylene, propyne, and 1-butyne. *J. Chem. Phys.* 40, 558–561.
- 6167 Narożnik, M., Niedzielski, J., 1986. Propylene photolysis at 6.7 eV: Calculation
6168 of the quantum yields for the secondary processes. *J. Photochem.* 32, 281–292.
- 6169 Naulin, C., Daugey, N., Hickson, K., Costes, M., 2009. Dynamics of the reactions
6170 of $\text{C}(^3\text{P}_J)$ atoms with ethylene, allene, and methylacetylene at low energy
6171 revealed by Doppler-Fizeau spectroscopy. *J. Phys. Chem. A* 113, 14447–
6172 14457.
- 6173 Neau, A., Al-Khalili, A., Rosén, S., Le Padellec, A., Derkatch, A., Shi, W.,
6174 Viktor, L., Larsson, M., Semaniak, J., Thomas, R., Någård, M., Andersson,
6175 K., Danared, H., af Ugglas, M., 2000. Dissociative recombination of D_3O^+
6176 and H_3O^+ : Absolute cross sections and branching ratios. *J. Chem. Phys.* 113,
6177 1762–1770.
- 6178 Nesbitt, F., Marston, G., Stief, L., 1990. Kinetic studies of the reactions of
6179 methyleneaminylium and dideuteromethyleneaminylium radicals with nitro-
6180 gen and hydrogen atoms. *J. Phys. Chem.* 94, 4946–4951.
- 6181 Nguyen, H., Nguyen, H., Nguyen, T.N., Hoang, H., Vereecken, L., 2014. The-
6182 oretical study on the reaction of the methylidyne radical, $\text{CH}(X^2\Pi)$, with
6183 formaldehyde, CH_2O . *J. Phys. Chem. A* 118, 8861–8871.
- 6184 Nguyen, M., Sengupta, D., Ha, T.K., 1996. Another look at the decomposition
6185 of methyl azide and methanimine: How is HCN formed? *J. Phys. Chem.* 100,
6186 6499–6503.

- 6187 Nguyen, T., Mebel, A., Lin, S., Kaiser, R., 2001. Product branching ratios of
6188 the $C(^3P) + C_2H_3(^2A')$ and $CH(^2\Pi) + C_2H_2(^1\Sigma_g^+)$ reactions and photodis-
6189 sociation of $H_2CC\hat{a}^\circ CH(^2B_1)$ at 193 nm and 242 nm: An ab initio/RRKM
6190 study. *J. Phys. Chem. A* 105, 11549–11559.
- 6191 Ni, C.K., Huang, J., Chen, Y., Kung, A., Jackson, W., 1999. Photodissociation
6192 of propyne and allene at 193 nm with vacuum ultraviolet detection of the
6193 products. *J. Chem. Phys.* 110, 3320–3325.
- 6194 Nicolas, C., Alcaraz, C., Thissen, R., Vervloet, M., Dutuit, O., 2003a. Disso-
6195 ciative photoionization of N_2 in the 24–32 eV photon energy range. *J. Phys.*
6196 *B At. Mol. Opt. Phys.* 36, 2239–2251.
- 6197 Nicolas, C., Torrents, R., Gerlich, D., 2003b. Integral and differential cross sec-
6198 tion measurements at low collision energies for the $N_2^+ + CH_4/CD_4$ reactions.
6199 *J. Chem. Phys.* 118, 2723–2730.
- 6200 Niedzielski, J., Wlodzimierz, M., Gawlowski, J., 1982. Gas phase photolysis of
6201 propylene at 8.4 and 10.0 eV. *J. Photochem.* 19, 123–131.
- 6202 Niemann, H., Atreya, S., Demick, J., Gautier, D., Haberman, J., Harpold,
6203 D., Kasprzak, W., Lunine, J., Owen, T., Raulin, F., 2010. Composition of
6204 Titan’s lower atmosphere and simple surface volatiles as measured by the
6205 Cassini-Huygens probe gas chromatograph mass spectrometer experiment. *J.*
6206 *Geophys. Res.* 115, #E12006.
- 6207 Niemann, H.B., Atreya, S.K., Bauer, S.J., Carignan, G.R., Demick, J.E., Frost,
6208 R.L., Gautier, D., Haberman, J.A., Harpold, D.N., Hunten, D.M., Israel, G.,
6209 Lunine, J.I., Kasprzak, W., Owen, T.C., Paulkovich, M., Raulin, F., Raaen,
6210 E., Way, S.H., 2005. The abundances of constituents of Titan’s atmosphere
6211 from the GCMS instrument on the Huygens probe. *Nature* 438, 779–784.
- 6212 Nixon, C., Achterberg, R., Teanby, N., Irwin, P., Flaud, J.M., Kleiner, I.,
6213 Dehayem-Kamadjeu, A., Brown, L., Sams, R., Bézard, B., Coustenis, A.,
6214 Ansty, T., Mamoutkine, A., Vinatier, S., Bjoraker, G., Jennings, D., Ro-
6215 mani, P., Flasar, F., 2010. Upper limits for undetected trace species in the
6216 stratosphere of Titan. *Faraday Discuss.* 147, 65–81.
- 6217 Nixon, C., Jennings, D., Bézard, B., Vinatier, S., Teanby, N., Sung, K., Ansty,
6218 T., Irwin, P., Goriús, N., Cottini, V., Coustenis, A., Flasar, F., 2013. Detec-
6219 tion of propene in Titan’s stratosphere. *Astrophys. J.* 776, #L14.
- 6220 Nixon, C.A., Teanby, N.A., Irwin, P.G.J., Hörst, S.M., 2013. Upper limits for
6221 PH_3 and H_2S in Titan’s atmosphere from Cassini CIRS. *Icarus* 224, 253–256.
- 6222 Nizamov, B., Dagdigian, P., 2003. Spectroscopic and kinetic investigation of
6223 methylene amidogen by cavity ring-down spectroscopy. *J. Phys. Chem. A*
6224 107, 2256–2263.

- 6225 Nizamov, B., Leone, S., 2004a. Kinetics of C_2H reactions with hydrocarbons
6226 and nitriles in the 104-296 K temperature range. *J. Phys. Chem. A* 108,
6227 1746–1752.
- 6228 Nizamov, B., Leone, S., 2004b. Rate coefficients and kinetic isotope effect for
6229 the C_2H reactions with NH_3 and ND_3 in the 104-294 K temperature range.
6230 *J. Phys. Chem. A* 108, 3766–3771.
- 6231 Noller, B., Fischer, I., 2007. Photodissociation dynamics of the 2-propyl radical,
6232 C_3H_7 . *J. Chem. Phys.* 126, #144302.
- 6233 North, S., Hall, G., 1996. The radical photodissociation channel of acrylonitrile.
6234 *Chem. Phys. Lett.* 263, 148–153.
- 6235 Nuth, J., Glicker, S., 1982. The vacuum ultraviolet spectra of HCN, C_2N_2 , and
6236 CH_3CN . *J. Quant. Spectr. Rad. Trans.* 28, 223–231.
- 6237 Obi, K., Akimoto, H., Ogata, Y., Tanaka, I., 1971. Photolyses of propane, n-
6238 butane, and cyclobutane at Xe and Kr resonance lines. *J. Chem. Phys.* 55,
6239 3822–3828.
- 6240 Oertel, H., Schenk, H., Baumgärtel, H., 1980. Ion pair formation from photon
6241 irradiation of O_2 , NO and CO in 17-30 eV. *Chem. Phys.* 46, 251–262.
- 6242 Ohmori, K., Miyoshi, A., Matsui, H., Washida, N., 1990. Studies on the reaction
6243 of acetaldehyde and acetyl radicals with atomic hydrogen. *J. Phys. Chem.*
6244 94, 3253–3255.
- 6245 Öjekull, J., Andersson, P., Någård, M., Pettersson, J., Derkatch, A., Neau, A.,
6246 Rosén, S., Thomas, R., Larsson, M., Österdahl, F., Semaniak, J., Danared,
6247 H., Källberg, A., af Ugglas, M., Marković, N., 2004. Dissociative recom-
6248 bination of NH_4^+ and ND_4^+ ions: Storage ring experiments and ab initio
6249 molecular dynamics. *J. Chem. Phys.* 120, 7391–7399.
- 6250 Okabe, H., 1978. *Photochemistry of Small Molecules*. volume 1. John Wiley &
6251 Sons, New York. 1st edition.
- 6252 Okabe, H., 1981. Photochemistry of acetylene at 1470 Å. *J. Chem. Phys.* 75,
6253 2772–2778.
- 6254 Okabe, H., Becker, D., 1963. Vacuum ultraviolet photochemistry. VII. Photol-
6255 ysis of n-butane. *J. Chem. Phys.* 39, 2549–2555.
- 6256 Okabe, H., McNesby, J., 1962. Vacuum ultraviolet photochemistry. IV. Photol-
6257 ysis of propane. *J. Chem. Phys.* 37, 1340–1346.
- 6258 Opansky, B., Leone, S., 1996. Rate coefficients of C_2H with C_2H_4 , C_2H_6 , and
6259 H_2 from 150 to 359 K. *J. Phys. Chem.* 100, 19904–19910.

- 6260 Operti, L., Rabazzana, R., Turco, F., Vaglio, G., 2004. Gas-phase ion chemistry
6261 of the propyne/ammonia and silane/propyne/ammonia systems. *Int. J. Mass*
6262 *Spectrom.* 232, 139–146.
- 6263 Orkin, V., Huie, R., Kurylo, M., 1997. Rate constants for the reactions of
6264 OH with HFC-245cb ($\text{CH}_3\text{CF}_2\text{CF}_3$) and some fluoroalkenes (CH_2CHCF_3 ,
6265 CH_2CFCF_3 , CF_2CFCF_3 , and CF_2CF_2). *J. Phys. Chem. A* 101, 9118–9124.
- 6266 Osamura, Y., Petrie, S., 2004. NCCN and NCCCCN formation in Titan’s
6267 atmosphere: 1. Competing reactions of precursor HCCN($^3\text{A}''$) with H(^2S)
6268 and $\text{CH}_3(^2\text{A}')$. *J. Phys. Chem. A* 108, 3615–3622.
- 6269 Osborne, D.J., Lawson, P., Adams, N., 2011. Flowing afterglow studies of
6270 dissociative electron-ion recombination for a series of single ring compounds
6271 at room temperature. *Int. J. Mass Spectrom.* 305, 35–39.
- 6272 Ozturk, F., Baykut, G., Moini, M., Eyler, J., 1987. Reactions of C_3H_3^+ with
6273 acetylene and diacetylene in the gas phase. *J. Phys. Chem.* 91, 4360–4364.
- 6274 Ozturk, F., Moini, M., Brill, F., Eyler, J., Buckley, T., Lias, S., Ausloos, P.,
6275 1989. Reactions of C_5H_3^+ and C_5H_5^+ ions with acetylene and diacetylene. *J.*
6276 *Phys. Chem.* 93, 4038–4044.
- 6277 Palmer, M.Y., Cordiner, M.A., Nixon, C.A., Charnley, S.B., Teanby, N.A.,
6278 Kisiel, Z., Irwin, P.G., Mumma, M.J., 2017. ALMA detection and astrobio-
6279 logical potential of vinyl cyanide on Titan. *Science Advances* 3, #e1700022.
- 6280 Pantos, E., Philis, J., Bolovinos, A., 1978. The extinction coefficient of benzene
6281 vapor in the region 4.6 to 36 eV. *J. Mol. Spectrosc.* 72, 36–43.
- 6282 Páramo, A., Canosa, A., Le Picard, S., Sims, I., 2008. Rate coefficients for
6283 the reactions of $\text{C}_2(\text{a}^3\Pi_u)$ and $\text{C}_2(\text{X}^1\Sigma_g^+)$ with various hydrocarbons (CH_4 ,
6284 C_2H_2 , C_2H_4 , C_2H_6 , and C_3H_8): A gas-phase experimental study over the
6285 temperature range 24–300 K. *J. Phys. Chem. A* 112, 9591–9600.
- 6286 Parent, D., 1989. Reactions of C_nN^+ with methane and the implications for
6287 interstellar chemistry. *Astrophys. J.* 347, 1183–1186.
- 6288 Parent, D., 1990. Reactions of the carbene ions C_nN^+ with labeled methane:
6289 mechanistic interpretation. *J. Am. Chem. Soc.* 112, 5966–5973.
- 6290 Parent, D., McElvany, S., 1989. Investigations of small carbon cluster ion struc-
6291 tures by reactions with HCN. *J. Am. Chem. Soc.* 111, 2393–2401.
- 6292 Park, J., Gheyas, S., Lin, M., 1999. Kinetics of C_6H_5 radical reactions with
6293 2-methylpropane, 2,3-dimethylbutane and 2,3,4-trimethylpentane. *Int. J.*
6294 *Chem. Kin.* 31, 645–653.

- 6295 Parker, D., Zhang, F., Kim, Y., Kaiser, R., 2011. On the formation of resonantly
6296 stabilized C_5H_3 radicals - A crossed beam and ab initio study of the reaction
6297 of ground state carbon atoms with vinylacetylene. *J. Phys. Chem. A* 115,
6298 593–601.
- 6299 Parkes, D., 1972. Oxygen negative ion reactions with carbon dioxide and carbon
6300 monoxide. Part 1. *J. Chem. Soc., Faraday Trans. 1* 68, 627–640.
- 6301 Parkinson, W., Rufus, J., Yoshino, K., 2003. Absolute absorption cross sec-
6302 tion measurements of CO_2 in the wavelength region 163–2000 nm and the
6303 temperature dependence. *Chem. Phys.* 290, 251–256.
- 6304 Payne, W., Monks, P., Nesbitt, F., Stief, L., 1996. The reaction between $N(^4S)$
6305 and C_2H_3 : Rate constant and primary reaction channels. *J. Chem. Phys.*
6306 104, 9808–9815.
- 6307 Peeters, J., Boullart, W., Langhans, I., 1994. Branching ratio of the $C_2H_2 + O$
6308 reaction at 290 K from kinetic modelling of relative methylene concentration
6309 versus time profiles in $C_2H_2/O/H$ systems. *Int. J. Chem. Kin.* 26, 869–886.
- 6310 Peko, B., Stephen, T., 2000. Absolute detection efficiencies of low energy H , H^- ,
6311 H^+ , H_2^+ and H_3^+ incident on a multichannel plate detector. *Nucl. Instrum.*
6312 *Meth. B* 171, 597–604.
- 6313 Pernot, P., Plessis, S., Carrasco, N., 2011. Probabilistic representations of partial
6314 branching ratios: bridging the gap between experiments and chemical models.
6315 *J. Phys. Conf. Ser.* 300, #012027.
- 6316 Peterson, J., Le Padellec, A., Danared, H., Dunn, G., Larsson, M., Larson, Å.,
6317 Peverall, R., Strömholm, C., Rosén, S., af Ugglas, M., van der Zande, W.,
6318 1998. Dissociative recombination and excitation of N_2^+ : Cross sections and
6319 product branching ratios. *J. Chem. Phys.* 108, 1978–1988.
- 6320 Petrank, A., Iraqi, M., Dotan, I., Lifshitz, C., 1992. Proton transfer reactions of
6321 $C_2H_4^+$: the bond energy $D(C_2H_3-H)$. *Int. J. Mass Spectrom. Ion Processes*
6322 117, 223–236.
- 6323 Petrie, S., 1996. Novel pathways to CN^- within interstellar clouds and circum-
6324 stellar envelopes: implications for IS and CS chemistry. *Mon. Not. R. Astron.*
6325 *Soc.* 281, 137–144.
- 6326 Petrie, S., 2001. Hydrogen isocyanide, HNC: A key species in the chemistry of
6327 Titan’s ionosphere? *Icarus* 151, 196–203.
- 6328 Petrie, S., 2002. Reactivity of HNC with small hydrocarbon radicals. *J. Phys.*
6329 *Chem. A* 106, 11181–11189.
- 6330 Petrie, S., Chirnside, T., Freeman, C., McEwan, M., 1991a. The ion/molecule
6331 chemistry of CH_2CHCN . *Int. J. Mass Spectrom.* 107, 319–331.

- 6332 Petrie, S., Freeman, C., McEwan, M., 1992. The ion-molecule chemistry of
6333 acrylonitrile: Astrochemical implications. *Mon. Not. R. Astron. Soc.* 257,
6334 438–444.
- 6335 Petrie, S., Herbst, E., 1997. Some interstellar reactions involving electrons and
6336 neutral species: Attachment and isomerization. *Astrophys. J.* 491, 210–215.
- 6337 Petrie, S., Knight, J., Freeman, C., MacLagan, R., McEwan, M., Sudkeaw, P.,
6338 1991b. The proton affinity and selected ion/molecule reactions of diacetylene.
6339 *Int. J. Mass Spectrom.* 105, 43–54.
- 6340 Petrie, S., Osamura, Y., 2004. NCCN and NCCCCN formation in Titan’s
6341 atmosphere: 2. HNC as a viable precursor. *J. Phys. Chem. A* 108, 3623–
6342 3631.
- 6343 Pino, T., Tulej, M., Güthe, F., Pachkov, M., Maier, J., 2002. Photodetachment
6344 spectroscopy of the $C_{2n}H^-$ ($n=2-4$) anions in the vicinity of their electron
6345 detachment threshold. *J. Chem. Phys.* 116, 6126–6131.
- 6346 Piper, L.G., 1993. Reevaluation of the transition-moment function and Einstein
6347 coefficients for the $N_2(A\ ^3\Sigma_u^+ - X\ ^1\Sigma_g^+)$ transition. *J. Chem. Phys.* 99, 3174–
6348 3181.
- 6349 Pirim, C., Gann, R., McLain, J., Orlando, T., 2015. Electron-molecule chem-
6350 istry and charging processes on organic ices and Titan’s icy aerosol surrogates.
6351 *Icarus* 258, 109–119.
- 6352 Pithawalla, Y., Meot-Ner, M., Gao, J., El Shall, M., Baranov, V., Bohme,
6353 D., 2001. Gas-phase oligomerization of propene initiated by benzene radical
6354 cation. *J. Phys. Chem. A* 105, 3908–3916.
- 6355 Plašil, R., Mehner, T., Dohnal, P., Kotrik, T., Glosík, J., Gerlich, D., 2011.
6356 Reactions of cold trapped CH^+ ions with slow H atoms. *Astrophys. J.* 737,
6357 #60.
- 6358 Plessis, S., Carrasco, N., Dobrijevic, M., Pernot, P., 2012. Production of neu-
6359 tral species in Titan’s ionosphere through dissociative recombination of ions.
6360 *Icarus* 219, 254–266.
- 6361 Polino, D., Klippenstein, S., Harding, L., Georgievskii, Y., 2013. Predictive the-
6362 ory for the addition and insertion kinetics of 1CH_2 reacting with unsaturated
6363 hydrocarbons. *J. Phys. Chem. A* 117, 12677–12692.
- 6364 Prasad, S., Huntress Jr., W., 1980. A model for gas phase chemistry in interstel-
6365 lar clouds: I. The basic model, library of chemical reactions, and chemistry
6366 among C, N, and O compounds. *Astrophys. J. Suppl. Ser.* 43, 1–35.
- 6367 Prodruk, S., Gronert, S., Bierbaum, V., DePuy, C., 1992. Gas-phase reactions
6368 of $C_3H_n^+$ ions. *Org. Mass Spectrom.* 27, 416–422.

- 6369 Raghavachari, K., Trucks, G., Pople, J., Head-Gordon, M., 1989. A 5th-order
6370 perturbation comparison of electron correlation theories. *Chem. Phys. Lett.*
6371 157, 479–483.
- 6372 Raksit, A., Bohme, D., 1983. An experimental study of the influence of hy-
6373 dration on the reactivity of the hydroxide anion in the gas phase at room
6374 temperature. *Can. J. Chem.* 61, 1683–1689.
- 6375 Ralchenko, Y., Kramida, A., Reader, J., Team, N.A., 2011. NIST Atomic Spec-
6376 tra Database (version 4.1.0) National Institute of Standards and Technology,
6377 Gaithersburg, MD Available: <http://physics.nist.gov/asd>.
- 6378 Randeniya, L., Smith, M., 1991. Gas phase reaction rates of N₂⁺ with CH₄,
6379 O₂, and n-H₂ at very low temperatures. *J. Chem. Phys.* 94, 351–356.
- 6380 Rapp, D., Briglia, D., 1965. Total cross sections for ionization and attachment
6381 in gases by electron impact. II. Negative-ion formation. *J. Chem. Phys.* 43,
6382 1480–1489.
- 6383 Rawat, P., Prabhudesai, V., Rahman, M., Bhargava Ram, N., Krishnakumar,
6384 E., 2008. Absolute cross sections for dissociative electron attachment to NH₃
6385 and CH₄. *Int. J. Mass Spectrom.* 277, 96–102.
- 6386 Rebrion-Rowe, C., Lehfaoui, L., Rowe, B., Mitchell, J., 1998. The dissociative
6387 recombination of hydrocarbon ions. II. Alkene and alkyne derived species. *J.*
6388 *Chem. Phys.* 108, 7185–7189.
- 6389 Rebrion-Rowe, C., Mostefaoui, T., Laubé, S., Mitchell, J., 2000. The dissocia-
6390 tive recombination of hydrocarbon ions. III. Methyl-substituted benzene ring
6391 compounds. *J. Chem. Phys.* 113, 3039–3045.
- 6392 Rengel, M., Sagawa, H., Hartogh, P., Lellouch, E., Feuchtgruber, H., Moreno,
6393 R., Jarchow, C., Courtin, R., Cernicharo, J., Lara, L., 2014. *Herschel/PACS*
6394 spectroscopy of trace gases of the stratosphere of Titan. *Astron. Astrophys.*
6395 561, #A4.
- 6396 Ribeiro, J., Mebel, A., 2014. Reaction mechanism and product branching ratios
6397 of the CH + C₃H₈ reaction: A theoretical study. *J. Phys. Chem. A* 118,
6398 9080–9086.
- 6399 Richard, M., Cravens, T., Robertson, I., Waite Jr., J., Wahlund, J.E., Crary,
6400 F., Coates, A., 2011. Energetics of Titan’s ionosphere: Model comparisons
6401 with Cassini data. *J. Geophys. Res.* 116, #A09310.
- 6402 Richard, M., Cravens, T., Wylie, C., Webb, D., Chediak, Q., Mandt, K.,
6403 Waite Jr., J., Rymer, A., Bertucci, C., Wellbrock, A., Windsor, A., Coates,
6404 A., 2015a. An empirical approach to modeling ion production rates in Titan’s
6405 ionosphere II: Ion production rates on the nightside. *J. Geophys. Res. Space*
6406 *Physics* 120, doi:10.1002/2014JA020343.

- 6407 Richard, M., Cravens, T., Wylie, C., Webb, D., Chediak, Q., Perryman, R.,
6408 Mandt, K., Westlake, J., Waite Jr., J., Robertson, I., Magee, B., Edberg, N.,
6409 2015b. An empirical approach to modeling ion production rates in Titan's
6410 ionosphere I: Ion production rates on the dayside and globally. *J. Geophys.*
6411 *Res.* 120, doi:10.1002/2013JA019706.
- 6412 Robertson, I., Cravens, T., Waite Jr., J., Yelle, R., Vuitton, V., Coates, A.,
6413 Wahlund, J.E., Ågren, K., Mandt, K., Magee, B., Richard, M., Fattig, E.,
6414 2009. Structure of Titan's ionosphere: Model comparisons with Cassini data.
6415 *Planet. Space Sci.* 57, 1834–1846.
- 6416 Robinson, J., Harris, S., Sun, W., Sveum, N., Neumark, D., 2002. Photofrag-
6417 ment translational spectroscopy of 1,3-butadiene and 1,3-butadiene-1,1,4,4-d4
6418 at 193 nm. *J. Am. Chem. Soc.* 124, 10211–10224.
- 6419 Robinson, J., Sveum, N., Goncher, S., Neumark, D., 2005. Photofragment
6420 translational spectroscopy of allene, propyne, and propyne-d3 at 193 nm.
6421 *Mol. Phys.* 103, 1765–1783.
- 6422 Roche, A., Sutton, M., Bohme, D., Schiff, H., 1971. Determination of pro-
6423 ton affinity from the kinetics of proton transfer reactions. I. Relative proton
6424 affinities. *J. Chem. Phys.* 55, 5480–5484.
- 6425 Roe, H., Greathouse, T., Richter, M., Lacy, J., 2003. Propane (C₃H₈) on Titan.
6426 *Astrophys. J.* 597, L65–L68.
- 6427 Roe, H.G., Greathouse, T., Tokunaga, A., 2011. Update on the TEXES Titan
6428 Mid-Infrared Spectral Survey, in: EPSC-DPS Joint Meeting 2011, p. 1398.
- 6429 Romanzin, C., Louarn, E., Lemaire, J., Žabka, J., Polášek, M., Guillemin, J.C.,
6430 Alcaraz, C., 2016. An experimental study of the reactivity of CN⁻ and C₃N⁻
6431 anions with cyanoacetylene (HC₃N). *Icarus* 268, 242–252.
- 6432 Rosén, S., Derkatch, A., Semaniak, J., Neau, A., Al-Khalili, A., Le Padellec,
6433 A., Viktor, L., Thomas, R., Danared, H., af Ugglas, M., Larsson, M., 2000.
6434 Recombination of simple molecular ions studied in storage ring: dissociative
6435 recombination of H₂O⁺. *Faraday Discuss.* 115, 295–302.
- 6436 Rosén, S., Peverall, R., Larsson, M., Le Padellec, A., Semaniak, J., Larson, Å.,
6437 Strömholm, C., van der Zande, W., Danared, H., Dunn, G., 1998. Absolute
6438 cross sections and final-state distributions for dissociative recombination and
6439 excitation of CO⁺ ($\nu=0$) using an ion storage ring. *Phys. Rev. A* 57, 4462–
6440 4451.
- 6441 Rowe, B., Marquette, J., Dupeyrat, G., Ferguson, E., 1985. Reactions of He⁺
6442 and N⁺ ions with several molecules at 8 K. *Chem. Phys. Lett.* 113, 403–406.
- 6443 Rowe, B., Marquette, J., Rebrion, C., 1989. Mass-selected ion-molecule re-
6444 actions at very low temperatures: the CRESUS apparatus. *J. Chem. Soc.*
6445 *Faraday Trans. 2* 85, 1631–1641.

- 6446 Rudolph, P., Melton, C., 1960. Ion-molecule charge transfer reactions in the
6447 alpha radiolysis of various hydrocarbons in a mass spectrometer. *J. Chem.*
6448 *Phys.* 32, 586–588.
- 6449 Ruscic, B., Berkowitz, J., 1990. Photoion-pair formation and photoelectron-
6450 induced dissociative attachment in C_2H_2 : $D_0(HCC-H)$. *J. Chem. Phys.* 93,
6451 5586–5593.
- 6452 Rutherford, J., Neynaber, R., Vroom, D., 1978. Measurements of selected charge
6453 transfer processes at low energies: Final report for period November 1977-
6454 November 1978 (contract No. DNA 001-77-C-0202). Defense Nuclear Agency
6455 Report DNA 4695F. IRT Corporation.
- 6456 Rutkowski, J., Drost, H., Spangenberg, H.J., 1980. Investigation of the in-
6457 elastic interaction of slow monoenergetic electrons with simple hydrocarbon
6458 molecules. *Ann. Phys.* 7, 259–270.
- 6459 Sagnières, L., Galand, M., Cui, J., Lavvas, P., Vigren, E., Vuitton, V., Yelle, R.,
6460 Wellbrock, A., Coates, A., 2015. Influence of local ionization on ionospheric
6461 densities in Titan’s upper atmosphere. *J. Geophys. Res. Space Physics* 120,
6462 5899–5921.
- 6463 Sailer, W., Pelc, A., Limão-Vieira, P., Mason, N., Limtrakul, J., Scheier, P.,
6464 Probst, M., Märk, T., 2003. Low energy electron attachment to CH_3CN .
6465 *Chem. Phys. Lett.* 381, 216–222.
- 6466 Samson, J., Haddad, G., Masuoka, T., Pareek, P., Kilcoyne, D., 1989. Ionization
6467 yields, total absorption, and dissociative photoionization cross sections of CH_4
6468 from 110-950 Å. *J. Chem. Phys.* 90, 6925–6932.
- 6469 Samson, J., Marmo, F., Watanabe, K., 1962. Absorption and photoionization
6470 coefficients of propylene and butene-1 in the vacuum ultraviolet. *J. Chem.*
6471 *Phys.* 36, 783–786.
- 6472 Samson, J.A.R., Masuoka, T., Pareek, P.N., Angel, G.C., 1987. Total and
6473 dissociative photoionization cross sections of N_2 from threshold to 107 eV. *J.*
6474 *Chem. Phys.* 86, 6128–6132.
- 6475 Sander, S., Friedl, R., Barker, J., Golden, D., Kurylo, M., Wine, P., Abbatt, J.,
6476 Burkholder, J., Kolb, C., Moortgat, G., Huie, R., Orkin, V., 2011. Chemical
6477 kinetics and photochemical data for use in atmospheric studies. Evaluation
6478 number 17.
- 6479 Sander, S., Friedl, R., Golden, D., Kurylo, M., Moortgat, G., Keller-Rudek, H.,
6480 Wine, P., Ravishankara, A., Kolb, C., Molina, M., Finlayson-Pitts, B., Huie,
6481 R., Orkin, V., 2006. Chemical kinetics and photochemical data for use in
6482 atmospheric studies. Evaluation number 15.

- 6483 Sato, K., Misawa, K., Kobayashi, Y., Matsui, M., Tsunashima, S., Kurosaki,
6484 K., Takayanagi, T., 1999. Measurements of thermal rate constants for the
6485 reactions of N(²D, ²P) with C₂H₄ and C₂D₄ between 225 and 292 K. *J.*
6486 *Phys. Chem. A* 103, 8650–8656.
- 6487 Sauer, M., Ward, B., 1967. The reactions of hydrogen atoms with benzene and
6488 toluene studied by pulsed radiolysis: Reaction rate constants and transient
6489 spectra in the gas phase and aqueous solution. *J. Phys. Chem.* 74, 3971–3983.
- 6490 Savić, I., Gerlich, D., 2005. Temperature variable ion trap studies of C₃H_n⁺ with
6491 H₂ and HD. *Phys. Chem. Chem. Phys.* 7, 1026–1035.
- 6492 Schofield, K., 1979. Critically evaluated rate constants for gaseous reactions of
6493 several electronically excited species. *J. Phys. Chem. Ref. Data* 8, 723–798.
- 6494 Schwanebeck, W., Warnatz, J., 1975. Reaktionen des butadiins. I. Die reaktion
6495 mit wasserstoffatomen. *Ber. Bunsenges. Phys. Chem.* 79, 530–535.
- 6496 Scott, G., Fairley, D., Freeman, C., McEwan, M., 1999. C_mH_n⁺ reactions with
6497 atomic and molecular nitrogen: an experimental study. *J. Phys. Chem. A*
6498 103, 1073–1077.
- 6499 Scott, G., Fairley, D., Freeman, C., McEwan, M., Anicich, V., 1998. Gas-phase
6500 reactions of some positive ions with atomic and molecular nitrogen. *J. Chem.*
6501 *Phys.* 109, 9010–9014.
- 6502 Scott, G., Milligan, D., Fairley, D., Freeman, C., McEwan, M., 2000. A selected
6503 ion flow tube study of the reactions of small C_mH_n⁺ ions with O atoms. *J.*
6504 *Chem. Phys.* 112, 4959–4965.
- 6505 Sebree, J., Stern, J., Mandt, K., Domagal-Goldman, S., Trainer, M., 2016.
6506 ¹³C and ¹⁵N fractionation of CH₄/N₂ mixtures during photochemical aerosol
6507 formation: Relevance to Titan. *Icarus* 270, 421–428.
- 6508 Seki, K., He, M., Liu, R., Okabe, H., 1996. Photochemistry of cyanoacetylene
6509 at 193.3 nm. *J. Phys. Chem.* 100, 5349–5353.
- 6510 Seki, K., Okabe, H., 1992. Photodissociation of methylacetylene at 193 nm. *J.*
6511 *Phys. Chem.* 96, 3345–3349.
- 6512 Seki, K., Okabe, H., 1993. Photochemistry of acetylene at 193.3 nm. *J. Phys.*
6513 *Chem.* 97, 5284–5290.
- 6514 Sekine, Y., Imanaka, H., Matsui, T., Khare, B., Bakes, E., McKay, C., Sugita,
6515 S., 2008a. The role of organic haze in Titan’s atmospheric chemistry I. Labo-
6516 ratory investigation on heterogeneous reaction of atomic hydrogen with Titan
6517 tholin. *Icarus* 194, 186–200.

- 6518 Sekine, Y., Lebonnois, S., Imanaka, H., Matsui, T., Bakes, E., McKay, C.,
6519 Khare, B., Sugita, S., 2008b. The role of organic haze in Titan's atmospheric
6520 chemistry II. Effect of heterogeneous reaction to the hydrogen budget and
6521 chemical composition of the atmosphere. *Icarus* 194, 201–211.
- 6522 Semaniak, J., Larson, Å., Le Padellec, A., Semaniak, J., Strömholm, C., Lars-
6523 son, M., Rosén, S., Peverall, R., Danared, H., Djuric, N., Dunn, G., Datz,
6524 S., 1998. Dissociative recombination and excitation of CH_5^+ : Absolute cross
6525 sections and branching fractions. *Astrophys. J.* 498, 886–895.
- 6526 Semaniak, J., Minaev, B., Derkatch, A., Hellberg, F., Neau, A., Rosén, S.,
6527 Thomas, R., Larsson, M., Danared, H., Paál, A., af Ugglas, M., 2001. Dis-
6528 sociative recombination of HCNH^+ : Absolute cross-sections and branching
6529 ratios. *Astrophys. J. Suppl. Ser.* 135, 275–283.
- 6530 Senosiain, J., Klippenstein, S., Miller, J., 2005. The reaction of acetylene with
6531 hydroxyl radicals. *J. Phys. Chem. A* 109, 6045–6055.
- 6532 Sharp, T., Dowell, J., 1967. Isotope effects in dissociative attachment of elec-
6533 trons in methane. *J. Chem. Phys.* 46, 1530–1531.
- 6534 Shaw, D.A., Holland, D.M.P., Macdonald, M.A., Hopkirk, A., Hayes, M.A.,
6535 McSweeney, S.M., 1992. A study of the absolute photoabsorption cross section
6536 and the photoionization quantum efficiency of nitrogen from the ionization
6537 threshold to 485 Å. *Chem. Phys.* 166, 379–391.
- 6538 Shebanits, O., Wahlund, J.E., Edberg, N., Crary, F., Wellbrock, A., Andrews,
6539 D., Vignen, E., Desai, R., Coates, A., Mandt, K., Waite Jr., J., 2016. Ion and
6540 aerosol precursor densities in Titan's ionosphere: A multi-instrument case
6541 study. *J. Geophys. Res. Space Physics* 121, 10,075–10,090.
- 6542 Shebanits, O., Wahlund, J.E., Mandt, K., Ågren, K., Edberg, N., Waite, J.J.,
6543 2013. Negative ion densities in the ionosphere of Titan-Cassini RPWS/LP
6544 results. *Planet. Space Sci.* 84, 153–162.
- 6545 Sheehan, C., Le Padellec, A., Lennard, W., Talbi, D., Mitchell, J., 1999. Merged
6546 beam measurement of the dissociative recombination of HCN^+ and HNC^+ .
6547 *J. Phys. B At. Mol. Opt. Phys.* 32, 3347–3360.
- 6548 Sheehan, C., St.-Maurice, J.P., 2004a. Dissociative recombination of N_2^+ , O_2^+ ,
6549 and NO^+ : Rate coefficients for ground state and vibrationally excited ions.
6550 *J. Geophys. Res.* 109, A03302.
- 6551 Sheehan, C., St.-Maurice, J.P., 2004b. Dissociative recombination of the
6552 methane family ions: Rate coefficients and implications. *Adv. Space Res.*
6553 33, 216–220.
- 6554 Shemansky, D., 1972. CO_2 extinction coefficient 1700 - 3000 Å. *J. Chem. Phys.*
6555 56, 1582–1587.

- 6556 Shemansky, D., Liu, X., 2005. Evaluation of electron impact excitation of N_2 X
6557 $^1\Sigma_g^+(0)$ into the N_2^+ X $^2\Sigma_g^+(\nu)$, A $^2\Pi_u^+(\nu)$, and B $^2\Sigma_u^+(\nu)$ states. *J. Geophys.*
6558 *Res.* 110, #A07307.
- 6559 Shiba, Y., Hirano, T., Nagashima, U., Ishii, K., 1998. Potential energy surfaces
6560 and branching ratio of the dissociative recombination reaction $HCNH^+ + e^-$:
6561 An ab initio molecular orbital study. *J. Chem. Phys.* 108, 698–705.
- 6562 Shindo, F., Bénilan, Y., Guillemin, J.C., Chaquin, P., Jolly, A., Raulin, F.,
6563 2003. Ultraviolet and infrared spectrum of C_6H_2 revisited and vapor pressure
6564 curve in Titan’s atmosphere. *Planet. Space Sci.* 51, 9–17.
- 6565 Shul, R., Passarella, R., DiFazio, L.T., J., Keesee, R., Castleman, A.W., J.,
6566 1988. Ion-molecule reactions involving H_3O^+ , H_2O^+ , and OH^+ at thermal
6567 energy. *J. Phys. Chem.* 92, 4947–4951.
- 6568 Sillanpää, I., Johnson, R., 2015. The role of ion-neutral collisions in Titan’s
6569 magnetospheric interaction. *Planet. Space Sci.* 108, 73–86.
- 6570 Silva, R., Gichuhi, W., Huang, C., Doyle, M., Kislov, V., Mebel, A., Suits, A.,
6571 2008. H elimination and metastable lifetimes in the UV photoexcitation of
6572 diacetylene. *P. Natl. Acad. Sci. USA* 105, 12713–12718.
- 6573 Silva, R., Gichuhi, W., Kislov, V., Landera, A., Mebel, A., Suits, A., 2009. UV
6574 photodissociation of cyanoacetylene: A combined ion imaging and theoretical
6575 investigation. *J. Phys. Chem. A* 113, 11182–11186.
- 6576 Sims, I., Queffelec, J.L., Travers, D., Rowe, B., Herbert, L., Karthausser, J.,
6577 Smith, I., 1993. Rate constants for the reactions of CN with hydrocarbons at
6578 low and ultra-low temperatures. *Chem. Phys. Lett.* 211, 461–468.
- 6579 Sivaramakrishnan, R., Su, M.C., Michael, J., Klippenstein, S., Harding, L.,
6580 Ruscic, B., 2011. Shock tube and theoretical studies on the thermal decom-
6581 position of propane: Evidence for a roaming radical channel. *J. Phys. Chem.*
6582 *A* 115, 3366–3379.
- 6583 Smith, D., Adams, N., 1978a. Binary and ternary reactions of CH_3^+ ions with
6584 several molecules at thermal energies. *Chem. Phys. Lett.* 54, 535–540.
- 6585 Smith, D., Adams, N., 1978b. Molecular synthesis in interstellar clouds: radi-
6586 ative association reactions of CH_3^+ ions. *Chem. Phys. Lett.* 220, L87–L92.
- 6587 Smith, D., Adams, N., Miller, T., 1978a. A laboratory study of the reactions of
6588 N^+ , N_2^+ , N_3^+ , N_4^+ , O^+ , O_2^+ , and NO^+ ions with several molecules at 300
6589 K. *J. Chem. Phys.* 69, 308–318.
- 6590 Smith, D., Church, M., Miller, T., 1978b. Mutual neutralization of simple and
6591 clustered positive and negative ions. *J. Chem. Phys.* 68, 1224–1229.

- 6592 Smith, D., Spanel, P., Mayhew, C., 1992. A selected ion-flow tube study of the
6593 reactions of O⁺, H⁺ and HeH⁺ with several molecular gases at 300 K. *Int.*
6594 *J. Mass Spectrom. Ion Processes* 117, 457–473.
- 6595 Smith, I., Herbst, E., Chang, Q., 2004. Rapid neutral-neutral reactions at low
6596 temperatures: A new network and first results for TMC-1. *Mon. Not. R.*
6597 *Astron. Soc.* 350, 323–330.
- 6598 Smith, I., Sage, A., Donahue, N., Herbst, E., Quan, D., 2006. The temperature-
6599 dependence of rapid low temperature reactions: experiment, understanding
6600 and prediction. *Faraday Discuss.* 133, 137–156.
- 6601 Smith, N., Bénilan, Y., Bruston, P., 1998. The temperature dependant absorp-
6602 tion cross sections of C₄H₂ at mid ultraviolet wavelengths. *Planet. Space Sci.*
6603 46, 1215–1220.
- 6604 Smith, N., Raulin, F., 1999. Modeling of methane photolysis in the reducing
6605 atmospheres of the outer solar system. *J. Geophys. Res.* 104, 1873–1876.
- 6606 Smith, P., Yoshino, K., Parkinson, W., Ito, K., Stark, G., 1991. High resolution
6607 VUV (147-201 nm) photoabsorption cross sections for C₂H₂ at 195 and 295
6608 K. *J. Geophys. Res.* 96, 17529–17533.
- 6609 Smyth, K., Lias, S., Ausloos, P., 1981. Can C₃H₃⁺ be an important soot pre-
6610 cursor, in: *Chemical and Physical Processes in Combustion*, pp. 187–190.
- 6611 Smyth, K., Lias, S., Ausloos, P., 1982. The ion-molecule chemistry of C₃H₃⁺
6612 and the implications for soot formation. *Combust. Sci. Technol.* 28, 147–154.
- 6613 Snow, M., McClintock, W.E., Rottman, G., Woods, T., 2005. Solar stellar
6614 irradiance comparison experiment II (SOLSTICE II): Examination of the
6615 solar stellar comparison technique. *Solar Phys.* 203, 295–324.
- 6616 Snow, T., Stepanovic, M., Betts, N., Eichelberger, B., Martinez, O., Bierbaum,
6617 V., 2009. Formation of gas-phase glycine and cyanoacetylene via associative
6618 detachment reactions. *Astrobiology* 9, 1001–1005.
- 6619 Snowden, D., Smith, M., Jimson, T., Higgins, A., 2018. Energy deposition and
6620 ion production from thermal oxygen ion precipitation during Cassini’s T57
6621 flyby. *Icarus* submitted.
- 6622 Snowden, D., Yelle, R., Galand, M., Coates, A., Wellbrock, A., Jones, G.,
6623 Lavvas, P., 2013. Auroral electron precipitation and flux tube erosion in
6624 Titan’s upper atmosphere. *Icarus* 226, 186–204.
- 6625 Song, Y., Lucas, M., Alcaraz, M., Zhang, J., Brazier, C., 2012. Ultraviolet pho-
6626 todissociation dynamics of the phenyl radical. *J. Chem. Phys.* 136, #044308.
- 6627 Song, Y., Zheng, X., Lucas, M., Zhang, J., 2011. Ultraviolet photodissociation
6628 dynamics of the benzyl radical. *Phys. Chem. Chem. Phys.* 13, 8296–8305.

- 6629 Spanel, P., Smith, D., Henchman, M., 1995. The reactions of some interstellar
6630 ions with benzene, cyclopropane and cyclohexane. *Int. J. Mass Spectrom. Ion*
6631 *Processes* 141, 117–126.
- 6632 Speller, C., Vacher, J., Duc, E., Fitaire, M., 1995. Mass spectrometric study of
6633 three-body ion-molecule clustering reactions of $C_pH_q^+$ ions with N_2 or CH_4 in
6634 N_2 - CH_4 mixtures. *Planet. Space Sci.* 43, 33–39.
- 6635 Stamatovic, A., Schulz, G., 1970. Dissociative attachment in CO and formation
6636 of C^- . *J. Chem. Phys.* 53, 2663–2667.
- 6637 Stancil, P., Dalgarno, A., 1998. Chemical processes in astrophysical radiation
6638 fields. *Faraday Discuss.* 109, 61–69.
- 6639 Stanton, J.F., Gauss, J., Harding, M.E., Szalay, P.G., 2010. with contributions
6640 from Auer, A. A., Bartlett, R. J., Benedikt, U., Berger, C., Bernholdt, D.
6641 E., Bomble, Y. J., et al. and the integral packages *MOLECULE* (Almlöf, J.,
6642 Taylor, P. R.), *PROPS* (Taylor, P. R.), *ABACUS* (Helgaker, T., Jensen, H.
6643 J., Jørgensen, P., Olsen, J.), and ECP routines by Mitin, A. V., van Wüllen,
6644 C. For the current version, see <http://www.cfour.de>.
- 6645 Stavish, L., Fondren, L., Adams, N., 2009. Reactions of N^+ and N_2^+ with
6646 several cyclic molecules studied using a selected ion flow tube. *Int. J. Mass*
6647 *Spectrom.* 281, 103–107.
- 6648 Stearns, J., Zwier, T., Kraka, E., Cremer, D., 2006. Experimental and compu-
6649 tational study of the ultraviolet photolysis of vinylacetylene. Part II. *Phys.*
6650 *Chem. Chem. Phys.* 8, 5317–5327.
- 6651 Steinbauer, M., Giegerich, J., Fischer, K., Fischer, I., 2012. The photodisso-
6652 ciation dynamics of the ethyl radical, C_2H_5 , investigated by velocity map
6653 imaging. *J. Chem. Phys.* 137, #014303.
- 6654 Stevens, M., Evans, J., Lumpe, J., Westlake, J., Ajello, J., Bradley, E., Esposito,
6655 L., 2015. Molecular nitrogen and methane density retrievals from Cassini
6656 UVIS dayglow observations of Titan’s upper atmosphere. *Icarus* 247, 301–
6657 312.
- 6658 Stief, L., Nesbitt, F., Payne, W., Kuo, S., Tao, W., Klemm, R., 1995. Rate
6659 constant and reaction channels for the reaction of atomic nitrogen with the
6660 ethyl radical. *J. Chem. Phys.* 102, 5309–5316.
- 6661 Stief, L., Payne, W., Klemm, R., 1975. A flash photolysis-resonance fluorescence
6662 study of the formation of $O(^1D)$ in the photolysis of water and the reaction
6663 of $O(^1D)$ with H_2 , Ar, and He. *J. Chem. Phys.* 62, 4000–4008.
- 6664 Stoliarov, S., Knyazev, V., Slagle, I., 2000. Experimental study of the reaction
6665 between vinyl and methyl radicals in the gas phase. Temperature and pressure
6666 dependence of overall rate constants and product yields. *J. Phys. Chem. A*
6667 104, 9687–9697.

- 6668 Stolte, W., He, Z., Cutler, J., Lu, Y., Samson, J., 1998. Dissociative photoion-
6669 ization cross sections of N₂ and O₂ from 100 to 800 eV. *At. Data Nucl. Data*
6670 *Tables* 69, 171–179.
- 6671 Stranges, D., Stemmler, M., Yang, X., Chesko, J., Suits, A., Lee, Y., 1998. UV
6672 photodissociation dynamics of allyl radical by photofragment translational
6673 spectroscopy. *J. Chem. Phys.* 109, 5372–5382.
- 6674 Strobel, D., 1974. The photochemistry of hydrocarbons in the atmosphere of
6675 Titan. *Icarus* 21, 466–470.
- 6676 Strobel, D., 2010. Molecular hydrogen in Titan’s atmosphere: Implications
6677 of the measured tropospheric and thermospheric mole fractions. *Icarus* 208,
6678 878–886.
- 6679 Strobel, D.F., 2008. Titan’s hydrodynamically escaping atmosphere. *Icarus* 193,
6680 588–594.
- 6681 Su, T., Bowers, M., 1973. Ion-polar molecule collisions: the effect of ion size on
6682 ion-polar molecule rate constants; the parameterization of the average-dipole-
6683 orientation theory. *Int. J. Mass Spectrom. Ion Processes* 12, 347–356.
- 6684 Suto, M., Lee, L., 1985. Photoabsorption cross section of CH₃CN: Photodis-
6685 sociation rates by solar flux and interstellar radiation. *J. Geophys. Res.* 90,
6686 13,037–13,040.
- 6687 Talbi, D., Ellinger, Y., 1998. Potential energy surface for the electronic disso-
6688 ciative recombination reaction of HCNH⁺: Astrophysical implications on the
6689 HCN/HNC abundance ratio. *Chem. Phys. Lett.* 288, 155–164.
- 6690 Teanby, N., Irwin, P., de Kok, R., Jolly, A., Bézard, B., Nixon, C., Calcutt,
6691 S., 2009. Titan’s stratospheric C₂N₂, C₃H₄, and C₄H₂ abundances from
6692 Cassini/CIRS far-infrared spectra. *Icarus* 202, 620–631.
- 6693 Teanby, N., Irwin, P., de Kok, R., Nixon, C., 2010. Mapping Titan’s HCN in the
6694 far infra-red: implications for photochemistry. *Faraday Discuss.* 147, 51–64.
- 6695 Teanby, N., Irwin, P., de Kok, R., Nixon, C., Coustenis, A., Royer, E., Cal-
6696 cutt, S., Bowles, N., Fletcher, L., Howett, C., Taylor, F., 2008a. Global and
6697 temporal variations in hydrocarbons and nitriles in Titan’s stratosphere for
6698 northern winter observed by Cassini/CIRS. *Icarus* 193, 595–611.
- 6699 Teanby, N., Irwin, P., Nixon, C., Courtin, R., Swinyard, B., Moreno, R., Lel-
6700 louch, E., Rengel, M., Hartogh, P., 2013. Constraints on Titan’s middle at-
6701 mosphere ammonia abundance from Herschel/SPIRE sub-millimetre spectra.
6702 *Planet. Space Sci.* 75, 136–147.
- 6703 Teanby, N., Irwin, P., Nixon, C., de Kok, R., Vinatier, S., Coustenis, A., Sefton-
6704 Nash, E., Calcutt, S., Flasar, F., 2012. Active upper-atmosphere chemistry
6705 and dynamics from polar circulation reversal on Titan. *Nature* 491, 732–735.

- 6706 Teanby, N., de Kok, R., Irwin, P., Osprey, S., Vinatier, S., Gierasch, P., Read,
6707 P., Flasar, F., Conrath, B., Achterberg, R., Bézard, B., Nixon, C., Calcutt,
6708 S., 2008b. Titan's winter polar vortex structure revealed by chemical tracers.
6709 *J. Geophys. Res.* 113, #E12003.
- 6710 Teanby, N.A., Irwin, P.G.J., de Kok, R., Nixon, C.A., Coustenis, A., Bézard, B.,
6711 Calcutt, S.B., Bowles, N.E., Flasar, F.M., Fletcher, L., Howett, C., Taylor,
6712 F.W., 2006. Latitudinal variations of HCN, HC₃N, and C₂N₂ in Titan's
6713 stratosphere derived from Cassini CIRS data. *Icarus* 181, 243–255.
- 6714 Teolis, B., Niemann, H., Waite, H., Gell, D., Perryman, R., Kasprzak, W.,
6715 Mandt, K., Yelle, R., Lee, A., Pelletier, F., Miller, G., Young, D., Bell, J.,
6716 Magee, B., Patrick, E., Grimes, J., Fletcher, G., Vuitton, V., 2015. A revised
6717 sensitivity model for Cassini INMS: Results at Titan. *Space Sci. Rev.* 190,
6718 47–84.
- 6719 Terzieva, R., Herbst, E., 2000. The possibility of nitrogen isotopic fractionation
6720 in interstellar clouds. *Mon. Not. R. Astron. Soc.* 317, 563–568.
- 6721 Teslja, A., Dagdigian, P., Banck, M., Eisfeld, W., 2006. Experimental and
6722 theoretical study of the electronic spectrum of the methylene amidogen radical
6723 (H₂CN): Verification of the ²A₁ ← ²B₂ assignment. *J. Phys. Chem. A* 110,
6724 7826–7834.
- 6725 Teslja, A., Nizamov, B., Dagdigian, P., 2004. The electronic spectrum of
6726 methyleneimine. *J. Phys. Chem. A* 108, 4433–4439.
- 6727 Thomas, R., Hellberg, F., Neau, A., Rosén, S., Larsson, M., Vane, C., Ban-
6728 nister, M., Datz, S., Petrigiani, A., van der Zande, W., 2005. Three-body
6729 fragmentation dynamics of amidogen and methylene radicals via dissociative
6730 recombination. *Phys. Rev. A* 71, 032711.
- 6731 Thomas, R., Kashperka, I., Vignen, E., Geppert, W., Hamberg, M., Larsson, M.,
6732 af Ugglas, M., Zhaunerchyk, V., 2013. Dissociative recombination of CH₄⁺.
6733 *J. Phys. Chem. A* 117, 9999–10005.
- 6734 Tichý, M., Rakshit, A., Lister, D., Twiddy, N., Adams, N., Smith, D., 1979.
6735 A study of the reactions of the ground and metastable states of C⁺, N⁺, S⁺
6736 and N₂⁺ at 300 K. *Int. J. Mass Spectrom. Ion Processes* 29, 231–247.
- 6737 Tickner, A., Lossing, F., 1951. The measurement of low vapor pressures by
6738 means of a mass spectrometer. *J. Phys. Colloid Chem.* 55, 733–740.
- 6739 Tobie, G., Lunine, J., Sotin, C., 2006. Episodic outgassing as the origin of
6740 atmospheric methane on Titan. *Nature* 440, 61–64.
- 6741 Tomasko, M., Doose, L., Engel, S., Dafoe, L., West, R., Lemmon, M.,
6742 Karkoschka, E., See, C., 2008. A model of Titan's aerosols based on mea-
6743 surements made inside the atmosphere. *Planet. Space Sci.* 56, 669–707.

- 6744 Tomasko, M.G., Archinal, B., Becker, T., Bézard, B., Bushroee, M., Combes,
6745 M., Cook, D., Coustenis, A., de Bergh, C., Dafoe, L.E., Doose, L., Douté, S.,
6746 Eibl, A., Engel, S., Gliem, F., Grieger, B., Holso, K., Howington-Kraus, E.,
6747 Karkoschka, E., Keller, H.U., Kirk, R., Kramm, R., Küppers, M., Lanagan,
6748 P., Lellouch, P., Lemmon, M., Lunine, J., McFarlane, E., Moores, J., Prout,
6749 G.M., Rizk, B., Rosiek, M., Rueffer, P., Schröder, S.E., Schmitt, B., See, C.,
6750 Smith, P., Soderblom, L., Thomas, N., West, R., 2005. Rain, winds and haze
6751 during the Huygens probe's descent to Titan's surface. *Nature* 438, 765–778.
- 6752 Tonokura, K., Koshi, M., 2000. Absorption spectrum and cross sections of the
6753 allyl radical measured using cavity ring-down spectroscopy: The $A \leftarrow X$ band.
6754 *J. Phys. Chem. A* 104, 8456–8461.
- 6755 Toubanc, D., Parisot, J., Brillet, J., Gautier, D., Raulin, F., McKay, C., 1995.
6756 Photochemical modeling of Titan's atmosphere. *Icarus* 113, 2–26.
- 6757 Trevitt, A., Prendergast, M., Goulay, F., Savee, J., Osborn, D., Taatjes, C.,
6758 Leone, S., 2013. Product branching fractions of the CH + propene reaction
6759 from synchrotron photoionization mass spectrometry. *J. Phys. Chem. A* 117,
6760 6450–6457.
- 6761 Trevitt, A., Soorkia, S., Savee, J., Selby, T., Osborn, D., Taatjes, C., Leone, S.,
6762 2011. Branching fractions of the CN + C₃H₆ reaction using synchrotron pho-
6763 toionization mass spectrometry: Evidence for the 3-cyanopropene product. *J.*
6764 *Phys. Chem. A* 115, 13467–13473.
- 6765 Troe, J., 1979. Predictive possibilities of unimolecular rate theory. *J. Phys.*
6766 *Chem.* 83, 114–126.
- 6767 Troe, J., 1983. Theory of thermal unimolecular reactions in the fall-off range. I.
6768 Strong collision rate constants. *Ber. Bunsenges. Phys. Chem.* 87, 161–169.
- 6769 Truhlar, D., Garrett, B., Klippenstein, S., 1996. Current status of transition-
6770 state theory. *J. Phys. Chem.* 100, 12771–12800.
- 6771 Tsai, S.T., Lin, C.K., Lee, Y., Ni, C.K., 2000. Dissociation rate of hot benzene.
6772 *J. Chem. Phys.* 113, #67.
- 6773 Tsang, W., 1987. Chemical kinetic database for combustion chemistry part II:
6774 methanol. *J. Phys. Chem. Ref. Data* 16, 471.
- 6775 Tsang, W., 1988. Chemical kinetic database for combustion chemistry part III:
6776 propane. *J. Phys. Chem. Ref. Data* 17, 887.
- 6777 Tsang, W., 1991. Chemical kinetic database for combustion chemistry part V:
6778 propene. *J. Phys. Chem. Ref. Data* 20, 221–274.
- 6779 Tsang, W., 1992. Chemical kinetic database for propellant combustion. II.
6780 Reactions involving CN, NCO, and HNCO. *J. Phys. Chem. Ref. Data* 21,
6781 753–791.

- 6782 Tsang, W., Hampson, R., 1986. Chemical kinetic data base for combustion
6783 chemistry. Part I. Methane and related compounds. *J. Phys. Chem. Ref.*
6784 *Data* 15, 1087–1279.
- 6785 Tsang, W., Herron, J., 1991. Chemical kinetic database for propellant combus-
6786 tion. I. Reactions involving NO, NO₂, HNO, HNO₂, HCN and N₂O. *J. Phys.*
6787 *Chem. Ref. Data* 20, 609–663.
- 6788 Tsuda, S., Yokohata, A., Umaba, T., 1973. Measurement of negative ions formed
6789 by electron impact. IX. Negative ion mass spectra and ionization efficiency
6790 curves of negative ions of m/e 25, 26, 27, 38, 39, 40 and 50 from acrylonitrile.
6791 *Bull. Chem. Soc. Jpn* 46, 2273–2277.
- 6792 Tsuji, M., Matsumura, K., Funatsu, T., Nishimura, Y., Obase, H., 1994.
6793 Ion/molecule reactions of CO₂⁺ with simple aliphatic hydrocarbons at ther-
6794 mal energy. *Int. J. Mass Spectrom. Ion Processes* 135, 165–180.
- 6795 Tsuji, M., Matsumura, K., Funatsu, T., Nishimura, Y., Obase, H., Kagawa,
6796 S., Kanetaka, Y., 1993. Ion-molecule reactions of CO₂⁺ with butane and
6797 isobutane at thermal energy. *B. Chem. Soc. Jpn.* 66, 2864–2870.
- 6798 Tucker, O.J., Waalkes, W., Tenishev, V.M., Johnson, R.E., Bieler, A., Combi,
6799 M.R., Nagy, A.F., 2016. Examining the exobase approximation: DSMC mod-
6800 els of Titan’s upper atmosphere. *Icarus* 272, 290–300.
- 6801 Tully, J., 1975. Reactions of O(¹D) with atmospheric molecules. *J. Chem. Phys.*
6802 62, 1893–1898.
- 6803 Vacher, J., Le Duc, E., Fitaire, M., 1997. Ion-molecule clustering reactions of
6804 HCNH⁺ ion with N₂ and/or CH₄ in N₂-CH₄ mixtures. *Planet. Space Sci.* 45,
6805 1407–1416.
- 6806 Vacher, J., Le Duc, E., Fitaire, M., 1999. Titan’s atmosphere: possible clustering
6807 reactions of HCNH⁺, HCNH⁺(N₂) and HCNH⁺(CH₄) ions with acetylene.
6808 *Planet. Space Sci.* 47, 151–162.
- 6809 Vacher, J., Le Duc, E., Fitaire, M., 2000. Clustering reactions of HCNH⁺,
6810 HCNH⁺(N₂) and HCNH⁺(CH₄) with ethane: application to Titan atmo-
6811 sphere. *Planet. Space Sci.* 48, 237–247.
- 6812 Vaghjiani, G., 1993. Ultraviolet absorption cross sections for N₂H₄ vapor be-
6813 tween 191–291 nm and H(²S) quantum yield in 248 nm photodissociation at
6814 296 K. *J. Chem. Phys.* 98, 2123–2131.
- 6815 Vaghjiani, G., 1995. Laser photolysis studies of hydrazine vapor: 193 and 222
6816 nm H-atom primary quantum yields at 296 K, and the kinetics of H + N₂H₄
6817 reaction over the temperature range 222–657 K. *Int. J. Chem. Kin.* 27, 777–
6818 790.

- 6819 Vakhtin, A., Heard, D., Smith, I., Leone, S., 2001a. Kinetics of C_2H radical re-
6820 actions with ethene, propene and 1-butene measured in a pulsed Laval nozzle
6821 apparatus at $T = 103$ and 296 K. *Chem. Phys. Lett.* 348, 21–26.
- 6822 Vakhtin, A., Heard, D., Smith, I., Leone, S., 2001b. Kinetics of reactions of
6823 C_2H radical with acetylene, O_2 , methylacetylene, and allene in a pulsed Laval
6824 nozzle apparatus at $T = 103$ K. *Chem. Phys. Lett.* 344, 317–324.
- 6825 Vejby-Christensen, L., Andersen, L., Heber, O., Kella, D., Pedersen, H.,
6826 Schmidt, H., Zajfman, D., 1997. Complete branching ratios for the dissocia-
6827 tive recombination of H_2O^+ , H_3O^+ , and CH_3^+ . *Astrophys. J.* 483, 531–540.
- 6828 Vereecken, L., Peeters, J., 1999. Detailed microvariational RRKM master equa-
6829 tion analysis of the product distribution of the $C_2H_2 + CH(X^2\Pi)$ reaction
6830 over extended temperature and pressure ranges. *J. Phys. Chem. A* 103, 5523–
6831 5533.
- 6832 Viggiano, A., Ehlerding, A., Arnold, S., Larsson, M., 2005. Dissociative recom-
6833 bination of hydrocarbon ions. *J. Phys. Conf. Ser.* 4, 191–197.
- 6834 Viggiano, A., Paulson, J., 1983. Temperature dependence of associative detach-
6835 ment reactions. *J. Chem. Phys.* 79, 2241–2245.
- 6836 Vigren, E., Galand, M., Shebanits, O., Wahlund, J.E., Geppert, W., Lavvas, P.,
6837 Vuitton, V., Yelle, R., 2014. Increasing positive ion number densities below
6838 the peak of ion-electron pair production in Titan’s ionosphere. *Astrophys. J.*
6839 786, #69.
- 6840 Vigren, E., Galand, M., Yelle, R., Cui, J., Wahlund, J.E., Ågren, K., Lavvas, P.,
6841 Müller-Wodarg, I., Strobel, D., Vuitton, V., Bazin, A., 2013. On the thermal
6842 electron balance in Titan’s sunlit upper atmosphere. *Icarus* 223, 234–251.
- 6843 Vigren, E., Galand, M., Yelle, R., Wellbrock, A., Coates, A., Snowden, D.,
6844 Cui, J., Lavvas, P., Edberg, N., Shebanits, O., Wahlund, J.E., Vuitton, V.,
6845 Mandt, K., 2015. Ionization balance in Titan’s nightside ionosphere. *Icarus*
6846 248, 539–546.
- 6847 Vigren, E., Hamberg, M., Zhaunerchyk, V., Kamińska, M., Thomas, R., Lars-
6848 son, M., Millar, T., Walsh, C., Geppert, W., 2009. The dissociative recom-
6849 bination of protonated acrylonitrile, CH_2CHCNH^+ , with implications for the
6850 nitrile chemistry in dark molecular clouds and the upper atmosphere of Titan.
6851 *Astrophys. J.* 695, 317–324.
- 6852 Vigren, E., Hamberg, M., Zhaunerchyk, V., Kamińska, M., Thomas, R., Trip-
6853 pel, S., Wester, R., Zhang, M., Kashperka, I., af Ugglas, M., Semaniak, J.,
6854 Larsson, M., Geppert, W., 2010a. Dissociative recombination of protonated
6855 propionitrile, $CH_3CH_2CNH^+$: Implications for Titan’s upper atmosphere. *As-
6856 trophys. J.* 722, 847–850.

- 6857 Vigren, E., Hamberg, M., Zhaunerchyk, V., Kamińska, M., Thomas, R., Trippel,
6858 S., Zhang, M., Kashperka, I., af Ugglas, M., Walsh, C., Wester, R., Sema-
6859 niak, J., Larsson, M., Geppert, W., 2010b. Dissociative recombination of the
6860 acetaldehyde cation, CH_3CHO^+ . *Phys. Chem. Chem. Phys.* 12, 11670–11673.
- 6861 Vigren, E., Kamińska, M., Hamberg, M., Zhaunerchyk, V., Thomas, R., Daniels-
6862 son, M., Semaniak, J., Andersson, P., Larsson, M., Geppert, W., 2008. Dissoc-
6863 iative recombination of fully deuterated protonated acetonitrile, CD_3CND^+ :
6864 product branching fractions, absolute cross section and thermal rate coeffi-
6865 cient. *Phys. Chem. Chem. Phys.* 10, 4014–4019.
- 6866 Vigren, E., Semaniak, J., Hamberg, M., Zhaunerchyk, V., Kamińska, M.,
6867 Thomas, R., af Ugglas, M., Larsson, M., Geppert, W., 2012a. Dissociative
6868 recombination of nitrile ions with implications for Titan’s upper atmosphere.
6869 *Planet. Space Sci.* 60, 102–106.
- 6870 Vigren, E., Zhaunerchyk, V., Hamberg, M., Kamińska, M., Semaniak, J., af Ug-
6871 glas, M., Larsson, M., Thomas, R., Geppert, W., 2012b. Reassessment of the
6872 dissociative recombination of N_2H^+ at CRYRING. *Astrophys. J.* 757, #34.
- 6873 Vinatier, S., Bézard, B., Fouchet, T., Teanby, N., de Kok, R., Irwin, P., Con-
6874 rath, B., Nixon, C., Romani, P., Flasar, F., Coustenis, A., 2007a. Vertical
6875 abundance profiles of hydrocarbons in Titan’s atmosphere at 15° S and 80°
6876 N retrieved from Cassini/CIRS spectra. *Icarus* 188, 120–138.
- 6877 Vinatier, S., Bézard, B., Nixon, C., 2007b. The Titan $^{14}\text{N}/^{15}\text{N}$ and $^{12}\text{C}/^{13}\text{C}$
6878 isotopic ratios in HCN from Cassini/CIRS. *Icarus* 191, 712–721.
- 6879 Vinatier, S., Bézard, B., Nixon, C., Mamoutkine, A., Carlson, R., Jennings,
6880 D., Guandique, E., Teanby, N., Bjoraker, G., Flasar, F., Kunde, V., 2010.
6881 Analysis of Cassini/CIRS limb spectra of Titan acquired during the nominal
6882 mission I. Hydrocarbons, nitriles and CO_2 vertical mixing ratio profiles. *Icarus*
6883 205, 559–570.
- 6884 Vuitton, V., Doussin, J.F., Bénilan, Y., Raulin, F., Gazeau, M.C., 2006a. Ex-
6885 perimental and theoretical study of hydrocarbon photochemistry applied to
6886 Titan stratosphere. *Icarus* 185, 287–300.
- 6887 Vuitton, V., Dutuit, O., Smith, M., Balucani, N., 2014. Chemistry of Titan’s
6888 atmosphere, in: Müller-Wodarg, I., Griffith, C., Lellouch, E., Cravens, T.
6889 (Eds.), *Titan: Interior, Surface, Atmosphere and Space Environment*. Cam-
6890 bridge University Press. chapter 7, pp. 224–284.
- 6891 Vuitton, V., Lavvas, P., Yelle, R., Galand, M., Wellbrock, A., Lewis, G., Coates,
6892 A., Wahlund, J.E., 2009. Negative ion chemistry in Titan’s upper atmosphere.
6893 *Planet. Space Sci.* 57, 1558–1572.
- 6894 Vuitton, V., Yelle, R., Anicich, V., 2006b. The nitrogen chemistry of Titan’s
6895 upper atmosphere revealed. *Astrophys. J.* 647, L175–L178.

- 6896 Vuitton, V., Yelle, R., Cui, J., 2008. Formation and distribution of benzene on
6897 Titan. *J. Geophys. Res.* 113, #E05007.
- 6898 Vuitton, V., Yelle, R., Lavvas, P., Klippenstein, S., 2012. Rapid association
6899 reactions at low pressure: Impact on the formation of hydrocarbons on Titan.
6900 *Astrophys. J.* 744, #11.
- 6901 Vuitton, V., Yelle, R., McEwan, M., 2007. Ion chemistry and N-containing
6902 molecules in Titan's upper atmosphere. *Icarus* 191, 722–742.
- 6903 Wagener, R., 1990. Influence of temperature on the removal rates of methylene
6904 (a^1A_1) by inert gases and hydrocarbons. *Z. Naturforsch. A* 45, 649–56.
- 6905 Wahlund, J.E., Boström, R., Gustafsson, G., Gurnett, D., Kurth, W., Pedersen,
6906 A., Averkamp, T., Hospodarsky, G., Persoon, A., Canu, P., Neubauer, F.,
6907 Dougherty, M., Eriksson, A., Morooka, M., Gill, R., André, M., Eliasson,
6908 L., Müller-Wodarg, I., 2005. Cassini measurements of cold plasma in the
6909 ionosphere of Titan. *Science* 308, 986–989.
- 6910 Waite, J.J., Niemann, H., Yelle, R., Kasprzak, W., Cravens, T., Luhmann, J.,
6911 McNutt, R., Ip, W., Gell, D., De La Haye, V., Müller-Wodarg, I., Magee, B.,
6912 Borggren, N., Ledvina, S., Fletcher, G., Walter, E., Miller, R., Scherer, S.,
6913 Thorpe, R., Xu, J., Block, B., Arnett, K., 2005. Ion Neutral Mass Spectrom-
6914 eter results from the first flyby of Titan. *Science* 308, 982–986.
- 6915 Waite, J.J., Young, D., Cravens, T., Coates, A., Crary, F., Magee, B., Westlake,
6916 J., 2007. The process of tholin formation in Titan's upper atmosphere. *Science*
6917 316, 870–875.
- 6918 Wakelam, V., Herbst, E., Loison, J.C., Smith, I., Chandrasekaran, V., Pavone,
6919 B., Adams, N., Bacchus-Montabonel, M.C., Bergeat, A., Béroff, K., Bier-
6920 baum, V., Chabot, M., Dalgarno, A., van Dishoeck, E., Faure, A., Geppert,
6921 W., Gerlich, D., Galli, D., Hébrard, E., Hersant, F., Hickson, K., Honvault,
6922 P., Klippenstein, S., Le Picard, S., Nyman, G., Pernot, P., Schlemmer, S.,
6923 Selsis, F., Sims, I., Talbi, D., Tennyson, J., Troe, J., Wester, R., Wiesenfeld,
6924 L., 2012. A kinetic database for astrochemistry (KIDA). *Astrophys. J. Suppl.*
6925 *Ser.* 199, #21.
- 6926 Wakelam, V., Loison, J.C., Herbst, E., Pavone, B., Bergeat, A., Béroff, K.,
6927 Chabot, M., Faure, A., Galli, D., Geppert, W., Gerlich, D., Gratier, P.,
6928 Harada, N., Hickson, K., Honvault, P., Klippenstein, S., Le Picard, S., Ny-
6929 man, G., Ruaud, M., Schlemmer, S., Sims, I., Talbi, D., Tennyson, J., Wester,
6930 R., 2015. The 2014 KIDA network for interstellar chemistry. *Astrophys. J.*
6931 *Suppl. Ser.* 217, #20.
- 6932 Wallington, T., Egsgaard, H., Nielsen, O., Platz, J., Sehested, J., Stein, T.,
6933 1998. UV-visible spectrum of the phenyl radical and kinetics of its reaction
6934 with NO in the gas phase. *Chem. Phys. Lett.* 290, 363–370.

- 6935 Walsh, C., Harada, N., Herbst, E., Millar, T., 2009. The effects of molecular
6936 anions on the chemistry of dark clouds. *Astrophys. J.* 700, 752–761.
- 6937 Walter, C.W., Cosby, P.C., Helm, H., 1993. $N(^4S_0)$, $N(^2D_0)$ and $N(^2P_0)$ yields in
6938 predissociation of exacted singlet state of N_2 . *J. Chem. Phys.* 99, 3553–3561.
- 6939 Wang, H., Frenklach, M., 1994. Calculations of rate coefficients for the chem-
6940 ically activated reactions of acetylene with vinylic and aromatic radicals. *J.*
6941 *Phys. Chem.* 98, 11465–11489.
- 6942 Wellbrock, A., Coates, A., Jones, G., Lewis, G., Waite, J., 2013. Cassini CAPS-
6943 ELS observations of negative ions in Titan’s ionosphere: Trends of density
6944 with altitude. *Geophys. Res. Lett.* 40, 4481–4485.
- 6945 Wendt, H., Hunziker, H., 1984. The UV spectra of primary, secondary, and
6946 tertiary radicals. *J. Chem. Phys.* 81, 717–723.
- 6947 Werner, H.J., Knowles, P., Knizia, G., Manby, F., Schutz, M., Celani, P., Ko-
6948 rona, T., Lindh, R., Mitrushenkov, A., Rauhut, G., et al., 2012. MOLPRO,
6949 version 2012.1, A package of ab initio programs. see <http://www.molpro.net>.
- 6950 Westlake, J., Waite, J., Bell, J., Perryman, R., 2014. Observed decline in
6951 Titan’s thermospheric methane due to solar cycle drivers. *J. Geophys. Res.*
6952 *Space Physics* 119, 8586–8599.
- 6953 Westlake, J., Waite Jr., J., Mandt, K., Carrasco, N., Bell, J., Magee, B.,
6954 Wahlund, J.E., 2012. Titan’s ionospheric composition and structure: Photo-
6955 chemical modeling of Cassini INMS data. *J. Geophys. Res.* 117, #E01003.
- 6956 Wiese, W.L., Fuhr, J.R., 2007. Improved critical compilations of selected atomic
6957 transition probabilities for neutral and singly ionized carbon and nitrogen. *J.*
6958 *Phys. Chem. Ref. Data* 36, 1287–1345.
- 6959 Wilhelm, M., Nikow, M., Letendre, L., Dai, H.L., 2009. Photodissociation of
6960 vinyl cyanide at 193 nm: Nascent product distributions of the molecular
6961 elimination channels. *J. Chem. Phys.* 130, #044307.
- 6962 Willacy, K., Allen, M., Yung, Y., 2016. A new astrobiological model of the
6963 atmosphere of Titan. *Astrophys. J.* 829, #79.
- 6964 Wilson, E., Atreya, S., 2000. Sensitivity studies of methane photolysis and its
6965 impact on hydrocarbon chemistry in the atmosphere of Titan. *J. Geophys.*
6966 *Res.* 105, 20263–20273.
- 6967 Wilson, E., Atreya, S., 2003. Chemical sources of haze formation in Titan’s
6968 atmosphere. *Planet. Space Sci.* 51, 1017–1033.
- 6969 Wilson, E., Atreya, S., 2004. Current state of modeling the photochemistry of
6970 Titan’s mutually dependent atmosphere and ionosphere. *J. Geophys. Res.*
6971 109, #E06002.

- 6972 Wilson, E., Atreya, S., Coustenis, A., 2003. Mechanisms for the formation of
6973 benzene in the atmosphere of Titan. *J. Geophys. Res.* 108, #5014.
- 6974 Wilson, P., McEwan, M., Meot-Ner, M., 1994a. Reactions of CH₃OCH₂⁺ with
6975 nitrogen bases: a mechanism for the formation of protonated imines. *Int. J.*
6976 *Mass Spectrom. Ion Processes* 132, 149–152.
- 6977 Wilson, S., Ashfold, M., Dixon, R., 1994b. The dissociation dynamics of the
6978 methyl radical following excitation to the B ²A₁' state. *Chem. Phys. Lett.*
6979 222, 457–464.
- 6980 Wilson, S., Howe, J., Rosser, K., Ashfold, M., Dixon, R., 1994c. A reinvestiga-
6981 tion of the near-ultraviolet photodissociation dynamics of the methyl radical.
6982 *Chem. Phys. Lett.* 227, 456–460.
- 6983 Wincel, H., Fokkens, R., Nibbering, N., 1989. On the structure and isomeriza-
6984 tion/dissociation reactions of C₃H₆N⁺ generated by methylation of acetonit-
6985 rile in the gas phase. *Int. J. Mass Spectrom. Ion Processes* 91, 339–355.
- 6986 Wincel, H., Wlodek, S., Bohme, D., 1988. Acetonitrile in gas-phase ion/molecule
6987 chemistry. *Int. J. Mass Spectrom. Ion Processes* 84, 69–87.
- 6988 Wong, A., Morgan, C., Yung, Y., Owen, T., 2002. Evolution of CO on Titan.
6989 *Icarus* 155, 382–392.
- 6990 Woodall, J., Agúndez, M., Markwick-Kemper, A., Millar, T., 2007. The UMIST
6991 database for astrochemistry 2006. *Astron. Astrophys.* 466, 1197.
- 6992 Woods, T., Eparvier, F., Bailey, S., Chamberlin, P., Lean, J., Rottman, G.,
6993 Solomon, S., Tobiska, W., Woodraska, D., 2005. Solar EUV Experiment
6994 (SEE): Mission overview and first results. *J. Geophys. Res.* 110, #A01312.
- 6995 Woon, D., Herbst, E., 2009. Quantum chemical predictions of the properties
6996 of known and postulated neutral interstellar molecules. *Astrophys. J. Suppl.*
6997 *Ser.* 185, 273–288.
- 6998 Woon, D., Park, J.Y., 2009. Modeling chemical growth processes in Ti-
6999 tan's atmosphere. 2. Theoretical study of reactions between C₂H and
7000 ethene, propene, 1-butene, 2-butene, isobutene, trimethylethene, and tetram-
7001 ethylethene. *Icarus* 202, 642–655.
- 7002 Wu, G., Jiang, B., Ran, Q., Zhang, J., Harich, S., Yang, X., 2004. Photodisso-
7003 ciation dynamics of the methyl radical at 212.5 nm: Effect of parent internal
7004 excitation. *J. Chem. Phys.* 120, 2193–2198.
- 7005 Wu, R.Y., Chien, T.S., Liu, G.S., Judge, D.L., Caldwell, J.J., 1989. Photoab-
7006 sorption and direct dissociation cross sections of C₂H₂ in the 1530–1930 Å
7007 region: A temperature dependant study. *J. Chem. Phys.* 91, 272–280.

- 7008 Xu, Y., Chang, Y., Lu, Z., Ng, C., 2013. Absolute integral cross sections and
7009 product branching ratios for the vibrationally selected ion-molecule reactions:
7010 $\text{N}_2^+(X^2\Sigma_g^+; \nu^+ = 0 - 2) + \text{CH}_4$. *Astrophys. J.* 769, #72.
- 7011 Xu, Z.F., Li, S.M., Yu, Y.X., Li, Z.S., Sun, C.C., 1999. Theoretical studies on the
7012 reaction path dynamics and variational transition-state theory rate constants
7013 of the hydrogen-abstraction reactions of the $\text{NH}(X^3\Sigma^-)$ radical with methane
7014 and ethane. *J. Phys. Chem. A* 103, 4910–4917.
- 7015 Yang, D., Yu, T., Lin, M., Melius, C., 1992a. Cyanogen (CN) radical reactions
7016 with hydrogen cyanide and ethanedinitrile (C_2N_2): comparison of theory and
7017 experiment. *J. Chem. Phys.* 97, 222–226.
- 7018 Yang, D., Yu, T., Wang, N., Lin, M., 1992b. CN radical reactions with selected
7019 olefins in the temperature range 174–740 K. *Chem. Phys.* 160, 317–325.
- 7020 Yang, D., Yu, T., Wang, N., Lin, M., 1992c. Temperature dependence of
7021 cyanogen radical reactions with selected alkanes: CN reactivities towards
7022 primary, secondary and tertiary C-H bonds. *Chem. Phys.* 160, 307–315.
- 7023 Yang, Z., Cole, C., Martinez, O.J., Carpenter, M., Snow, T., Bierbaum, V.,
7024 2011. Experimental and theoretical studies of reactions between H atoms and
7025 nitrogen-containing carbanions. *Astrophys. J.* 739, #19.
- 7026 Ye, L., Georgievskii, Y., Klippenstein, S., 2015. Pressure-dependent branching
7027 in the reaction of $^1\text{CH}_2$ with C_2H_4 and other reactions on the C_3H_6 potential
7028 energy surface. *Proc. Comb. Inst.* 35, 223–230.
- 7029 Yelle, R., Cui, J., Müller-Wodarg, I., 2008. Methane escape from Titan’s atmo-
7030 sphere. *J. Geophys. Res.* 113, #E10003.
- 7031 Yelle, R., Vuitton, V., Lavvas, P., Klippenstein, S.J., Smith, M.A., Hörst, S.M.,
7032 Cui, J., 2010. Formation of NH_3 and CH_2NH in Titan’s upper atmosphere.
7033 *Faraday Discuss.* 147, 31–49.
- 7034 Yen, T., Garand, E., Shreve, A., Neumark, D., 2010. Anion photoelectron
7035 spectroscopy of C_3N^- and C_5N^- . *J. Phys. Chem. A* 114, 3215–3220.
- 7036 Yoshino, K., Esmond, J., Sun, Y., Parkinson, W., Ito, K., Matsui, T., 1996.
7037 Absorption cross section measurements of carbon dioxide in the wavelength
7038 region 118.7 - 175.5 nm and the temperature dependence. *J. Quant. Spectrosc.*
7039 *Radiat. Transfer* 55, 53–60.
- 7040 Yu, T., Lin, M., 1993. Kinetics of phenyl radical reactions studied by the
7041 ”cavity-ring-down” method. *J. Am. Chem. Soc.* 115, 4371–4372.
- 7042 Yung, Y.L., Allen, M., Pinto, J.P., 1984. Photochemistry of the atmosphere of
7043 Titan: Comparison between model and observations. *Astrophys. J. Suppl.*
7044 *Ser.* 55, 465–506.

- 7045 Zabarnick, S., Fleming, J., Lin, M., 1989. Kinetics of methylidyne ($\text{CH } X^2\Pi$)
7046 radical reactions with ammonia and methylamines. *Chem. Phys.* 132, 407–
7047 411.
- 7048 Zabarnick, S., Fleming, J., Lin, M., 1991. Direct measurement of rate constants
7049 for the reactions of CH and CD with HCN and DCN. *Chem. Phys.* 150,
7050 109–115.
- 7051 Zabarnick, S., Lin, M., 1989. Kinetics of $\text{CN}(X^2\Sigma^+)$ radical reactions with
7052 HCN, BrCN and CH_3CN . *Chem. Phys.* 134, 185–191.
- 7053 Žabka, J., Polášek, M., Ascenzi, D., Tosi, P., Roithová, J., Schröder, D., 2009.
7054 Reactivity of C_2H_5^+ with benzene: Formation of ethylbenzenium ions and
7055 implications for Titan’s ionospheric chemistry. *J. Phys. Chem. A* 113, 11153–
7056 11160.
- 7057 Žabka, J., Roithová, J., Španěl, P., Herman, Z., 2010. Dynamics of formation
7058 of products D_2CN^+ , DCN^+ , and CD_3^+ in the reaction of N^+ with CD_4 : A
7059 crossed-beam and theoretical study. *J. Phys. Chem. A* 114, 1384–1391.
- 7060 Zhang, F., Kim, S., Kaiser, R., 2009. A crossed molecular beams study of the
7061 reaction of the ethynyl radical ($\text{C}_2\text{H}(X^2\Sigma^+)$) with allene ($\text{H}_2\text{CCCH}_2(X^1A_1)$).
7062 *Phys. Chem. Chem. Phys.* 11, 4707–4714.
- 7063 Zhang, F., Parker, D., Kim, Y., Kaiser, R., Mebel, A., 2011. On the formation
7064 of ortho-benzyne ($o\text{-C}_6\text{H}_4$) under single collision conditions and its role in
7065 interstellar chemistry. *Astrophys. J.* 728, 141–150.
- 7066 Zhang, Q., Zhang, R., Chan, K., Bello, I., 2005. Ab initio and variational
7067 transition state approach to $\beta\text{-C}_3\text{N}_4$ formation: Kinetics for the reaction of
7068 CH_3NH_2 with H. *J. Phys. Chem. A* 109, 9112–9117.
- 7069 Zhao, Z.X., Liu, J.Y., Wang, L., Zhang, H., Hou, C.Y., Sun, C.C., 2008. A study
7070 of the hydrogen abstraction reactions of C_2H radical with CH_3CN , $\text{C}_2\text{H}_5\text{CN}$,
7071 and $\text{C}_3\text{H}_7\text{CN}$ by dual-level generalized transition state theory. *J. Phys. Chem.*
7072 *A* 112, 8455–8463.
- 7073 Zhu, Z., Zhang, Z., Huang, C., Pei, L., Chen, C., Chen, Y., 2003. Kinetics of
7074 CCN radical reactions with a series of normal alkanes. *J. Phys. Chem. A* 107,
7075 10288–10291.
- 7076 Zielinska, T., Wincel, H., 1970. Ion-molecule reactions in methylamine and
7077 methylamine-ammonia systems. *Nukleonika* 15, 26–36.
- 7078 Zymak, I., Hejduk, M., Mulin, D., Plašil, R., Glosík, J., Gerlich, D., 2013. Low-
7079 temperature ion trap studies of $\text{N}^+(^3P_{ja}) + \text{H}_2(j) \rightarrow \text{NH}^+ + \text{H}$. *Astrophys*
7080 *J.* 768, #86.